Atmospheric chemistry of new 'green' solvents

Caterina Mapelli

PhD

Abstract

Solvents represent one on the main sources of pollution from the chemical industry, and the search for alternative molecules that are less problematic for the environment and human health has become one of the greatest challenges of green chemistry. However, despite the known impact of volatile solvents on air quality, little attention has been given to the atmospheric behaviour of these new 'green' organic compounds. In this work, the atmospheric degradation of five promising 'green' solvents was investigated, using both laser-based methods at University of York and the relative rate technique at the University of Iaşi.

The rate coefficient for the reaction of 2,2,5,5-tetramethyloxolane (TMO) with OH was studied via PLP-LIF and RR and was estimated to measure $k_{3.1}$ (296 K) = $(3.1 \pm 0.4) \times 10^{-12}$ cm^3 molecule^{-1} s^{-1}. Reactivity of cyclopentyl methyl ether (CPME) with OH was also investigated through both PLP-LIF and RR, and the rate coefficients determined was $k_{5.1}$(296 K) = $(1.5 \pm 0.3) \times 10^{-11}$ cm^3 molecule^{-1} s^{-1}. Rate coefficients for the reaction of OH with pinacolone (PCO), methylpivalate (MPA), and cyclopentanone (CPO) were studied via PLP-LIF and were estimated to measure respectively $k_{4.1}$ (296 K) = $(1.2 \pm 0.2) \times 10^{-12}$ cm^3 molecule^{-1} s^{-1}, $k_{4.2}$(296 K) = $(1.3 \pm 0.3) \times 10^{-12}$ cm^3 molecule^{-1} s^{-1}, and $k_{5.3}$(296 K) = $(2.8 \pm 0.4) \times 10^{-12}$ cm^3 molecule^{-1} s^{-1}. Temperature dependence studies revealed non-Arrhenius behaviour for all the observed k(296 − 480 K), confirming the complex behaviour of oxygenated compounds and the need for experimental data. Structure Activity Relationship (SAR) calculations were able to predict each k(296 K) value with satisfactory accuracy with the exception of $k_{3.1}$ (OH + TMO) for which the steric hindrance of the methyl groups conferred to the reaction a level of complexity beyond the SAR outreach. SAR calculations were less successful at prediction of k(T) trends, suggesting that in some cases the SAR was estimating a satisfactory k(296 K) value for the wrong reasons.

Reaction with Cl was also investigated via RR experiments for TMO and CPME, leading to $k_{3.2,RR}$ (296 K) = $(1.2 \pm 0.1) \times 10^{-10}$ cm^3 molecules^{-1} s^{-1} for TMO + Cl, and $k_{5.2}$(296 K) = $(3.1 \pm 0.6) \times 10^{-10}$ cm^3 molecule^{-1} s^{-1}. CPME showed the fastest reactivity with OH and Cl, thanks to the activated C-H bonds next to the ether oxygen. Accordingly, its estimated lifetime was the smallest with a value of 14 hours, followed by CPO with a lifetime of 63 hours, 3 days for TMO and 9 days for PCO and MPA. For the ketones CPO and PCO, photolysis by UV light in the troposphere was an alternative degradation route. In this work, UV-vis. absorption spectroscopy of dilute (in cyclohexane) solutions was used to gain insight into gas-phase photolysis rates. Large uncertainty remains in these parameters, mainly because of a lack of quantum yield information. Inclusion of these parameters into lifetime estimation suggested much smaller values of 35 hours for CPO and of 3 days for PCO. Finally, estimated Photochemical Ozone Creation Potential (POCP$_E$) was calculated leading to a value of 11 for MPA,18 for TMO, 26 for PCO and CPO, and 45 for CPME, reaching the same POCP$_E$ value of toluene, and suggesting that the most reactive CPME would have also the most severe impact on air quality.

Acknowledgements

I declare that this thesis is a presentation of original work. I am the author of this work and, where other people have contributed, this is clearly acknowledged. This work has not previously been presented for a degree or other qualification at this University or elsewhere. From this study, two papers were published in the journal Atmospheric Chemistry and Physics and were quoted in the thesis. All sources are acknowledged as references.

Table of Contents

1. Introduction

In the past 20 years, thanks to the increasing public awareness on issues like pollution and climate change, the attention toward sustainability and green technology has strikingly grown. In this context, scientists of all fields, particularly chemistry, are developing new alternatives that will lead to a substantial change in technological trends. The chemical industry is recognized as major source of pollution and in many chemical processes solvents represent more than a half of the material used (Jiménez-González et al., 2004). Since many of these chemicals present toxicological and environmental issues, many efforts have been made to formulate new 'green' solvents, solvents that are more sustainable in terms of health, safety, and environmental impact. The use of solvents affects water, soil, and air pollution in different ways. In this study, we wanted to focus on the atmospheric chemistry of 'green' solvents, as most of these compounds are volatile organic species and lack of the basic data necessary for an assessment of their impact on air quality.

1.1.   Solvents and the Environment

There are several definitions of the term 'solvent' (Clark et al., 2017). The IUPAC Compendium of Chemical Terminology, also known as IUPAC gold book, describes solvents in the context of liquid-liquid distribution as *"the term applied to the whole initial liquid phase containing the extractant"* (Mcnaught et al., 2006). The same source explains again the concept of solvent in the definition of solution: *"A liquid or solid phase containing more than one substance, when for convenience one (or more) substance, which is called the solvent, is treated differently from the other substances, which are called solutes"*. This definition includes a wide variety of chemical substances of different nature, like ionic solvents and hydrocarbons, and it could be expanded to gas phase solvents like CO_2. However, the most common and frequently used solvents are organic compounds, only preceded by water. Organic solvents are used to dissolve other compounds in industrial or domestic applications that involve all the chemical sectors. Considering the function and the large-scale usage of solvents, their impact on the environment is a matter of concern. Organic solvents are in fact one of the main sources of pollution from the chemical sector, with contamination of water, soil, and the air. In this chapter, sources and uses of solvents will be analysed, together with the implications on pollutant emissions and air quality.

1.1.1. Solvent applications and uses.

Solvents are ubiquitous both in our everyday life and in the chemical industry. Countless applications of organic solvents were developed since the industrialization in the 19th century and since then, their importance in innumerable fields and sectors has enormously grown. In 2020, the solvent industry reached 5 million tonnes of annual sold volumes only in Europe and 4 billion euro turnover for the European manufacturers (Esig, 2020).

The applications of solvents include a wide variety of activities. Figure 1.2 shows the solvent uses by sector in Europe in 2017 (Winterton, 2021). The main category, with a percentage of 46%, was Paints and Coatings, where organic solvents, thanks to their relatively high volatility, carry out their function evaporating quickly and leaving a film of paint or a coating on a surface. Their role in solubilising or dispersing resins and pigments is essential and

requires large volumes of material. The next most important sector, even though accounting for just 9%, was the pharmaceutical industry. Here they are used in both reaction and purification media, solvents (water excluded) representing the largest part (by mass) of the material used in the manufacturing of an API (Active Pharmaceutical Ingredient) (Jimenez-Gonzalez et al., 2011).

Solvent use by sector:
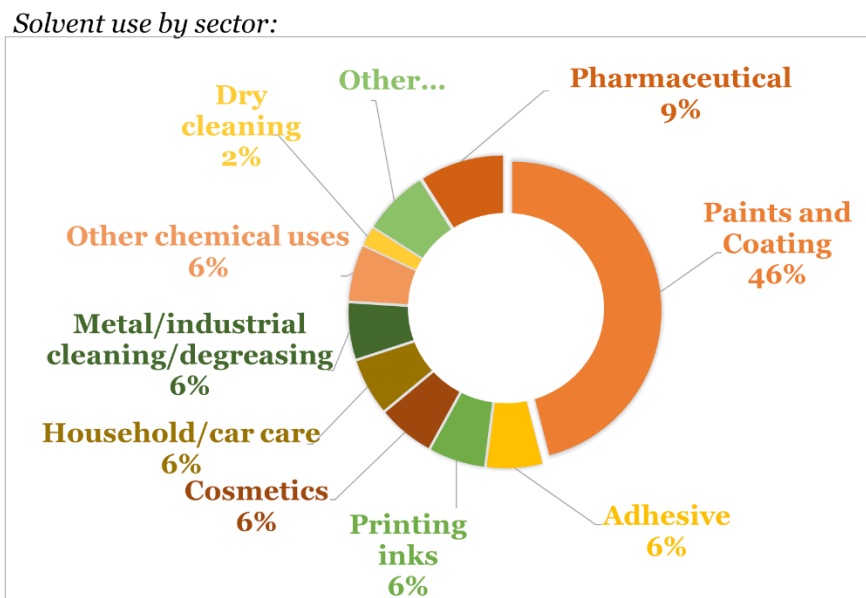
Figure 1. 1: Solvent use in Europe by application (Winterton, 2021).

The following sectors, as illustrated in Figure 1.2 include printing inks, cosmetics, household and car care, industrial cleaning, and degreasing. It is no surprise then, that to be useful in such a diverse ensemble of applications, different types of solvents are needed and must present disparate characteristics in terms of chemical structure and physical and chemical properties such as boiling point, polarity, density, viscosity, and many others.

Solvents can be classified as protic (with a molecular structure that provides a labile proton available for hydrogen bonding) and aprotic (molecules which lack proton donor functionality for hydrogen bonding), as well as polar or non-polar. Again, another classification can be based on the presence of aromatic functional groups, separating organic compounds into aromatics and aliphatic solvents. Classification and definition of solvents depend on the use and application they are being considered for.

1.1.2. Solvent life cycle

All classes of solvents listed above (save water), are manufactured from the building blocks of the petrochemical industry (Clark et al., 2017), e.g. methane, propane, ethylene, butene, benzene, toluene, xylene, and many others. Each of these are, in turn, obtained from crude oil or natural gas via processes such as distillation, fractionation and cracking (Farmer and Mascal, 2015).

In 2020, around 20% of every barrel of crude oil refined in the USA went to production of petrochemical products, with the remainder to energy generation (Eia, 2020). In view of the depletion of fossil fuel reserves, the replacement of oil and gas by renewable raw material may be the only alternative available in the future. As the demand for solvents keeps growing, these compounds will soon need to be manufactured by renewable sources.

Another important aspect of the use of solvents is their end-of-life. In 2017, the highest volume solvent end-of-life in the USA included incineration, releases, recycling and other waste transfer (Clark et al., 2017). As shown in Figure 1.2, the main end-of-life processes for toluene, for instance, were releases into the environment and incineration. In the case of *n*-hexane, releases represent the main removal method. Recycling covers only a small fraction for most solvents, that as of today still contaminate water and soil and pollute the air.
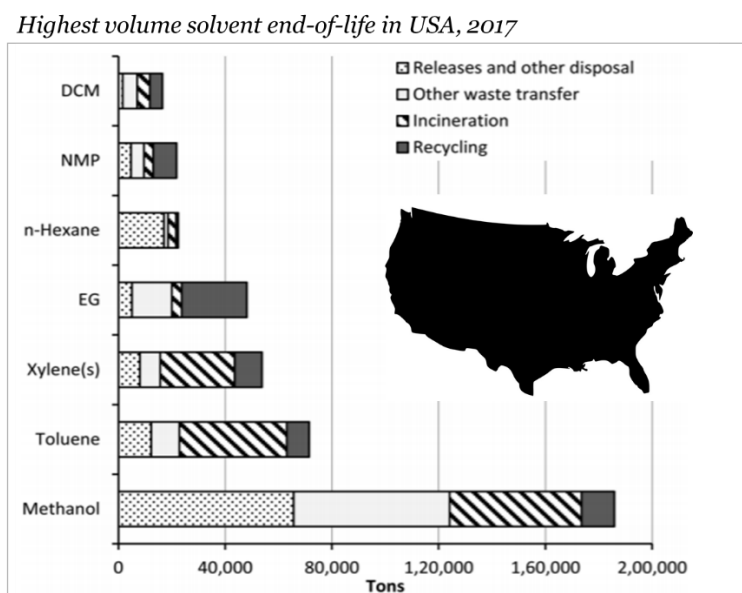
Figure 1. 2: Solvent end-of-life in the USA, 2017 (Clark et al., 2017).

Clearly solvent processes, from synthesis to application to end-of-life, have a deleterious impact on the environment. In the light of a continually growing global economy, these processes must be optimised, and waste kept to a minimum.

1.1.3. Solvent impact

There are many aspects that need to be considered when talking about solvents and their impact on humans and the environment. Some of the most important are listed below:

o   *Toxicity:* toxicity of organic compounds depends on their chemical structure and their ability to be absorbed by inhalation and contact and to pass the blood-brain barrier (Joshi and Adhikari, 2019). The acute or chronic toxicity depends on time of exposure and the amount of substance and can lead to multiple health issues.
    Other health hazards related to solvent exposure are carcinogenicity and mutagenicity. Solvents with highest toxicity include benzene, chloroform, other chlorinated solvents, and dioxane (Joshi and Adhikari, 2019). Their use should be avoided, and other solvents should be preferred to minimize health risks.

o   *Fire and explosion hazard*: organic compound usage and manipulation implies a considerable risk of fire and explosion that must be minimised and prevented in all conditions. Most organic solvents are flammable, and the large scale of chemical plants mean that fire or explosion may lead to disaster. Solvents with low flammability and low risk of explosion (evaluated according to the compound flash point and the ability to form peroxides) should be preferred.

- *Pollution of water and soil*: depending on the lipophilicity and solubility in water, some organic solvents can be more hazardous for water and soil and can develop bioaccumulation. Most modern water treatment technologies are effective in filtering and removing chemical contaminants before they can reach rivers and sea waters. However some molecules, like dioxane for instance, require special treatments and can otherwise contaminate the environment reaching tap water, soil, and food (Stepien et al., 2014).

- *Pollution of air*: volatility is an important requirement for many applications of solvents, like the use in paint and coatings as described in section 1.1.1. Thus, releases into the atmosphere are quite abundant. Volatile Organic Compounds are one of the main pollutants of the atmosphere and their degradation leads to generation of secondary air pollutants.

All data available on the issues described above must be included in the solvent MSDS (Material Safety Data Sheet) to protect the users and workers from explosion risk and to make it possible for manufacturers to choose the safest alternative. Usually, the most common and traditional solvents have complete MSDS that inform users on all risks to for humans and the environment. Lack of data is frequent for new molecules and unused compounds and must be sorted out before large scale usage.

The most problematic organic solvents are often listed as red category solvents (Joshi and Adhikari, 2019) and their impact on health and the environment must be addressed. Some of these solvents have been targeted for abatement strategies or replacement by an alternative. It is the case of benzene, recognised as a carcinogen (Who, 2015), and carbon tetrachloride, which use has been restricted with Montreal Protocol (Unep, 1987) in 1989 to tackle the ozone layer depletion. In other cases, like toluene, chloroform and dichloromethane, problematic solvents have been subjected to specific restrictions by the European Union with the Registration, Evaluation, Authorisation and Restriction of Chemicals (REACH) (Byrne et al., 2016). As a result, in the past years chemists have been searching for an alternative to problematic solvents, designing and selecting organic compounds, often described as 'green' solvents, with good solvent performance but less drawbacks than their traditional counterparts.

1.2. Green Solvents

Much recent effort has been directed to the design and selection of new alternative and sustainable solvents, the so called 'green' solvents. The number of publications on the topic *green solvents* has exponentially grown since 1997 (Fig. 1.3), reaching more than 5000 publications in the year 2021 (Data derived from Clarivate Web of Science, Copyright Clarivate 202_. All rights reserved.).
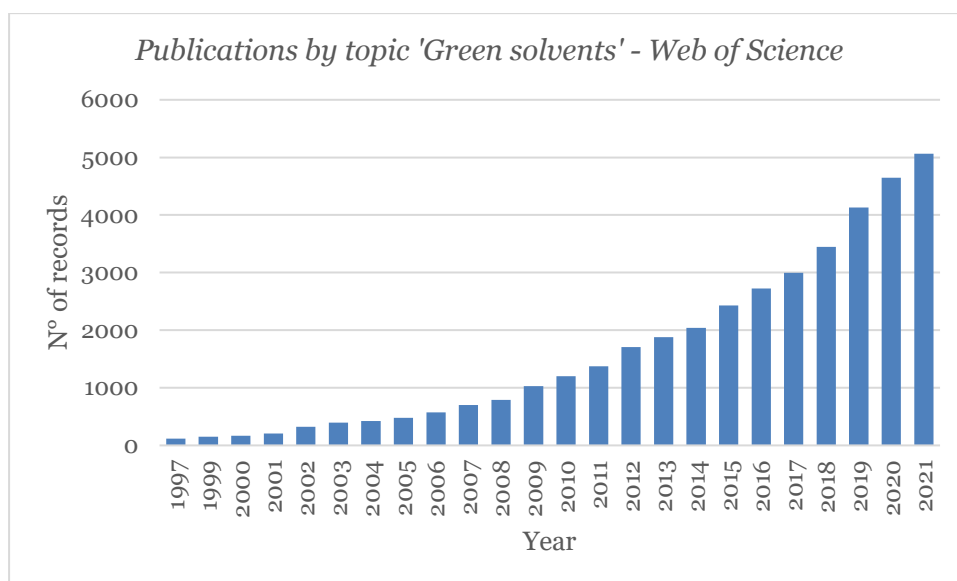
Figure 1. 3: Number of scientific publications with topic 'green solvents' by year according to Web of Science.

The term *green solvents* can be traced back to the largest category of *green chemistry*, phrase that was coined by Paul Anastas in 1991. According to Anastas *"Green chemistry is about inventing new materials and new manufacturing processes that are conducive to life. [...] It cuts across the entire lifecycle, from the origins of the feedstock all the way through a manufacturer and the use of the substance."* (Höfer, 2009). Together with John Warner he formulated in 1998 the 12 Principles of Green Chemistry (Anastas and Eghbali, 2010) that are listed as follow:

1) Prevention: *It is better to prevent waste than to treat or clean up waste after it has been created.*

2) Atom Economy: *Synthetic methods should be designed to maximize incorporation of all materials used in the process into the final product.*

3) Less Hazardous Chemical Synthesis: *Wherever practicable, synthetic methods should be designed to use and generate substances that possess little or no toxicity to human health and the environment.*

4) Designing Safer Chemicals: *Chemical products should be designed to preserve efficacy of function while reducing toxicity.*

5) **Safer Solvents and Auxiliaries:** *The use of auxiliary substances (e.g., solvents, separation agents, etc.) should be made unnecessary wherever possible and, innocuous when used.*

6) Design for Energy Efficiency: *Energy requirements should be recognized for their environmental and economic impacts and should be minimized. Synthetic methods should be conducted at ambient temperature and pressure.*

7) Use of Renewable Feedstocks: *A raw material or feedstock should be renewable rather than depleting whenever technically and economically practicable.*

8) Reduce Derivatives: *Unnecessary derivatization (use of blocking groups, protection/deprotection, temporary modification of physical/chemical processes) should be minimized or avoided, if possible, because such steps require additional reagents and can generate waste.*

9) Catalysis: *Catalytic reagents (as selective as possible) are superior to stoichiometric reagents.*

10) Design for Degradation: *Chemical products should be designed so that at the end of their function they break down into innocuous degradation products and do not persist in the environment.*

11) Real-time Analysis for Pollution Prevention: *Analytical methodologies need to be further developed to allow for real-time, in-process monitoring and control prior to the formation of hazardous substances.*

12) Inherently Safer Chemistry for Accident Prevention: *Substances and the form of a substance used in a chemical process should be chosen to minimize the potential for chemical accidents, including releases, explosions, and fires.*

The principles listed above are in conformity with the UN sustainability goals (Undp, 2022), and indicate a strategy for reducing the impact of chemical industry on the environment that donot focus anymore on just reducing and minimizing exposure to hazardous materials but also on replacing problematic substances with new alternatives. The 12 Principles general view is also in line with the so called 'green growth', that is the definition of an economic growth in compliance with environmental sustainability and not against it. If on one hand criticism has been rightly raised regarding the decoupling of economic growth and environmental impact, and toward the use of green growth as the unique strategy to contrast the ecosystem devastation (Parrique et al., 2019), on the other hand the 12 Principles of Green Chemistry provide useful methods to tackle essential challenges of our times, and should be used accordingly. The 12 principles are a valuable guide for the development of new green chemicals, and there is a principle entirely dedicated to solvents (5: safer solvents and auxiliaries). Further, the other principles may be applied to the selection of sustainable compounds and are used to define the criteria for solvent selection guides.

1.2.1. Green Solvents Selection Criteria

There are several solvent guides that provide selection criteria to choose solvents with the lowest impact on health and the environment. CHEM21 (21st Century Pharmaceutical Industries) selection guide (Prat et al., 2016), reviews a good number of classical and less classical solvents and classifies them into recommended, problematic, and hazardous according to health, safety and environmental criteria. The criteria are defined as follow:

o **Health:** an evaluation of the effects on health after exposure to the solvent based on GHS (Global Harmonised System) symbols and statements. This category is strictly related to occupational hazard and considers the volatility of the solvent as a worsening factor, as it facilitates exposure. The solvents for which toxicology data are not available have a default ranking of 5 (out of 10).

o **Safety:** this section mainly covers flammability and explosion risk, and again it relies on GHS data. Flash point, boiling point, auto-ignition temperature, resistivity

(potential to build up static charge in an industrial setting), and ability to form explosive peroxides are some of the properties involved in the ranking choice.

o **Environment:** the environment criteria is the most complex and the authors acknowledge the lack of data for an adequate assessment. Ozone layer depletion, acute ecotoxicity, bioaccumulation, volatility, are some of the properties that were analysed again according to the available GHS symbols and sentences. Recyclability and manufacture from renewable sources were also considered. The only criteria to account for the impact of solvents on the atmosphere and air quality were ozone layer depletion and volatility.

Prat et al. (2016) point out that the environmental criteria are particularly lacking atmospheric chemistry info, such as the ability to generate harmful Volatile Organic Compounds. Volatility itself, cannot be used as a sole parameter to judge the impact on air quality as it does not provide any insight on the atmospheric fate of the molecule once it has been emitted. In addition, volatility has been also considered as a favourable property as it facilitates chemical synthesis processes such as product isolation and recovery. (Byrne et al., 2017)

Other solvent guides, like the ones published by companies Pfizer, GlaxoSmithKline (GSK) (Alder et al., 2016), and Sanofi, are also based on Health, Safety and Environment (HSE) criteria and were reviewed by Byrne et al. (2016) with the aim of unifying different guides. These scales use slightly different HSE criteria but lead to similar conclusions on the 'greenness' of the solvents selected. However, all these rankings depend on the data available and on properties that can be easily compared and need further improvement.

Energy demand, life cycle assessment, and many other environmental criteria are important, but greater attention should be given to the assessment of the impact of solvents on air quality and air pollution. Most neoteric solvents are Oxygenated Volatile Organic Compounds, and their atmospheric chemistry is often unknown and quite unpredictable. The OVOCs selected and studied in this work were described in the following sections.

1.2.2. TMO (2,2,5,5-Tetramethyloxolane) and the oxolanes

The oxolanes are a class of organic heterocyclic compounds characterised by the presence of a saturated 5-member ring including an O atom. Oxolanes are therefore cyclic ethers; the simplest is tetrahydrofuran (THF), itself also known as oxolane. Similarly, both "oxolane" and "tetrahydrofuran" root nomenclature is commonly used when describing substituted oxolanes. For example, a compound studied in this work may be named 2,2,5,5-tetramethyloxolane or 2,2,5,5-tetramethyltetrahydrofuran. However, 'oxolane' is the preferred IUPAC nomenclature and will be used henceforth in this study. Structures and acronyms used for all the oxolanes studied in this worked are illustrated in Figure 1.4. For simplicity we refer to 2,2,5,5-tetramethyloxolane as "TMO".

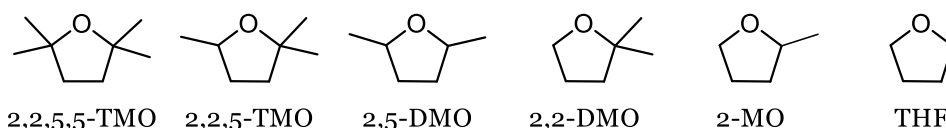2,2,5,5-TMO   2,2,5-TMO   2,5-DMO   2,2-DMO   2-MO   THF

Figure 1. 4: Chemical structure of 2,2,5,5-TMO and the other oxolanes studied in this work, with corresponding acronyms.

This work began with an investigation of the atmospheric chemistry of TMO and was prompted by interesting results from an undergraduate research project (Juliette V.

Schleicher, BSc report, University of York and University of Heidelberg, 2019). This molecule was designed at the Green Chemistry Centre of Excellence at University of York (Byrne et al., 2017), and its chemical structure was specifically elaborated to create a sustainable solvent that would be a safer choice than other non-polar volatile solvents. In particular, the choice of TMO derives from the need of a new solvent with physical and chemical properties like those of toluene and hexane. Toluene has been identified as air pollutant by US EPA (Epa, 1990), hexane is a potential mutagen and carcinogen, and both are suspected to affect fertility (Byrne et al., 2017).
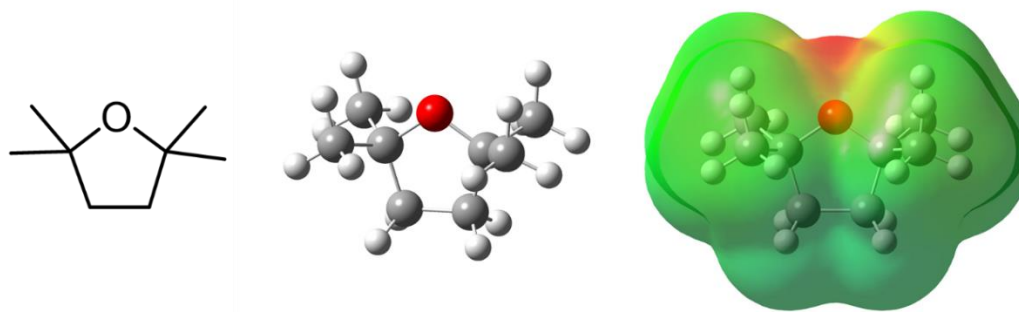
Figure 1. 5: Starting from the left, chemical structure of TMO, ball-and-stick model of TMO, and lastly the electrostatic potential surface calculated with Gauss View 9 (Hartree-Fock 3-21G method, total density, Self-consistent field SCF matrix), colour scale from -0.05 H (1H = 1Hartree = 27.2 eV) in red to +0.05 H in green), (see Fig. 3.1).

Other 'green' solvents are good candidate for replacement of toluene and hexane, but present important drawbacks. Limonene and *para*-cymene for instance have similar solubility properties but low volatility. This makes it impractical to use them in chemical synthesis and other industrial processes that require volatility. Other candidates are ethers like CPME (Cyclopentyl Methyl Ether), but its use was questioned because of their ability to form explosive peroxides, that needs to be controlled by the use of a peroxidation inhibitor(Byrne et al., 2017).

TMO and toluene have similar boiling points and vapour pressures as shown in Table 1.1. Thanks to this similarities TMO was selected for toluene replacement and tested in many applications such as resin swelling and chemical synthesis, where solubility parameters for both solvents were studied (Byrne et al., 2019; Ran et al., 2019). The results suggest that TMO could be used as an alternative to TMO in a number of applications. Boiling points for the other oxolanes show a decrease in line with the degree of substitution, and accordingly the values of vapour pressure increase for oxolanes with lower mass. This indicates that oxolanes could be useful in replacing toluene or other solvents in uses where a higher volatility is required.

Table 1.1: Boling point and vapour pressure of TMO, the oxolanes and toluene.

	TMO	2,2,5-TMO	2,5-DMO	2,2-DMO	2-MO	Toluene
Boiling point (°C)	112	101	90	92	78	110
Vapour Pressure (Torr) at 298 K	26	-	62	57	97	28

Notes: Data from Pubchem (Pubchem).

The special characteristic of the chemical structure of TMO that makes it an ideal candidate are the methyl groups next to the ether oxygen and the absence of H in alpha position which consequently lead to the following properties:

- o Low peroxide formation: the lack of protons next to the ether oxygen prevents the risk of autoxidation and peroxide formation. The C-C bond of the methyl groups is much stronger and less likely to decompose and initiate the autoxidation. The remonstrance to peroxide formation was experimentally proved by (Byrne et al., 2017).

- o Low basicity: the presence of the bulky methyl groups affects the basicity of the molecule by hiding the ethereal oxygen. This characteristic gives TMO good solubility properties and good acid stability.

Proof of the low basicity of TMO was its good performance Fisher esterification and amidation reactions, which are known to be enhanced by the use of low basicity solvents. TMO does not perform well in Grignard reactions, where the hindered basicity inhibits the solubilisation and stabilitation of the Grignard reactant. This again shows how TMO has solvent properties that are more in line with those of toluene than those of other ethereal compounds (Byrne et al., 2017). Other reactions were radical-initiated vinyl polymerizations and Buchwald-Hartwig aminations (Trowse et al., 2021), where in some cases TMO performed even better than toluene. These results indicate that replacement of toluene with TMO seems promising and achievable in many applications. To further promote the use of TMO, the solvation properties of TMO and toluene on a wide variety of solutes were compared by (Byrne et al., 2019).

In addition to the low peroxide formation, other characteristics that make TMO a 'green' choice are the low toxicity, which has been analysed by Byrne et al. (2017) via Ames mutagenicity testing and nearest neighbour toxicity prediction, and the renewable synthetic route that's described below (Fig. 1.6):
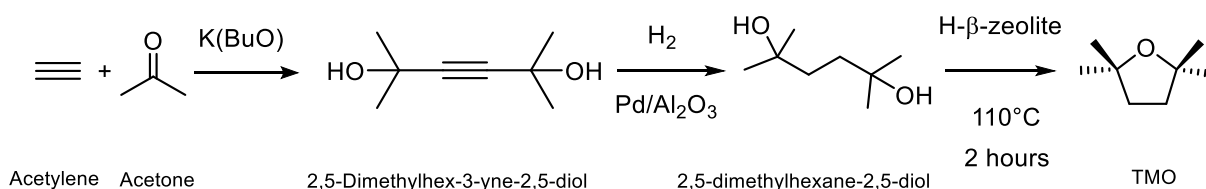
Figure 1. 6: Synthesis of TMO by Byrne et al. (2017).

This synthesis has a very high atom economy (96%), the starting materials are acetylene and acetone that can be both manufactured from renewable sources. The TMO precursor, 2,5-dimethylhexane-2,5-diol, can be synthesised by catalytic hydrogenation of 2,5-dimethylhex-3-yne-2,5-diol. The ring-closure can then be obtained by dehydration with zeolite.

TMO has a boiling point of 112°C (very similar to toluene, 111°C) and is a volatile compound (Table 1.1). Once emitted into the troposphere, the reaction that is likely to drive the degradation of TMO is the oxidation by radicals naturally occurring in the air, first and foremost OH radicals and Cl radicals, especially in coastal areas.

The other oxolanes illustrated in Figure 1.4 were also studied to investigate the effect of methyl groups alpha-positioned to the ethereal oxygen and the effect of different degrees of substitution on the atmospheric reactivity of these compounds. THF was classified as problematic by the CHEM21 selection guide (Prat et al., 2016) because of the chance of carcinogenicity and the high peroxide formation potential, and its production is known to be

very energy demanding (Byrne et al., 2016). The monosubstituted 2-MO (2-methyloxolane) was also ranked as problematic, mainly because of the lack of data on toxicity and because of the peroxide formation potential. However, 2-MO is commercially available and marketed as 'green solvent' (Sigma-Aldrich.Com, 2015) and can be synthesised from renewable sources. Many applications of this solvent have been reported (Phanopoulos et al., 2015; Aycock, 2007), especially as alternative to THF. Lastly 2,5-DMO (2,5-dimethyloxolane) was not included in the CHEM21 selection guide, but the synthesis from renewable sources has been investigated (Zhou et al., 2015; Grochowski et al., 2012). Similarly to what was said for TMO, the gas phase degradation of 2-MO and 2,5-DMO was investigated in this study, observing the reaction of these compounds with OH radicals. Reaction with Cl can also occur but was not studied in this work, as literature data were available. Photolysis and reactivity with other oxidants of the air can be neglected because of the lack of absorbing functional groups like doble bounds in the chemical structure. The other oxolanes 2,2-DMO and 2,2,5-TMO have not been considered as green solvent candidate and their synthesis from renewable sources hasn't been investigated yet.

1.2.3. CPME: Cyclopentyl Methyl Ether

Cyclopentyl Methyl Ether (CPME) is marketed as green solvent by chemicals companies like Sigma-Aldrich (Sigma-Aldrich.Com, 2015) (Fig.1.7).

Figure 1. 7: Starting from the left, chemical structure of CPME, ball-and-stick structure of CPME, electrostatic potential surface calculated with Gauss View 9 (Hartree-Fock 3-21G method, total density, Self-consistent field SCF matrix, colour scale from -0.05 H in red to +0.05 H in green), and lastly, an informative brochure of 'Greener solvent alternatives' by Sigma Aldrich.

Several studies were published on CPME and the use of this molecule as a green solvent (Azzena et al., 2019; Abreu et al., 2016; Watanabe et al., 2007; Watanabe, 2013). CPME is a commercially available compound and is industrially produced with a 100% atom economy synthesis (Fig. 1.8) starting from non-renewable sources (cyclopentene). The high atom economy and the efficiency of the synthesis from cyclopentene and methanol is believed to outperform the derivation of CPME from renewable sources (Azzena et al., 2019) with the technologies available at this time. However, efforts have been made to develop an alternative synthetic route through cross-esterification of biomass-derived cyclopentanol and methanol (Gołąbek et al., 2022). This reaction (Fig. 1.9) leads to undesired dehydration of CPME and production of cyclopentene, reducing the yield of CPME. A higher selectivity of the zeolites may provide a more efficient synthetic route in the future.
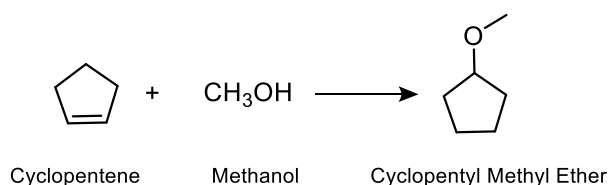
Figure 1. 8: Synthesis of CPME from non-renewable sources (Azzena et al., 2019).
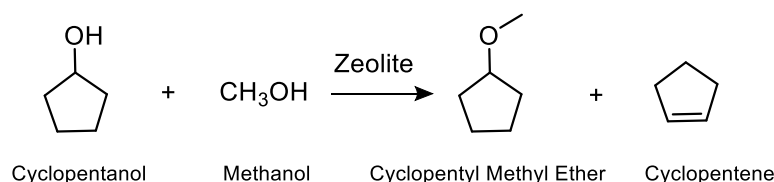
Figure 1. 9: Synthesis of CPME from renewable sources leading to undesired cyclopentene (Gołąbek et al., 2022).

CPME could represent a valid alternative to highly polluting solvents such as tetrahydrofuran (THF), toluene and 1,4-dioxane (Abreu et al., 2016), and the properties that makes it a desirable choice as 'green' solvent are summarised below:

- Low toxicity: toxicity of CPME was assessed by Watanabe (2013), who found that CPME has low toxicity, negative mutagenicity and shows only moderate to severe irritation to skin and eye, as indicated by the GHS.

- Higher boiling point then THF and low heat vaporization: this means that reactions can be carried out at higher temperature and in less time, with lower solvent loss.

- Hydrophobicity and facile drying: it can be easily recovered, and it is useful in synthesis that require anhydrous solvents.

Peroxide formation was also indicated as a favourable feature for CPME as the peroxide production rate is lower than for THF and other ethers like diisopropyl ether. However, CPME autoxidation can occur and leads to formation of explosive peroxide. The commercially available CPME contains 50 ppm of BHT (2,6-di-tertbutyl-4-methyl phenol) to avoid safety concerns. According to the CHEM21 selection guide of solvents (Prat et al., 2016), CPME ranks as 'problematic' due to safety concerns from its low auto-ignition point (180 °C) (Prat, 2013), but 'recommended' on the environmental ranking. None of these evaluations considered any data regarding the atmospheric chemistry of CPME.

With a vapour pressure of 44 Torr at 20°C, CPME can be classified as a volatile organic compound that evaporates rapidly in standard conditions. Once released into the troposphere, it can react with gas-phase oxidants such as OH and Cl radicals. These oxidation processes are likely to represent the main removal pathways for CPME. Since they were not previously reported in the literature, this study aimed to provide useful insight about the reaction mechanism and kinetics of these reactions.

1.2.4. CPO: Cyclopentanone

Cyclopentanone (CPO) (Fig.1.10) is a cyclic ketone. Recent interest has focused on its use as a biofuel (Bao, 2017; Liu et al., 2019). CPO can be readily derived from biomass through aqueous hydrogenation of furfural (Fig. 1.11) (Hronec and Fulajtarová, 2012) or biomass pyrolysis (Thion et al., 2017).
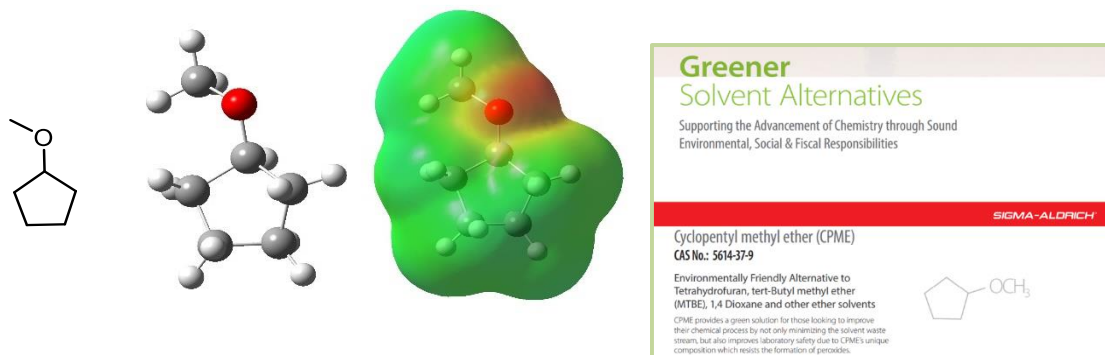

Figure 1. 10: Starting from the left, chemical structure of CPO, ball-and-stick diagram of CPO, and electrostatic potential surface calculated with Gauss View 9 (Hartree-Fock 3-21G method, total density, Self-consistent field SCF matrix, colour scale from -0.05 H in red to +0.05 H in green).
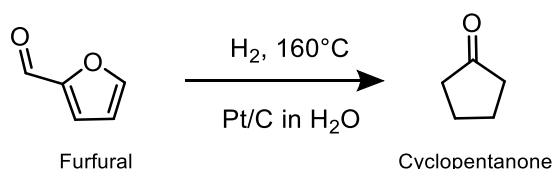
Figure 1. 11: Synthesis of Cyclopentanone from biomass derived furfural (Hronec and Fulajtarová, 2012).

Although CPO has been used mainly as building block for the pharmaceutical industry and as biofuel, the application as solvent has raised interest in the past years (Duereh et al., 2018; Lawrenson et al., 2017). The GSK solvent sustainability guide (Alder et al., 2016) has classified CPO with 'Few known issues' that is the equivalent of 'Recommended' in the ranking used by CHEM21 selection guide. This favourable definition comes from the low toxicity of cyclic ketones and other physical and chemical properties that were similar to those of ethanol. CPO is a volatile compound and, once released into the atmosphere, the main reactions that can occur are the oxidation by OH and Cl radicals, and photolysis. As some literature data was available for Cl + CPO, the focus of this work was CPO photolysis and reaction with OH.

1.2.5. Methyl Pivalate and Pinacolone

Methyl Pivalate (Methyl 2,2-dimethylpropanoate, henceforth MPA) (Fig. 1.12) and Pinacolone (3,3-Dimethylbutan-2-one, henceforth PCO) (Fig. 1.13) have been suggested by Byrne et al. (2018) as promising green solvents. Using a top-down approach starting from 19 esters and ketones with suitable properties, MPA and PCO were found suitable for the replacement of Volatile Nonpolar Solvents (VNP) such as toluene and hexane.

Figure 1. 12: Starting from the left, chemical structure of PCO, ball-and-stick diagram of PCO, and electrostatic potential surface calculated with Gauss View 9 (Hartree-Fock 3-21G method, total density, Self-consistent field SCF matrix, colour scale from -0.05 H in red to +0.05 H in green).
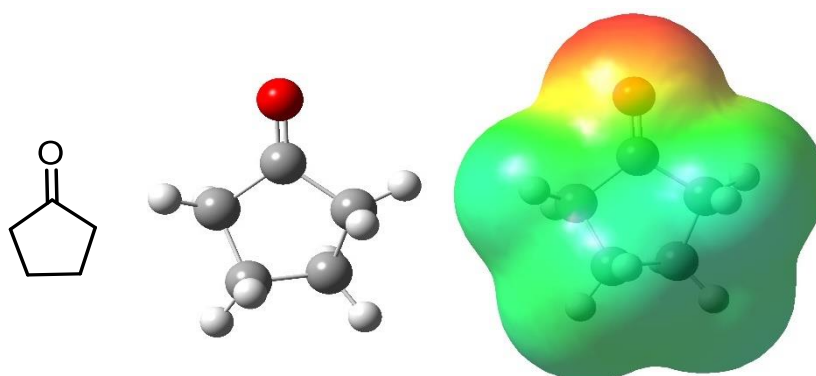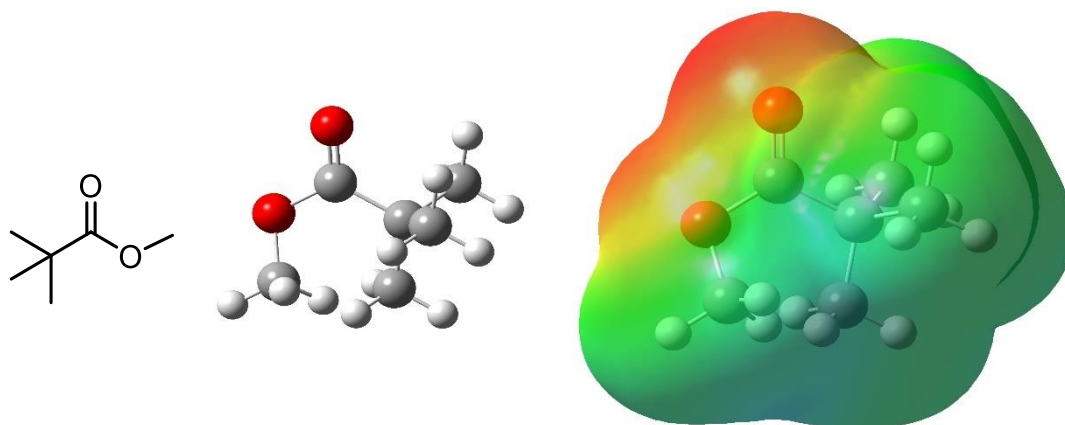
Figure 1. 13: Starting from the left, chemical structure of MPA, ball-and-stick diagram of MPA and electrostatic potential surface calculated with Gauss View 9 (Hartree-Fock 3-21G method, total density, Self-consistent field SCF matrix, colour scale from -0.05 H in red to +0.05 H in green).
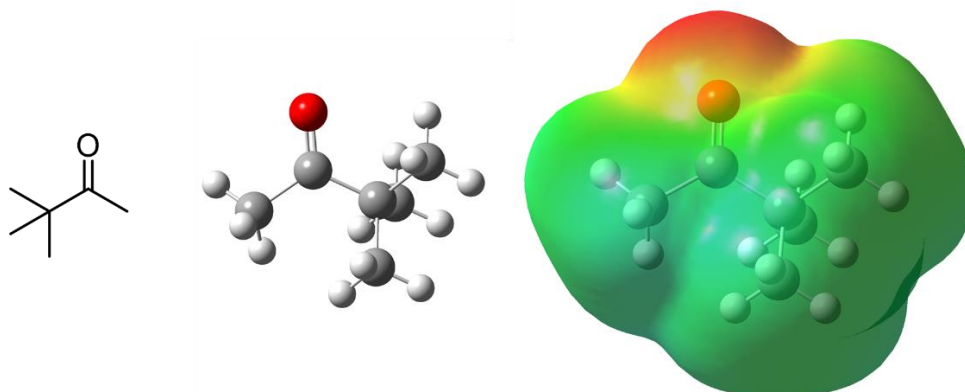
Esters and ketones are known for their low toxicity and are readily derivable from oxygen-rich biomass (Farmer and Mascal, 2015). PCO and MPA can be produced from pivalic acid, itself derived from isobutene via Koch reaction. Isobutene can be sustainably sourced from fermentation of sugars (Byrne et al., 2018). The subsequent ketonisation of pivalic acid with acetone leads to PCO (Fig. 1.14 B) and the esterification of the same precursor pivalic acid leads to MPA (Fig.1.14 C).
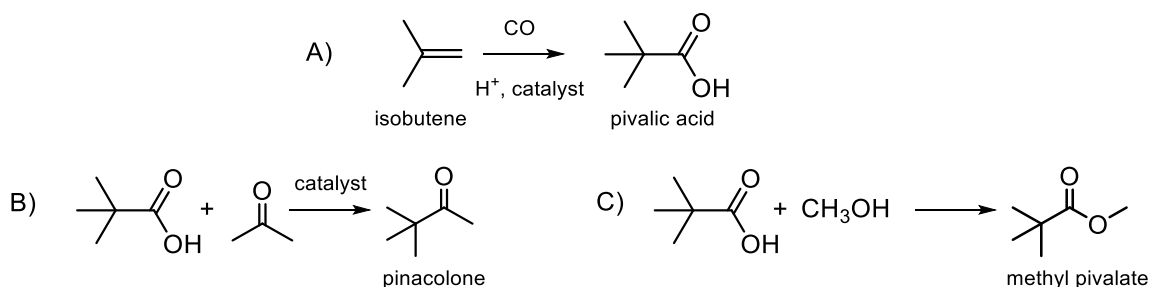
Figure 1. 14: Synthetic route leading to pinacolone (B) and methyl pivalate (C). Both compounds can be produced from pivalic acid that can be obtained from biomass-derived isobutene via Koch reaction (A) (Byrne et al., 2018).

The electronegative O-atom is responsible for the high polarity of most simple ketones and esters. However, variation of the alkyl substituents next to the carbonyl (for ketones) and the RC(O)O- (for esters), can make a considerable difference and it strongly affects the overall polarity of the molecule. Accordingly, after a screening of 12 esters and 7 ketones, pinacolone and methyl pivalate were identified by Byrne et al. (2018) as good solvents for natural rubber with solubilities properties in line with those of toluene and hexane, together with a boiling point of around 100°C, as required from many applications of non-polar solvents. Even though the toxicity assessment of pinacolone and methyl pivalate needs further studies and finalisation, their application as green solvents seem promising and add diversity to the spectrum of sustainable compounds available. Because of their volatility, the atmospheric chemistry of these compounds must be investigated, and the most important removal process will be reactivity with OH, photolysis for pinacolone, and reactivity with Cl where relevant.

1.3. Atmospheric Chemistry of OVOCs

As discussed in sections 1.1.2 and 1.1.3, every step of the life cycle of a solvent determines an impact on the environment and environmental pollution. As for air pollution, most common solvents in use are Volatile Organic Compounds (VOCs), and their impact on air quality is significant. According to the Directive of the European Parliament (Ep, 2010):

'Volatile organic compound means any organic compound as well as the fraction of creosote, having at 293.15 K a vapour pressure of 0,01 kPa or more, or having a corresponding volatility under the particular conditions of use'

setting the lower limit of vapour pressure to 0.01 kPa (0.075 Torr, 1×10^{-4} bar) at room temperature.

In the case of traditional compounds made from non-renewable sources, emissions start at refineries (Beauregard, 1993), where solvents are obtained through distillation. The solvent loss by evaporation then continues during the utilization of solvents, especially for paint and coating applications, where solvent recovery is quite unpractical, but also for chemical synthesis, where leaks and solvent losses are common, and other industrial processes, like cleansing. Lastly, most common solvent end-of-life is for some OVOCs represented by releases into the environment, which often includes evaporation (Clark et al., 2017).

Evidence for large scale emissions deriving from solvent use comes from the emblematic case of England, a country with intensively industrialised areas. The Air Pollutant Inventory reported in top Figure 1.15 (Jones et al., 2021), shows how in the past decade the main anthropogenic source of VOCs was represented by solvent processes coming from industrial and domestic use. Interestingly, other sources of VOCs, like transport, decreased consistently in the same period thanks to policy actions that specifically addressed this kind of emission source (Gov.Uk, 2015). On the other hand, the quite steady number of emissions coming from solvent processes shows how equivalent policy actions were not taken or were not effective on tackling this source of VOCs. This trend is then likely to get worse in the view of the constant economic growth of the chemical sector.

The second graph shown in Fig. 1.15 reports the emissions coming from the main solvent uses in the UK from 1970 to 2021 (Naei). Domestic solvents and coating applications represent the most important sources, with the first one showing a steady increase in the last decades. Chemical products, including solvent use in chemical industry, affect much less the overall emission figures, probably thanks to the solvent recovery processes which can be used in pharmaceutical and chemical industries, and are not applied in domestic uses and coatings. Solvent use has also been identified as one of the main sources of VOCs in other countries around the world, like USA (Calvert et al., 2011b), China (Li et al., 2021), and India (Singh et al., 2016).

VOC Emissions in England
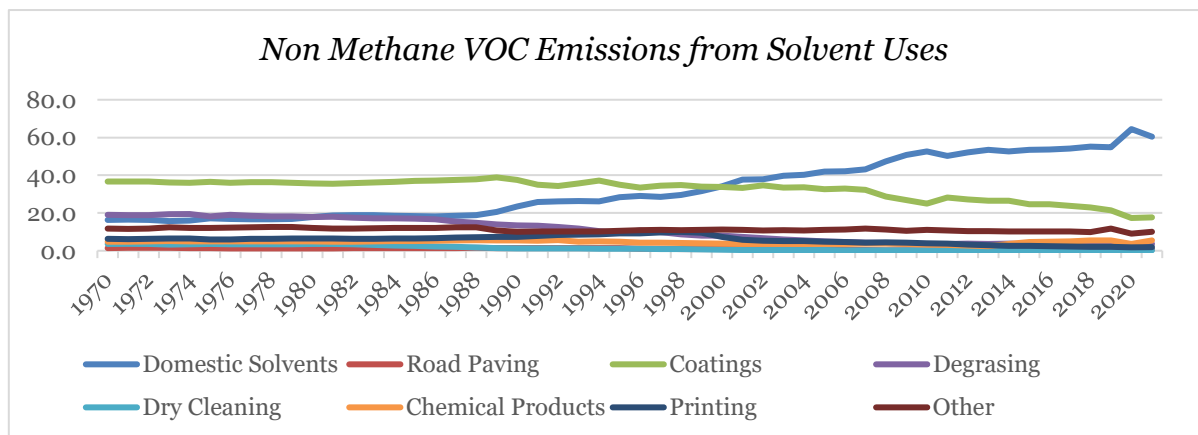

Non Methane VOC Emissions from Solvent Uses
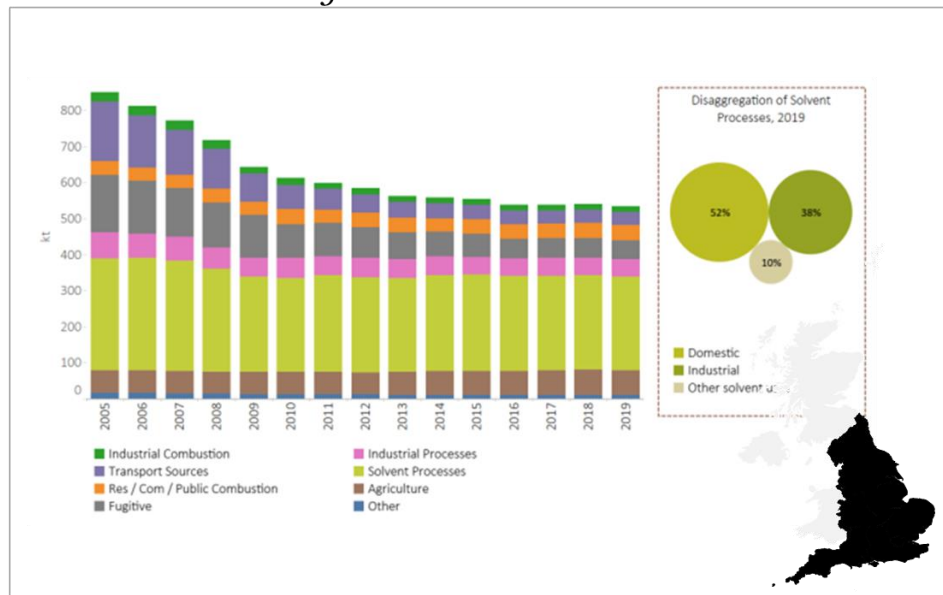
Figure 1. 15: Top: Emissions of non-methane VOC in England from 2005to 2019 broken down by source (Jones et al., 2021). Bottom: Emissions of non-methane VOC deriving from solvent uses in UK (Naei).

VOCs not only are primary air pollutants, but they're also a source of secondary pollutants, such as ozone and oxygenated compounds leading to Secondary Organic Aerosol (SOA) and Particulate Matter (PM). The VOCs that are known to be more dangerous for health and affect the most air quality with generation of secondary air pollutants have been targeted for abatement strategies or for replacement with an alternative (Jenkin et al., 2017).

In the case of solvents, the alternative may be represented by 'green' sustainable organic compounds that present favourable properties assessed by solvent guides, such us low toxicity and sustainable manufacturing. Interestingly, most organic compounds proposed as green solvents are Oxygenated Volatile Organic Compounds (OVOCs). If on one hand chemical composition of fossil-derived chemicals is characterised by lack of heteroatoms, on the other hand biomass is highly functionalised and naturally rich in oxygen. Where traditional chemistry is based on functionalization of hydrocarbons, synthesis from biomass may require dehydration and reduction to obtain the desired product. Accordingly, oxygenated compounds are easily derivable from biomass and their occurrence in fragrances and food (in the case of esters) confirms in some case their lower toxicity (Byrne et al., 2018) compared to hydrocarbons. The term OVOCs includes many classes of organic compounds like ethers, alcohols, ketones, aldehydes, esters, and carboxylic acids with high volatility. The

troposphere is an extremely complex reactor in which emitted species are degraded through what can be defined as a 'self-cleansing capacity' of the atmosphere (Prinn, 2003). For saturated OVOCs, the main removal process is the reaction with OH radicals, but also reaction with another oxidant, Cl, is likely to happen quite rapidly. OH radicals are much more abundant in the atmosphere, and even though reaction with Cl radicals is often faster than the reaction with OH, their concentration is often irrelevant and oxidation by OH radicals represents the major fate of VOCs (Mellouki et al., 2015).

Photolysis can also occur for OVOCs with functional groups that absorbs sun light ($\lambda > 290$ nm in the troposphere), like aldehydes and ketones (Mellouki et al., 2003). Unsaturated OVOCs react not only with OH and Cl, but also with other atmospheric oxidants such as NO_3 and O_3. Photolysis can also contribute to the loss of unsaturated molecules which absorb solar light (Moriarty et al., 2003; Calvert et al., 2011b). The following sections introduce and discuss photochemical processes responsible for the degradation of VOCs of interest to this work.

1.3.1. OVOC + OH

OH radicals are the most important oxidisers of the troposphere and they drive the chemical degradation of most organic compounds in air. OH concentration in the clean troposphere can change quite considerably and it usually varies from 2×10^5 to 3×10^6 molecule cm^{-3} (Jacobson, 2002). In this work, an average concentration representative of the atmosphere equal to 1×10^6 molecule cm^{-3} as estimated by (Lelieveld et al., 2016) was used. Not only it initiates the breakdown path of VOCs and OVOCs, but in some case the reaction with OH is also the rate determining step of the overall removal process. The oxidation of CH_3OH is a good example of a well-known atmospheric degradation of an OVOC (Mellouki et al., 2015; Calvert et al., 2011b). The steps involved in this process are described below and start with the H abstraction by OH radical that lead to formation of HO_2, an important radical intermediate:

$$HO + CH_3OH \rightarrow H_2O + CH_2OH \tag{R1.1}$$

$$CH_2OH + O_2 \rightarrow HCHO + HO_2 \tag{R1.2}$$

Formaldehyde (methanal, henceforth HCHO) is produced from (R1.2) and can subsequently react itself with OH or alternatively undergo photolysis. The first of these routes proceed as follow:

$$HO + HCHO \rightarrow HCO + H_2O \tag{R1.3}$$

$$HCO + O_2 \rightarrow HO_2 + CO \tag{R1.4}$$

More HO_2 is developed from the reaction of CO with OH (R1.5) and form the consequent formation of H (R1.6).

$$HO + CO \rightarrow H + CO_2 \tag{R1.5a}$$

$$HO + CO + M \rightarrow HOCO + M \tag{R1.5b}$$

$$H + O_2 + M \rightarrow M + HO_2 \tag{R1.6}$$

The HO_2 radicals deriving from all these reactions (R1.1-R1.6) have a crucial role in conversion of NO to NO_2 (R1.7), a process that in turn is involved in photochemical O_3 formation (R1.8-R1.9).

$$HO_2 + NO \rightarrow HO + NO_2 \tag{R1.7}$$

$$NO_2 + h\nu \ (\lambda < 420 \text{ nm}) \rightarrow NO + O \tag{R1.8}$$

$$O + O_2 + M \rightarrow O_3 + M \tag{R1.9}$$

Reactions equivalent to those reported above (R1.1-R1.9) are also valid for other VOCs and a summary of the reaction scheme for an unspecified VOC is illustrated in Figure 1.16.
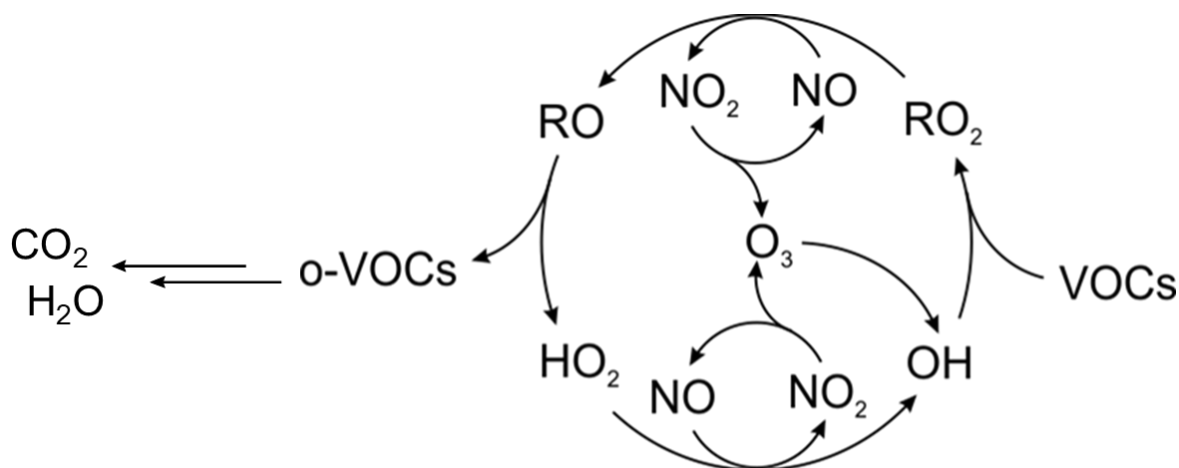

Figure 1. 16: Reaction scheme summarising the chemical processes leading to VOCs degradation and O_3 formation.

Ozone plays an important role in atmospheric chemistry, being the primary source of OH in the daytime:

$$O_3 + h\nu \rightarrow O_2 + O \ (^1D) \tag{R1.10}$$

$$O(^1D) + H_2O \rightarrow 2HO \tag{R1.11}$$

In this way, OH radical are regenerated within the oxidation cycle (Fig.1.16). However, ozone is toxic to human and vegetation, and it is also a greenhouse gas, and human activities resulted in a considerable increase of its concentration in the years following the start of industrialization (Mellouki et al., 2015). Consequently, understanding the mechanism and the sources of O_3 generation is of crucial importance for mitigation strategies and improvement of air quality. Formation of O3 is not the only contribution of VOCs to poor air quality. Some VOCs are themselves toxic or otherwise harmful to human, animal, or plant life. Other secondary effects include contributions to formation of hazardous OVOCs, Secondary Organic Aerosol (SOA) and formation of Particulate Matter (PM).

Determining the rate of the initiation reaction (VOC + OH) can give an idea of the lifetime of these compounds and studying the mechanism of the oxidation gives more insights on the primary products of oxidation. As these reactions involve the interaction of two chemical species, the VOC and OH, the rate will be described by a second order rate coefficient:

$$\frac{d[VOC]}{dt} = -k[OH][VOC] \tag{Eq. 1.1}$$

The rate coefficient k can depend on pressure and on temperature. The temperature dependence of the rate of a chemical reaction was described by Svante Arrhenius in 1889 with Equation 1.2:

$$k = A\,exp(-\frac{E_a}{RT})$$
(Eq.1.2)

However, this equation describes only the 'classical' behaviour of some chemical reactions, and it is not representative of reactions that require a higher degree of complexity and more than two parameters, like the reaction of OH with some OVOCs. Figure 1.17 shows the three main kinds of exothermic reaction (Sims, 2013). The first case is a typical reaction with an energy barrier that could be represented by the need of a bond breakage. The Arrhenius plot in this case shows a classical behaviour with a linear negative trend. The mild plateau at low temperatures might be observed when quantum-mechanical tunnelling (QMT) makes it possible for light atoms such as H to cross the barrier below the energy peak. The second scenario takes place for barrierless reactions, such as radicals forming new bonds. In this case the Arrhenius plot shows a positive slope, indicating that the rate of the reaction increases with the temperature. The third and last scenario is a combination of the latter two cases. First there's formation of a barrierless pre-reaction complex, then the reaction proceeds with a barrier leading to the intermediate and the products. At high T, the pre-rection complex is formed with high internal energy and it rapidly decomposes back to reactants. Accordingly, the reaction proceeds in a single step over a barrier to the products, showing a classical Arrhenius behaviour. At low T however, the pre-reaction complex has a longer lifetime, and the reaction rate will be determined by the rate of formation of the barrierless pre-reaction complex, whereas the following step will occur very rapidly thanks to QMT, by tunnelling the potential barrier.
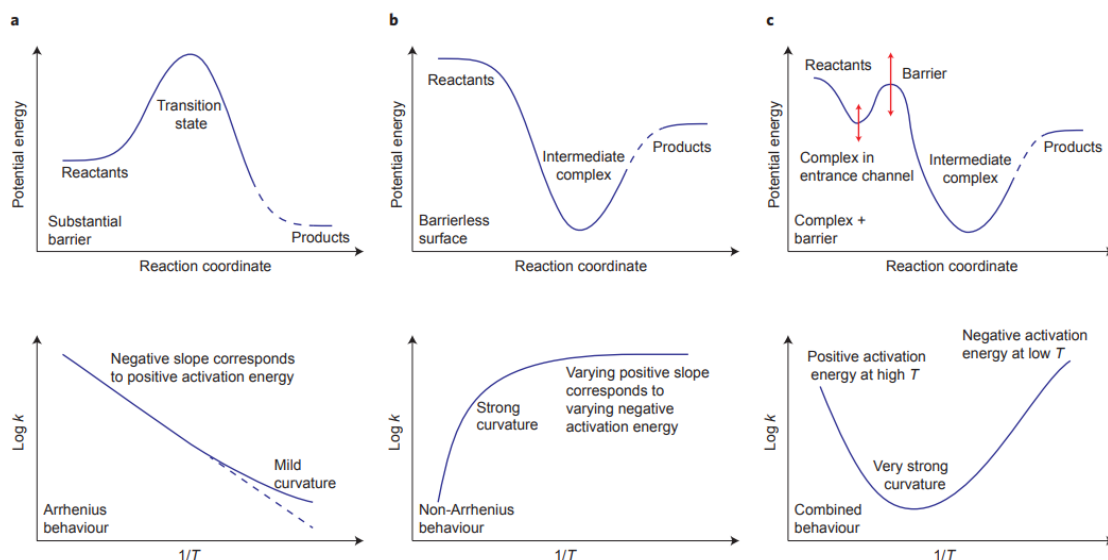

Figure 1. 17: Schematic by Sims (2013) showing the three typical cases of exothermic reactions. Each upper panel depicts the potential energy of the system, and the lower panels show the Arrhenius plot that would describe that kind of reaction.

The third behaviour has been observed for many reactions involving a neutral species and a radical. Taking the example of methanol, R1.1 ($CH_3OH + OH$) has been studied in depth and over a range of temperatures (200 < T / K < 800) via different techniques; all results used to derive the IUPAC recommended value (Atkinson et al., 2006) are reported in Figure 1.18 (Wallington and Kurylo, 1987b; Hess and Tully, 1989; Jiménez et al., 2003; Dillon et al., 2005). The temperature dependence can be described by a non-classical three-parameter expression:

$k_{1.1}(200\text{-}800 \text{ K}) = 6.38 \times 10^{-18} \; T^2 \exp(144/T) \text{ cm}^3 \text{ molecule}^{-1} \text{ s}^{-1}$ (Eq.1.3)
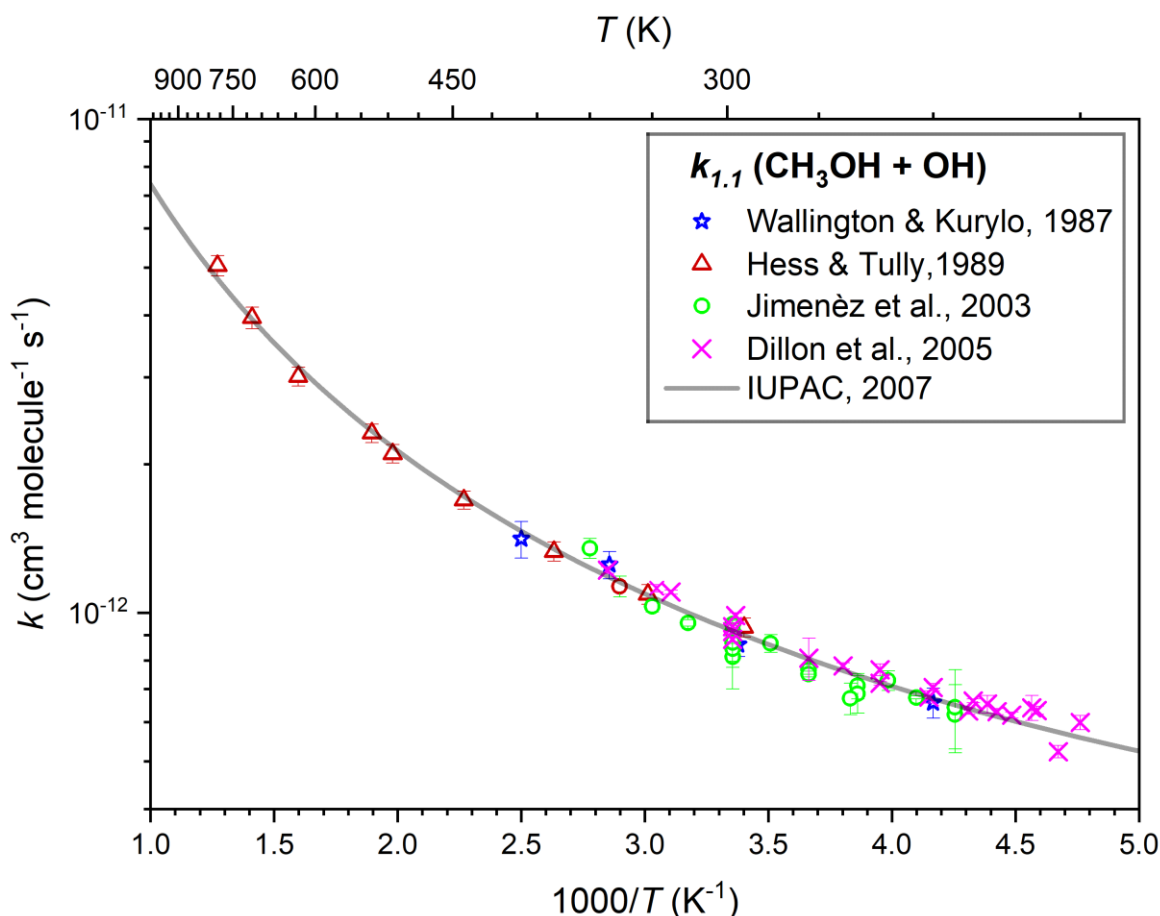

Figure 1. 18: Arrhenius plot showing the literature data recommended by IUPAC for $k_{1.1}$ (CH$_3$OH + OH).

In addition to these recommended values, Shannon et al. (2013) also studied R1.1 at interstellar temperatures, finding a rate coefficient at 63 K two order of magnitude larger than the one measured at 200 K. After making sure that the reaction was no pressure dependent, and that gas density would not affect the rate, the authors concluded that the complex was not significantly stabilised by collision and that QMT is responsible for the increase of the reaction rate at low T.

Another example of the unpredictability and complexity of OVOCs reactions is the reaction of OH with acetone ((CH$_3$)$_2$CO):

OH + (CH$_3$)$_2$CO $\rightarrow$ products (R1.12)

The data for $k_{1.17}$ recommended by IUPAC (Atkinson et al., 2006) are shown in Figure 1.19. In this case, the temperature dependence requires a four-parameter expression:

$k_{1.12}(195 - 440 \text{ K}) =$

$[8.8 \times 10^{-12} \exp(-1320/T) + 1.7 \times 10^{-14} \exp(423/T)] \text{ cm}^3 \text{ molecule}^{-1} \text{ s}^{-1}$ (Eq.1.4)
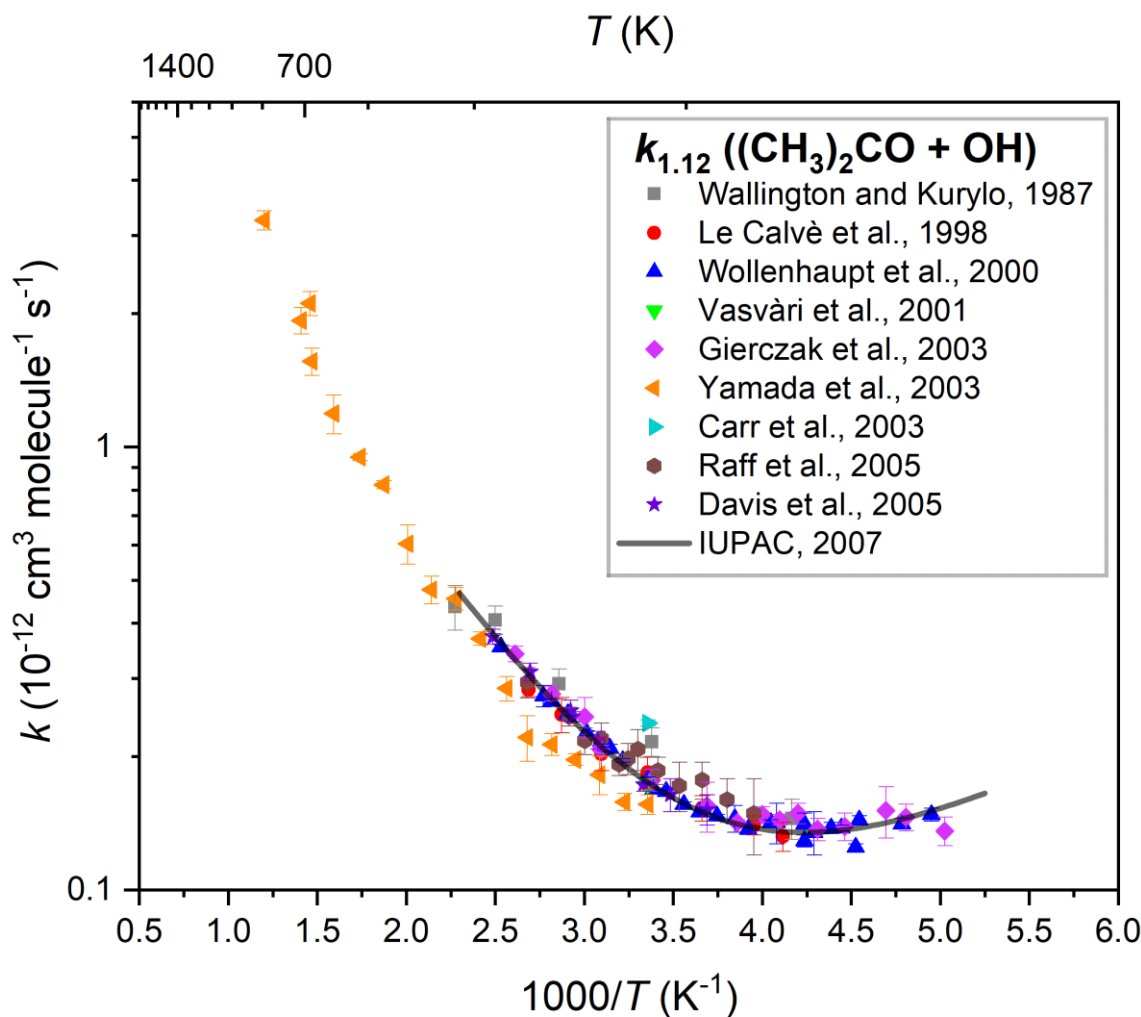
Figure 1. 19: Arrhenius plot displaying $k_{1.12}(T)$ literature determinations (Wallington and Kurylo, 1987a; Le Calvé et al., 1998; Wollenhaupt et al., 2000; Vasvári et al., 2001; Yamada et al., 2003; Gierczak et al., 2003; Carr et al., 2003; Raff et al., 2005) and the most recent evaluation from IUPAC (Atkinson et al., 2006), recommending $k_{1.12}(195 - 440$ K$) = [8.8 \times 10^{-12}$ exp(-1320/T) + 1.7×10^{-14} exp(423/T)] cm^3 molecule^{-1} s^{-1} (the solid black line).

The U-shaped non-Arrhenius behaviour reported in Figure 1.19 shows an unexpected increase of reactivity at low temperatures. At room temperature and above, the reaction takes place through direct H-abstraction from the methyl groups. At 250 K and below, the reaction proceeds via formation of a pre-reaction complex as discussed above and illustrated in Fig. 1.17. In early studies, this alternative mechanism was thought to be OH addition to the carbonyl group, followed by elimination of methyl radical (Vasvári et al., 2001). However, computational calculations and experimental studies provided exhaustive evidence that this mechanism is irrelevant at room temperature and temperatures of interest for atmospheric studies (240-350 K) (Talukdar et al., 2003). Instead, experimental studies and the observed primary isotopic effect observed, suggest that the reaction will proceed through formation of a 6-membered ring hydrogen bonded complex, formed between the carbonyl oxygen, the OH and C-H bond of the methyl group, as illustrated in Figure 1.20.
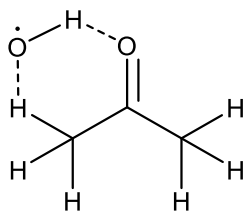
Figure 1. 20: Six-member ring hydrogen-bonded complex forming in the reaction of acetone with OH (R1.12).

This mechanism is likely to occur in reactions of many other oxygenated compounds with OH, making it harder to predict their reactivity and rate coefficient.

1.3.2. OVOC + Cl

Chlorine atoms are known to be important atmospheric oxidant, as they rapidly react with organic molecules to abstract H atoms. Occurrence of Cl radicals mainly depends on the following reactions:

$$Cl_2 + h\nu \rightarrow 2Cl \hspace{4cm} (R1.13)$$

$$ClNO_2 + h\nu \rightarrow Cl + NO_2 \hspace{3cm} (R1.14)$$

Unlike OH, Cl radicals are not regenerated in the oxidation cycle, but the reactions of VOCs and OVOCs with Cl proceed through a mechanism analogous to the reaction with OH radicals. Interestingly, Cl usually reacts much faster than OH (Faxon and Allen, 2013), and in some case the two oxidation routes are competitive even when Cl concentration is much lower than OH. However, the average concentration of Cl is still hard to determine, and it is generally quite smaller than OH, with an estimate of 10^3 atom cm^{-3} in the northern hemisphere (Alwe et al., 2013). This makes Cl less relevant than OH in determining the atmospheric fate of VOCs. On the other hand, it is been reported how Cl concentration can reach peaks of 10^5 atom cm^{-3} in coastal regions and at the marine boundary layer (MBL) (Spicer et al., 1998), in the way that their influence on atmospheric chemistry might be locally very important. To establish whether this condition is meaningful for the purpose of this work and the atmospheric fate of solvents, it is significant to note how industrial sites are often concentrated on coastal areas, especially on estuaries or ports (Lotze et al., 2006). Figure 1.21 shows a map of the location quotients for the manufacturing of chemicals and chemical products (Ons, 2015) in the UK, and some of the most affected regions have a coastal area.
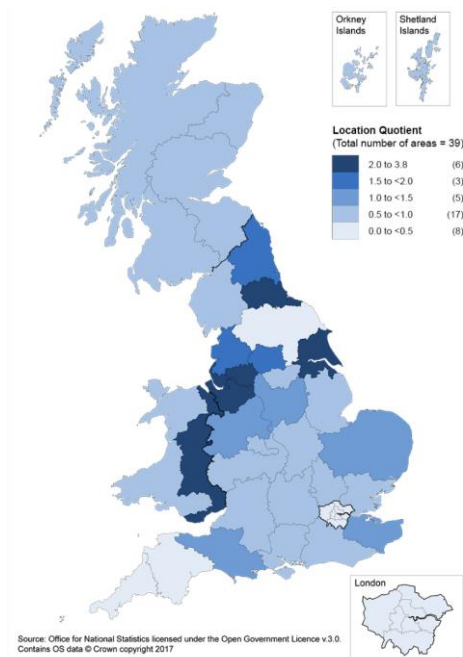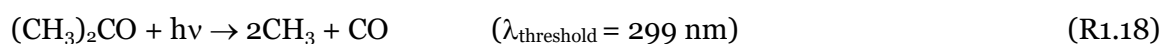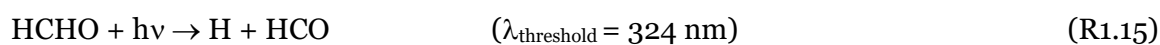
Figure 1. 21: Location quotients for manufacturing of chemicals and chemical products (Ons, 2015).

However, recent studies have shown that Cl concentration could also be significantly high in non-marine sites, where nytril chloride ($ClNO_2$) can be transported or produced from air masses influenced by anthropogenic and marine sources. Thornton et al. (2010) measured $ClNO_2$ concentrations in a mid-continental site of Colorado (USA), 1400 Km from the coast, recording amounts similar to global estimates for marine areas. Phillips et al. (2012) observed high night-time concentrations of $ClNO_2$ in southwest Germany leading to formation of an amount of Cl in the daytime that could exceed the OH production. All this suggests that Cl could significantly affect the atmospheric composition, both in coastal and continental areas.

1.3.3. OVOC + hν

Photochemistry plays an important role in the chemistry of the atmosphere. Some of the reactions introduced in the previous sections involves the interaction of light and are essential for the atmospheric chemistry of the outdoors. Oxygenated compounds such as aldehydes and ketones can absorb in the region of the spectrum of light ($\lambda > 290$ nm) typical of the actinic flux (F). The absorption involves the forbidden $n \rightarrow \pi^*$ transition, where the nonbonding electrons on the O atom are excited to the antibonding π orbital. Because the peak λ of the $n \rightarrow \pi^*$ absorption band corresponds to the ΔH of the carbonyl bond, aldehydes and ketones are subjected to photodecomposition, leading to formation of radicals, and contributing quite considerably to ozone emissions (Mellouki et al., 2015; Wang et al., 2022). Coincidence of λ and ΔH determines the occurrence of the photolysis event and thus the quantum yield (ϕ) relative to that reaction path. In the case of formaldehyde and acetone, these are two main photolysis routes leading to decomposition:

$$HCHO + h\nu \rightarrow H + HCO \qquad (\lambda_{threshold} = 324 \text{ nm}) \qquad \text{(R1.15)}$$

$$HCHO + h\nu \rightarrow H_2 + CO \qquad \text{(R1.16)}$$

$$(CH_3)_2CO + h\nu \rightarrow CH_3 + CH_3CO \qquad (\lambda_{threshold} = 388 \text{ nm}) \qquad \text{(R1.17)}$$

$$(CH_3)_2CO + h\nu \rightarrow 2CH_3 + CO \qquad (\lambda_{threshold} = 299 \text{ nm}) \qquad \text{(R1.18)}$$

What is more, ketones have relatively long lifetimes when considering the removal by OH radicals, and they can travel to the upper troposphere where photolysis is more likely to happen (Romero et al., 2005). Other classes of oxygenated compounds, like alcohols and ethers, absorbs light at lower wavelengths because of $n \rightarrow \sigma^*$ transitions, whereas acids and esters also undergo $n \rightarrow \pi^*$ transitions, but because of the presence of an electron-withdrawing group next to the carbonyl, these absorption bands are shifted to wavelengths lower than 290 nm (Figure 1.22 (Calvert et al., 2011b)).
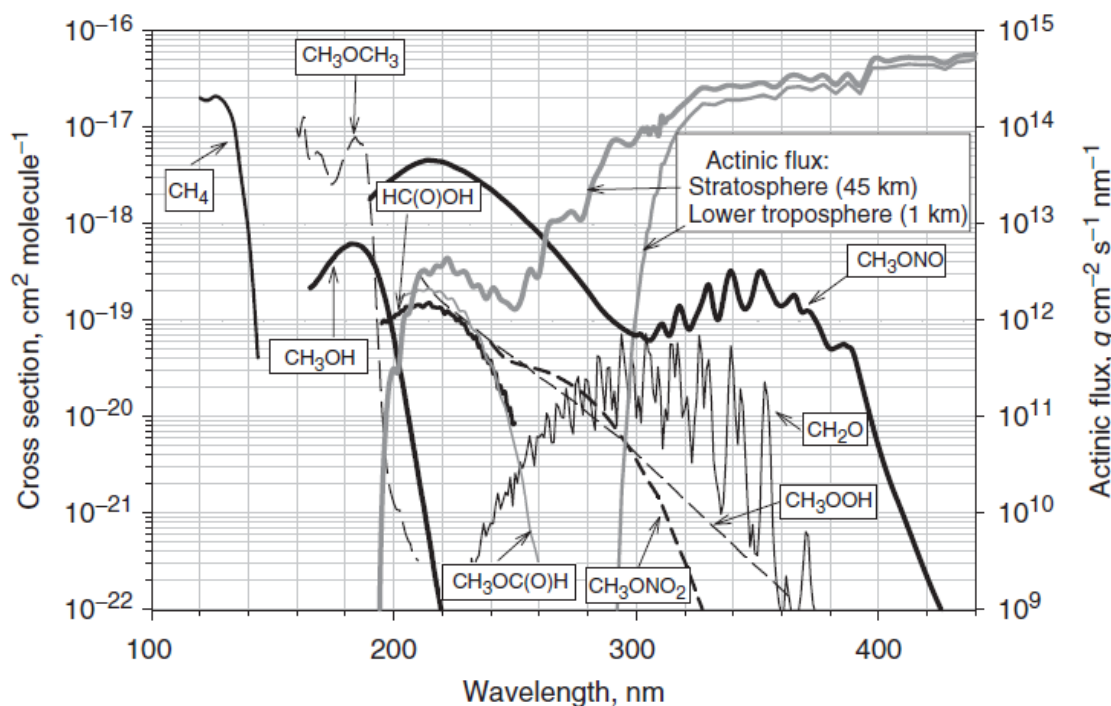

Figure 1. 22: Cross sections for CH4 and various oxidation products of methane as reported by Calvert et al. (2011b).

The photolysis rate, often indicated as j, depends on the absorption cross section σ, the quantum yield ϕ, and the solar irradiance, also known as actinic flux, F, as expressed in Equation 1.5:

$$j = \int \varphi(\lambda, T)\sigma(\lambda, T)F(\vartheta, \lambda)\, d\lambda \qquad \text{(Eq. 1.5)}$$

As there are limited studies on the quantum yield of ketones and aldehydes, and the absorption cross section as well is known only for a limited number of compounds, it is often difficult to estimate the photolysis rate. In some case, atmospheric models assume a value of 1 for the quantum yield. However, ϕ is known to be much lower for some VOC and this assumption may lead to a large overestimate. The importance of photolysis and photodecomposition may strongly depend on the altitudes of interest. At low altitudes, the oxidation initiated by OH radical is often the dominant process, whereas at high altitudes, photolysis is more likely to prevail. Recent studies (Wang et al., 2022) suggests that photodegradable OVOCs have an important impact on emissions of radicals and formation of ozone, and must be included in atmospheric models.

1.4. Reaction Kinetics and Lifetimes

Knowing the rate coefficient of a chemical or photochemical process is essential for the estimation of the lifetime of the species involved. Lifetime, indicated as τ, is known as the time required for the concentration of a compound to drop down to $1/e$ of its initial value (Finlayson-Pitts and Pitts, 2000).

The lifetime of a first-order reactions is simply given by the reciprocal of the rate coefficient. For a second-order reaction, the lifetime of the compound of interest also depends on the concentration of the second reactant, as expressed by Equation 1.6:

$$\text{A} + \text{B} \rightarrow \text{products} \qquad\qquad \tau_A = \frac{1}{k[\text{B}]} \qquad\qquad \text{(Eq. 1.6)}$$
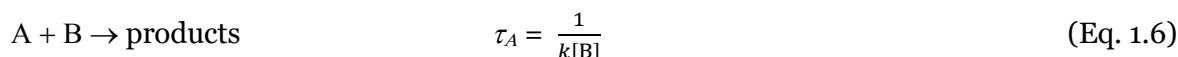
When more reactions compete for the same substrate, the lifetimes associated to each reaction must be considered to obtain the overall lifetime. For a VOC, the main removal pathway is represented by the reaction with OH, photolysis, reaction with Cl, NO_3 or O_3, and the overall lifetime can be calculated as expressed in Equation 1.7 (Seinfeld and Pandis, 2016):

$$\frac{1}{\tau} = \frac{1}{\tau_{OH}} + \frac{1}{\tau_p} + \frac{1}{\tau_{Cl}} + \frac{1}{\tau_{NO_3}} + \frac{1}{\tau_{O_3}} \qquad\qquad \text{(Eq. 1.7)}$$

In this study, the VOCs that were investigated are aliphatic OVOCs, and as such, their reactivity with NO_3 and O_3 can be neglected. Photolysis in the actinic region of light is relevant only for ketones and can be overlooked for ethers. The reaction with Cl was studied for some of the solvents selected and calculation of its lifetime strongly depends on the concentration used. Overall, it is safe to say that reaction with OH was the dominant path and the one that affected the most the lifetime of the OVOCs observed, and as such, more effort was dedicated to it.

It is important to stress out that in addition to chemical transformations, physical processes also represent a major removal route for most air pollutants, including VOCs. These processes are described as *wet and dry deposition* and depend mainly on meteorological conditions, together with other parameters such as solubility and pH. In this work, the lifetime was intended as the lifetime related to chemical transformation, as expressed in eq. 1.7. A more comprehensive estimation of the lifetime in a specific emission event would require the study of wet and dry deposition.

Table 1.2 lists the atmospheric lifetimes of some of the most common VOCs. A summary of three scenarios can be listed according to lifetimes:

1. A lifetime of hours means that emission is likely to affect the local source site with primary and secondary pollution.
2. A longer lifetime (days) indicates that the VOC will travel a longer distance before producing secondary emissions. Compounds of this kind will have a greater impact on global ozone production rather than local.
3. A lifetime of years characterizes compounds such as CH_4 and represents a reason of concern for climate forcing and greenhouse effect more than secondary emissions.

Table 1.2: Atmospheric lifetime of common VOCs expressed in hours (Ragothaman and Anderson, 2017).

Compound	Atmospheric Lifetime (h)
Benzene	226
Toluene	48
Ethylbenzene	38
o-Xylene	20
p-Xylene	19
m-Xylene	12
Methane	84096
Ethane	1440
Propane	240
Butane	120
Ethylene	96
Styrene	4.9

1.5.   Structure Activity Relationship (SAR) calculations

Structure Activity Relationships (SAR) are a very useful and straightforward method for the calculation of rate coefficients solely from the chemical structure of the compound of interest. One of the first SAR methods was developed by Atkinson (1986), as an instrument usable by regulatory agencies to assess the chemicals emitted into the atmosphere. In fact, in those years, the number of rate constants of OH-initiated oxidation of organic compounds and database of information on VOC became enough to start the formulation of a reliable method to calculate unknown rate coefficients. The method was since then regularly updated with the most recent data and knowledge available (Kwok and Atkinson, 1995; Jenkin et al., 2018) and it is based on nonlinear least-squares analyses of the kinetic data determined experimentally. These calculations are used to estimate substituent factors $F(x)$ that accounts for the effect of the neighbour functional groups on the reactivity of each C-H site of the molecule. Substituent factors are then used to calculate the partial coefficient of each C-H bond, which are then summed to obtain the final rate coefficient.

The most recent SARs, formulated by Jenkin et al. (2018), are based on a set of preferred kinetic data that include reactions of OH with 556 organic compounds. These quite extensive database leads to formulation of substituent factors which can account for complex mechanistic aspects such as:

o   Inductive effects of heteroatoms on α and β positioned C-H.
o   H-bonded complex formation.
o   Ring strain.

In addition, this method led to formulation of fixed rate coefficients for H abstraction from specific C-H bond which are believed to behave independently from the nature of the neighbour groups. The simplicity and benefit of using SARs for predicting missing values in chemical models is outstanding. However, if SARs have been well studied for small reactants and hydrocarbons, larger molecules and in general oxygenated compounds with a certain degree of complexity still represent a challenge for this method (Vereecken et al., 2018).

1.6. Photochemical Ozone Creation Potential (POCP)

The Photochemical Ozone Creation Potential (POCP) is a measure of the ability of a VOC to form ground level ozone, relatively to another reference compound (Calvert et al., 2015). POCP values are usually estimated using atmospheric models that considers specific atmospheric conditions and a detailed background of the chemical and photochemical breakdown of the VOC of interest and its degradation products. An example of POCP index is the one developed by Derwent et al. (1996), where the contribution to the ozone formation of a VOC is compared to the contribution of ethene according to the following equation:

$$POCP = \frac{O_3(VOC) - O_3(base\ case)}{O_3(ethene) - O_3(base\ case)} \times 100 \qquad \text{Eq.1.8}$$

Where O_3(base case) is the O_3 is the ozone formation for a base case, O_3(VOC) is the simulated amount of O_3 formed after the increase of VOC concentration, and O_3(ethene) is the amount of O_3 formed because of ethene emissions, all in mass units. The simulated O_3 values are based on several detailed mechanisms such as the MCM – Master Chemical Mechanism (Saunders et al., 2003).

Since for many VOCs a detailed mechanism information is missing, Jenkin et al. (2017) formulated an estimated POCP scale (POCP$_E$) that links chemical structure and rate coefficient of the reaction with OH to the estimation of POCP for the north-west European and USA urban conditions.

$$POCP_E = (A \times \gamma_s \times R \times S \times F) + P + R_{O_3} - Q \qquad \text{(Eq.1.9)}$$

Where A is a multiplier and γ_s accounts for the molecule structure and depends on n_B the number of oxidizable bonds, and M, the molecular mass (Eq. 1.10). R is a parameter which express the relative reactivity with OH, considering the ratio of the rate constant of the VOC with OH k_{OH} and the rate constant for ethene + OH, $k_{OH}°$ (Eq. 1.11-1.12). S is related to the size of the molecule and and depends on the number of carbons n_C (Eq. 1.13). F accounts for the formation of stable carbonyl products and is set to a default value of 1 in the absence of enough details on the oxidation products. P accounts for the ozone formation related to free radicals produced from photolysis, R_{O_3} accounts for reactivity with O_3, and Q is a parameter that accounts for the aromaticity of the molecule.

$$\gamma_s = (n_B/6) \times (28.05/M) \qquad \text{Eq. (1.10)}$$

$$R = 1 - (B \times \gamma_R + 1)^{-1} \qquad \text{Eq. (1.11)}$$

$$\gamma_R = (k_{OH}/k_{OH}°) \times (6/n_B) \qquad \text{Eq. (1.12)}$$

$$S = (1 - \alpha) \times exp(-C \times n_C{}^{\beta}) + \alpha \qquad \text{Eq. (1.13)}$$

A, B, a, C are optimised parameters calculated by Jenkin et al. (2017) for several classes of compounds. The POCP$_E$ values estimated for some of the most common VNP solvents were reported in Figure 1. 23: POCP$_E$ values estimated for diethyl ether, di-isopropyl ether, toluene and hexane in north-west European and USA urban reference conditions (Jenkin et al., 2017).
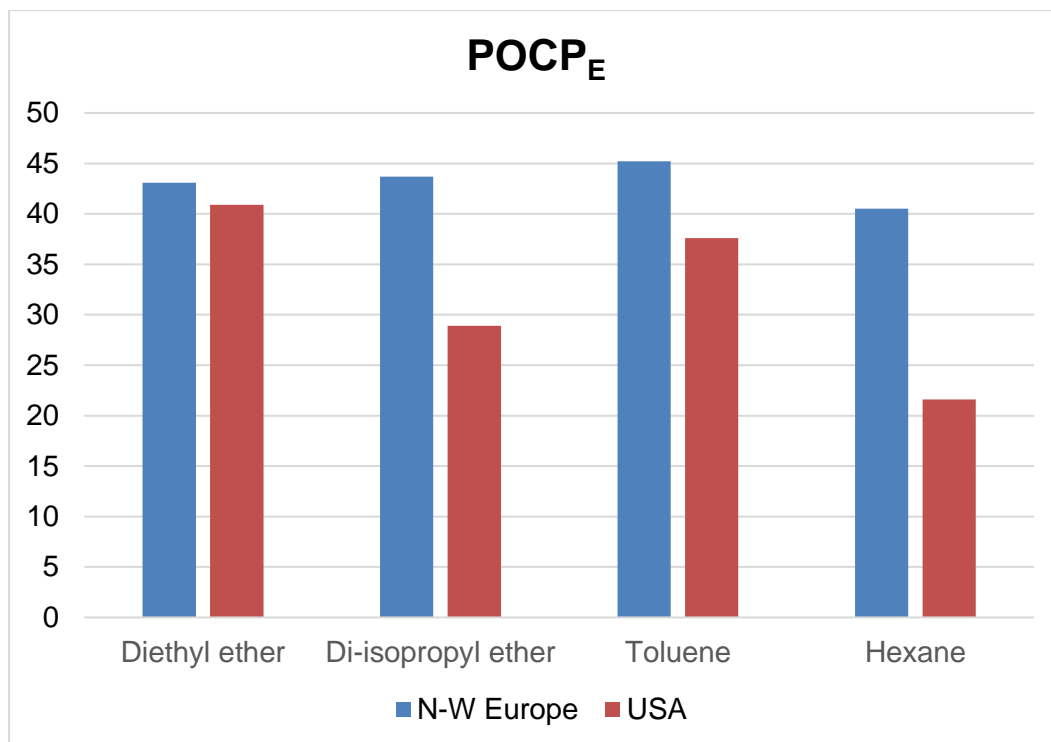
POCP$_E$

Figure 1. 23: POCP$_E$ values estimated for diethyl ether, di-isopropyl ether, toluene and hexane in north-west European and USA urban reference conditions (Jenkin et al., 2017).

The north-west Europe conditions considered by Jenkin et al. (2017) are multi-day scenarios, whereas the USA conditions are a one-day average representative of American urban sites. Figure 1.23 shows how the results for the one-day conditions (USA) have a greater variability, which reflect the higher compound-to-compound variability of the early degradation stages of the VOCs.

2. Experimental

The study of the atmospheric degradation of new 'green' solvents included a variety of techniques that will be described in detail in this chapter. Direct kinetic experiments were carried out with a Pulsed Laser Photolysis-Laser Induced Fluorescence (PLP-LIF) apparatus at the University of York and will be described in section 2.1. Relative Rate (RR) kinetic studies were then performed with the ESC-Q-UAIC environmental simulation chamber at the 'Alexandru Ioan Cuza' University in Iasi, Romania, and was introduced in section 2.2. Section 2.3 is dedicated to the UV-visible experiments for the study of absorption cross sections.

2.1. PLP-LIF Experiments

The observation of chemical reactions is one of the most important goals of chemists and scientists. The study of fast reactions (10^{-3} s or faster) became possible in the 1950's, when the method of 'Flash Photolysis' (FP) was introduced by Manfred Eigen, Ronald Norrish and George Porter (Norrish and Porter, 1949), who then won the Nobel prize in 1967 *"for their studies of extremely fast chemical reactions, effected by disturbing the equilibrium by means of very short pulses of energy"* (Nobelprize, 1967). In his Nobel lecture Porter introduces flash photolysis saying that

"One of the principal activities of man as scientist and technologist has been the extension of the very limited senses with which he is endowed so as to enable him to observe phenomena with dimensions very different from those he can normally experience."

In this context, flash photolysis represented an innovative technique which consisted in perturbing a system with a powerful pulse of extremely short duration, generating a transient intermediate that is then observable using a spectroscopic method, e.g., UV-vis. Pulsed Laser Photolysis (PLP) is a development of FP where the intermediate is generated by photolysis of a precursor with a very fast and powerful pulse generated by a laser. Having started using gas discharge lamps that could reach only the microsecond time scale, Porter predicted in his Nobel lecture that the use of lasers would bring flash photolysis to the nanosecond range, and today laser flash photolysis can reach the scale of the femtoseconds.

In this study, the intermediate of interest was the hydroxyl radical, OH. Various techniques have been applied to the detection of OH, including UV-vis. spectroscopy, mass-spectrometry and resonance fluorescence. Given the well-known spectroscopic characteristics of OH (Voráč et al., 2018; Kinsey, 1977), the direct Laser Induced Fluorescence (LIF) technique is well suited to direct (if not absolute), sensitive and selective detection of OH. In fact, LIF is another application of lasers with short pulses that has shown a great efficacy in the detections of molecules in a certain quantum state. LIF was first developed by Richard Zare in 1968 (Tango et al., 1968) and consists in exciting a sample with a tuneable laser beam. When the spectral range of the laser overlaps one of the absorption lines of the molecule of interest, the fluorescence of the molecule is induced, and the subsequent emission can be detected. The association of PLP with LIF is a very efficient method for the study of second-order reactions of OH radicals with other species, in this case Volatile Organic Compounds (VOC).

2.1.1. Apparatus description

The PLP-LIF apparatus is illustrated in Fig. 2.1 and Fig. 2.2. and was briefly described in this section. Its components were then outlined in detail in the following sections.

Figure 2.1 shows the gas flow system used to generate a continuum flow of a gas mixture of known concentration into the reactor cell. The N_2 and O_2 supply lines, and the glass bulbs containing gas mixtures were connected to the spherical reactor cell, passing through the Mass Flow Controllers (MFCs). The pressure in the system was measured using two calibrated gauges, a 10 Torr (±0.1 Torr) capacitance manometer and a 1000 Torr (± 0.5 Torr) capacitance manometer. The gas mixture preparation was carried out using a Schlenk line and will be described in section 2.1.2.
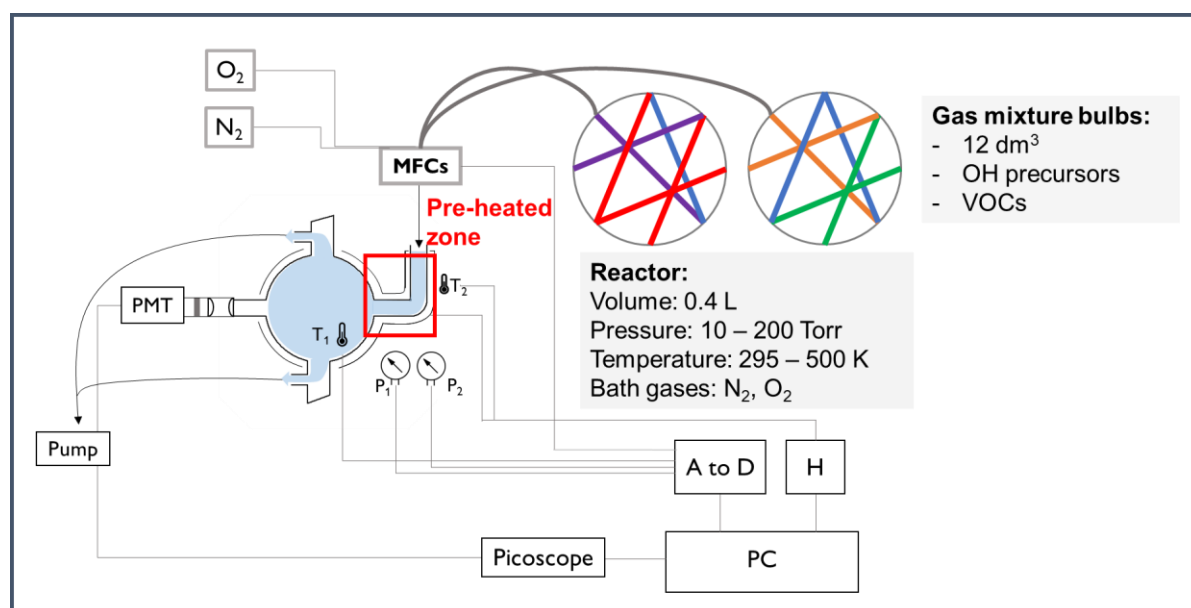
Figure 2. 1: Schematic of the gas flow system. MFCs: Mass Flow Controllers regulate the gas flow coming from the N_2 and O_2 lines and from the gas bulbs. T1 and T2 = thermocouples; P1 and P2 = 1000 Torr and 10 Torr pressure gauges; DG = delay generator; H = thermal control box; A to D = analogue to digital converter to allow PC control of gas flows and logging of cell temperature and pressure.

Figure 2.2 shows the PLP-LIF apparatus where the beams coming from the photolysis laser (Laser#1) and the fluorescence laser (Laser#2) are directed into the reactor cell and aligned via a set of mirrors. The temperature in the reactor cell was monitored with a K-type thermocouple that could be easily moved in and out the photolysis region.

37
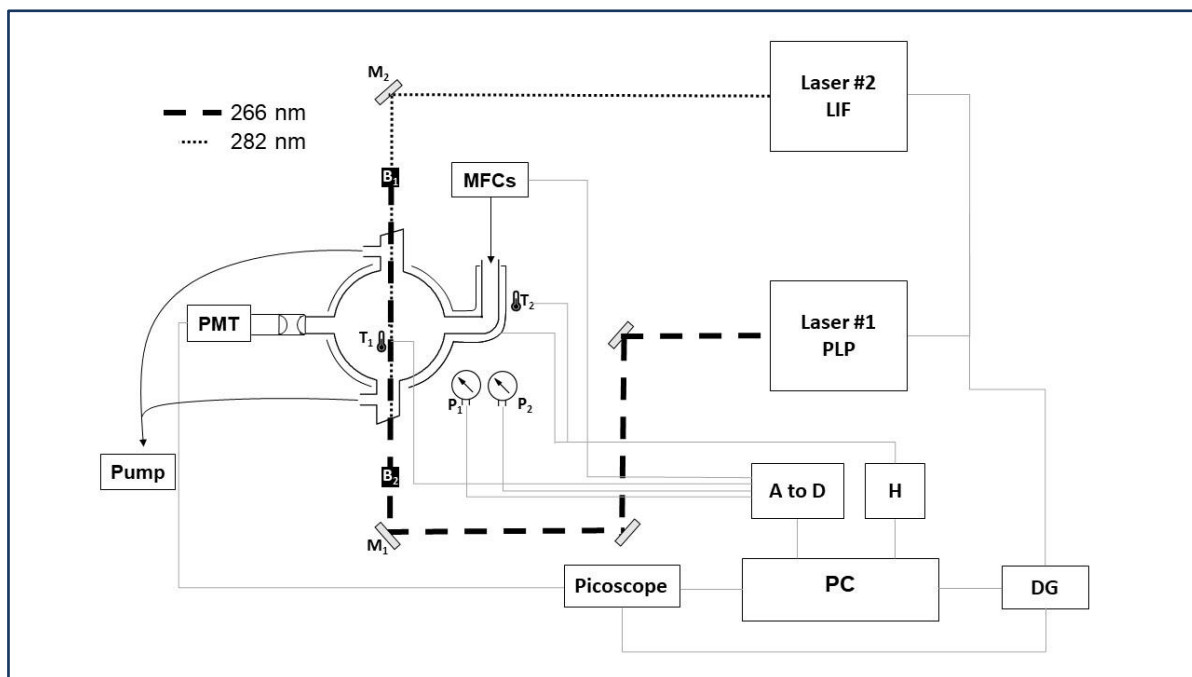
Figure 2. 2: Schematic of the PLP-LIF apparatus. Laser#1 = 266 nm YAG for PLP OH generation; Laser#2 = 532 nm YAG-pumped dye, frequency doubled for output at 282 nm for OH LIF detection; M1 = 266 nm dichroic mirrors; M2 = 282 nm dichroic mirror; B1 and B2 = beam stoppers; T1 and T2 = thermocouples; P1 and P2 = 1000 Torr and 10 Torr pressure gauges; DG = delay generator; H = thermal control box; A to D = analogue to digital converter to allow PC control of gas flows and logging of cell temperature and pressure.

The reactor cell is illustrated in Fig. 2.3, where the 2-D schematics show the directions of the gas flow, the position of the photomultiplier (PMT) and the thermocouple (T). The picture on the right shows the reactor cell partially unwrapped. The reactor cell is a spherical Pyrex vessel with a volume of 250 cm³ and four cylindrical arms. Two arms work as laser beam inlets and were equipped with quartz Brewster windows to minimize optical loss. The third arm, perpendicular to the laser arms, is the gas inlet, and the last arm is connected to the PMT. The entire reactor amounts to an overall volume of around 400 cm³. The gas flow enters the reactor approximately 30 cm upstream of the photolysis region through one of the side arms which is bent to a 90° angle and wrapped with heating tape to allow the gas mixture to gradually warm up while reaching the photolysis area. The insulation tape covers the gas inlet arm and the reactor cell and was connected to feedback electronics to control the temperature of the system. The PMT arm is located perpendicularly to the laser arms and contains 2 lenses that focus light into the PMT, together with a 308 nm interference filter and a 305 nm cut-off filter that minimize detection of scattered laser light (266 nm or 282 nm).
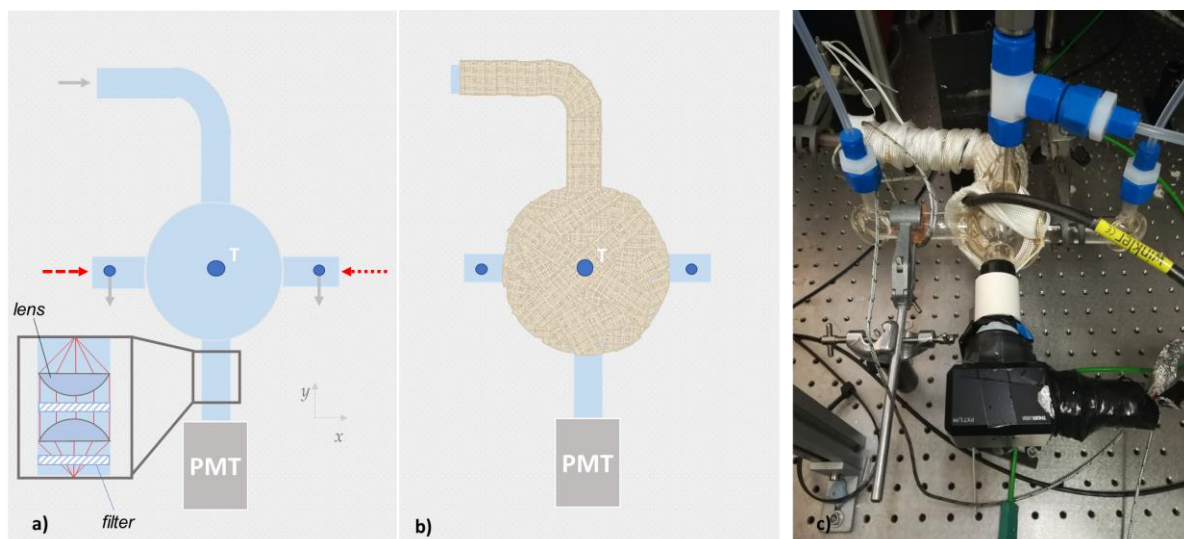
Figure 2. 3: a) 2D-schematic of the reactor cell showing the glass cell, the gas flow directions (grey arrows), the laser beams (red arrows), the photomultiplier box (PMT), the top section of the thermocouple junction (T) and enlargement showing the optics; b) 2D-schematic of the reactor cell showing again the glass cell covered up with hot tape; c) picture of the cell where the hot tape was partially unwrapped to show the reactor cell.

2.1.2. Gas mixtures

The PLP-LIF experiments required the formulation of a continuous flow of gas containing the OH precursor, the VOC of interest, and the bath gas. The VOCs were directed into the reactor using 12 dm^3 glass bulbs containing gas mixtures of known concentration. The OH precursors used in this study were H_2O_2 and tBuOOH.

H_2O_2 could not be easily transferred into a bulb, and it was flowed to the reactor using a bubbler (Figure 2.4). In fact, the highest purity H_2O_2 commercially available is a 60% w/v solution in water. For a further purification, this solution was poured into a 250 ml round bottom flask equipped with a bubbler made of a glass cylinder provided with a porous end realised in the glass workshop of the University of York by Abigail Mortimer. The N_2 line was connected to the bubbler and a continuum flow was transferred through the porous glass into the solution. The other side of the bubbler was connected to the MFCs, that then move the flow into the reactor and finally to the pump. Before using the H_2O_2 for the experiment, the solution was concentrated flowing N_2 into the bubbler for at least 12 hours. Because of the difference in volatility, H_2O was preferably removed, leaving a more concentrated solution of H_2O_2 in the bubbler. SAFETY WARNING: this procedure leads to concentrated H_2O_2 which is an explosive, safety measures such as a by-passed bubbler and a protection screen, together with PPE, were always used. After this procedure, the N_2 passing through the solution carried mostly H_2O_2 with an unimportant water impurity. An ice bath was sometime used to suppress the vapour pressure of H_2O_2 and hence lower concentrations in the reactor. The bubbler was also equipped with a bypass to allow for N_2 flowing through the line before and after the experiment.
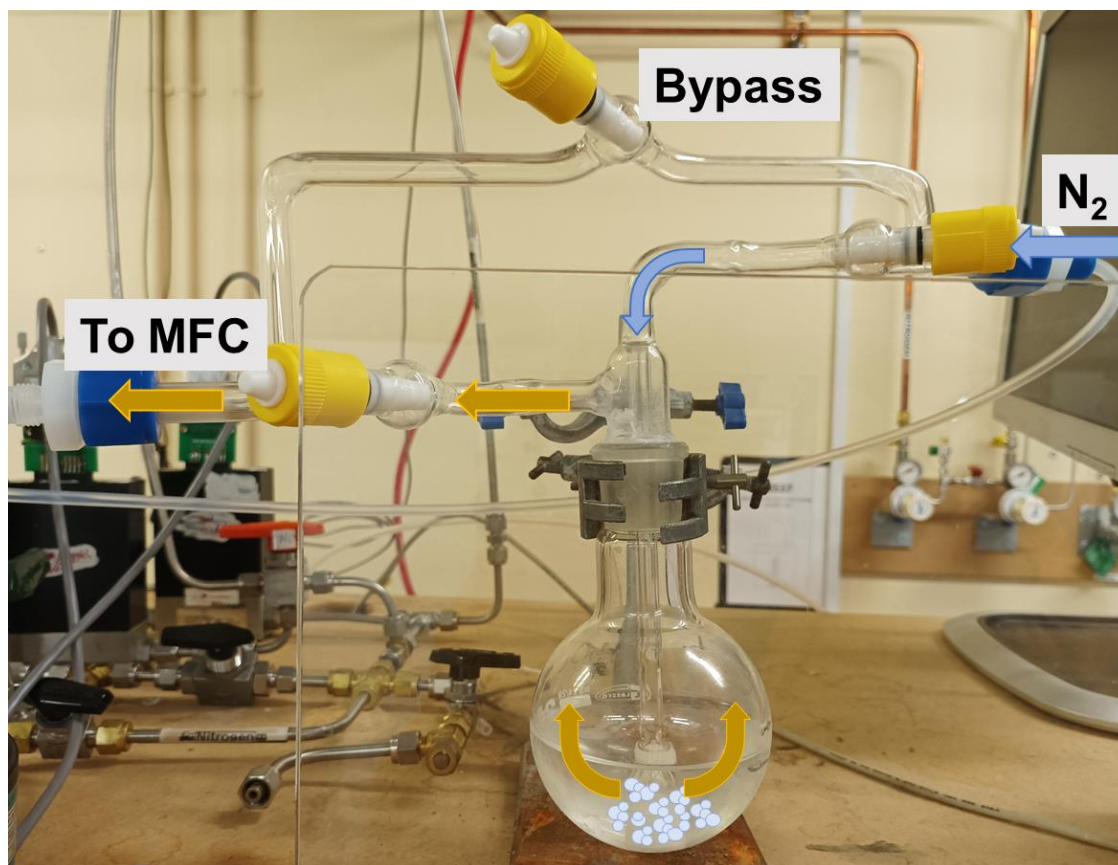
Figure 2. 4: H₂O₂ bubbler connected to the N₂ line and to the MFCs. The blue arrows represent the N₂ flow, the yellow arrows represent the flow of N₂ carrying the OH precursor after passing through the solution.

The other OH precursor (tBuOOH) and all the VOCs used were each transferred to a glass bulb that was then connected to an MFC and to the PLP-LIF apparatus. Dilute mixtures of VOC in N2 were prepared using a Schlenk line and their concentration were determined through manometric measurements. Figure 2.5 shows the Schlenk line apparatus which is essentially composed by a glass line connected to the N_2 flow and to a pump. The line is equipped with four taps through which the glass finger containing the solvent and the bulb were connected. The pressure in the line was monitored with two MKS Baratron capacitance manometers, a 10 Torr and 1000 Torr manometers. For the realization of the gas mixtures, a few millilitres of VOC were poured into the glass finger and were subjected to at least three cycles of freeze-pump-thaw purification. After that, the desired amount of VOC was transferred into the bulb that was then filled with N_2 up to a pressure of 900-1000 Torr depending on the wanted final concentration.
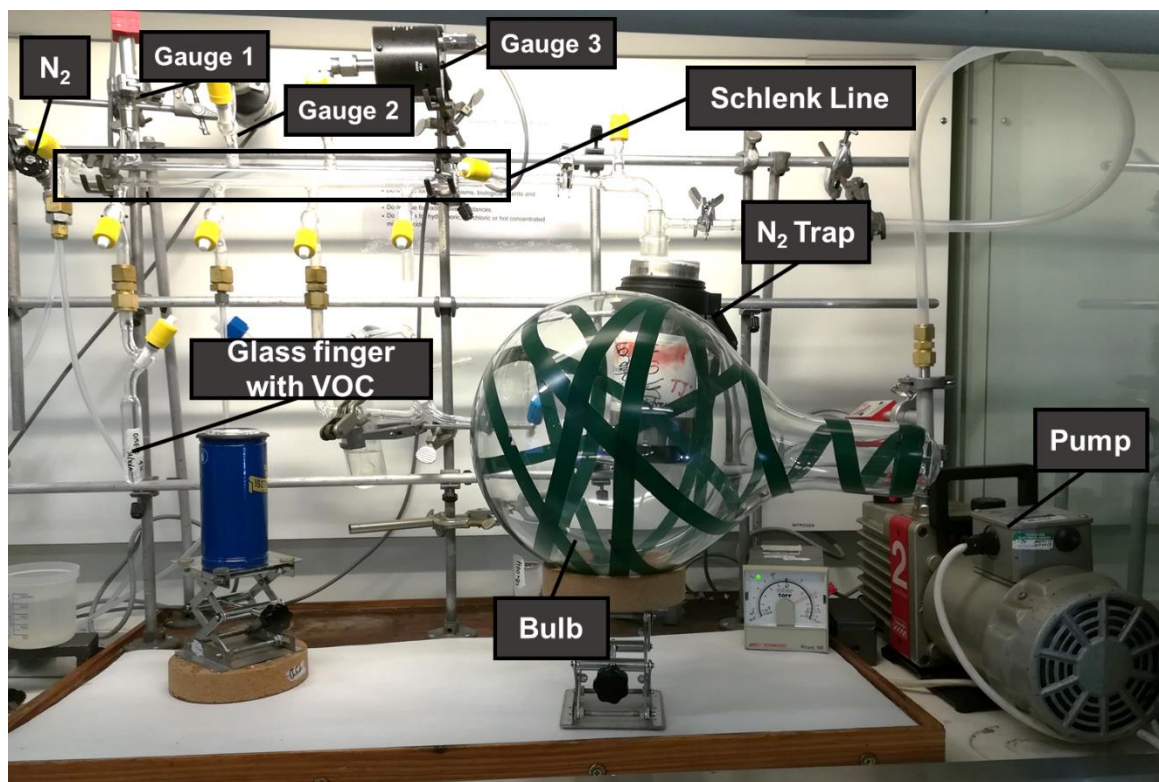
Figure 2. 5: Schlenk Line apparatus. The glass line is connected to N₂, to three gauges, to the glass bulb and to a glass finger containing a VOC. At the end of the line the liquid N₂ trap prevents any VOC to condense into the pump.

The 10 Torr and 1000 Torr gauges were cross calibrated regularly to ensure consistency in the measurements. Typical pressure readings for the 10 Torr gauge would lie around 0.5-9 Torr, whereas readings on the 1000 Torr would go up to 990 Torr. An example of a set of routine calibrations is shown in Fig. 2.6, and the linear plots can be described according to the following equation:

$$P_{1000\,Torr} = P_{10\,Torr} \times CG + I \qquad \text{(Eq. 2.1)}$$

Where $P_{1000\,Torr}$ and $P_{10\,Torr}$ are the pressure values read from the 1000 Torr and 10 Torr gauges respectively, *CG* stands for calibration gradient and *I* for the intercept. The value read from the 10 Torr gauge was calibrated according to Eq. 2.2 to give the pressure of the VOC in the glass bulb:

$$P_{VOC} = P_{10\,Torr} \times CG + I \qquad \text{(Eq. 2.2)}$$

Accordingly, the uncertainty on P_{VOC} was estimated using the following expressions for the propagation of uncertainty:

$$\Delta(P_{10\,Torr} \times CG) = P_{10\,Torr} \times CG \times \sqrt{\left(\frac{\Delta P_{10\,Torr}}{P_{10\,Torr}}\right)^2 + \left(\frac{\Delta CG}{CG}\right)^2} \qquad \text{(Eq. 2.3)}$$

$$\Delta_{P_{VOC}} = \sqrt{(\Delta(P_{10\,Torr} \times CG))^2 + (\Delta I)^2} \qquad \text{(Eq. 2.4)}$$
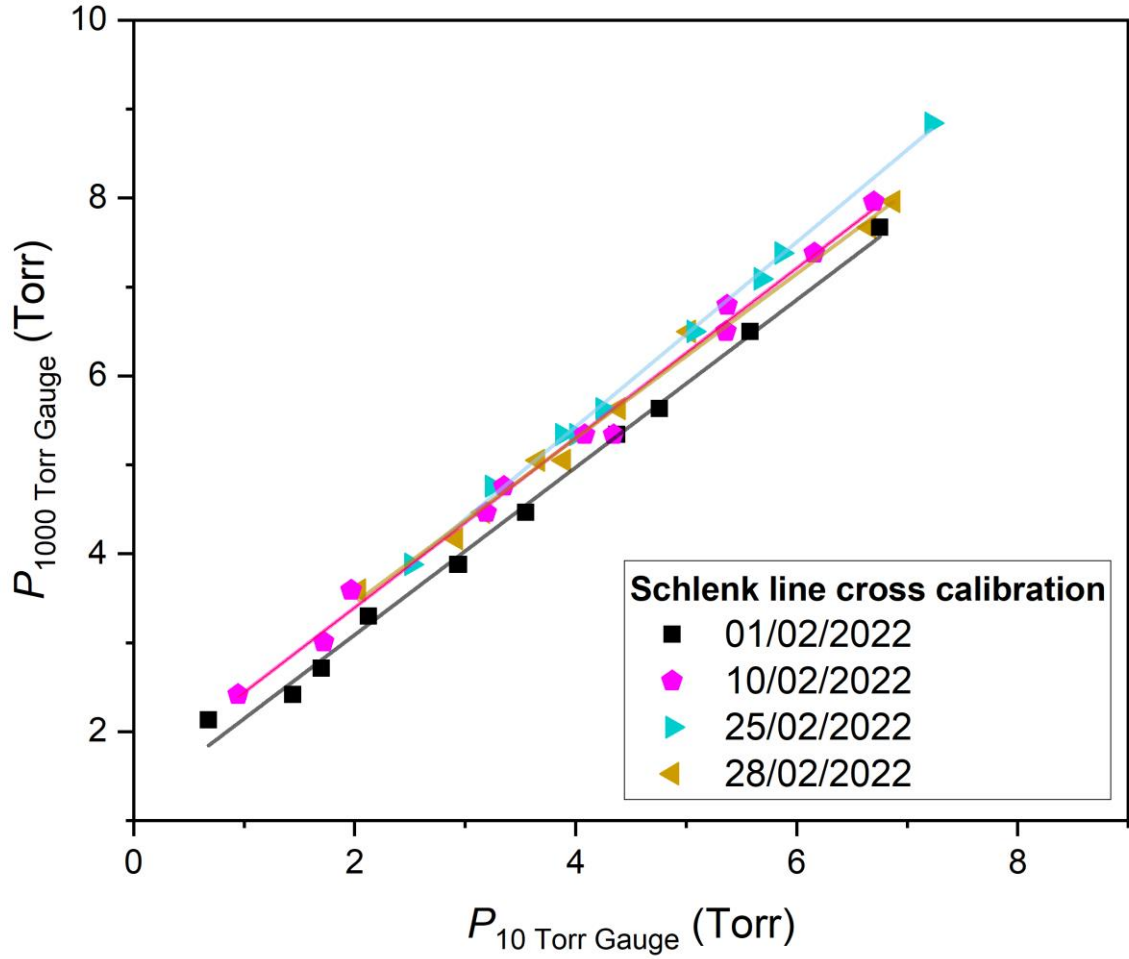
Figure 2. 6: Exemplary linear plots for the cross calibration of the Baratron 10 Torr and 1000 Torr Schlenk line gauges performed during a set of experiments from 01/02/2022 to 28/02/2022.

The concentration of VOC in the bulb was calculated according to Eq. 2.5, where P_{VOC} represents the pressure of the solvent in the bulb estimated according to Eq. 2.2 and P_{tot} is the total pressure in the bulb.

$$c_{bulb} = \frac{P_{VOC}}{P_{tot}} \times 100 \qquad\qquad (Eq.\ 2.5)$$

The uncertainty on the concentration of VOC was estimated using Eq. 2.6:

$$\Delta c_{bulb} = c_{bulb} \times \sqrt{\left(\frac{\Delta P_{VOC}}{P_{VOC}}\right)^2 + \left(\frac{\Delta P_{tot}}{P_{tot}}\right)^2} \qquad\qquad (Eq.\ 2.6)$$

A typical calculation for a routine bulb of a VOC with a concentration of around 0.5% is reported below (see Appendix A, Table A1):

$$\Delta(P_{10\ Torr} \times CG) = 5.0\ Torr \times 0.98 \times \sqrt{\left(\frac{0.23}{5.0}\right)^2 + \left(\frac{0.02}{0.98}\right)^2 + 2\frac{4.6 \times 10^{-3}}{4.9}} = 0.32 \qquad (Eq.\ 2.7)$$

$$\Delta_{P_{VOC}} = \sqrt{(0.32)^2 + (0.09)^2} = 0.33 \qquad\qquad (Eq.\ 2.8)$$

$$\Delta c_{bulb} = c_{bulb} \times \sqrt{\left(\frac{0.33}{5.0}\right)^2 + \left(\frac{0.23}{998.0}\right)^2 + 2\frac{0.08}{4990}} = 0.03 \qquad\qquad (Eq.\ 2.9)$$

Equations 2.7-2.9 lead to Δc_{bulb}=0.03 which represents 7% of the estimated concentration. However, this value represents the minimum uncertainty as it doesn't account for other factors such as impurities that may occur in the VOC sample and in the N_2 flow, and measurement glitches.

2.1.3. Gas Flow

The flow of gases into the reactor cell was controlled using 4 Mass Flow Controllers (MFC). Figure 2.7 shows the MFCs setup and the connection to the gas sources and the reactor cell. MFC1 was connected to the N_2 line and was used to flow N_2 into the mixing chamber and then to the reactor cell. Similarly, MFC2 was used to flow N_2 and the gas line could be switched to the O_2 line to provide O_2 during the experiments in air. MFC3 was connected to the VOC bulb and was used to supply a VOC to the reactor cell. The MFC4 inlet was linked to the N_2 line and the outlet was connected to the H_2O_2 bubbler, flowing N_2 through the bubbler as described in the previous section, to provide the OH precursor to the cell.
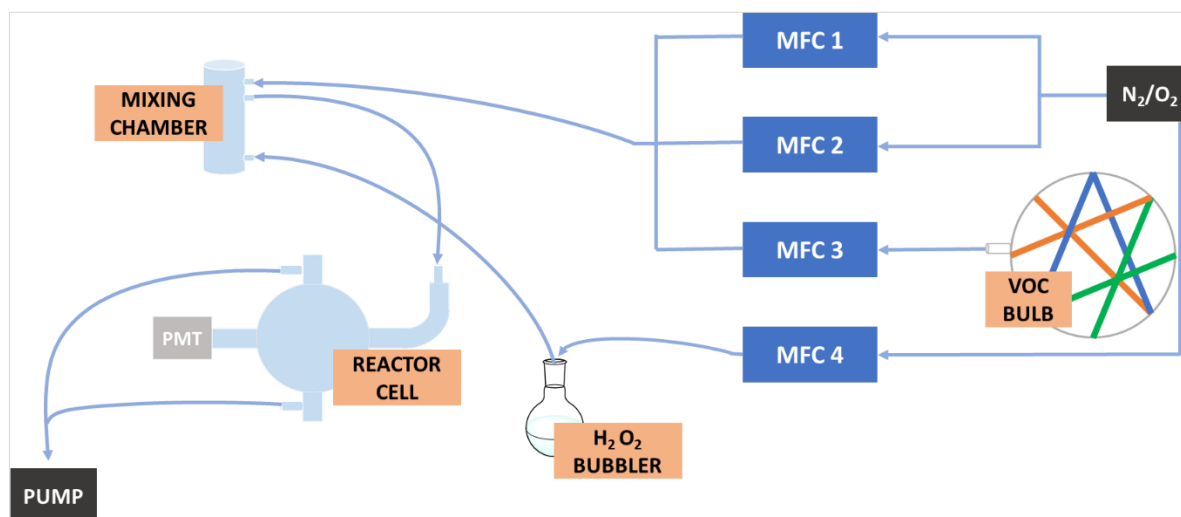
Figure 2. 7: Schematic of the flow system showing the four MFCs. MFC1 and MFC2 were connected to the N_2/O_2 line, MFC3 was connected to the VOC bulb, and MFC4 was connected on the N_2 line on one hand and to the H_2O_2 bubbler on the other end.

The four MFCs had different flow rate scales (Table 2.1) and were operating in the 5%-80% of their full scale for an optimal accuracy. MFC$_S$ were calibrated periodically with a Restek Proflow 6000 flowmeter.

Table 2.1: MFCs used in the PLP-LIF experiments with their flow rate scales and the flow rate ranges used.

	Gas	Flow rate (sccm)	Experiment flow rate range (sccm)
MFC1	N_2	0-1000	100-700
MFC2	N_2/O_2	0-1000	100-700
MFC3	VOC	0-200	10-150
MFC4	H_2O_2	0-100	20-80

Notes: flow rates are in standard cubic centimetres per minute (sccm).

The concentration in the reactor cell was estimated using the ideal gas law (Eq. 2.10)

$$PV = nRT \qquad \text{(Eq. 2.10)}$$

43

leading to the following expression for the concentration of molecules in the reactor cell (Eq. 2.11 – Eq. 2.12):

$$c_{cell}(mol\ cm^{-3}) = \frac{P_{cell}}{R\,T_{cell}} \tag{Eq. 2.11}$$

$$c_{cell}(molecule\ cm^{-3}) = \frac{T_{standard}}{P_{standard}V_m}\frac{P_{cell}}{T_{cell}} \times N_A \tag{Eq. 2.12}$$

where c_{cell} stands for the concentration of molecules in the reactor cell, P_{cell} and T_{cell} are respectively the pressure and the temperature of the reactor cell, R is the ideal gas constant, $P_{standard}$ and $T_{standard}$ are the standard values of pression and temperature equal to 1 atm (760 Torr) and 273.15 K, and V_m is the molar volume, equal to 24790 cm³. Accordingly, the estimation of the uncertainty on the concentration of molecules in the reactor cell will be as follow:

$$\Delta c_{cell} = c_{cell} \times \sqrt{\left(\frac{\Delta P_{cell}}{P_{cell}}\right)^2 + \left(\frac{\Delta T_{cell}}{T_{cell}}\right)^2 + 2 \times \frac{(\Delta P_{cell} \times \Delta T_{cell})}{(P_{cell} \times T_{cell})}} \tag{Eq. 2.13}$$

For a typical room temperature experiment (T = 298 K) where the pressure of the reactor cell was 60 Torr, and the concentration of the molecules was 2×10^{18} molecules cm⁻³, the uncertainty was estimated to be around 1% (Eq. 2.14).

$$\Delta c_{cell} = 2 \times 10^{18} \times \sqrt{\left(\frac{0.5}{60}\right)^2 + \left(\frac{2}{298}\right)^2 + 2\frac{1}{17880}} = 3 \times 10^{16} \tag{Eq. 2.14}$$

For the calculation of the VOC concentration in the reactor cell, the concentration of the bulb and the MFC flow (F) must be also considered, leading to the following expression (Eq. 2.15)

$$c_{VOC}(molecule\ cm^{-3}) = c_{cell} \times \frac{F_{MFC_{VOC}}}{\sum_i F_{MFC_i}} \times c_{bulb} \tag{Eq. 2.15}$$

where $F_{MFC_{VOC}}$ represents the flow rate for the VOC (MFC3 in Fig. 2.7), and $\sum_i F_{MFC_i}$ is the sum of all the flows coming from the four MFCs. Equations similar to the ones used for the Schlenk line gauges calibrated pressures were also used to determine the uncertainty of the calibrated flows and the equations were reported in Appendix A (Table A2). The uncertainty on the VOC concentration can then be calculated according to equation 2.16-2.18:

$$\Delta\left(\sum_i F_{MFC_i}\right) = \sqrt{\sum_i(\Delta F_{MFC_i}^{\ 2} \times f_i)} \tag{Eq. 2.16}$$

$$\Delta\left(\frac{F_{MFC_{VOC}}}{\sum_i F_{MFC_i}}\right) = \frac{F_{MFC_{VOC}}}{\sum_i F_{MFC_i}} \times \sqrt{\left(\frac{\Delta F_{MFC_{VOC}}}{F_{MFC_{VOC}}}\right)^2 + \left(\frac{\Delta\left(\sum_i F_{MFC_i}\right)}{\sum_i F_{MFC_i}}\right)^2 + 2\frac{\Delta F_{MFC_{VOC}} \times \Delta\left(\sum_i F_{MFC_i}\right)}{F_{MFC_{VOC}} \times \sum_i F_{MFC_i}}} \tag{Eq. 2.17}$$

$$\Delta(c_{VOC}) = c_{VOC} \times$$
$$\sqrt{\left(\frac{\Delta(c_{cell})}{c_{cell}}\right)^2 + \left(\frac{\Delta\left(\frac{F_{MFC_{VOC}}}{\sum_i F_{MFC_i}}\right)}{\frac{F_{MFC_{VOC}}}{\sum_i F_{MFC_i}}}\right)^2 + \left(\frac{\Delta(c_{bulb})}{c_{bulb}}\right)^2 + 2\frac{\Delta(c_{cell}) \times \Delta\left(\frac{F_{MFC_{VOC}}}{\sum_i F_{MFC_i}}\right)}{c_{cell} \times \frac{F_{MFC_{VOC}}}{\sum_i F_{MFC_i}}} + 2\frac{\Delta(c_{bulb}) \times \Delta\left(\frac{F_{MFC_{VOC}}}{\sum_i F_{MFC_i}}\right)}{c_{bub} \times \frac{F_{MFC_{VOC}}}{\sum_i F_{MFC_i}}} + 2\frac{\Delta(c_{cell}) \times \Delta(c_{bulb})}{c_{cell} \times c_{bulb}}} \tag{Eq. 2.18}$$

where f_i in Eq. 2.16 is the scaling factor that accounts for the differential flow rates used for the MFCs. For the conditions of a typical experiment conducted at 60 Torr, from a bulb of 0.5% concentration, the calculated uncertainty of the VOC concentration in the reactor cell was around ±10% (mean uncertainty for the typical flows, see Appendix A, Table A3). However, the equations described above are an expression of the minimum uncertainty that can be estimated for the VOC concentration, as it doesn't account for all factors that may affect the measurements, such as impurities in the VOC sample and in the N₂ line, and

experiments glitches. Overall, considering the potential systematic errors, we estimate an uncertainty of ± 15% on the VOC concentration in the reactor cell.

2.1.4. Pulsed Laser Photolysis

The photolysis laser used in the PLP-LIF experiments is a Quantel Q-Smart operating at the fourth harmonic generation from a Nd:YAG laser with a repetition time of 10 Hz (Table 2.2). The laser fluence was 100 mJ/pulse according to the manufacturer specification. However, after measuring the laser fluence up- and down-stream of the reactor with a power meter, we estimated a fluence of 20 mJ/pulse. The laser was directed into the reactor via a quartz Brewster window and was used to generate OH via 266 nm PLP (R2.1 or R2.2) of one of two suitable radical precursors.

$$H_2O_2 + h\upsilon \rightarrow 2OH \qquad\qquad (R2.1)$$

$$(CH_3)_3COOH + h\upsilon \rightarrow (CH_3)_3CO + OH \qquad\qquad (R2.2)$$

Table 2.2 summarises the properties of the photolysis laser:

Table 2.2: Photolysis laser specification

	λ (nm)	Pulse duration (ns)	Repetition Rate (Hz)	Power (W)	Delay Flashlamp - Qswitch (μs)	Laser Fluence[a] (mJ/cm²)
PLP	266	6	10	1	300	20

Notes: [a]Laser fluence after up- and down-stream measurements.

The concentration of OH generated by PLP from R2.2 was estimated according to the following expression:

$$[OH] = \sigma(\lambda)\varphi(\lambda)[ROOH]F \qquad\qquad (Eq. 2.19)$$

Where σ is the absorption cross section of the OH precursor, ROOH, φ is the quantum yield for the photolysis reaction and F is the number of photons per unit area. The number of photons per unit area depends on the laser energy (20 mJ/pulse) and was estimated via the following expressions (Eq.2.20-2.22):

$$\nu = \frac{c}{\lambda} = \frac{3 \cdot 10^8 \, m \, s^{-1}}{266 \cdot 10^{-9} m} = 1.13 \cdot 10^{15} \text{ Hz} \qquad\qquad (Eq. \; 2.20)$$

$$N° \, of \, photons = \frac{Pulse \, Energy}{Photon \, Energy} = \frac{20 \, mJ/pulse}{h\nu} = 2.68 \cdot 10^{16} \text{ photon/ pulse} \qquad (Eq. 2.21)$$

$$N° \, of \, photons \, per \, unit \, area = \frac{\frac{N \, of \, photons}{pulse}}{Cross \, section \, of \, pulse} = \frac{2.68 \cdot 10^{16} \, photon/pulse}{0.3 \, cm^2} =$$

$$8.92 \cdot 10^{16} \text{photon cm}^{-2} \text{ pulse}^{-1} \qquad\qquad (Eq. 2.22)$$

As we estimated a concentration of ROOH of around 10^{14} molecule cm⁻³, and the cross section of the OH precursors used is known, the only missing value for the estimation of [OH] is the quantum yield. Using a value of 1 for φ, we can estimate an upper limit for [OH], and using Eq. 2.19 we obtained the following values for a typical [ROOH] of 1×10^{14} molecule cm⁻³:

$$[OH]_{(CH3)3COOH} \approx \sigma(\lambda)\varphi(\lambda)[(CH_3)_3COOH]F = \qquad\qquad (Eq. 2.23)$$

$= 0.941 \times 10^{-20}$ cm^2 molecule$^{-1}\times 1\times 10^{14}$ molecule cm$^{-3}\times 8.92 \cdot 10^{16} photon\ cm^{-2}\ pulse^{-1} =$

$= 8.4 \times 10^{10}$ molecule cm^{-3}

$$[OH]_{H2O2} = \sigma(\lambda)\varphi(\lambda)2[H_2O_2]F = \qquad\qquad (Eq.\ 2.24)$$

$= 4.2 \times 10^{-20}$ cm^2 molecule$^{-1}\times 1\times 2\times 10^{14}$ molecule cm$^{-3}\times 8.92 \cdot 10^{16} photon\ cm^{-2}\ pulse^{-1} =$

$= 7.6 \times 10^{11}$ molecule cm^{-3}

Equation 2.23 is the expression used for the calculation of [OH] initiated by $(CH_3)_3COOH$, using the cross section determined by Baasandorj et al. (2010). Similarly, Eq. 2.24 is the expression used for the calculation of [OH] initiated by H_2O_2, using the cross section evaluated by IUPAC (Atkinson et al., 2004).

2.1.5. Laser Induced Fluorescence

The detection of OH radicals for the kinetic study of second order reactions was carried out via Laser Induced Fluorescence (LIF). As mentioned in the previous sections, LIF is a useful technique for detection of chemical species in specific quantum states. In this study, the $Q_1(1)$ transition of $A^2\Sigma^+(v = 1) \leftarrow X^2\Pi(v = 0)$ at 281.997 nm was used for direct, off-resonant LIF detection of OH (Figure 2.8 -2.9).
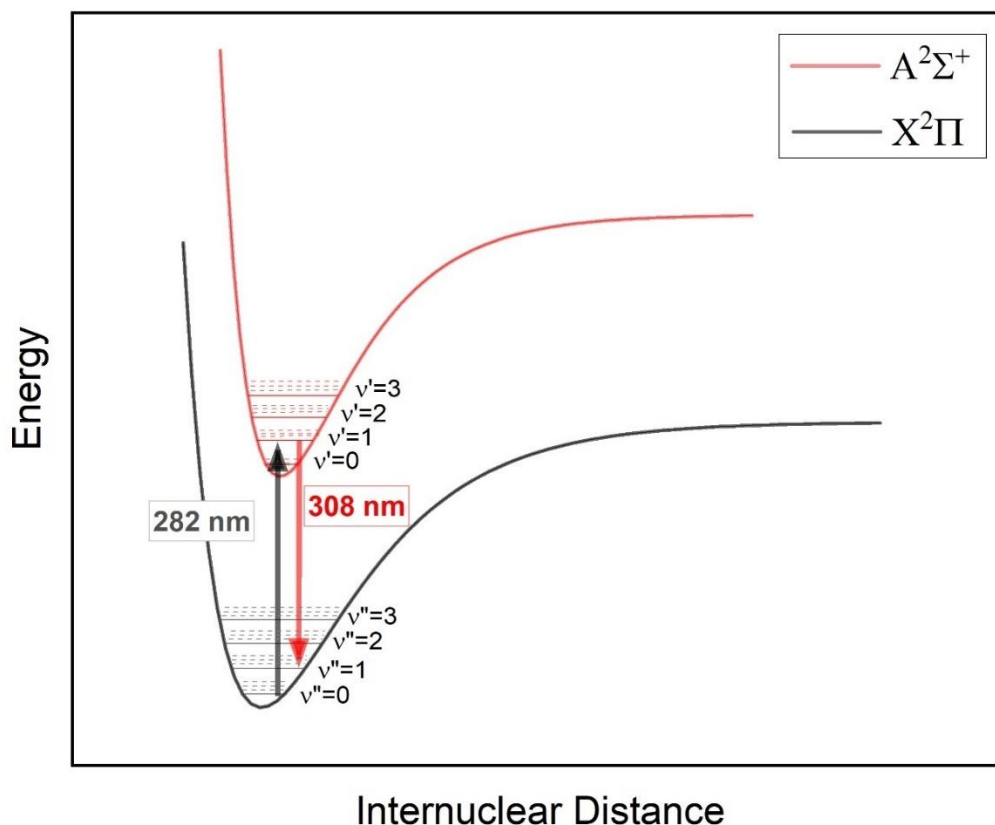
Figure 2. 8: Morse potentials for the X²Π ground state and the A²Σ⁺excited state of OH radical. The black arrow indicates the A²Σ⁺(v = 1) ← X²Π(v = 0) transition (282 nm) and the red arrow represents the corresponding fluorescence emission at 308 nm.
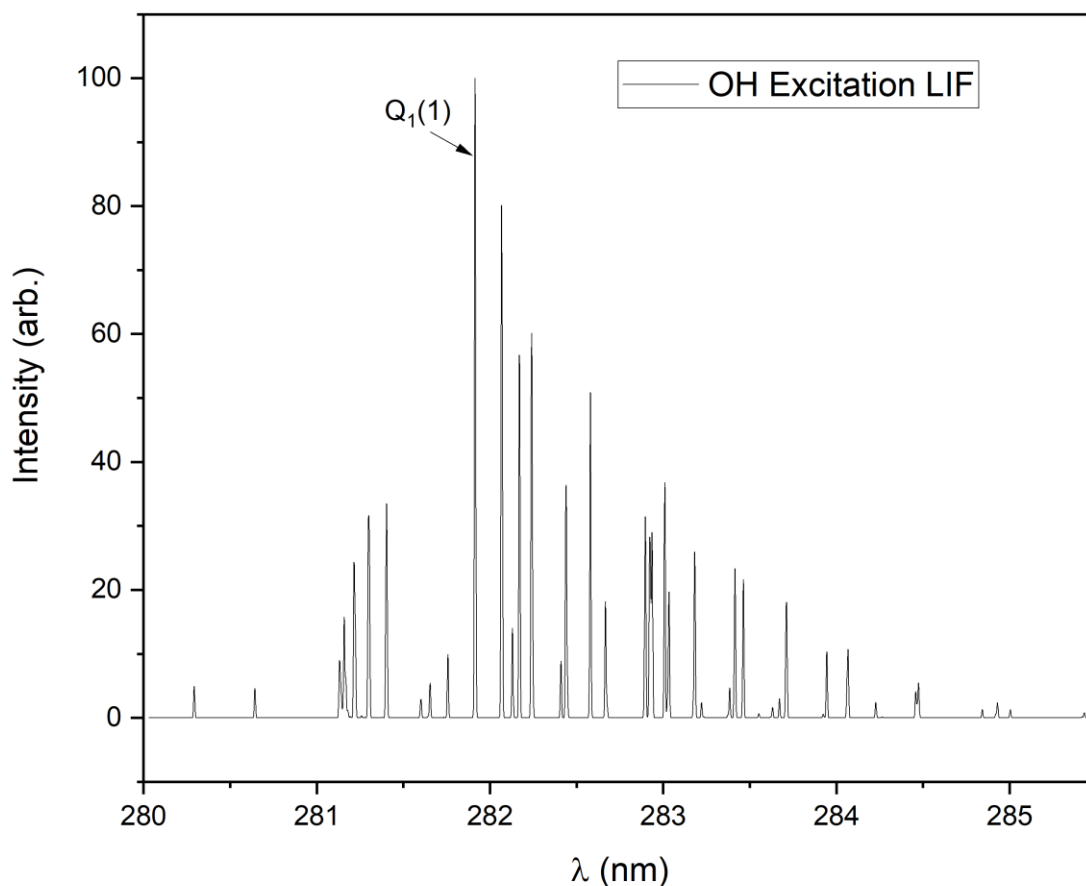
Figure 2. 9: LIF excitation spectrum of OH for the $A^2\Sigma^+(v = 1) \leftarrow X^2\Pi(v = 0)$ transition, showing the $Q_1(1)$ roto-vibrational band. Spectrum simulated via LIFBASE (Luque and Crosley, 1999).

A Continuum Nd:YAG laser operating at the second harmonic (532 nm) was pumped into a NarrowScan Pulsed Dye laser equipped with a Rhodamine-6G solution. Figure 2.10 shows the typical spectrum of Rhodamine 6G and the Nd:YAG wavelength, lying within the absorption maximum.
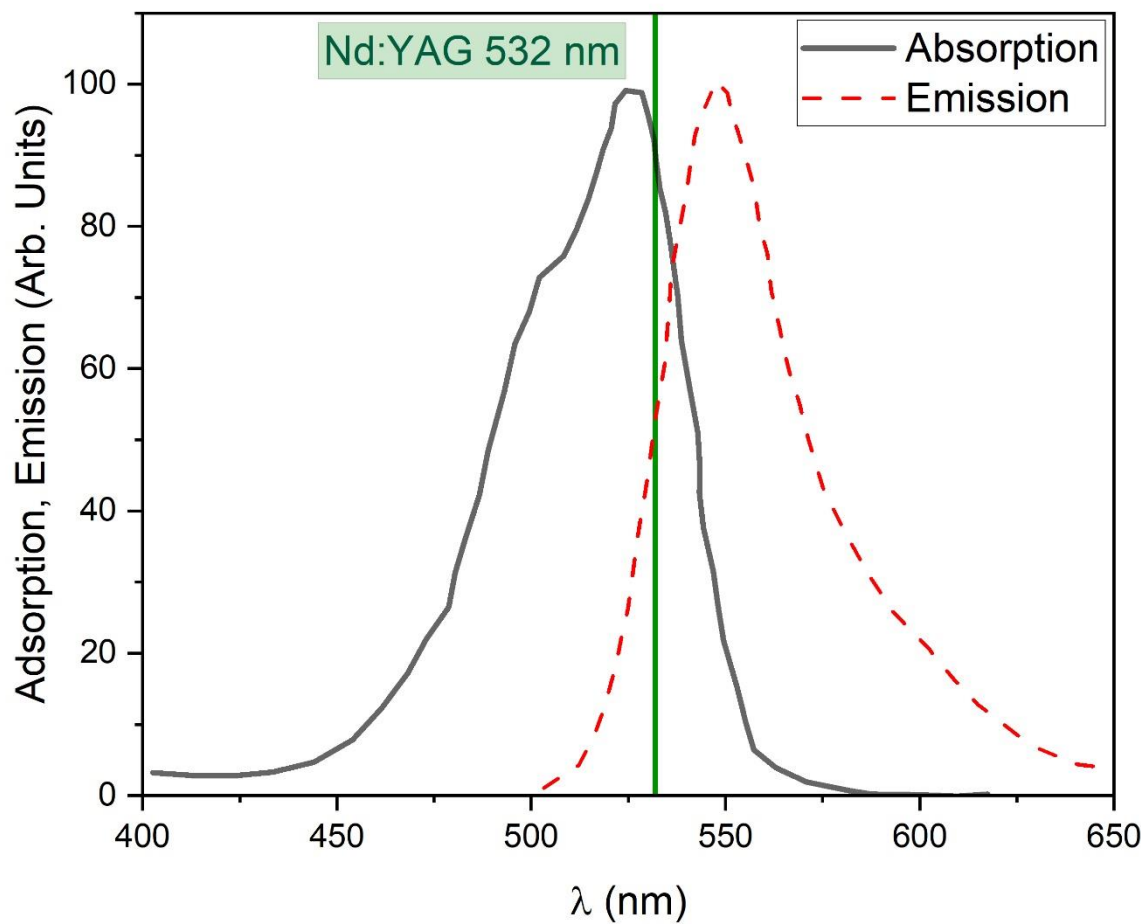
Figure 2. 10: Absorption (solid grey line) and emission (red dashed line) spectra of Rhodamine 6G from Fluorescence Spectrum Viewer of AAT Bioquest (Bioquest, 2023). The green vertical line indicates the Nd:YAG second harmonic wavelength.

The tuneable laser output was set to 564 nm and doubled with a potassium dideuterium phosphate (KDP) crystal to get a 282 nm beam (Fig. 2.11). The output beam was then directed through a quartz Brewster window, co-linear but counter-propagating to the PLP laser (see Fig. 2.2). Perpendicular to the laser beams, a pair of biconvex lenses was used to collect the 308 nm fluorescence from OH, direct it through a 309 nm interference filter, and onto a photomultiplier (PMT, Hamamatsu). The PMT output was passed through a fast pre-amplifier to an oscilloscope (Picoscope 6000) for collection, digitisation, and analysis.
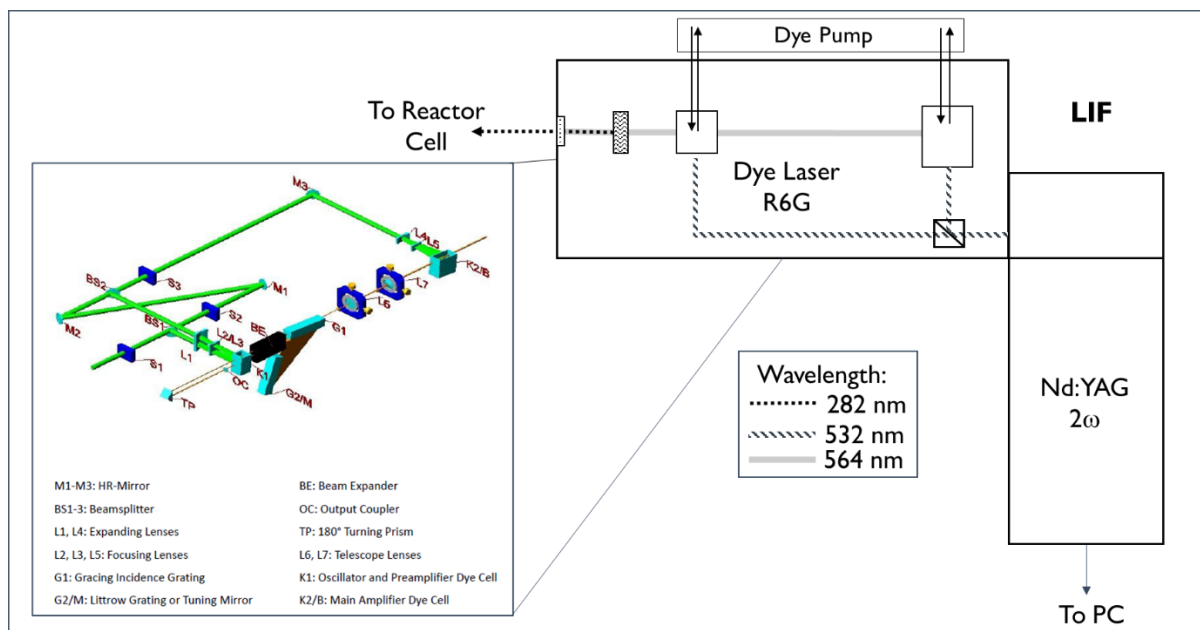
Figure 2. 11: Simplified scheme of the dye laser configuration with enlargement of the light path provided by the manufacturer NarrowScan.

PLP-LIF studies were carried under pseudo-first order conditions of [VOC] >> [OH] such that (following subtraction of measured baseline) OH LIF time profiles, $S(t)$, were described by a monoexponential decay, expression Eq. (2.25):

$$S(t) = S_0 \exp(-Bt) \hspace{4cm} \text{Eq. (2.25)}$$

The parameter S_0 describes (in arbitrary units) the LIF signal at $t = 0$ and is proportional to the initial [OH] produced by the laser pulse in (R2.1) or (R2.2). The parameter B is the pseudo-first-order rate coefficient for OH decay (and includes components from both reactive and transport losses). Figure 2.12 displays a typical OH decay profile recorded in the absence of VOC. This and other similar OH LIF profiles were typically exponential over at least an order of magnitude and were fit with Eq. (2.25) to yield values of B with a high degree of precision (standard errors were generally less than $\pm$ 5%).
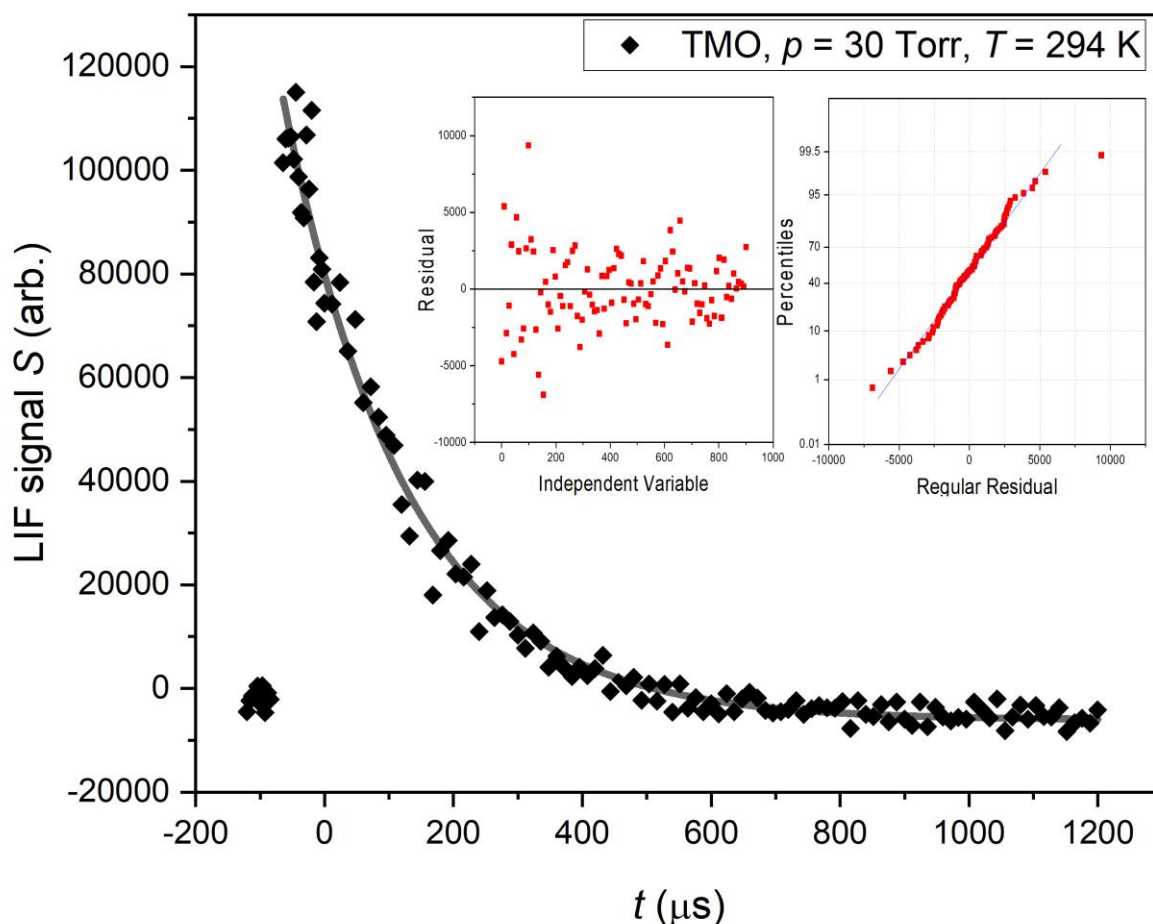
Figure 2. 12: Exemplary OH decay obtained via PLP-LIF from a mixture of H_2O_2 and N_2 fit with Eq. 2.25 to obtain B = (510 ± 18) s^{-1}, together with the residual plots (red squares)

In the absence of any VOC, the main removal process for the OH radical is the reaction with the unreacted precursor, as in the case of R2.3:

$$OH + H_2O_2 \rightarrow H_2O + HO_2 \tag{R2.3}$$

The rate coefficient for this reaction has been measured multiple times and the IUPAC preferred value at room temperature is $k_{2.3}$(298 K) = 1.7 × 10^{-12} cm^3 molecule^{-1} s^{-1} (Atkinson et al., 2004). Pseudo-first order rate coefficient B is directly linked to $k_{2.3}$ according to Eq.2.26:

$$B = k_{2.3}[H_2O_2] + k_{loss} \tag{Eq.2.26}$$

Where k_{loss} represents the rate coefficient for the loss of OH via diffusion or flow out of the photolysis region. Figure 2.12 represents an exemplary decay obtained from a mixture of OH and H_2O_2 for which a constant B of (340 ± 20) s^{-1} was determined. In these conditions, a concentration of OH equal to 2 × 10^{14} molecule cm^{-3} was estimated, confirming the pseudo-first order requirements.

2.1.6. Delay times

A BNC555 delay generator was used to generate pulses from the lasers and coordinate the PLP and the LIF laser delay times. Channel A and Channel B were connected to the Quantel

Q-Smart to control the Flashlamp and the Q-switch respectively. Channels C, D and G were linked to the Continuum laser to regulate the Flashlamp and the Q-switch and the flashlamp recharging (Table 2.3).

Table 2.3: Delay generator channels, corresponding lasers input and delay times

Channel	Laser	Control	Delay (µs) Low Power[a]	Delay (µs) Exp. Power[b]
A	Quantel Q-smart (PLP)	Flashlamp	100	100
B		Q-switch	400 + A	300 + A
C	Continuum (LIF)	Flashlamp	x[c]	x[c]
D		Q-switch	350 + C	350 + C

Notes: [a]**Low power delays were used when necessary for maintenance and alignment operations.** [b]**Experimental power delays were used during normal use of the lasers.**[c] **Delay of channel C varied according to desired time span.**

Figure 2.13 illustrates the content of Table 2.3. Channel A, the photolysis laser flashlamp, was triggered after 100 µs from the start, and the photolysis Q-switch, or channel B, was triggered 300 µs after channel A. Channel D, that is the fluorescence laser Q-switch, was triggered 350 µs after C. Varying the delay time of C allowed to observe different time span and different decay times according to the VOC concentration level.
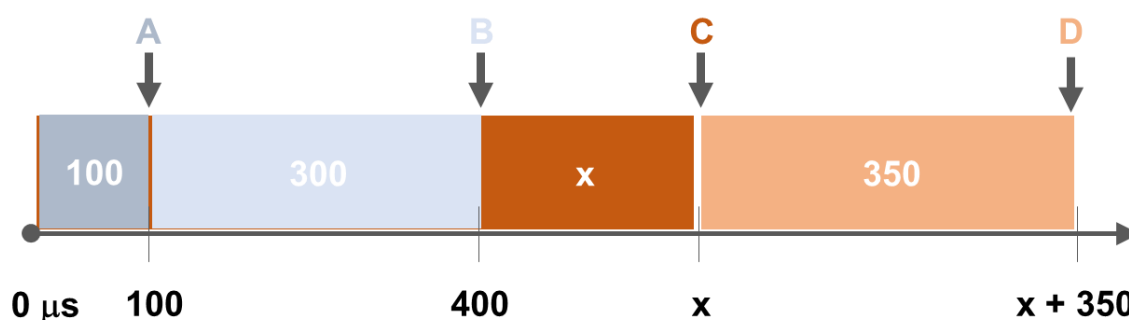
Figure 2. 13: Schematic of the delay times where Channel A is connected to the PLP flashlamp, B is the PLP Q-switch, C is the LIF flashlamp and D the LIF Q-switch.

2.1.7. Data acquisition and analysis

Data acquisition was possible thanks to a LabVIEW program developed by the Dainton Laboratory at the University of Leeds. With the help of Katherine Manfred, some useful improvements were introduced, and the acquisition process was optimised. For instance, the oscilloscope settings, time resolution and capture period were set to be adjustable to improve the signal sampling and minimize the signal to noise ratio. Figure 2.14 reports an example of the Picoscope acquisition settings used during the experiment. The signal amplitude could reach values up to -35000.
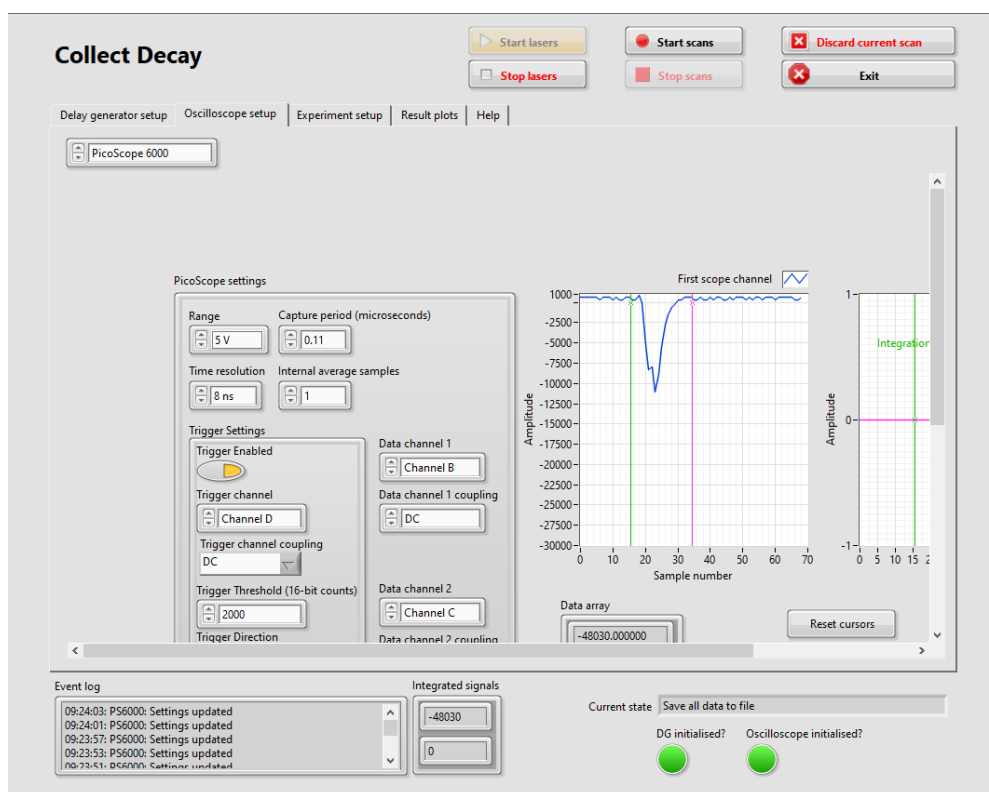
Figure 2. 14. Exemplary acquisition settings for LIF signal observation.

Data were analysed using Origin software. After subtracting the baseline, the datapoints were fitted to the following exponential function:

$$y = y_0 + A\, e^{-R_0 x} \tag{Eq. 2.27}$$

This function can then be resolved as Eq. 2.25, where R_o corresponds to B, and A is S_o.

To make the data processing easier and faster, MChem student Alex Hawtin developed a Python script programmed to fit the data with the exponential Eq. 2.26. Origin was used on random datasets to test the reliability of the script over all the experiments done.

Chemicals: N_2 > 99.9999% was obtained directly from N_2(l) boil-off; O_2 (99.995%, BOC) was used as supplied; H_2O_2 (JT Baker, 60% in H_2O); $(CH_3)_3COOH$ (70%, SigmaAldrich, Luperoxr TBH70X) (mixing ratio ≈ 2% in N_2); TMO (> 97%, synthesised within the Green Chemistry Centre of Excellence, University of York), MPA (98%, Sigma-Aldrich), PCO (97%, Sigma-Aldrich), CPME (Sigma Aldrich, 99.9%), CPO (Sigma Aldrich, 99%), and C_2H_5OH (99%, Sigma-Aldrich), CH_3OH (99.9%, SigmaAldrich) (mixing ratios ≈ 1% for solvents, ≈ 3% for CH_3OH).

2.2. Atmospheric Chamber Experiments

Relative rate experiments were conducted in the 760 dm$_3$ ESC-Q-UAIC environmental simulation chamber of CERNESIM at "Alexandru Ioan Cuza" University of Iasi, Romania (Roman et al., 2022) thanks to the Eurochamp project (Eurochamp). The experiments were carried out during a Trans-Nationa Access (TNA) activity of two weeks that took part in December 2019. During this time, the reactions of TMO and CPME with OH and Cl radical were investigated.

The relative rate technique is an affirmed analysis method for the study of reaction kinetics and counts of numerous methods designed to observe different reaction systems (Atkinson, 1986). The general technique consists in measuring the rate of disappearance of the compound of interest in the presence of a reacting species (usually OH, Cl, NO3...), and at the same time the rate of disappearance of a reference compound with the same reacting agent. Knowing the rate coefficient of the reference reaction, it is possible to determine the rate of the unknown reaction, as explained in detail in section 2.2.2. In the relative rate method, the estimation of the inorganic reactant concentration is not needed, and considering how complicated this measurement can be, this represents one of the main advantages with respect to absolute methods.

2.2.1. Chamber Description

The ESC-Q-UAIC chamber is a sophisticated instrument developed for the study of atmospheric degradation processes. The enclosed reactor is a quartz cylindrical vessel with a volume of 760 L (4.2 m of length and 0.48 m of diameter) and a signal-to-noise ratio (S/N) equal to 8.8 m^{-1} (Fig.2.15). The chamber was equipped with inlet ports, sampling lines, and mixing fans to ensure homogeneity of the gas mixture. The light sources were 2 sets of UV lamps, 32 fluorescent actinic Philips TL-DK 36W lamps which provide light in the range of 310 nm to 430 nm with a maximum at 365 nm and 32 germicidal Philips TUV 30 W/G30 T8 lamps providing light at 254 nm. The monitoring system used was a Fourier Transform Infrared (FTIR) instrumentation (Vertex 80 Bruker) for observation of reference VOC, the VOC of interest, and the oxidation products (Fig. 2.15). The FTIR was interfaced with a multiple "White" path cell to give an overall optical path length of (492 ± 0.2) m. All experiments were conducted at p = (1000 ± 10) mbar (synthetic air) and T = (296 ± 2) K.
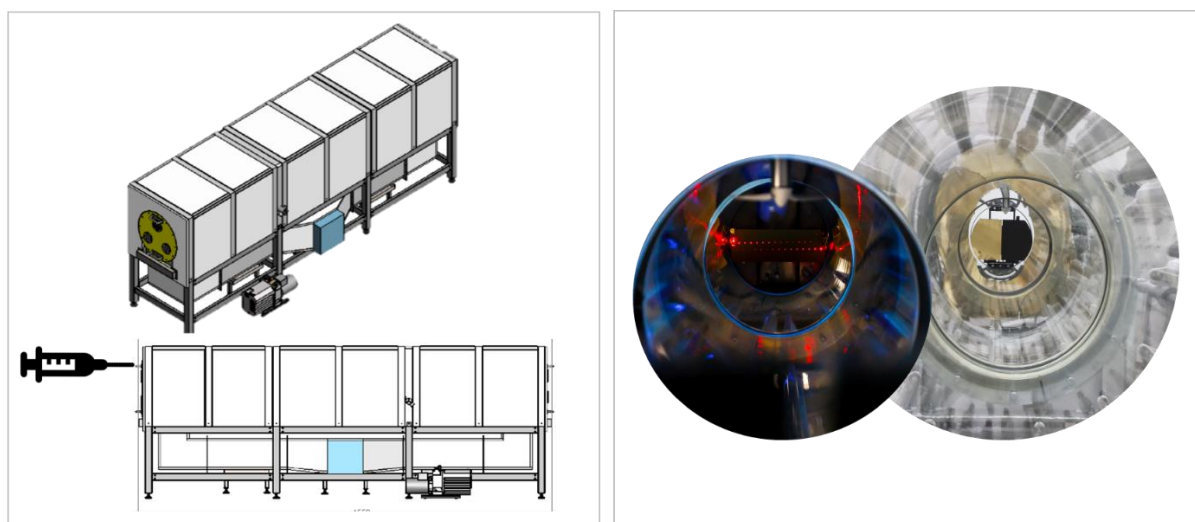
Figure 2. 15: On the left, schematic of the chamber external structure from the top and from the side, with indication of the inlet ports and the pump. On the right, pictures of the internal surface of the chamber showing the UV lamps. Figures were kindly provided by Iustinian Bejan and Claudiu Roman.

2.2.2. Relative Rate Experiments

A typical relative rate experiment consists in the observation of a VOC reacting with an oxidant species (X), together with a reference compound (Ref) reacting with the same species (X). The main chemical and physical phenomena that can take part are the reaction between VOC and X, Ref and X, loss of VOC and Ref via wall deposition and loss of VOC and Ref via photolysis (R 2.4-R2.7).

VOC + OH → Products   (R2.4)

Ref + OH → Products   (R2.5)

VOC → VOC (wall)   (R2.6)

VOC + hν → Photolysis Products   (R2.7)
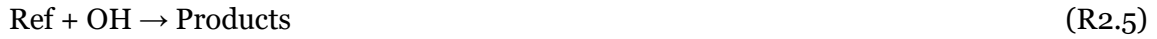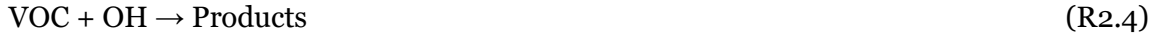
Choice of reference compounds should always fall on organic species for which wall loss and photolysis loss are negligible and thus reactions of Ref equivalent to R2.6 and R2.7 were omitted. According to R2.4-2.7, the rate equation for VOC can be written as follow:

$$\frac{d\,[VOC]}{dt} = -[VOC](k_{2.4}[X] + k_{2.6} + k_{2.7})$$ (Eq.2.28)

In optimal conditions, the VOC under investigation does not incur into significant wall and photolysis losses, and rate coefficients $k_{2.6}$ and $k_{2.7}$ are negligeable. Alternatively, when the VOC absorbs light, wall loss and photolysis rate must be assessed and included into the determination of $k_{2.4}$. In the first situation, the rate equations for VOC and for Ref can be expressed as:

$$\frac{1}{[VOC]}d\,[VOC] = -k_{2.4}[X]\,dt$$ (Eq.2.29)

$$\frac{1}{[Ref]}d\,[Ref] = -k_{2.5}[X]\,dt$$ (Eq.2.30)

Integration of Eq.2.29 and Eq.2.30 gives:

$$\int_{[VOC]_0}^{[VOC]_t} \frac{1}{[VOC]}d\,[VOC] = \int_0^t -k_{2.4}[X]\,dt$$ (Eq.2.31)

$$\int_{[Ref]_0}^{[Ref]_t} \frac{1}{[Ref]}d\,[Ref] = \int_0^t -k_{2.5}[X]\,dt$$ (Eq.2.32)

$$ln\frac{[VOC]_0}{[VOC]_t} = k_{2.4}[X](t - t_0)$$ (Eq.2.33)

$$ln\frac{[Ref]_0}{[Ref]_t} = k_{2.5}[X](t - t_0)$$ (Eq.2.34)

Equating Eq.2.33 and Eq.2.34, the following expression can be obtained:

$$ln\frac{[VOC]_0}{[VOC]_t} = \frac{k_{2.4}}{k_{2.5}} ln\frac{[Ref]_0}{[Ref]_t}$$ (Eq.2.35)

Using a monitoring method proportional to $[VOC]$ and to $[Ref]$, Eq.2.35 can be used to determine $k_{2.4}$. In this work, the monitoring method used in the ESC-Q-UAIC is an FTIR instrumentation interfaced to the chamber. The properties observed during the experiments were the 'extinction factors' (*f*) at time 0 and time *t* (Eq.2.36, Eq.3.37):

$$f_0{}^{VOC} = \frac{A_0^{VOC}}{A_{ref}^{VOC}}$$ (Eq.2.36)

$$f_t^{VOC} = \frac{A_t^{VOC}}{A_{ref}^{VOC}}$$
(Eq.2.37)

Where f_0VOC is equal to the ratio between A_0^{VOC}, the absorbance of a selected peak at time t_0 (injection of VOC in the chamber), and A_{ref}^{VOC}, the absorbance of the peak from a reference spectrum of the same molecule recorded in the chamber in similar conditions. Similarly, f_t can be estimated recording the absorbance of the selected peak at time t (A_0^{VOC}). As the Beer-Lambert law relates the proportionality between absorbance of a chemical species and its concentration, factors f_0 and f_t can be directly linked to VOC concentration as shown in Eq.2.38:

$$ln\frac{f_0^{VOC}}{f_t^{VOC}} = ln\frac{A_0^{VOC}}{A_t^{VOC}} = ln\frac{[VOC]_0}{[VOC]_t}$$
(Eq.2.38)

The same equation is true for the reference compound selected. Recording FTIR spectra every 2 minute and plotting $ln\frac{f_0^{VOC}}{f_t^{VOC}}$ against $ln\frac{f_0^{REF}}{f_t^{REF}}$, a linear plot with a slope equal to $\frac{k_{2.4}}{k_{2.5}}$ will be obtained (see section 3.2.3 and Fig.3.9). Knowing the value of $k_{2.5}$, also $k_{2.4}$ can be finally determined.

In preliminary experiments, wall deposition and photolysis rates (365 nm and 254 nm) were measured to ensure the validity of the experiment and to correct raw kinetic data when necessary. Spectral lines were tested for proportionality to the concentration of VOCs and for available subtraction spectral features of solvents and reference compounds. Two distinct OH generation methods were used. CH_3ONO was injected into the chamber for photolysis at 365 nm (R2.8) to obtain a concentration of around 5 ppmv. The presence of an excess of NO ensured rapid conversion (R2.9 – R2.10) to OH.

$CH_3ONO + h\nu \rightarrow CH_3O + NO$
(R2.8)

$CH_3O + O_2 \rightarrow HCHO + HO_2$
(R2.9)

$HO_2 + NO \rightarrow OH + NO_2$
(R2.10)

Alternatively, OH was generated directly via 254 nm photolysis of H_2O_2 (R2.1), usually with a concentration of around 6 ppmv. Atomic chlorine was generated by the photolysis of Cl_2 at 365 nm (R1.13). All the VOCs, and their oxidation products were monitored by FTIR. Spectra were recorded every 2 minutes by combining 120 scans for a spectrum, with approximately 15 such spectra at a resolution of 1 cm^{-1} completing each experiment. Conversion of VOCs through the reaction with OH and Cl radicals were usually achieved at least to 50%.

Choice of reference compound for kinetic experiments was informed by three factors.

- o Experimental and existing library data were used to ensure that reference compound FTIR spectra contained strong features that did not overlap with those of the VOC of interest.
- o Reference compound rate coefficient k(296 K) data needed to be well-characterised and available in the literature;
- o Rate coefficient values were preferably of a similar magnitude to measured (PLP-LIF) or predicted k values of the reactions under investigation.

In the event that the selected reference did not have IUPAC recommended data, the following steps were considered:

1. Choice of a compound with well-established k attested by different research groups using complementary techniques, i.e. absolute determinations and relative rate in agreement.
2. Choice of a compound with a few absolute studies that do agree, as any uncertainties here most likely to be random than for RR;
3. When only relative studies were available, the selected rate coefficient needed to be a very clearly documented trail leading back to an absolute determination.

According to these principles the selected reference compounds for the reaction with OH and Cl were dimethylether (CH_3OCH_3), cyclohexane (c-C_6H_{12}), and propene (C_3H_6), as listed in Table 2.4.

Table 2.4: Literature kinetic data for reference reactions used in this work.

Reaction Number	Reference Reaction	k^a	Uncertainty	Method	References
R2.11	CH_3OCH_3 + OH	2.86	± 5%	RR(GC)	(Demore and Bayes, 1999)
R2.12	c-C_6H_{12} + OH	6.97	± 15%	Review	(Atkinson, 1986)
R2.13	C_3H_6 + OH	29	± 20%	Review	(Atkinson, 1986)
R2.14	CH_3OCH_3 + Cl	173	± 15%	RR (GC)	(Giri and Roscoe, 2010)
R2.15	c-C_6H_{12} + Cl	383	± 5%	RR (GC-MS)	(Anderson et al., 2007)
R2.16	C_3H_6 + Cl	223	± 25%	RR (FTIR)	(Ceacero-Vega et al., 2009)

Notes: [a] Rate coefficient units are in 10^{12} cm^3 molecule^{-1} s^{-1}.

The uncertainty over the relative rate could be affect by a number of factors, but the one that we could estimate was the uncertainty related to the reference rate coefficient k_{ref}, according to equation 2.39:

$$\Delta(k) = k \times \sqrt{\left(\frac{\Delta k_{ref}}{k_{ref}}\right)^2} \qquad \text{(Eq. 2.39)}$$

Chemicals: Liquid samples of the following were supplied to the reactor by direct injection through a septum: H2O2 (60% in H2O); TMO (> 97%, synthesised within the Green Chemistry Centre of Excellence, University of York); CPME (Sigma Aldrich, 99.9%); CH3ONO was prepared in CERNESIM laboratory using an adapted method from Taylor et al. (1980); CH3OCH3 >99.9% (suitable for GC analysis, Sigma-Aldrich), c-C6H12 99.5% (anhydrous, Sigma-Aldrich), and C3H6 >99.9% (Sigma-Aldrich) were used as supplied.

2.3. UV-Visible Spectrometry

UV-Visible spectrometry can be a useful method for the study of the interaction of molecules with sunlight. The UV-vis. spectra give important information to the atmosphere scientists:

○ If the molecule absorbs in the solar actinic range (280 – 420 nm), there's a chance that a photolytic event may occur in the troposphere; on the other hand, the absence of absorption in the near-UV-visible area suggests that photolysis does not occur.

○ The intensity of the absorption is also crucial in the study of the interaction of molecules with light. The determination of the absorption cross section gives an index of the ability of the molecule to absorb photon and quantify the intensity of the absorption.

UV-vis. studies were carried out using a double beam Shimadzu UV-2600 spectrometer over the wavelength range 250-400 nm at $T = (298 \pm 1)$ K and with a resolution of 1 nm. The spectra were recorded in Hellma Analytics quartz cuvettes with a path length of 10 mm or 2 mm. As no suitable apparatus was available at University of York for gas-phase $\sigma_4(\lambda)$ determinations, all spectra recorded were solution phase, diluted in cyclohexane (c-C_6H_{12}). This choice was based on the work of Nakashima et al. (1982a), who studied the solvent effect on the absorption spectra of ketones. Spectra in perfluorohexane (C_6F_{14}) were reported as *quasi*-vapour spectra. Use of C_6F_{14} was avoided for environmental reasons (Tsai, 2009); hence the similarly non-polar and weakly polarisable cyclohexane was chosen to imitate C_6F_{14}. Solutions (0.03 M – 0.3 M) were prepared using volumetric flasks and micropipettes, with the concentration uncertainty estimated at around 10%. Once the spectra were recorded, the absorption cross section, σ (cm^2 molecule^{-1}), was estimated using Eq.2.40:

$$\sigma(\lambda) = \frac{A(\lambda)}{l \times c \times N} \times 1000 \times 2.3 \qquad \text{(Eq.2.40)}$$

where A is the absorbance at wavelength λ, l is the cell path length in cm, c is the molar concentration (mol dm^{-3}), N is the Avogadro number (6.022×10^{23}), 1000 is a conversion factor and 2.3 accounts for the conversion from base 10 (from spectrometer) to base e.

3. Atmospheric Chemistry of TMO and the Oxolanes

TMO (2,2,5,5-tetramethyloxolane or 2,2,5,5-tetramethyltetrehydrofuran) was designed at the Green Chemistry Centre of Excellence of the University of York as a new green solvent. Its selection comes from the need to replace toluene and other problematic solvents with a new non-polar volatile solvent with low toxicity, a straightforward synthesis from renewable sources and a high safety level. Other ethers, such as CPME (see Chapter 5), were previously selected with the same purpose because of their chemical and physical properties, but their use has prompted concern because of the high peroxide formation (Byrne et al., 2017) that makes them unsafe, especially on the large scale. This issue was then addressed with the use of an inhibitor to slow down the peroxide formation (Azzena et al., 2019), but the search for other ether solvents with a lower risk of auto-decomposition and that can broaden the spectrum of sustainable solvents continued and led to the selection of TMO. The chemical structure of this compound, thanks to presence of methyl groups, and the absence of protons on the alpha-carbon to the ethereal oxygen, provides to it resistance to any oxidation (autoxidation, OH, O_2, etc.), making it a much safer molecule. The presence of the methyl groups is thus an important shaping feature, and it affects other properties of the molecule such as basicity and solvation properties.

For what concerns the atmospheric chemistry, ethers show a behaviour that is very similar to the alkanes, the main oxidation process being the reaction with OH that takes place through H-abstraction from the weaker C-H bonds. However, ethers are usually much more reactive than alkanes, thanks to the effect of the ether oxygen on adjacent C-H bonds. The electron-withdrawing effect of O weaken the C-H bonds and together with the hydrogen bond interactions with OH, activate them towards H atom abstraction. The subsequent steps of the atmospheric decomposition are also similar to those of the alkanes, with formation of peroxyl radicals and subsequently alkoxy radicals, and proceed via a complex series of radical reactions, that ultimately lead to the end products CO_2 and H_2O (Calvert et al., 2011b).

In this work, the atmospheric chemistry of TMO was studied by direct laser-based methods at the University of York and relative rate experiments at the University of Iaşi. The work was subsequently published in Atmospheric Chemistry and Physics journal (ACP) (Mapelli et al., 2022) and described here in detail. The investigation was then expanded to other oxolanes with a different number of methyl groups in the alpha position (from 4 methyl groups of TMO to 0 methyl groups of THF). Figure 3.1 shows all the oxolanes of interest with their chemical structure and electrostatic potential (ESP) surface calculated with Gauss View 9 (Hartree-Fock 3-21G method, the surface calculations were carried out on total density, Self-consistent field SCF matrix). Tetrahydrofuran (THF or oxolane), 2-methyloxolane (2-MO or 2-methyltetrahydrofuran) and 2,5-dimethyloxolane (2,5-DMO or 2,5-dimethyltetrahydrofuran, mixture of stereoisomers) were commercially available, whereas 2,2,5,5-tetramethyloxolane (TMO or 2,2,5,5-tetramethyltetrahydrofuran) was provided by the Green Centre of Excellence at the University of York and 2,2,5-trimethyloxolane (2,2,5-TMO or 2,2,5-trimethyltetrahydrofuran) and 2,2-dimethyloxolane (2,2-DMO or 2,2-dimethyloxolane) were synthesized specifically in this work. For each oxolane, Fig. 3.1 reports the ESP surface viewed from 2 different perspectives. The surface area in red, overlooking the oxygen atom, appears distinctly shrunk in TMO if compared to the simple oxolane (THF), and it gradually expands as methyl groups are removed from the molecule. This gives an idea of how the ethereal oxygen is affected by the alpha methyl groups and interaction with oxygen from external molecules may be altered or compromised. Accordingly, the investigation of the atmospheric chemistry of oxolanes may be important for the following reasons:

- *TMO chemistry*: new insights on the chemistry of TMO and the other oxolanes and a deeper understanding of how the methyl groups affect the reactivity with oxidants species such as OH.
- *OVOC reactivity*: studying new oxygenate molecules gives important insights about OVOC reactivity which is generally more complex than other classes of VOC compounds such as the alkanes.
- *SAR development*: a fundamental tool for the formulation of SAR (see section 1.5) is the knowledge of VOC reactivity and introducing molecules with peculiar chemical features to the background of SAR development is crucial in order to improve the rate coefficients prediction of complex compounds. Estimating SAR for TMO and comparing it to the experimental results can be helpful in this sense.
- *Design for green atmospheric chemistry*: more information on how to design molecules to obtain solvents that have a low impact on air quality.

With this purpose, the reactivity of TMO with OH (R3.1) was investigated via PLP-LIF and RR experiments, and the reactivity of TMO with Cl (R3.2) was studied via RR experiments.

$$TMO + OH \rightarrow products \tag{R3.1}$$

$$TMO + Cl \rightarrow products \tag{R3.2}$$

Then the reactivity of 2,2,5-TMO, 2,5-DMO, 2,2-DMO ad 2-MO with OH was also studied via PLP-LIF.

$$2,2,5\text{-TMO} + OH \rightarrow products \tag{R3.3}$$

$$2,5\text{-DMO} + OH \rightarrow products \tag{R3.4}$$

$$2,2\text{-DMO} + OH \rightarrow products \tag{R3.5}$$

$$2\text{-MO} + OH \rightarrow products \tag{R3.6}$$

$$THF + OH \rightarrow products \tag{R3.7}$$
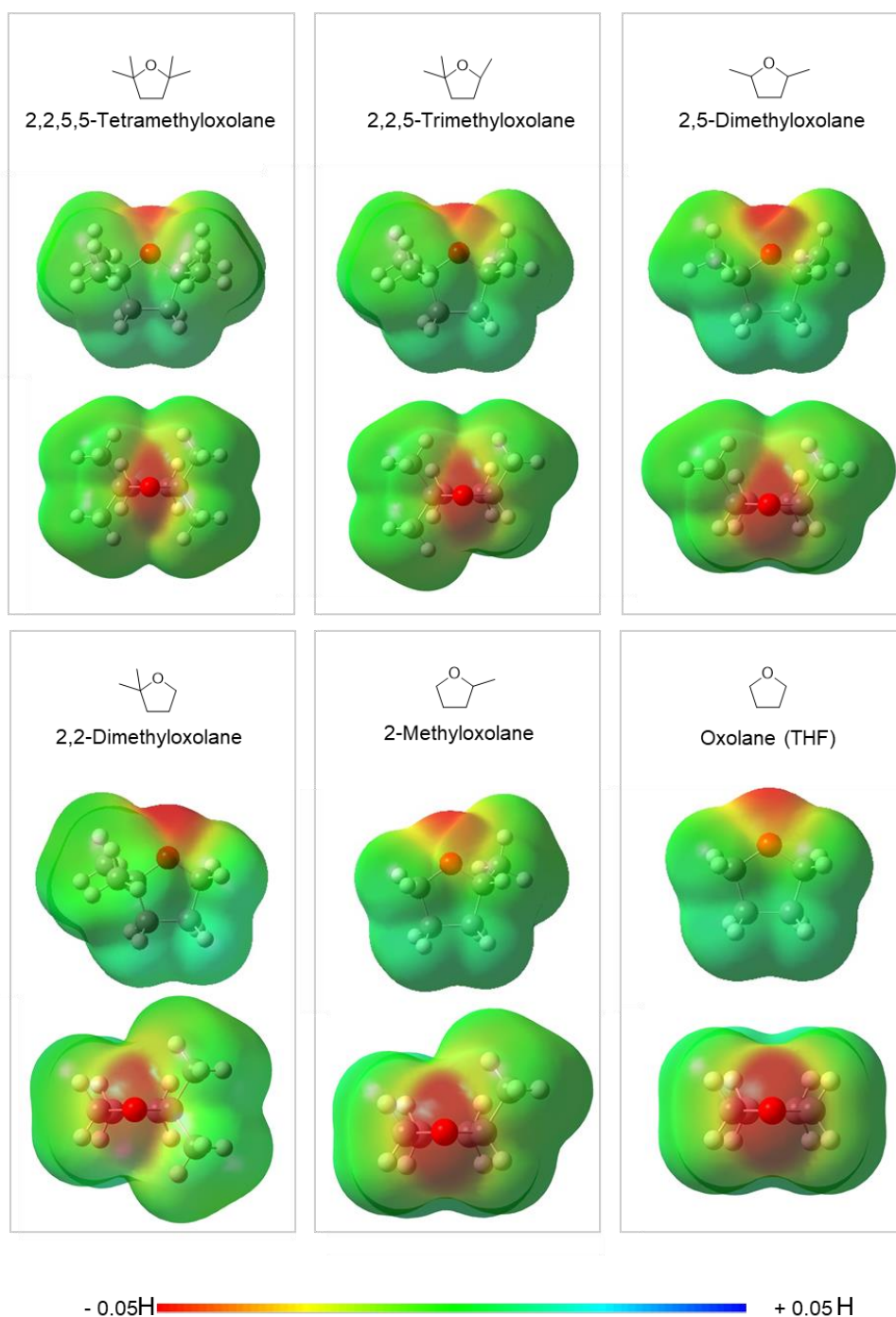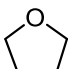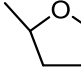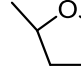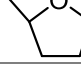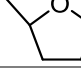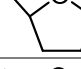
Figure 3. 1: Electrostatic potential (ESP) surfaces expressed in Hartrees for the oxolanes of interest for this study, surface calculated with Gauss View 9 (Hartree-Fock 3-21G method, total density, Self-consistent field SCF matrix).

3.1. Previous Studies and SAR Calculations

To the best of our knowledge, rate coefficients for the reaction of TMO with OH and Cl were unknown, and this is the first study to report them. The same is true for 2,2,5-TMO and 2,2-DMO. The other oxolanes in Figure 3.1 (2,5-DMO and 2-MO) have at least one reported measurement for the reaction with OH or OD, and THF (tetrahydrofuran or oxolane) has an extensive record of experiments available (Ravishankara and Davis, 1978; Wallington et al.,

1988; Moriarty et al., 2003) (Atkinson, 1986), being a very common molecule widely used in chemical processes. In the lack of recommended values from IUPAC, all the rate coefficients reported in NIST Kinetics Database (Manion et al.) for THF + OH and THF + Cl were included in Table 3.1. Table 3.1 summarises the data available in literature for the reaction of oxolanes with OH, OD and Cl.

Table 3.1: Rate coefficients available in literature for the reaction of THF, 2-MO and 2,5-TMO with OH, OD and Cl.

Molecule	Reaction	Method [b]	k (298 K) [a]	Reference
THF	+ OH	RR PLP-LIF	18.0 ± 0.7 16.7 ± 0.7	(Moriarty et al., 2003)
		FP-RF	17.8 ± 1.6	(Wallington et al., 1988)
		FP-RF	16.3 ± 1.6	(Ravishankara and Davis, 1978)
	+ OD	RR	18.1 ± 2.7	(Andersen et al., 2016)
	+ Cl	RR	250 ± 39	(Alwe et al., 2013)
		RR	271 ± 34	(Giri and Roscoe, 2010)
2-MO	+ OH	PLP-LIF RR	22.7 ± 1.7 25.3 ± 3.1	(Wallington et al., 1990)
	+ OD	RR	24.1 ± 5.1	(Andersen et al., 2016)
	+ Cl	RR	265 ± 43	(Andersen et al., 2016)
2,5-DMO	+ OH	-	-	-
	+ OD	RR	45.6 ± 6.8	(Andersen et al., 2016)
	+ Cl	RR	284 ± 34	(Andersen et al., 2016)

Notes: [a] Rate coefficient units are in 10^{-12} cm^3 molecule^{-1} s^{-1}. [b] **RR stands for relative rate, FP-RF for flash photolysis-resonance fluorescence, PLP-LIF for pulsed laser photolysis-laser induced fluorescence.**

To predict the rate coefficients of the oxolanes for the reaction with OH and to compare calculations with experimental data, SAR calculations by Jenkin et al. (2018) were used, and the following equation was formulated for the ethereal molecules:

$$k = n_{CH_3}\ k_{CH_3} + n_{CH_2}\ k_{CH_2} + n_{CH}\ k_{CH} \qquad \text{Eq. (3.1)}$$
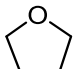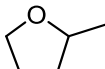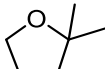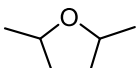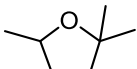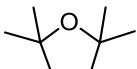
$$k_{CH_3} = k_{prim}\ F_X \qquad \text{Eq. (3.2)}$$

$$k_{CH_2} = k_{sec}\ F_X\ F_Y\ F_{ring} \qquad \text{Eq. (3.3)}$$

$$k_{CH} = k_{tert}\ F_X\ F_Y\ F_Z\ F_{ring} \qquad \text{Eq. (3.4)}$$

where n_{CH_3}, n_{CH_2} and n_{CH} are respectively the number of primary, secondary and tertiary CH groups; k_{CH_3}, k_{CH_2}, k_{CH} are the partial coefficients for the H-abstraction from CH_3, CH_2 and CH groups; k_{prim}, k_{sec} and k_{tert} are the group rate coefficients for the H-abstraction from CH_3, CH_2 and CH groups; F_X, F_Y and F_Z are substituent factors that takes into account the effect of the neighbour groups X, Y and Z; and finally F_{ring} is the ring factor, that accounts for the effect of the ring shape of the molecule on its reactivity. Results for the SAR predictions are summarised in Table 3.2. The substituent factor $F_X = 3.50$ accounts for the presence of ethereal oxygenated groups (CH_2OR, $-CH(OR)-$, $-C(OR)<$), whereas the $F_Y = 1.35$ accounts for the presence of neighbour alkyl groups ($-CH_2-$, $-CH<$, $>C<$). The partial coefficient for C-H bonds adjacent to the ethereal O is estimated to be equal to 5.6×10^{-12} cm^3 $molecule^{-1}$ s^{-1} regardless of the neighbour substituent R.

Table 3.2: SAR calculations based on Jenkin et al. (2018).

Molecule	Group	k_x [a]	F_X [d]	F_Y [d]	F_Z [d]	F_{RING} [e]	k_{CH_x} [a]	n [b]	%k [c]	k [a]
THF	α-CH$_2$	-	-	-	-	1	5.6	2	61	18.5
	β-CH$_2$	0.769	3.50	1.35	-	1	3.63	2	39	
2-MO	α-CH	-	-	-	-	1	5.6	1	30	18.9
	α-CH$_2$	-	-	-	-	1	5.6	1	30	
	β-CH$_2$	0.769	3.50	1.35	-	1	3.63	2	38	
	CH$_3$	0.13	3.50	-	-	-	0.91	1	2	
2,2-DMO	α-CH$_2$	-	-	-	-	1	5.6	1	53	13.8
	β-CH$_2$	0.769	3.50	1.35	-	1	3.63	2	41	
	CH$_3$	0.13	3.50	-	-	-	0.91	2	7	
2,5-DMO	α-CH	-	-	-	-	1	5.6	2	58	19.4
	β-CH$_2$	0.769	3.50	1.35	-	1	3.63	2	38	
	CH$_3$	0.13	3.50	-	-	-	0.91	2	5	
2,2,5-TMO	α-CH	-	-	-	-	1	5.6	1	39	14.2
	β-CH$_2$	0.769	3.50	1.35	-	1	3.63	2	52	
	CH$_3$	0.13	3.50	-	-	-	0.91	3	10	
2,2,5,5-TMO	β-CH$_2$	0.769	3.50	1.35	-	1	3.63	2	80	9.1
	CH$_3$	0.13	3.50	-	-	-	0.91	4	20	

Notes: [a] Units are in 10^{-12} cm^3 $molecule^{-1}$ s^{-1}. [b] n = number of equivalent groups. [c] Percentage distribution for the partial rate coefficients. [d] Fx, Fy, and Fz are the substituent factors for the neighbour groups x, y and z respectively. [e] F_{RING} is the ring factor that accounts for the ring strain.

According to SAR (Table 3.2), 2,5-DMO is the most reactive molecule with a rate coefficient of $k_{OH, SAR}$ (298 K) = 19.4 × 10^{-12} cm^3 molecule^{-1} s^{-1}, and interestingly this value is well distant from the literature value available for the reaction with OD, that is $k_{OD, EXP}$ (298 K) = 45.6 × 10^{-12} cm^3 molecule^{-1} s^{-1} and should be consistent with the rate coefficient for reaction with OH. To a lesser degree, SAR overestimate also the rate constant for 2-MO as well with a predicted SAR of $k_{OH, SAR}$ (298 K) = 18.9 × 10^{-12} cm^3 molecule^{-1} s^{-1} compared to the experimental value of $k_{OH, EXP}$ = 25.2 × 10^{-12} cm^3 molecule^{-1} s^{-1}.

SAR calculations also provide a useful prediction of the branching ratio of these reactions. As reported in Table 3.2 (see *%k*) the C-H bonds with the highest branching ratio are the secondary and tertiary C-H and their reactivity is thus responsible for large part of the rate coefficient values. This is not surprising considering that the BDE of CH bonds depends on the C degree of substitution (tertiary CH<secondary CH<primary CH). Taking the example of TMO, the partial coefficient assigned to the secondary CH represents 80% of the total rate constant, leaving 20% to the primary CH. SAR calculations and experimental studies found in literature were also summarised in the bar chart reported in Figure 3.2. The missing information and the discrepancies between SAR calculations and the scarce experimental data available made further experimental studies necessary for a better understanding of the chemistry of THF and other oxolanes, for the improvement of SAR calculation theory and ultimately for the assessment of oxolane impact on air quality.
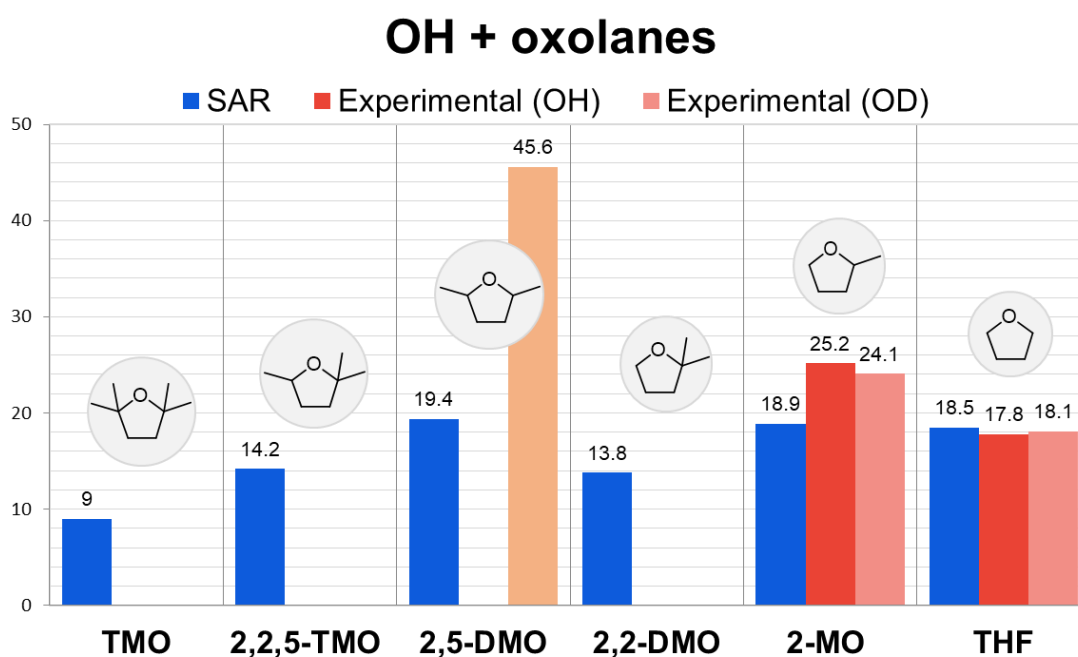
Figure 3. 2: Bar chart showing the rate coefficients for the reactions of the oxolanes with OH calculated via SAR (Jenkin et al., 2018) in blue; in red the rate coefficients from experimental results available in literature for the reaction with OH; and in units of 10^{-12} cm^3 molecule^{-1} s^{-1}.

3.2. Rate Coefficients of OH with 2,2,5,5-Tetramethyloxolane (TMO) (R3.1)

The rate coefficient for the reaction of 2,2,5,5-tetramethyloxolane (TMO) with OH (R3.1, see Figure 3.1) at room temperature was investigated via PLP-LIF at the University of York and via RR studies with the environmental simulation chamber ESC-Q-UAIC of the "Alexandru Ioan Cuza" University of Iasi, in Romania. The study was then expanded to a wider range of temperatures and the rate constants between 296 K and 502 K were determined by PLP-LIF. The main reaction pathways that are expected to occur were illustrated in the reaction scheme shown in Figure 3.3.
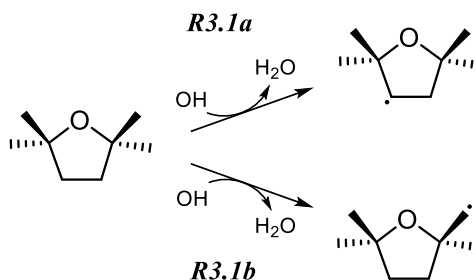
Figure 3. 3: The chemical structure of TMO and the two possible H-abstraction routes indicated as (R3.1a) for the reaction on the secondary C-H and (R3.1b) for the reaction on the primary C-H.

3.2.1. PLP-LIF Results: Room Temperature Studies of TMO + OH (R3.1)

Experiments were conducted with the PLP-LIF apparatus described in section 1.6.1, in conditions of pseudo-first order, where the VOC concentration, in this case TMO, was much higher than OH concentration: [TMO] >> [OH]. More precisely, TMO concentrations were estimated to lie within the range of $(1\text{-}28) \times 10^{14}$ molecule cm^{-3}, whereas the OH concentration were estimated to be 10^{11} molecule cm^{-3}, with a minimum ratio [TMO]/[OH] of 10. In these conditions, monoexponential decays of OH were observed, as the OH LIF time profiles were described by equation 2.25, where S_o (arbitrary units) refers to the LIF signal at time 0 and is proportional to the initial [OH] generated by the photolysis of H_2O_2 or $(CH_3)_3COOH$; and B (in s^{-1}), is the pseudo-first order rate constant, often referred as k' or k_{obs} and it accounts for both reactive and transport losses.

Normally, a typical experiment would require a minimum of ten exponential decays, one for each concentration of TMO. Figure 3.4 shows three examples for clarity. The OH LIF decays in the figure were recorded in the presence of 3 different excess concentrations of TMO, in the same conditions of temperature over the range of 296-298 K (variation due to the change of temperature in the laboratory room), same pressure of 30 Torr (40 mbar) and the same concentration of OH precursor, $[(CH_3)_3COOH] = 1 \times 10^{14}$ molecule cm^{-3}. The decays were typically exponential over at least an order of magnitude and after subtraction of the baseline, they were fit to Eq. (2.25), from which the values of B were usually determined with a high degree of precision and a standard error of about 5%.
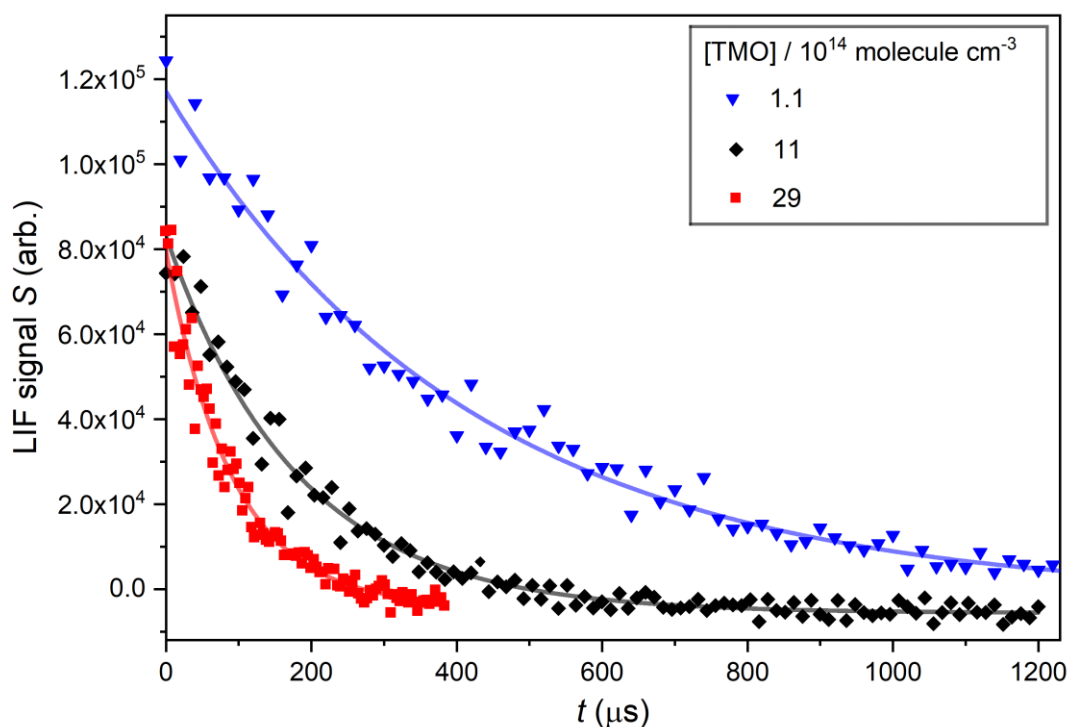
Figure 3. 4: OH decays obtained in PLP-LIF experiments using three different [TMO], each fit with Eq. (2.25) to determine pseudo-first order rate coefficients: $B = (2390 \pm 69)$ s⁻¹ at [TMO] = 1.1 × 10^{14} **molecule cm⁻³;** $B = (5530 \pm 172)$ **s⁻¹ at [TMO] = 11 × 10^{14} molecule cm⁻³; and** $B = (11200 \pm 464)$ **s⁻¹ at [TMO] = 29 ×10^{14} molecule cm⁻³.**

Several preliminary studies were conducted to address the following points:

- **Secondary radical chemistry:** operating at a low concentration of OH radicals guarantee that loss of OH via reaction with itself, with its precursor, or alternatively with the products of the reaction with TMO was unimportant.
- **Reactivity in air:** "back-to-back" experiments were performed in a previous study by BSc student Juliette V. Schleicher, alternating the bath gas between N_2 and air and no systematic changes in parameter B were observed. On the contrary, the pseudo-first order rate constants were consistent, with $B_{air}/B_{N2} = 1.01 \pm 0.05$.
- **Pressure dependence:** the experiments were conducted at different condition of pressure, from 20 Torr to 200 Torr, and the coefficient rate showed no pressure dependence. The optimal conditions for determination of B however were over the range 30-70 Torr.
- **Photolysis:** Cyclic ethers do not absorb light at wavelength longer than 200 nm (Christianson et al., 2021), meaning that photodecomposition is absent under our experimental conditions.

Many determinations of TMO + OH were conducted back-to-back with well-characterised (R1.1) (OH + CH_3OH), a reaction with extensive literature available over a wide range of temperatures (Wallington and Kurylo, 1987b; Hess and Tully, 1989; Jiménez et al., 2003; Dillon et al., 2005). The reaction was also chosen as reference because its rate coefficient at room temperature was on the same order of magnitude as the one predicted for TMO by SAR calculations. All the preliminary studies listed above were also valid for CH_3OH.

Parameter B was determined at different concentrations of TMO and CH_3OH. For each set of experiments, the concentration in the cell was regulated changing the flow from the bulb mixture of TMO and N_2 (or CH_3OH and N_2) with a mass flow controller (MFC) and balancing the overall pressure adjusting the N_2 flow accordingly. Figure 3.5 shows an example of a linear plot of B (s^{-1}) against the concentration of TMO, [TMO], at room temperature (296 K). The linear fit then leads to the determination of the second order rate constant k according to the following equation:

$B = k[VOC] + k_{loss}$ Eq. (3.5)

Where k is the second order reaction coefficient, [VOC] is the concentration of the VOC of interest, in this case TMO, and the term k_{loss} represents the rate by which OH is lost in the reactor chamber by other losses processes that include reaction with H_2O_2, diffusion and flow out of the reaction zone. Reaction with the photolysis precursor H_2O_2 is the most important of these alternatives (R2.3). The data display good linearity, with intercept values (around a few hundred s^{-1}) in line with the predicted rate for (R2.3) that is $k_{2.3}$(298 K) = 1.7×10^{-12} cm^3 molecule^{-1} s^{-1} (Atkinson et al., 2004), with an estimated $[H_2O_2]$ = 10^{14} molecule cm^{-3}. From this $[H_2O_2]$ value and our photolysis laser fluence, we estimate [OH] = 5×10^{11} molecule cm^{-3}, a concentration that guarantees pseudo-first order conditions.
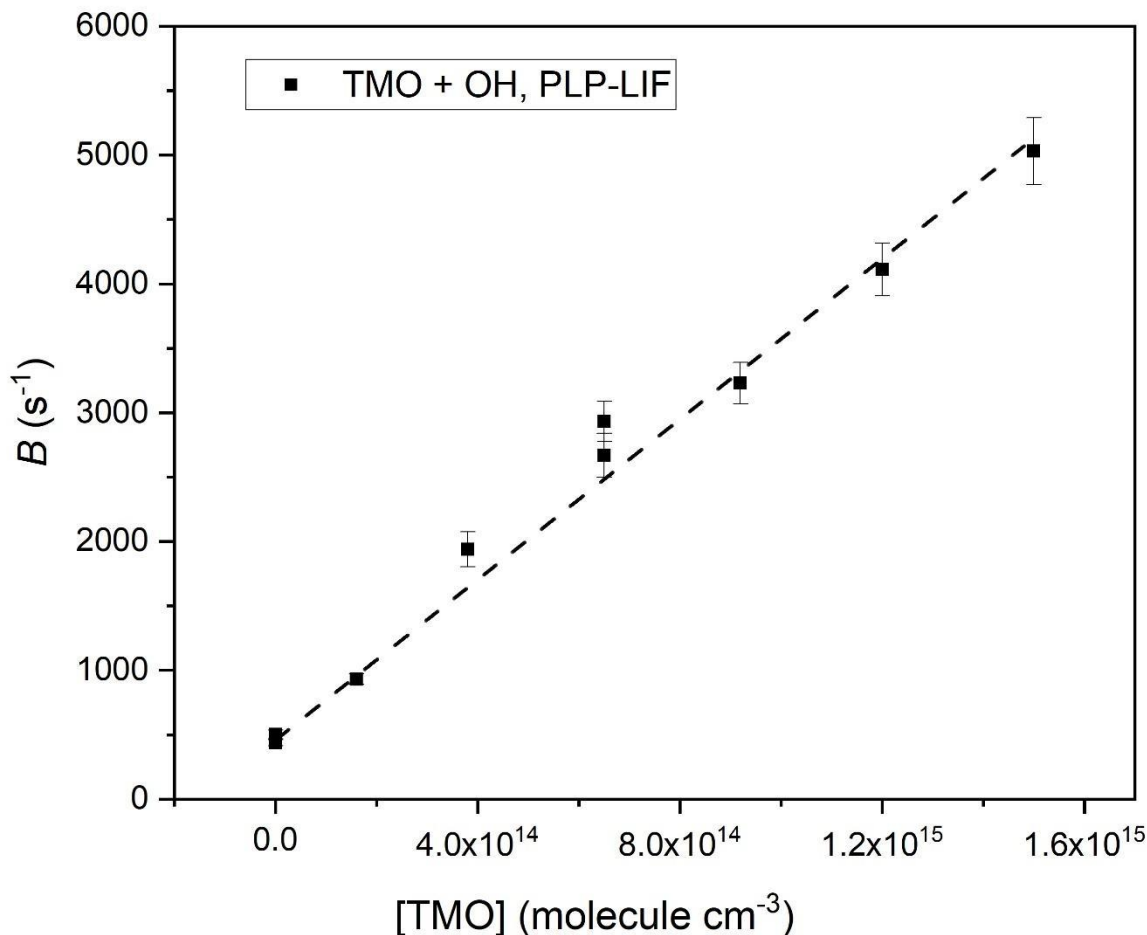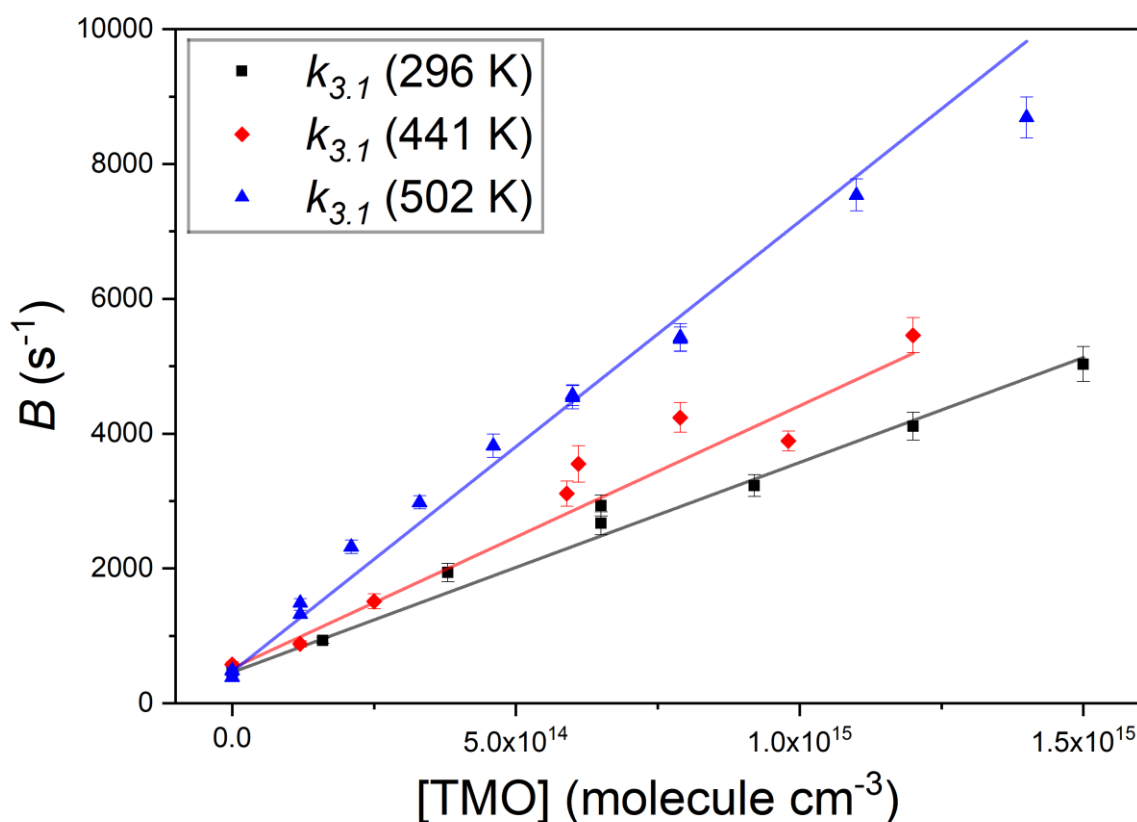

Figure 3. 5: Typical bimolecular plot of B vs [TMO] used to obtain $k_{3.1}$(T) for OH+TMO, fit with Eq.(3.6) to obtain $k_{3.1}$(296 K) = (3.1 ± 0.1) × 10^{-12} cm^3 molecule^{-1} s^{-1}.

A mean of four values obtained at around room temperature yielded $k_{3.1}(296\ \text{K}) = (3.07 \pm 0.04) \times 10^{-12}$ cm^3 molecule^{-1} s^{-1}, independent of the bath gas pressure or identity (N$_2$ or air). To the best of our knowledge these are the first kinetic data for the reaction of TMO with OH and all experimental conditions and results at room temperature were listed in Table 3.3. Every effort was made to calibrate MFC and pressure gauges, and to conduct experiments using a variety of conditions of pressure, flow rate, and different TMO supply bulbs. Some of the experiments to determine $k_{3.1}(296\ \text{K})$ were conducted "back-to-back" with the well-characterised reaction between OH and CH$_3$OH (R1.1) and these are also listed in Table 3.3.

Table 3.3: Rate coefficients for R3.1 (TMO + OH) and R1.1 (CH$_3$OH + OH) determined via PLP-LIF at RT.

Reaction	T / K	p / Torr	OH precursor	n [a]	[TMO] [b]	$k(T) \pm$ SE [c]
(R3.1)	298	30	(CH$_3$)$_3$COOH	9	1-28	2.9 ± 0.2
(R3.1)	297	60	(CH$_3$)$_3$COOH	11	1-28	3.3 ± 0.6
(R3.1)	296	60	H$_2$O$_2$	9	1-37	3.1 ± 0.1
(R3.1)	297	59	H$_2$O$_2$	16	2-15	3.2 ± 0.2
(R1.1)	299	30*	(CH$_3$)$_3$COOH	10	3.5 - 97.1	0.84 ± 0.03
(R1.1)	299	30	(CH$_3$)$_3$COOH	11	3.5 - 97.1	0.87 ± 0.07

Notes: [a] n is the number of different [TMO] used (not including [TMO] = 0); [b] = range of [TMO] in units of 10^{14} molecule cm^{-3} ; [c] = $k(T)$ in units of 10^{-12} cm^3 molecule^{-1} s^{-1} ± standard error; bath gas M = N$_2$ unless denoted * where M = air.

The results for CH$_3$OH were in good agreement with literature data available and the IUPAC preferred value at room temperature that is $k_{1.1}(298\ \text{K}) = 0.93 \times 10^{-12}$ cm^3 molecule^{-1} s^{-1} (Dillon et al., 2005; Jiménez et al., 2003; Wallington and Kurylo, 1987b). The rate coefficient values were reported with their standard errors and the average weighted on these errors leads to

$k_{3.1,\text{PLP-LIF}}(296\ \text{K}) = (3.10 \pm 0.07) \times 10^{-12}$ cm^3 molecule^{-1} s^{-1}.

Where 0.07 indicates the standard error calculated according to the formula $\text{SE} = \frac{\sigma}{\sqrt{n}}$, where SE stand for standard error, σ is the standard deviation and n is the number of datapoints. This value though, does not include the systematic error that is estimated to be around 20%. We therefore conclude that, at ambient temperature, OH reacts with TMO considerably more slowly than with other oxolanes, e.g.: oxolane (tetrahydrofuran) $k = 1.7 \times 10^{-11}$ cm^3 molecule^{-1} s^{-1} (Moriarty et al., 2003); 2-methyloxolane, $k = 2.65 \times 10^{-11}$ cm^3 molecule^{-1} s^{-1} (Illes et al., 2016); and 2,5-dimethyloxolane for which only data for the reaction with isotopically-labelled OD is available and where $k = 4.6 \times 10^{-11}$ cm^3 molecule^{-1} s^{-1} (Andersen et al., 2016) as reported in Table 3.1. That the measured ambient temperature $k_{3.1}$ values determined by PLP-LIF were indeed anomalously small is further confirmed by calculations using the most up-to-date structure activity relationship from Jenkin et al. (2018) which may be used to predict $k_{3.1}$ (298 K) = 9.1×10^{-12} cm^3 molecule^{-1} s^{-1}. Even within the estimated factor-of-two accuracy of the SAR, the values of $k_{3.1}$ obtained from this work would appear anomalously small.

3.2.2. PLP-LIF Results: Temperature Dependence Studies of TMO + OH (R3.1)

The study of TMO with OH (R3.1) by PLP-LIF was extended to a broad range of temperatures, starting from room temperature up to 502 K, that was the limit imposed by our heating system. The temperature was steadily monitored during the experiments with a thermocouple that was positioned on the top of the reactor chamber and was regularly moved to the centre of the reactor, in the reactivity zone, to ensure temperature consistency over the kinetics measurements that usually counted around 10 measurements at the same T and different concentrations. Again, some of the experiments to determine $k_{3.1}(296$ K) were conducted "back-to-back" with the well-characterised reaction of OH with CH_3OH (R1.1). The results for both compounds are listed in Table 3.4.

Table 3.4: Rate coefficients for R3.1 (TMO + OH) and R1.1 (CH_3OH + OH) determined via PLP-LIF at ΔT (314-501 K).

Reaction	T / K	p / Torr	OH precursor	n [a]	[TMO] [b]	$k(T) \pm$ SE [c]
(R3.1)	314	58	H_2O_2	8	$2-18$	2.75 ± 0.3
(R3.1)	336	34	$(CH_3)_3COOH$	10	$1-30$	2.7 ± 0.3
(R3.1)	344	58	H_2O_2	8	$2-18$	2.7 ± 0.3
(R3.1)	383	58	H_2O_2	8	$2-25$	3.0 ± 0.1
(R3.1)	421	60	H_2O_2	10	$1-14$	3.4 ± 0.3
(R3.1)	441	60	H_2O_2	8	$1-12$	3.6 ± 0.3
(R3.1)	464	29	H_2O_2	8	$1-15$	4.7 ± 0.5
(R3.1)	502	29	H_2O_2	13	$1-14$	5.9 ± 0.3
(R1.1)	346	62	H_2O_2	14	$3.2-85.4$	1.44 ± 0.08
(R1.1)	400	38	H_2O_2	8	$1.6-44.0$	1.5 ± 0.2
(R1.1)	441	60	H_2O_2	12	$3.4-34.0$	1.8 ± 0.1

| (R1.1) | 471 | 29 | H$_2$O$_2$ | 9 | 4.0 - 38.0 | 1.8 ± 0.1 |
| (R1.1) | 501 | 29 | H$_2$O$_2$ | 7 | 3.4 - 40.0 | 2.4 ± 0.2 |

Notes: [a] n is the number of different [TMO] used (not including [TMO] = 0); [b] = range of [TMO] in units of 10^{14} molecule cm^{-3} ; [c] = $k(T)$ in units of 10^{-12} cm^3 molecule^{-1} s^{-1} ± standard error.

Figure 3.6 shows an example of three linear plots of experiments taken at different temperatures which show a good linearity and a slope that increase with temperature. Here again the intercept values (around 500 s^{-1}) lead to an estimated [H$_2$O$_2$] = 10^{14} molecule cm^{-3} for a rate constant of H$_2$O$_2$ with OH (R2.3) equal to $k_{2.3}$(T) = 2.9 × 10^{-12} exp(-160/T) cm^3 molecule^{-1} s^{-1} (Atkinson et al., 2004).

Figure 3. 6: Three typical bimolecular plots of B vs. [TMO] used to determine $k_{3.1}(T)$ for OH + TMO, each fit with Eq. (3.6) to obtain: $k_{3.1}$(297 K) = (3.1 ± 0.1) × 10^{-12} cm^3 molecule^{-1} s^{-1}, from the black squares; $k_{3.1}$(441 K) = (3.6 ± 0.3) × 10^{-12} cm^3 molecule^{-1} s^{-1}, from the red diamonds; $k_{3.1}$(502 K) = (5.9 ± 0.3) × 10^{-12} cm^3 molecule^{-1} s^{-1}, from the blue triangles.

Figure 3.7 presents the results from these PLP-LIF experiments in Arrhenius format. Results for (R1.1) were in reasonable agreement with previous determinations (Wallington et al., 1988; Hess and Tully, 1989; Jiménez et al., 2003; Dillon et al., 2005) and with a three-parameter expression, $k_{3.1}$(210 − 866 K) = 6.38×10^{-18} T^2 exp(144 / T) cm^3 molecule^{-1} s^{-1}, recommended by IUPAC (Atkinson et al., 2006) (see Fig. 3.6). This satisfactory agreement lends some confidence to the assessment of uncertainties in $k_{3.1}(T)$. Over the limited range of temperatures explored in this work, the results for (R1.1) appear to conform closely to the Arrhenius equation, with the smallest values of $k_{1.1}(T)$ found at the lowest temperature. The

contrast with the $k_{3.1}(294 - 502$ K) data was stark, where a local minimum was observed at around $T = 340$ K; values of $k_{3.1}$ increased to both lower and to higher temperatures. This trend is better represented by a four-parameter expression (Equation 3.7):

$$k(T) = A_1 \, exp^{(-E_1/T)} + A_2 \, exp^{(E_2/T)}$$

Eq. (3.7)

The curve fitting gives $k_{3.1}(294 - 502$ K) = 5.33×10⁻¹⁰ exp(-2237/T) + 2.22×10⁻¹³ exp(+766/T) cm³ molecule⁻¹ s⁻¹, as represented in Figure 3.7.

Figure 3. 7: Arrhenius plot displaying $k_{3.1}(T)$ results from this work obtained via PLP-LIF (filled blue diamonds) and RR (filled blue triangle) all fit with the four-parameter Eq. (3.7). to yield $k_{3.1}(294 - 502$ K) = 5.33×10⁻¹⁰ exp(-2237 / T) + 2.22×10⁻¹³ exp(+766 / T) cm³ molecule⁻¹ s⁻¹ (the blue dashed line). Calculated $k_{3.1}(298 - 370$ K) using the SAR proposed by Jenkin et al. (2018) is displayed as the blue dotted line. Also displayed are $k_{1.1}(299 - 501$ K) from this work (filled red squares) alongside literature determinations (Hess and Tully, 1989; Wallington et al., 1988; Jiménez et al., 2003; Dillon et al., 2005) and the most recent evaluation from IUPAC (Atkinson et al., 2006), recommending $k_{1.1}(210 - 866$ K) = 6.38×10⁻¹⁸ T^2 exp(144 / T) cm³ molecule⁻¹ s⁻¹ (the solid red line).

The non-Arrhenius behaviour is unlikely to be predicted by SARs and in fact, the SAR calculations lead to a straight non-Arrhenius behaviour over the short range of temperatures recommended by Jenkin et al. (2018). The SAR trend reminds of the Arrhenius plot of diethyl ether and di-isopropyl ether (Calvert et al., 2011b), which both show a similar non-Arrhenius behaviour. On the other hand, the non-Arrhenius behaviour experimentally determined for TMO, has been observed before with other oxygenated compounds. The reaction of acetone $(CH_3)_2CO$ with OH for instance (R1.12), has been extensively studied over a much wider range of temperatures (200-1000 K) and it shows a similar U-shaped trend (Calvert et al., 2011b), as discussed in section 1.3.1. The values recommended by the latest IUPAC evaluation (Atkinson et al., 2006) were shown in Figure 1.18. The case of acetone has been explained by

70

the occurrence of two different reaction mechanisms (Wollenhaupt et al., 2000; Vasvári et al., 2001). The first one, likely to be predominant at high temperatures (T > 240 K), is the H-abstraction from CH_3 groups. The second one, occurring at low temperatures (T < 240 K) is based on hydrogen-bond complex formation $(CH_3)_2CO\cdots OH$. In a similar way, the reaction of OH with TMO is expected to occur through hydrogen bond transition state and the curve of $k_{3.1}(T)$ can be rationalized with a change in the mechanism. To gain more insights on the reaction routes involved, (R3.1) was investigated by quantum chemical calculations (QCC) made by Conor Rankine and Juliette Schleicher and the results were summarised in section 3.2.4.

3.2.3. RR Results for TMO + OH (R3.1)

Figure 3.8 displays FTIR spectra of TMO recorded at the CERNESIM atmospheric simulation chamber ESC-Q-UAIC (Roman et al., 2022) described in section 2.2. Qualitatively, the spectra compare well to predictions (Frisch et al., 2016), thus allowing deployment of pre-planned reference compounds (Table 2.4) for relative rate experiments. Preliminary experiments conducted in the presence of radical precursors were carried out to ensure that neither TMO nor the various reference VOC were significantly impacted by wall losses or photolytic removal.. The wall loss has been treated as a first order kinetic for adsorption of the gaseous compounds on the chamber's walls. For each experiment, the spectra of the mixture of the VOCs including the OH radical precursor were recorded in dark prior to the start of the photolytic light for a period of 10 minutes recording 5-10 spectra in dark. FTIR peak intensities were directly proportional to species concentrations and were used to calculate the logarithmic depletion for TMO and for the reference compound. CH_3OCH_3 and $c\text{-}C_6H_{12}$ were chosen as reference compounds for the study of R3.1. Figure 3.8 displays also the spectrum of C_3H_6 that was selected in addition to the other compounds for the study of R3.2 (see section 3.3).
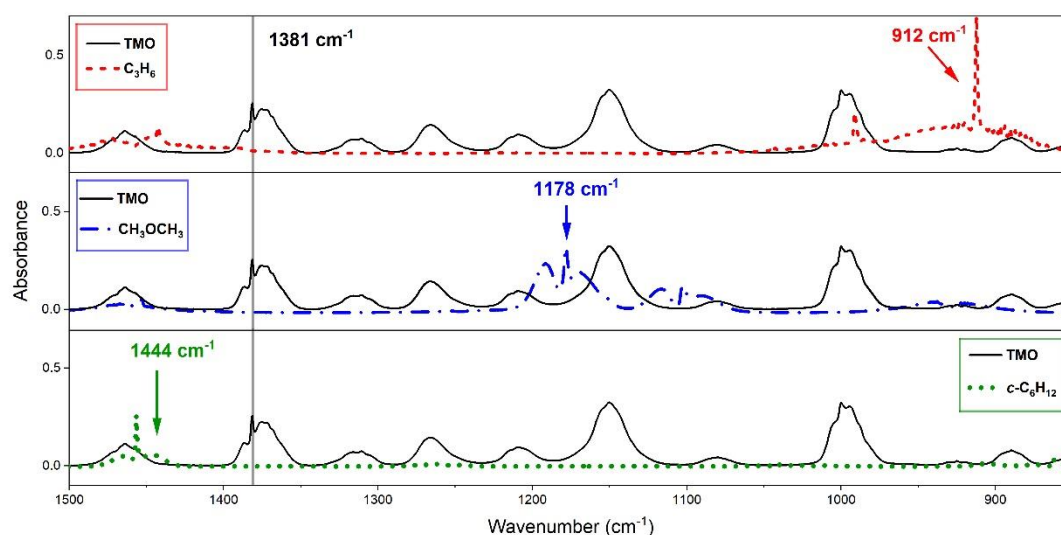
Figure 3. 8: Observed FTIR spectra with typical monitoring frequencies indicated: TMO (black solid line), monitored at 1381 cm^{-1} where reference compounds did not appreciably absorb; for C$_3$H$_6$ (the red dashed line) at 1381 cm^{-1}; CH$_3$OCH$_3$ (blue dot-dash line) and c-C$_6$H$_{12}$ (green dotted line) at 1444 cm^{-1}.

Results from studies using c-C$_6$H$_{12}$ and CH$_3$OCH$_3$ as reference compounds to determine $k_{3.1}$(296 K) are displayed in Fig. 3.9.
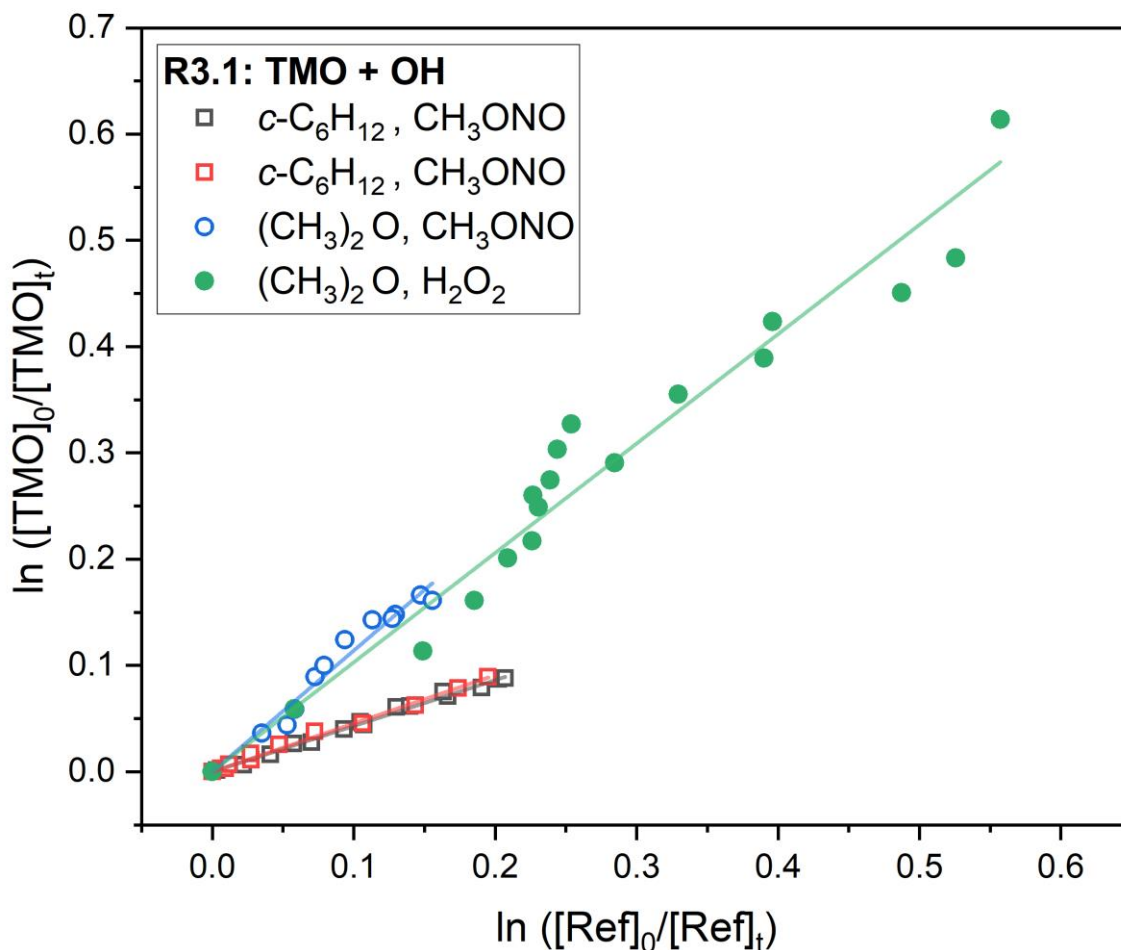
Figure 3. 9: Relative rate plots, used to determine $k_{3.1}$(296 K) for OH + TMO (R3.1). The circles correspond to use of CH$_3$OCH$_3$ (R2.11) as reference; the squares c-C$_6$H$_{12}$ (R2.12). Empty circles and squares indicate experiments where CH$_3$ONO was used as a precursor, whereas the filled circles indicate the use of H$_2$O$_2$. The solid lines are linear fits, with gradient values used (Eq.3.8) in conjunction with literature data (Table 2) to obtain $k_{3.1}$. The full results, summarised in Table 4, were averaged to obtain $k_{3.1}$(296 K) = (3.07 ± 0.05) × 10^{-12} cm^3 molecules^{-1} s^{-1}.

According to Eq. (3.8), the relative rate plot should be a straight line with zero intercept and be identified with the relative rate $k_{3.1}$ / k_{ref}.

$$ln\frac{[TMO]_{t_0}}{[TMO]_t} = \frac{k_{3.1}}{k_{ref}} ln\frac{[reference]_{t_0}}{[reference]_t}$$

Eq. (3.8)

Plots of R3.1 vs R2.12 (c-C$_6$H$_{12}$ + OH) represented in Fig.3.9 show a good proportionality. The results obtained from these and a similar series of experiments are presented in Table 3.5. The spread of values seems reasonable given both statistical uncertainties and the (approximately 20%) systematic uncertainties in the literature reference k-values. A weighted mean value from these four relative rate determinations and the relative standard error was

$k_{3.1,RR}$(296 K) = (3.07 ± 0.07) × 10^{-12} cm^3 molecules^{-1} s^{-1}

Table 3.5: Relative rate experiments of TMO + OH.

OH precursor	Ref. VOC	λ / nm	$[\text{Ref}]_0{}^a$	$[\text{TMO}]_0{}^a$	$k_{3.1}$ / $k_{\text{refOH}}{}^b$	$k_{3.1}$(296 K) $\pm$ SE^c
CH_3ONO	c-C_6H_{12}	365	3.30	3.28	0.435 ± 0.009	3.03 ± 0.07
CH_3ONO	c-C_6H_{12}	365	2.35	1.48	0.44 ± 0.01	3.10 ± 0.08
CH_3ONO	CH_3OCH_3	365	3.30	2.84	1.14 ± 0.07	3.3 ± 0.2
H_2O_2	CH_3OCH_3	254	3.30	2.84	1.01 ± 0.05	2.9 ± 0.2

Notes: all experiments were conducted at p = 750 Torr (air) and T = 296 K ; ^{a} = initial [Ref] and [TMO] values calculated from the injected amount (in mass units) in 10^{13} molecule cm^{-3}; ; ^{b} = see Table 2.4 for values of $k_{2.11}$(298 K) and $k_{2.12}$(298 K) used here as k_{ref}; ^{c} = $k_{3.1}$(296 K) in units of 10^{-12} cm^3 molecules^{-1} s^{-1} ± standard error.

The value of $k_{3.1}$ determined by RR studies shows an extremely good agreement with the PLP-LIF determinations. The results from both methods are shown in Figure 3.10, where the rate constants were fitted against pressure to weight the error bars. The obtained averaged value, comprehensive of the potential systematic uncertainty estimated according to Eq. 2.39 is equal to:

$k_{3.1}$ (296 K) = (3.1 ± 0.5) × 10^{-12} cm^3 molecule^{-1} s^{-1}

The fact that two very different and complementary methods lead to the same result, brings a further and solid confirmation of the low reactivity of TMO.
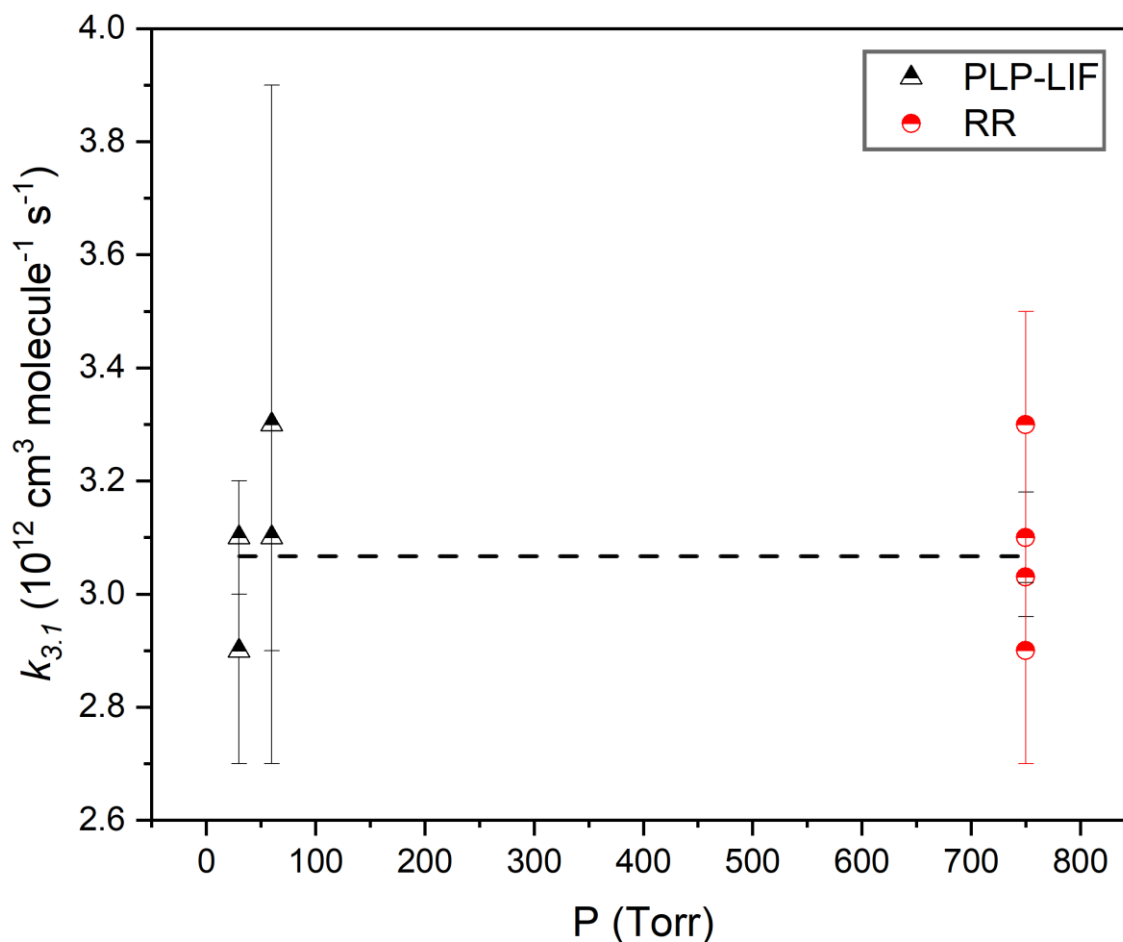
Figure 3. 10: Rate coefficients values for (R3.1) determined by PLP-LIF and RR experiments fitted with a liner plot of slope fixed at 0 to determine the average $k_{3.1}$ weighted on error bars.

3.2.4. Product Study of TMO + OH (R3.1)

Degradation schemes for TMO were proposed following H-abstraction from either the secondary C-H (R3.1a) or the primary C-H (R3.1b). Subsequent oxidations were defined using MCM (Master Chemical Mechanism) (Jenkin et al., 1997; Saunders et al., 2003) protocols and are here represented in Figure 3.11 and Figure 3.12.
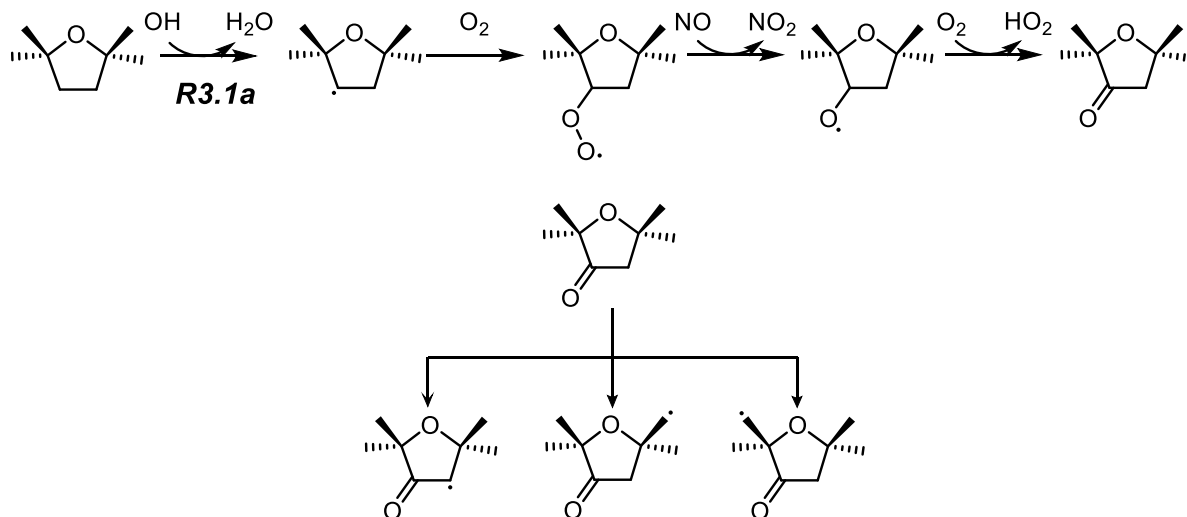
Figure 3. 11: Proposed reaction scheme for (R3.1a) leading to the first stable ketone product that can subsequently undergo three different routes, according to where the H-abstraction takes place. The following steps are omitted for clarity.

Reaction (R3.1a) leads quite early to formation of a potentially stable compound, that is 2,2,5,5-tetramethyldihydrofuran-3-one. This ketone product can then undergo three alternative pathways of unknown branching ratio. On the other hand, reaction (R3.1b) (Figure 3.12) doesn't seem to lead to any stable compound until it breaks down forming acetone and CO_2.
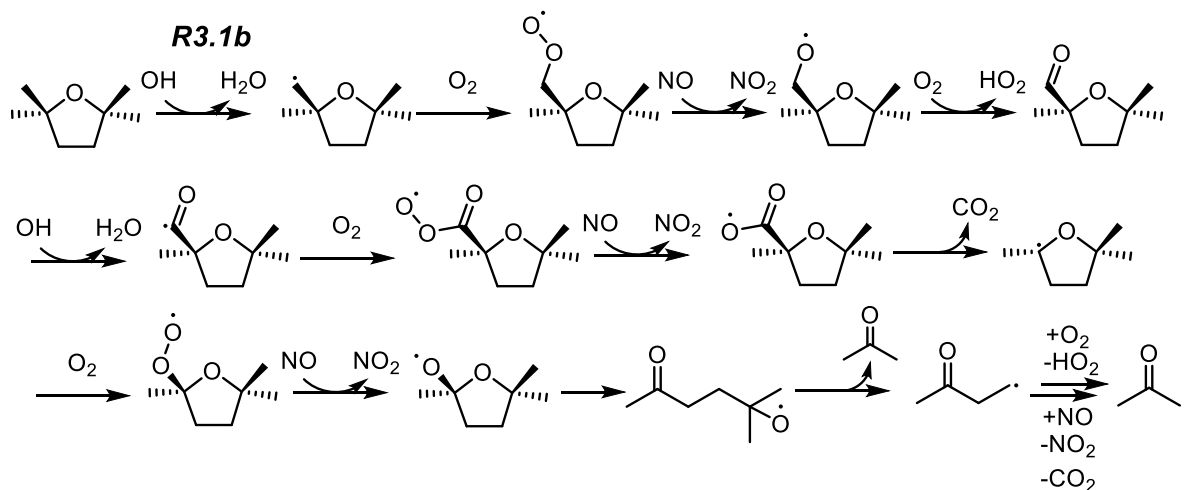
Figure 3. 12: Proposed reaction scheme for (R3.1b) for which the most stable product was identified as acetone.

Product studies were carried out at the CERNESIM atmospheric simulation chamber (Roman et al., 2022). Differently to the RR experiments, this time the observation of the chemical species inside the reactor chamber was carried out in the absence of reference compounds, in the attempt of avoiding any intruding FTIR peaks that could overlap with the

ones of the oxidation products. TMO and the OH precursor were injected in the reactor chamber previously filled with air, and NO was injected as well to simulate a pollute atmosphere with excess of NO. FTIR spectra were then recorded every 2 minutes until disappearance of TMO. An accurate study of the FTIR spectra aimed to the identification of the oxidation products to gain mechanistic insights. The spectrum of the predicted first stable product for (R3.1a), 2,2,5,5-tetramethyldihydrofuran-3-one, was recorded in preliminary studies to make the identification easier. Only acetone was detected from the FTIR spectra and being a product of both reaction routes (R3.1a) and (R3.1b), it wasn't useful to lead to any conclusion on the branching ratio of the reaction. The characteristic peaks of 2,2,5,5-tetramethyldihydrofuran-3-one were not identified in the recorded spectra, and this may lead to two observations:

- Only a minor amount of 2,2,5,5-tetramethyldihydrofuran-3-one formed during the experiment and was not detectable because of the complex FTIR spectra of air and TMO that may have hidden its presence. This would suggest that (R3.1b) is the preferred route of the reaction, as indicated by QCC studies.
- Formation of 2,2,5,5-tetramethyldihydrofuran-3-one is not detectable on the experiment timescale, and it reacts quickly with OH to form other unstable products that break down into CO_2 and acetone.

3.2.5. Quantum Chemical Calculations Studies of TMO + OH

The following Quantum Chemical Calculations were conducted by Conor Rankine (University of York) and Juliette Schleicher (École Polytechnique Fédérale de Lausanne) and were here reported for completeness and to show how this project aimed to a comprehensive and multidisciplinary approach to the study of atmospheric chemistry. QCC were carried out at the CBS-QB3 (Montgomery et al., 1999) and G4 (Curtiss et al., 2007) model chemical levels of theory to further study $k_{3.1}(T)$ determined in laboratory experiments, explore the hydrogen abstraction pathways (R3.1a) and (R3.1b) set out in Figure 3.3 and possibly predict the products of (R3.1). The results are now published on ACP (Atmospheric Chemistry and Physics)(Mapelli et al., 2022).

A total of five pseudo-equivalent channels were characterised, three were associated with generation of (R3.1b) products, corresponding to abstraction of each of the three unique hydrogen atoms at the β position on a methyl (-CH_3) substituent; two were associated with (R3.1a), corresponding to abstraction of each of the two unique hydrogen atoms of the β methylene (-CH_2-) on the aliphatic ring. QCC located transition states (TS) for each hydrogen abstraction ($TS_{1-3}^{R3.1b}$ and $TS_{4-5}^{R3.1a}$ depicted in Figure 3.13), together with corresponding pre- (OH + TMO) and post- [H_2O + TMO($-H$)] reaction complexes. The free energy profiles of the reaction channels at the G4 level of theory were presented in Figure 3.14, while a summary of the relative free energies ($\Delta G^{\ddagger}_{298K}$), were tabulated for each of the TS in Table 3.6.
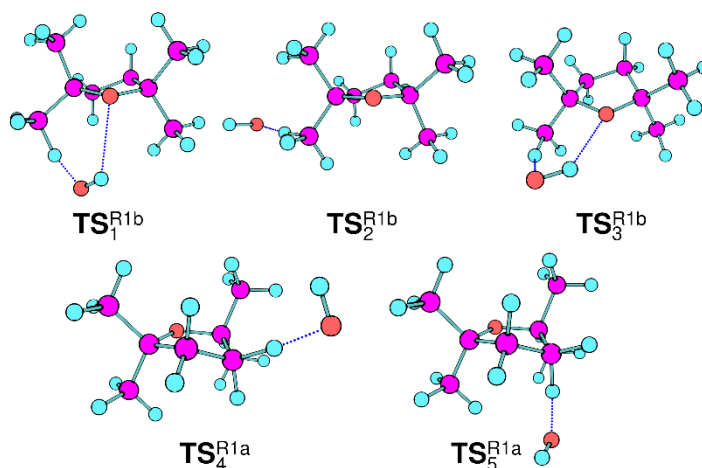
Figure 3. 13: The five transition states (TS) characterised via QCC of which $TS_2^{R3.1b}$, $TS_4^{R3.1a}$, and $TS_5^{R3.1a}$ are associated with 'direct', non-stabilised hydrogen abstraction; $TS_1^{R3.1b}$ and $TS_3^{R3.1b}$ are associated with stabilised hydrogen abstraction that proceeds via a hydrogen-bound pre-reaction complex and TS. This figure was kindly provided by Conor Rankine. See Fig. 3.3 for description of reaction channels proceeding to (R3.1a) and (R3.1b) products which in the figure are labelled as R1a and R1b.
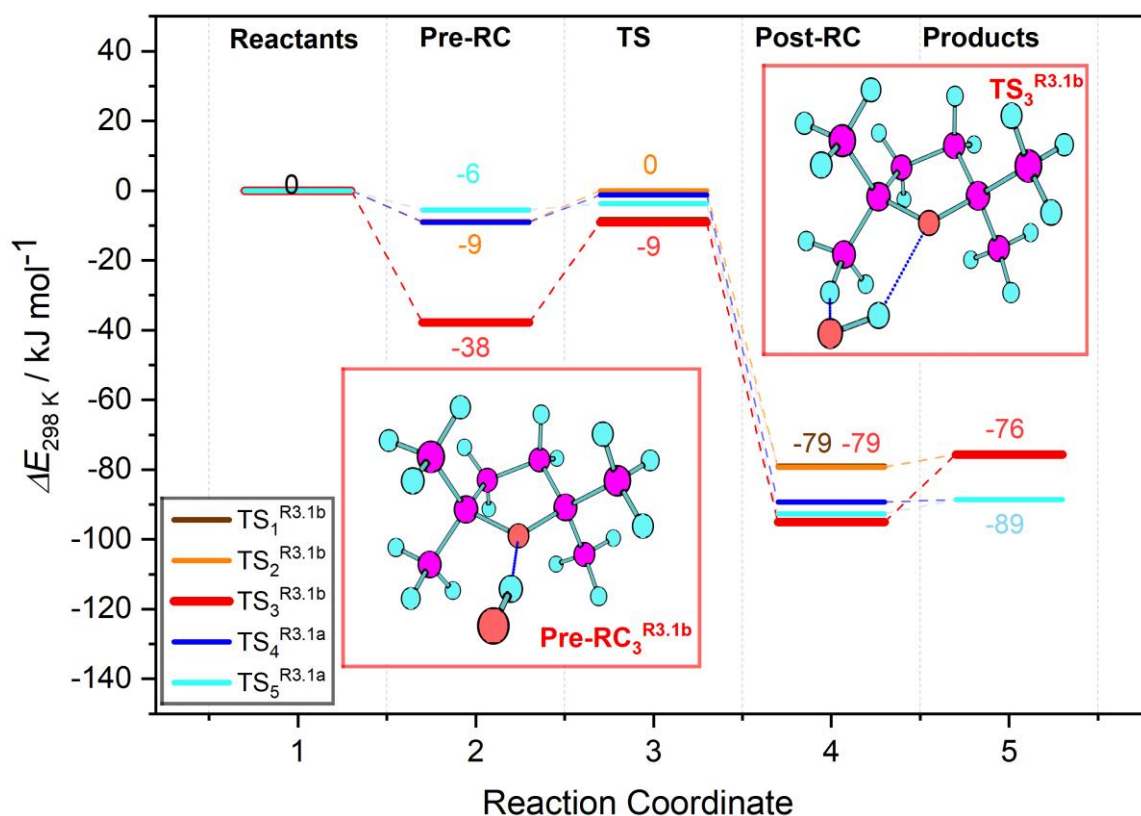
Figure 3. 14. Free energy profile of (R3.1) hydrogen abstraction pathways: two leading to (R3.1a) products via ($TS_{4-5}^{R3.1a}$) and three ($TS_{1-3}^{R3.1b}$) leading to (R3.1b) products, labelled according to the associated transition state in the legend. For each of the five pathways along the reaction coordinate, five stationary point energies (1 = separated reactants, 2 = pre-reaction complex, 3 = transition state, 4 = post-reaction complex and 5 = separated products) were calculated using G4 model chemistry, p = 1 bar and T = 298 K.

The energetic barrier $\Delta G^{\ddagger}_{298K}$ along the reaction coordinate was similar for hydrogen abstraction pathways (R3.1a) and (R3.1b), indicating no dominant reaction by kinetic control; However, the distinctive energy profile was found in the pre-reaction complex. In fact, the loosely-bound pre-reaction complexes associated with $TS_2^{R3.1b}$, $TS_4^{R3.1a}$, and $TS_5^{R3.1a}$ are located in a less-accessible, higher-energy part of the free energy surface (ca. 15 – 20 kJ mol^{-1}), while the hydrogen-bound pre-reaction complex through which the reaction channel bifurcates towards $TS_1^{R3.1b}$ and $TS_3^{R3.1b}$ is submerged (ca. -8.5 kJ mol^{-1}) relative to reactants. In other terms, the hydrogen-bound pre-reaction complex acts as a funnel on the free energy surface to lead the reaction towards preferential production of the kinetic (via R3.1b), rather than the thermodynamic (via R3.1a), radical products (Fig. 3.3). The formation of hydrogen-bound pre-reaction complexes and TS in the (R3.1a) channels is precluded by strong steric interactions and charge screening by methyl substituents on TMO.

Table 3.6: Summary of relative TS free energies ($\Delta G^{\ddagger}_{298K}$) and Pre-RC free energies (Pre-RC ΔG) for R3.1 (TMO + OH).

TS	$\Delta G^{\ddagger}_{298K}$	Pre-RC ΔG
$TS_1^{R3.1b}$	28.7	-8.5
$TS_2^{R3.1b}$	32.6	15
$TS_3^{R3.1b}$	26.9	-8.5
$TS_4^{R3.1a}$	28.5	15
$TS_5^{R3.1a}$	29.2	20

Notes: values are in kJ mol^{-1}.

3.3. Rate Coefficients of TMO + Cl (R3.2)

A series of experiments similar to those described in section 3.2.3 were conducted to determine $k_{3.2}$(296 K) for Cl + TMO (R3.2). The reaction scheme is illustrated in Figure 3.15, and it occurs via a H-abstraction that is essentially the same mechanism involved in the reaction with OH.
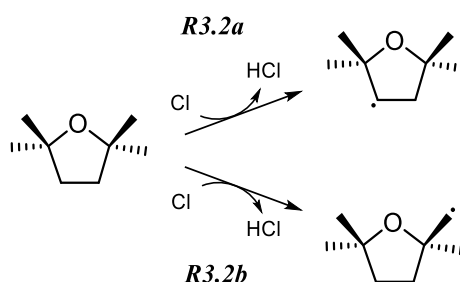
Figure 3. 15: Reaction scheme for TMO + Cl (R3.2) with two possible H-abstraction routes indicated as (R3.2a) for the reaction on the secondary C-H and (R3.2b) for the the primary C-H.

Details of reference compounds used were given in Table 2.4, exemplary results presented in Figure 3.16, and the full dataset summarized in Table 3.7.
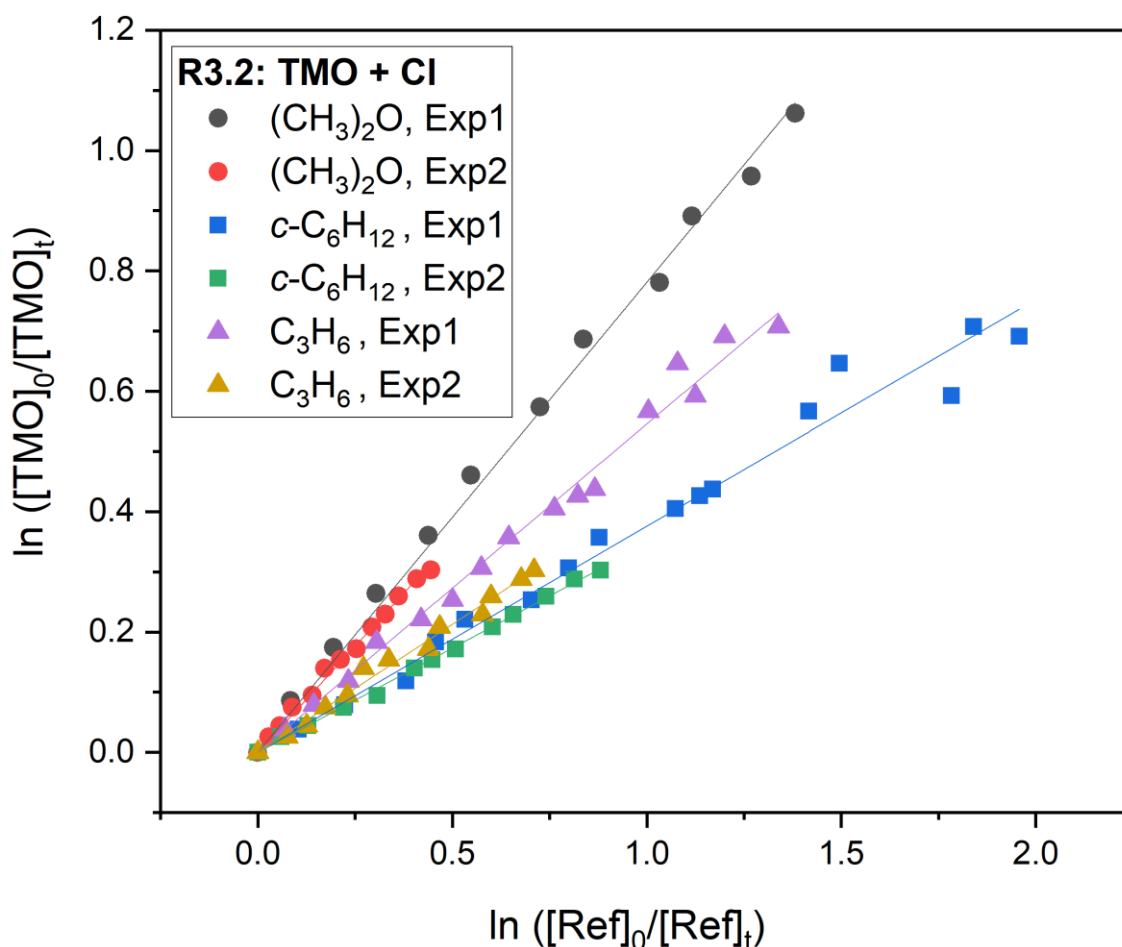
Figure 3. 16: Relative rate plots used to determine $k_{3.2}(296\ K)$ for Cl + TMO (R3.2) using reference reactions of Cl with CH_3OCH_3, c-C_6H_{12} and C_3H_6 (R2.14, R2.15, R2.16) . Gradients obtained from linear fits (the solid lines) were used in conjunction with literature data (Table 2.4) to obtain $k_{3.2}$. The full results were summarised in Table 3.7, were averaged to obtain $k_{3.2}(296\ K)$ = (1.2 ± 0.1) × 10^{-10} cm³ molecule⁻¹ s⁻¹.

Table 3.7: Rate coefficients determined via RR for R3.2 (TMO + Cl)

Ref. VOC	[Ref]$_0$ [a]	[TMO]$_0$ [a]	$k_{3.2}$ / k_{refCl} [b]	$k_{3.2}(296\ K)$ ± SE [c]
CH_3OCH_3	3.30	3.71	0.76 ± 0.01	1.31 ± 0.02
CH_3OCH_3	6.60	4.90	0.68 ± 0.01	1.18 ± 0.02
c-C_6H_{12}	1.47	5.32	0.37 ± 0.01	1.22 ± 0.08
c-C_6H_{12}	2.20	4.90	0.349 ± 0.005	1.15 ± 0.02
C_2H_6	6.57	5.32	0.55 ± 0.01	1.23 ± 0.03
C_2H_6	6.57	4.90	0.425 ± 0.01	0.95 ± 0.03

Notes:[a] all experiments were conducted at p = 1 bar (air) and T = 296 K using 365 nm Cl_2 photolysis to generate Cl-atoms; a = initial [Ref]$_0$ and [TMO]$_0$ calculated from the injected amount (in mass units) in 10^{13} molecule cm⁻³; b = see Table 2.4 for values of k_{refCl} used here; c = $k_{3.2}(296\ K)$ from this work reported in 10^{-10} cm³ molecules⁻¹ s⁻¹ ± standard error.

The weighted mean value and standard error obtained was

$k_{3.2,RR}(296\ K)$ = (1.18 ± 0.05) × 10^{-10} cm³ molecules⁻¹ s⁻¹

with $k_{3.2}(296\ K)$ = (1.2 ± 0.3) × 10^{-10} cm³ molecules⁻¹ s⁻¹ representing a more realistic overall uncertainty estimate from Eq. 2.39. This result is, to the best of our knowledge, the first such reported value for (R3.2). The value of k_2 is 2 orders of magnitude higher than $k_{3.1}$, as it is

often the case for VOCs. The fast reactivity of Cl with VOC may indicate that Cl is relevant to the removal of this VOC, especially in areas with high concentrations of Cl such as the marine boundary layer.

3.4. Atmospheric Implications and Modified SAR

The study of the rate constants for (R3.1) and (R3.2) gives important information on TMO atmospheric chemistry, leading to a preliminary assessment of this new green solvent. From the rate coefficients, important air quality indicators such as lifetime and POCP can be deduced. The comparison of these indicators with the ones measured for toluene, a solvent that TMO may replace and that is known to be a bad air pollutant, can tell us more on whether this new green solvent would be a safer alternative for air quality.

3.4.1. Modified SAR for TMO + OH (R3.1)

The unpredictably low value of $k_{3.1}$, together with the non-Arrhenius behaviour of $k_{3.1}$(T) and the mechanistic insights predicted by QCC studies, all indicate the inability of SAR calculations to predict the behaviour of a complex molecule like TMO. As suggested by QCC investigations, the presence of four methyl groups adjacent to the ether oxygen is a structural feature that is critical in defining the interaction with OH radicals. In the case of route (R3.1a) in fact, the formation of a loosely bound, hydrogen-bond proceeding pre-reaction complex is obstructed by the steric hindrance of the methyl groups. On the other hand, route (R3.1b) can occur with a pre-reaction complex based on hydrogen bond formation at a low energy, determining in this way the most likely fate of the reaction. In other terms, because of the effect of the methyl groups, the kinetic radical product may be prevalent to the thermodynamic one.

The introduction of this concept into SAR calculations may be quite complex and requires further study, but to improve (R3.1) predictions a modified SAR was formulated. The new calculation aimed to 'hide' the presence of oxygen from the expression of k_{CH2}, as the methyl groups somehow hide the effect of O that promotes the pre-reaction complex for the H-abstraction. Instead of the original expression for the partial rate coefficient reported in Table 3.2 for CH_2 that includes the substituent factor $F_X = 3.50$ which accounts for the presence of ethereal oxygenated groups (CH_2OR, $-CH(OR)-$, $-C(OR)<$), to F_X was instead given a value of 1.35. Applying this correction is equivalent to calculate the partial rate coefficient for the CH_2 of 2,2,5,5-tetramethylcyclopentane, the structurally similar alkane equivalent of TMO. The result of this modification is a new SAR expression that leads to a predicted $k_{3.1}$(298 K) = 4× 10^{-12} cm³ molecules⁻¹ s⁻¹, a value that is strikingly closer to our experimental results. The temperature dependence of the modified $k_{3.1,SAR}$(T) illustrated in Figure 3.17.
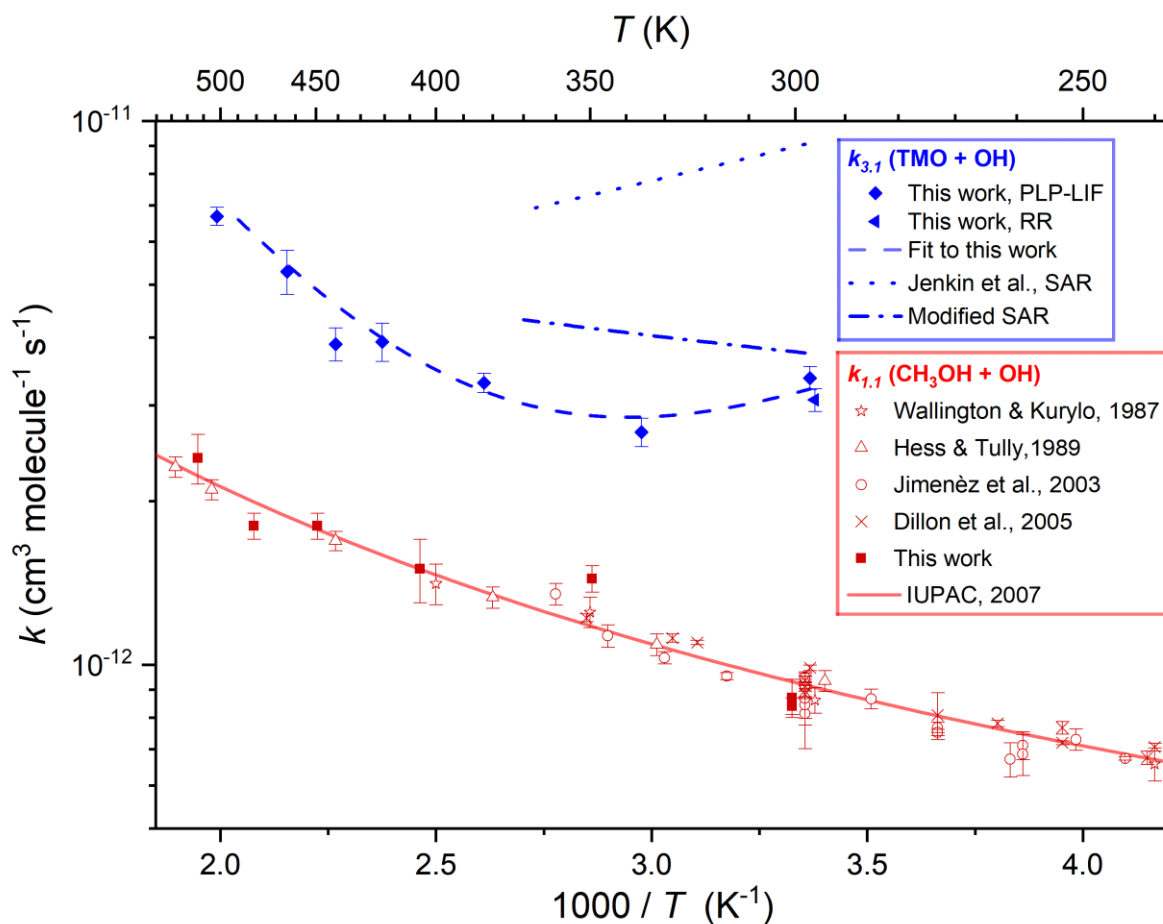
Figure 3. 17: Arrhenius plot displaying $k_{3.1}(T)$ results from this work obtained via PLP-LIF (filled blue diamonds) and RR (filled blue triangle) all fit with the four-parameter Eq. (3.7). to yield $k_{3.1}(294 - 502 \text{ K}) = 5.33\times10^{-10} \exp(-2237 / T) + 2.22\times10^{-13} \exp(+766 / T) \text{ cm}^3 \text{ molecule}^{-1} \text{ s}^{-1}$ (the blue dashed line). Calculated $k_{3.1}(298 - 370 \text{ K})$ using the SAR proposed by Jenkin et al. (2018) is displayed as the blue dotted line. Also displayed are $k_{1.1}(299 - 501 \text{ K})$ from this work (filled red squares) alongside literature determinations (Hess and Tully, 1989; Wallington et al., 1988; Jiménez et al., 2003; Dillon et al., 2005) and the most recent evaluation from IUPAC (Atkinson et al., 2006), recommending $k_{1.1}(210 - 866 \text{ K}) = 6.38\times10^{-18} T^2 \exp(144 / T) \text{ cm}^3 \text{ molecule}^{-1} \text{ s}^{-1}$ (the solid red line). The blue dot-dashed line represents a modified SAR calculation (see section 3.4.1).

3.4.2. Lifetime of TMO

The lifetime of a VOC, as described in detail in the introduction, is the time required for its concentration to drop to $1/e$ of the initial concentration. To determine the lifetime of TMO relative to the removal process indicated as (R3.1), it is indispensable to know $k_{3.1}$ and the concentration of OH, as expressed in Eq. (3.9):

$$\tau = \frac{1}{k_{3.1}[\text{OH}]}$$
Eq. (3.9)

Using a concentration of $[\text{OH}] = 1.13 \times 10^6$ molecule cm^{-3} representative of the troposphere (Lelieveld et al., 2016), we obtain $\tau_{3.1} \approx 3$ days. This lifetime value may be an overestimate for two reasons. First, our ambient-temperature value may underestimate $k_{3.1}$ for colder troposphere conditions. Second, in regions highly impacted by atmospheric chlorine, the lifetime of TMO may be affected by (R3.2) with chlorine atoms. Estimates for ambient [Cl] vary widely and will anyway be subject to a high degree of spatial variability. An average

ambient concentration of [Cl] = 1×10^3 (Fantechi et al., 1998), and the rate constant measured in this work as $k_{3.2}(296 \pm 2$ K$) = (1.2 \pm 0.1) \times 10^{-10}$ cm^3 molecule^{-1} s^{-1}, lead to a lifetime $\tau_{3.2} \approx$ 100 days. Nonetheless, using a large estimate of [Cl] = 1×10^4 molecule cm^{-3} (Li et al., 2018), we can determine a lifetime with respect to Cl atoms of $\tau_{3.2} \approx 10$ days which, when combined with data for (R3.1), could reduce the overall atmospheric lifetime for TMO. A more thorough expression of TMO's lifetime is then expressed as:

$$\tau = \frac{1}{\tau_1} + \frac{1}{\tau_2} = \frac{\tau_1\tau_2}{\tau_1+\tau_2} \qquad\qquad \text{Eq. (3.15)}$$

From Eq. (3.15), if $\tau_{3.2} >> \tau_{3.1,}$ then $\tau_{3.1}$ will be the lifetime associated to the rate determining process and $\tau \approx \tau_{3.2}$. Normally, for an average ambient concentration of Cl, we can imagine a condition where $\tau_{3.2} >> \tau_{3.1}$ and $\tau = 3$ days. But it is worth to notice that in specific cases, like the marine boundary layer, where high Cl concentrations ([Cl] = 1×10^4 molecule cm^{-3}) were measured, $\tau_{3.2} > \tau_{3.1}$ and (R3.1) will have an effect over TMO lifetime, that will decrease up to $\tau \approx 2$ days. Losses of TMO to other atmospheric radicals, to O_3, or to photolysis appear unlikely and, to date, unmeasured.

As discussed in section 1.2.2, TMO was designed to replace toluene ($C_6H_5CH_3$) in solvent applications. The reaction of $C_6H_5CH_3$ with OH is known to be the main degradation route (R3.8).

$$C_6H_5CH_3 + OH \rightarrow \text{products} \qquad\qquad (R3.8)$$

A lifetime calculation for $C_6H_5CH_3$, with $k_{3.8}(298$ K$) = 5.6 \times 10^{-12}$ cm^3 molecule^{-1} s^{-1} (Mellouki et al., 2021) and [OH] = 1.13×10^6 molecule cm^{-3}, yields $\tau_{3.8} \approx 2$ days. However, other processes such as photolysis, reaction with Cl, and with other important chemical species such as O_3 and NO_3 are known to be relevant for the removal of this aromatic molecule and may considerably affect the overall lifetime depending on the atmospheric conditions.

All in all, TMO showed to have a longer lifetime than the solvent it is proposed to replace. A superficial assessment would indicate that, once emitted, TMO would have more time to disperse, leading to a less spatially concentrated build-up of harmful products such as O_3, HCHO, and other aldehydes.

3.4.3. Photochemical Ozone Creation Potential (POCP) of TMO

Given lack of experimental proves for a detailed chemical mechanism of reaction (R3.1) (TMO + OH), as it is often the case for uncommon, oxygenated compounds, the rate coefficient is the main data on which we can base our reasoning over the impact of TMO on air quality. Regarding the formation of secondary pollutants and in particular ozone formation, knowing TMO chemical structure and the rate coefficient $k_{3.1}$, an estimated POCP (POCP$_E$) for North-West European and USA urban atmospheric conditions can be calculated following the method formulated by Jenkin et al. (2017), as described in Section 1.6 (Eq. 1.9-1.13).

As TMO is an aliphatic VOC that does not absorb in the troposphere ($\lambda > 290$ nm), the calculations for POCP did not include parameter P, Q or R_{O_3}. Details on POCP calculation are provided in the Appendix. The results for TMO, respectively in Europe and USA, are 17.6 and 6.7. The same calculation carried out using $k_{3.1}$ predicted by SAR (9×10^{-12} cm^3 molecules^{-1} s^{-1}) leads to a much higher POCP$_E$ of 32.8 and 17.2. The bar chart displayed in Figure 3.18 shows the POCP$_E$ calculated for TMO, and the ones calculated for other common ethers (dimethyl ether, diethyl ether and di-isopropyl ether) and for toluene. It is interesting to notice how the

POCP$_E$ estimated for TMO is quite lower than other ethers, except for dimethyl ether, and it is less than half the POCP of toluene.
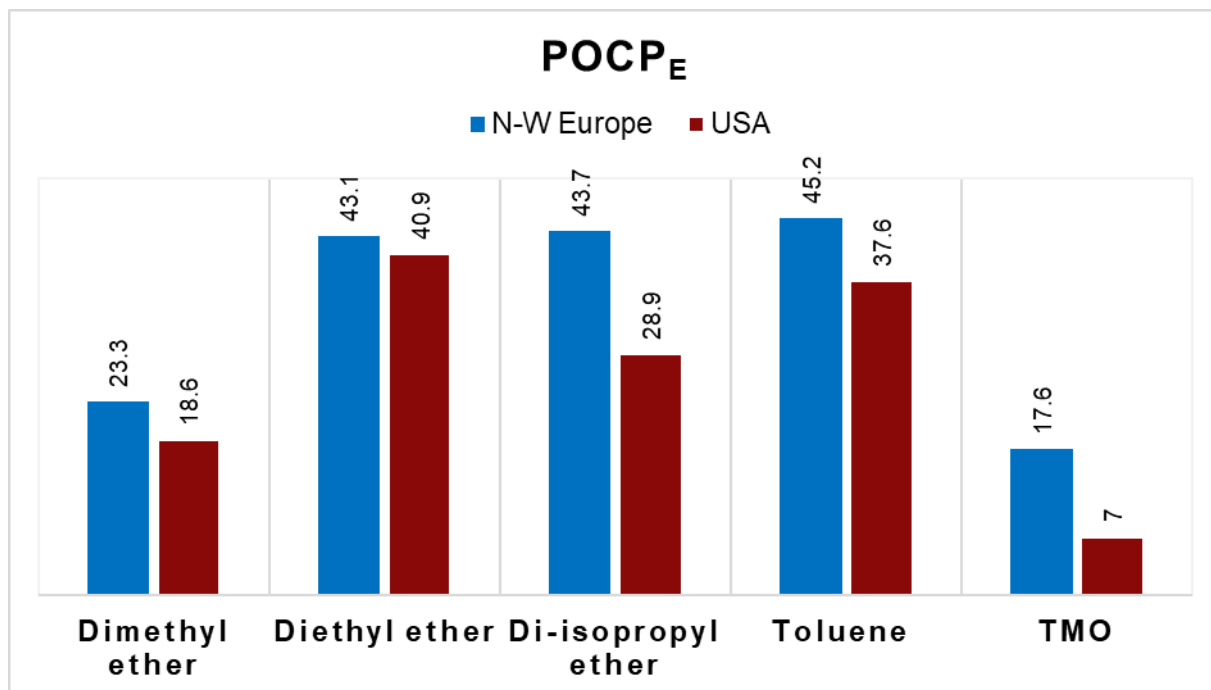
Figure 3. 18: Bar chart showing the POCP$_E$ values for dimethyl ether, diethyl ether, di-isopropyl ether, toluene and TMO for the atmospheric conditions of north-western Europe and urban USA.

3.5. Rate Coefficients of OH with 2-Metyloxolane and 2,5-Dimethyloxolane

The oxolanes 2-methyloxolane (2-MO) and 2,5-dimethyloxolane (2,5-DMO) are commercially available, and their reaction with OH or the isotopic equivalent OD (Fig. 3.19) has been reported previously (Andersen et al., 2016; Wallington et al., 1990) as discussed in section 3.1.
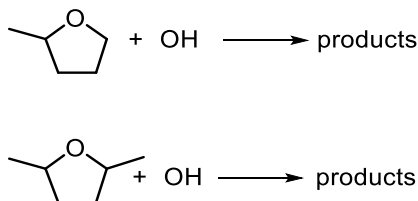
Figure 3. 19: Chemical structure of 2-MO (top) and 2,5-DMO (below) and reaction scheme for R3.6 and R3.4.

The reaction of 2-MO with OH (R3.6) was studied by Wallington et al. (1990) and the reaction with OD by Andersen et al. (2016), whereas reaction of 2,5-DMO with OH at the best of our knowledge doesn't have any records except for the reaction with the isotopic equivalent OD investigated by (Andersen et al., 2016). Reactions of 2-MO and 2,5-DMO (R3.6 and R3.4) were studied by PLP-LIF experiments in this work to complement the scarce literature data. The experiment procedure was the same described in section 3.2.1 and each measurement was repeated twice. The results are summarised in Table 3.8.

Table 3.8: Rate coefficients for the reactions of some oxolanes with OH determined via PLP-LIF at RT.

Reaction	T / K	p / Torr	OH precursor	n [a]	[VOC] [b]	$k(T)$ [c]
(R3.6)	298	59	H_2O_2	12	2-18	18.5 ± 0.7
(R3.6)	298	85	H_2O_2	9	2-14	18.9 ± 0.8
(R3.4)	294	55	H_2O_2	11	1-10	44 ± 3
(R3.4)	294	73	H_2O_2	13	1-10	46 ± 2

Notes: [a] n **is the number of different [VOC] used (not including [VOC] = 0);** [b] **= range of [VOC] in units of 10^{14} molecule cm^{-3} ;** [c] **= $k(T)$ in units of 10^{-12} cm^3 molecule^{-1} s^{-1}; bath gas M = N_2.**

The results for R3.6 bring to a weighted average value and standard error of $k_{3.6}$ (298 K) = $(18.7 \pm 0.1) \times 10^{-12}$ cm³ molecule^{-1} s^{-1}, that is in quite good agreement with literature data available. The consideration of the potential systematic errors that were estimated to be around 20%, leads to a more conservative value of:

$k_{3.6}$ (298 K) = $(19 \pm 4) \times 10^{-12}$ cm³ molecule^{-1} s^{-1}

Similarly, we obtained a rate constant for R3.4 equal to $k_{3.4}$ (298 K) = $(44.8 \pm 0.7) \times 10^{-12}$ cm³ molecule^{-1} s^{-1}, which including the systematic error brings to:

$k_{3.4}$ (294 K) = $(45 \pm 9) \times 10^{-12}$ cm³ molecule^{-1} s^{-1}

While the experimental results for $k_{3.6}$ (2-MO + OH) agree with literature data and SAR calculations, it is interesting to notice the striking difference between the experimental results and the SAR calculations for $k_{3.4}$ (2,5-DMO + OH). As opposed to what was observed for TMO, in this case SAR calculations seem to greatly underestimate the rate value, with a rate constant of around 19×10^{-12} cm³ molecule^{-1} s^{-1} instead of 45×10^{-12} cm³ molecule^{-1} s^{-1}.

Experimental rate coefficients, as discussed in section 3.4.2, can be used for the calculation of the lifetime of 2-MO and 2,5-DMO with respect to the reaction with OH. The lifetime resulting from a OH concentration of [OH] = 1×10^6 molecule cm^{-3} (Lelieveld et al., 2016) is $\tau_{3.6}$ = 13 hours for 2-MO and $\tau_{3.4}$ = 5 hours for 2,5-DMO. As follows from the values of the rate constants, 2-MO and 2,5-DMO presents a much shorter lifetime than TMO. The chemical feature accountable for this increase in reactivity seems to be the presence of more secondary and primary C-H and little or no steric hindrance. The overall lifetime for these two compounds may include also the other relevant degradation processes. Given the molecular structure of the oxolanes, these are mainly represented by the reaction with Cl atoms. The reaction of 2-MO and 2,5-DMO with Cl was investigated by Andersen et al. (2016), who found a rate constant of $k_{2\text{-}MO,Cl}$ (298 K) = $(2.65 \pm 0.43) \times 10^{-10}$ cm³ molecule^{-1} s^{-1} for 2-MO and $k_{2,5\text{-}TMO,Cl}$ (298 K) = $(2.84 \pm 0.34) \times 10^{-10}$ cm³ molecule^{-1} s^{-1} for 2,5-TMO. Frome these values, and high Cl concentrations ([Cl] = 1×10^4 molecule cm^{-3}) we can deduce a lifetime of 4 days for both 2-MO and 2,5-DMO. Accordingly, in conditions of high [Cl], the lifetime of 2-MO decreases to 11 hours whereas the one estimated for 2,5-DMO is largely unchanged.

The POCP$_E$ calculated for 2-MO and for 2,5-DMO as illustrated in section 3.2.6 was respectively POCP$_{E, 2\text{-}MO}$ = 49 and for 2,5-DMO POCP$_{E, 2,5\text{-}DMO}$ = 53 Again, also this indicator reflects the higher reactivity of 2-MO and 2,5-DMO compared to TMO, whose POCP$_E$ is estimated to be much lower.

3.6. Summary and Implications on Green Solvent Design

The kinetic study of TMO, 2-MO, and 2,5-DMO gave us insightful information on this class of methyl-substituted oxolanes. Starting from TMO, the most important concepts deduced from PLP-LIF experiments, RR experiments, QCC investigations and the comparison of these studies with SAR calculations can be summarised as below:

- o PLP-LIF and RR studies show complementary features and lead to a consistent value for the rate coefficient of TMO + OH.
- o Room temperature and temperature dependent kinetics studies showed large discrepancies with SAR calculations, pointing out the limits of the SAR for molecules with a certain degree of complexity.
- o QCC investigations gave more insights on the mechanism involved in the H-abstraction and are likely to explain the unpredictable behaviour of TMO.
- o The rate coefficients for R3.1 and R3.2 suggest a lifetime of 3 days for TMO, quite longer than the one estimated for toluene (2 days). In conditions of high [Cl], lifetime of TMO may decrease up to 2 days.
- o The $POCP_E$ calculated for TMO is 18, less than half the one estimated for toluene (45).

All these results not only provide valuable insights for the chemistry of oxolanes but also give a preliminary assessment of the impact of TMO on the air quality, especially when compared to impact of toluene, that is the traditional solvent TMO is likely to replace. Overall, these results suggest that use of TMO is likely to be less problematic than toluene in terms of impact on air quality. Moreover, considering all the other characteristics that make TMO an ideal candidate for a 'green' alternative to toluene, use of TMO may provide several advantages for a lower impact on the environment. Expanding the study to other methyl-substituted oxolanes provided more insightful results that were helpful to complete the picture. All the results for the rate coefficients were reported in the bar chart of Figure 3.20, whereas Figure 3.21 shows the lifetimes of the oxolanes expressed in hours and calculated from experimental results from this work, the literature data, and the SAR calculations. The $POCP_E$ (Jenkin et al., 2017) were calculated only for the oxolanes whose rate constants were experimentally determined and are summarised in the bar chart reported in Figure 3.22.

OH + oxolanes - k_{OH} (10^{-12} cm^3 molecule^{-1} s^{-1})
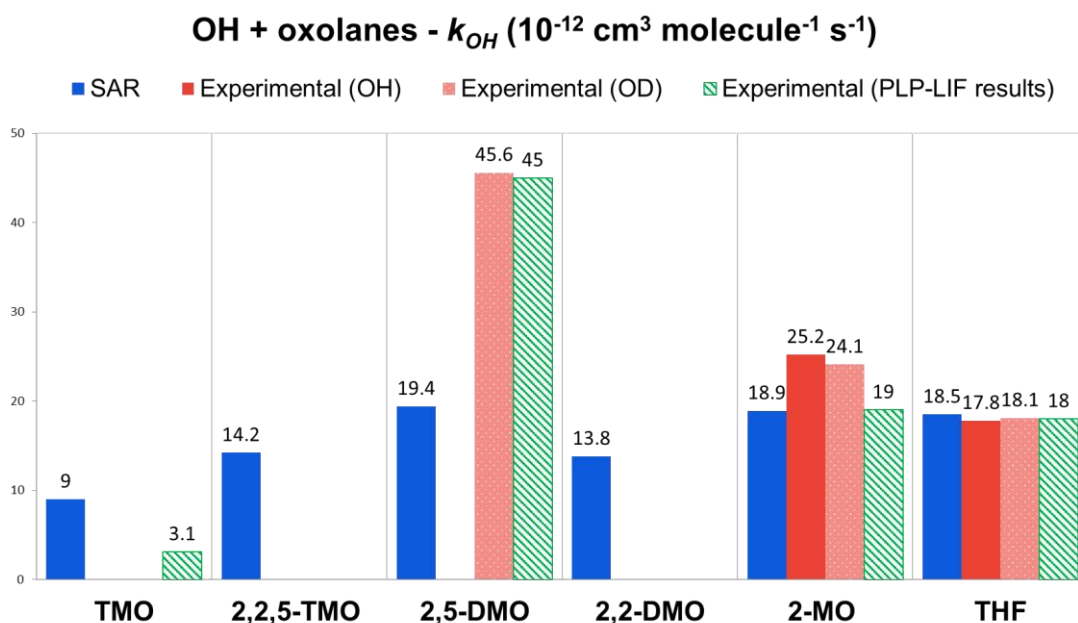
Figure 3. 20: Bar chart showing the rate coefficients for the reactions of the oxolanes with OH calculated via SAR (Jenkin et al., 2018) in blue; in red the rate coefficients from experimental results available in literature for the reaction with OH; in striped green the experimental results from this work; all data in units of 10^{-12} cm^3 molecule^{-1} s^{-1}.

Oxolanes Lifetme τ (hours)
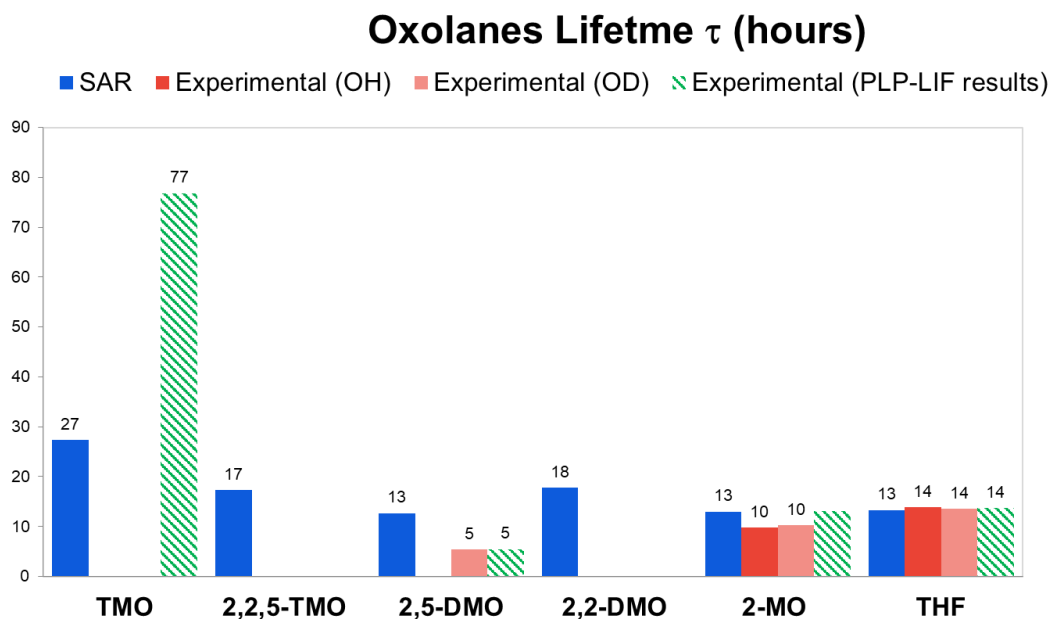
Figure 3. 21: Bar chart showing the lifetime of the oxolanes studied in this project, calculated from the rate coefficients for the reactions of the oxolanes with OH. In blue the lifetime estimated from the rate coefficient calculated via SAR (Jenkin et al., 2018); in red the lifetime from the rate coefficients from experimental results available in literature; in striped green the lifetime from the experimental results from this work; all lifetimes are in hours.
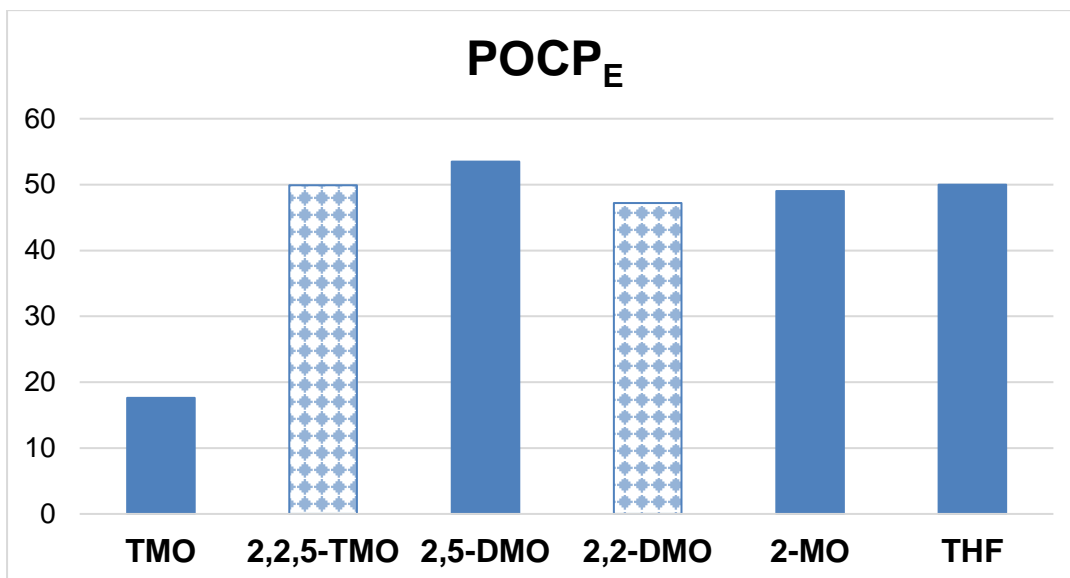
Figure 3. 22: Bar chart showing the POCP$_E$ calculated via Jenkin et al. (2017) method for the oxolanes with available experimental rate constants for the reaction with OH. Values for 2,2,5-TMO and 2,2-DMO (blue and white squares) were estimated using the rate coefficients for the reaction with OH calculated via the SAR method described above (Jenkin et al., 2018), in the lack of experimental values.

The interesting pattern deducible from the figures represented above is that the addition of methyl groups to the oxolane ring doesn't bring a regular contribution to the rate constant. There is no linearity between the reaction rate and the methyl group addition. On the contrary, for TMO the addition of CH_3 groups induce a decrease in reactivity. Observing the pattern from a different perspective, the chemical feature that seems to affect the most the reactivity is the presence of primary C-H, that explain the striking value of the rate constant for 2,5-DMO. This observation may lead to an interesting conclusion, suggesting that the design of TMO, lacking primary C-H bonds, shows a milder reactivity in air and a lighter impact on air quality. On the other hand, Figure 3.23 shows how the POCP$_E$, the pattern now justified with the presence of primary C-H seems to disappear, suggesting that secondary emissions chemistry may be less affected by this chemical feature. The study of 2,2-DMO and 2,2,5-TMO are the missing pieces that may bring more clarifications. In the lack of experimental results, POCP$_E$ values for these molecules were calculated using SAR rate coefficients (Jenkin et al., 2018), and confirm the trend variation compared to the rate coefficients. However, future works will be needed to confirm this result.

4. Atmospheric Chemistry of Methyl Pivalate and Pinacolone

Because of their low toxicity and simple production from biomass, the OVOC Pinacolone (3,3-dimethyl-2-butanone, $(CH_3)_3CC(O)CH_3$)), henceforth PCO, and Methyl Pivalate (methyl 2,2-dimethylpropanoate, $(CH_3)_3CC(O)OCH_3$)), henceforth MPA, have been identified by the Green Chemistry Centre of Excellence at the University of York as potential replacements for hazardous Volatile Non-Polar (VNP) solvents (see Section 1.2.5). A particularly problematic VNP is toluene, a molecule which poses significant human health and environmental hazards (Byrne et al., 2018) and that was classified as air pollutant of concern (Montero-Montoya et al., 2018; Zhang et al., 2019). Whilst the atmospheric chemistry of toluene is well known and the air quality impacts have been quantified, the atmospheric breakdown of PCO or of MPA has seldom been studied. No air quality consideration has been included in their selection as "green" solvents. In addition to any direct emission of PCO, the Master Chemical Mechanism (MCM) (Saunders et al., 2003; Jenkin et al., 1997) reports this compound as a product of the oxidation of 2,2-dimethylbutane and 3,3-dimethyl-2-butanol.

Once emitted, an important removal process for virtually all OVOCs, including PCO and MPA is reaction with the hydroxyl radical, OH, in the troposphere (Figure 4.1).

$$OH + (CH_3)_3CC(O)CH_3 \qquad \rightarrow \text{(products)} \qquad\qquad (R4.1)$$

$$OH + (CH_3)_3CC(O)OCH_3 \qquad \rightarrow \text{(products)} \qquad\qquad (R4.2)$$
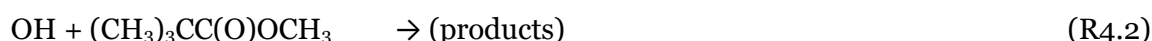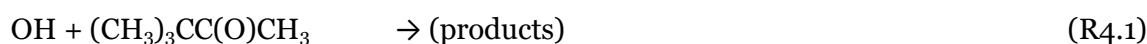
Hydrogen-atom abstraction can proceed from two sites on each of the molecules, as described in Figure 4.1.
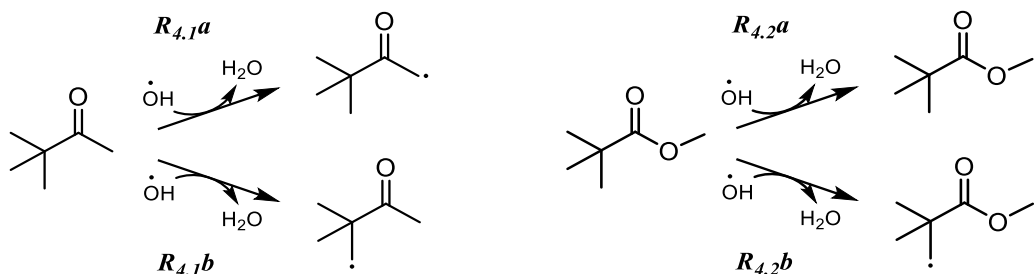
Figure 4. 1: Proposed pathways for the reaction of PCO with OH, where the H abstraction may proceed from the alfa C-H (R4.1a) or from the beta C-H (R4.1b), and for the reaction of Methyl Pivalate with OH, where the abstraction occurs on the C-H next to the ester oxygen (R4.2a) or alternatively from the beta C-H (R4.2b).

An alternative breakdown process for carbonyl containing OVOC in the atmosphere is photolysis (R4.3 and R4.4), where the C=O function may absorb abundant UV light at $\lambda >$ 290 nm via the n $\rightarrow$ π∗ electronic transition.

$$(CH_3)_3CC(O)CH_3 + h\nu \qquad \rightarrow \text{Products} \qquad\qquad (R4.3)$$

$$(CH_3)_3CC(O)OCH_3 + h\nu \qquad \rightarrow \text{Products} \qquad\qquad (R4.4)$$

The reactivity of PCO and MPA in the troposphere and their breakdown processes were investigated in this study. The results were subsequently published in Atmospheric Chemistry and Physics journal (ACP) (Mapelli et al., 2023) and described here in detail.

4.1. Previous Studies and SAR Calculations
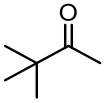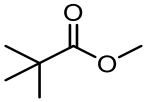
The ambient temperature rate coefficient of reaction R4.1 was measured by Wallington and Kurylo (1987a) in 1987 as $k_{4.1}$(296 K) = (1.21± 0.05) × 10^{-12} cm³ molecule⁻¹ s⁻¹. Together with data for other ketones, this parameter was used to explore a reactivity index for C-H bonds next to carbonyl groups. The study found that the reactivity of ketone aliphatic groups is independent and additive, with the partial rate coefficient of one β-CH$_3$ having an approximate value of 3.7 × 10^{-13} cm³ molecule⁻¹ s⁻¹. This result shows an increment of reactivity of β-CH$_3$ by a factor 3 compared to the α-position and compared to simple alkyl systems and it can be explained by a reaction mechanism alternative to the direct H-abstraction, that goes through the formation of a six-membered ring complex involving the coordination of the hydroxy radical to the carbonyl group.

MPA was previously considered as a (low ozone formation potential) solvent, prompting Wallington et al. (2001) to study R4.2 at 298 K, reporting $k_{4.2}$(298 K) = (1.20± 0.03) × 10^{-12} cm³ molecule⁻¹ s⁻¹, and over a range of temperatures (250-370 K), that resulted in a non-Arrhenius behaviour with a minimum reactivity reached at 298 K and a slight increase of reactivity below and above room temperature.

The Master Chemical Mechanism MCM v3.2 website (http://mcm.leeds.ac.uk/MCM) (Saunders et al., 2003; Jenkin et al., 1997) reports the reaction of PCO with OH (R4.1), indicating R4.1b as the main removal pathway, which involves the H abstraction from the β-CH$_3$, leading to the peroxide that can then undergo multiple routes.

SAR (Structure Activity Relationship, see section 1.5) calculations for R4.1 and R4.2 were in agreement with literature data (Table 4.1), and SAR product distribution was in accordance with the one observed by (Wallington and Kurylo, 1987a) and recommended by the MCM (Master Chemical Mechanism)(Jenkin et al., 2003; Saunders et al., 2003), which indicate R4.1b as the dominant route (Fig.4.1). However, the absence of any further $k_{4.1}$ or $k_{4.2}$ determinations in the literature is concerning, especially given that OH + OVOC reactions are notoriously complex, with several examples displaying non-Arrhenius kinetic behaviour at atmospherically relevant temperatures (Calvert et al., 2011b; Wollenhaupt et al., 2000). This paucity of data, together with the recent increase in interest around green solvents were prime motivations for this work.

Table 4.1: SAR calculations based on Jenkin et al. (2018) for R4.1 and R4.2.

Molecule	Group	k_x [a]	F_X [d]	F_Y [d]	F_Z [d]	F_{RING} [e]	k_{CHx} [a]	n [b]	$\%k$ [c]	k [a]
PCO	α-CH_3	0.13	1	-	-	-	0.13	1	9	1.46
	β-CH_3	0.13	3.4	-	-	-	1.33	3	91	
MPA	α-CH_3	0.13	2.2	-	-	-	0.29	1	21	1.34
	β-CH_3	0.13	2.7	-	-	-	1.05	3	79	

Notes: [a] Units are in 10^{-12} cm^3 molecule^{-1} s^{-1}. [b] n = number of equivalent groups. [c] Percentage distribution for the partial rate coefficients. [d] F_x, F_y, and F_z are the substituent factor for the neighbour groups x, y and z respectively. [e] F_{RING} is the ring factor that accounts for the ring strain.

In addition, scarce knowledge of the role of photodecomposition as a removal path for PCO was also an important aspect of the study. PCO is known to have an absorption maximum at 278 nm (Pocker et al., 1988) though quantitative absorption cross sections were to date unknown. In the absence of quantitative cross-sections or quantum yields, the state-of-science MCM represents photolysis of PCO via parameters reported for methyl ethyl ketone (MEK, $CH_3C(O)C_2H_6$) (R4.5) and represents PCO photodissociation going to $(CH_3)_3C$ + CH_3CO in the troposphere.

$$CH_3C(O)C_2H_6 + h\nu \quad \rightarrow \text{Products} \quad\quad\quad\quad (R4.5)$$

By contrast, the UV absorption spectrum of MPA was reported by Wallington et al. (2001), who measured an absorption maximum at around 210 nm and concluded that the molecule does not undergo photolysis (R4.4) in the troposphere ($\lambda > 290$).

This work aims to improve our knowledge of the atmospheric chemistry of PCO and MPA, two promising green solvents. Rate coefficients for reaction with OH were reported, together with absorption cross sections for PCO obtained in lab-based experiments. These latter parameters were complemented by data obtained via in-silico computational experiments conducted by Basile Curchod and Daniel Hollas at the University of Bristol. These fundamental photochemical parameters were used to obtain estimates for PCO and MPA tropospheric lifetimes. Finally, photochemical ozone production potentials POCP were estimated, allowing for air quality assessments to play a role in any recommendation of these molecules as green solvents.

4.2. Rate Coefficient of OH and PCO (R4.1)

The absolute rate study of the reaction of PCO with OH was conducted by the PLP-LIF method described in Section 2.1, with the help of MChem students Úna Hogan and James Donnelly. The use of moderate laser fluences (see section 2.1.4) was important in this kind of experiments, as PCO absorbs UV light at 266 nm (see section 1.3.3). Using a cross-section determined in this work of σ(266 nm) = 5.33×10^{-20} cm^2 molecule^{-1}, we calculate that < 0.1% of PCO could be converted to highly reactive species in the laser flash. This calculation used an (unknown) quantum yield of unity and thus represents an upper-limit. The effect of direct PCO photolysis on these results was therefore predicted to be insignificant. However, the

potential impact of PCO photolysis was assessed via experiments where the 266 nm laser fluence was changed by a factor of three (by adjusting the Q-switch delay) and no significant change was recorded in the determination of B (Eq. 3.5). Figure 4.2 shows a typical pseudo-first order exponential decay, where PCO concentration was more than 10^3 times larger than the OH radical concentration. The linear plot on the top-right of Figure 4.2 shows the 12 pseudo-first order rate constants recorded, plotted against concentrations of PCO at a temperature of 460 K, with a slope equal to the second order rate constant $k_{4.1}$.
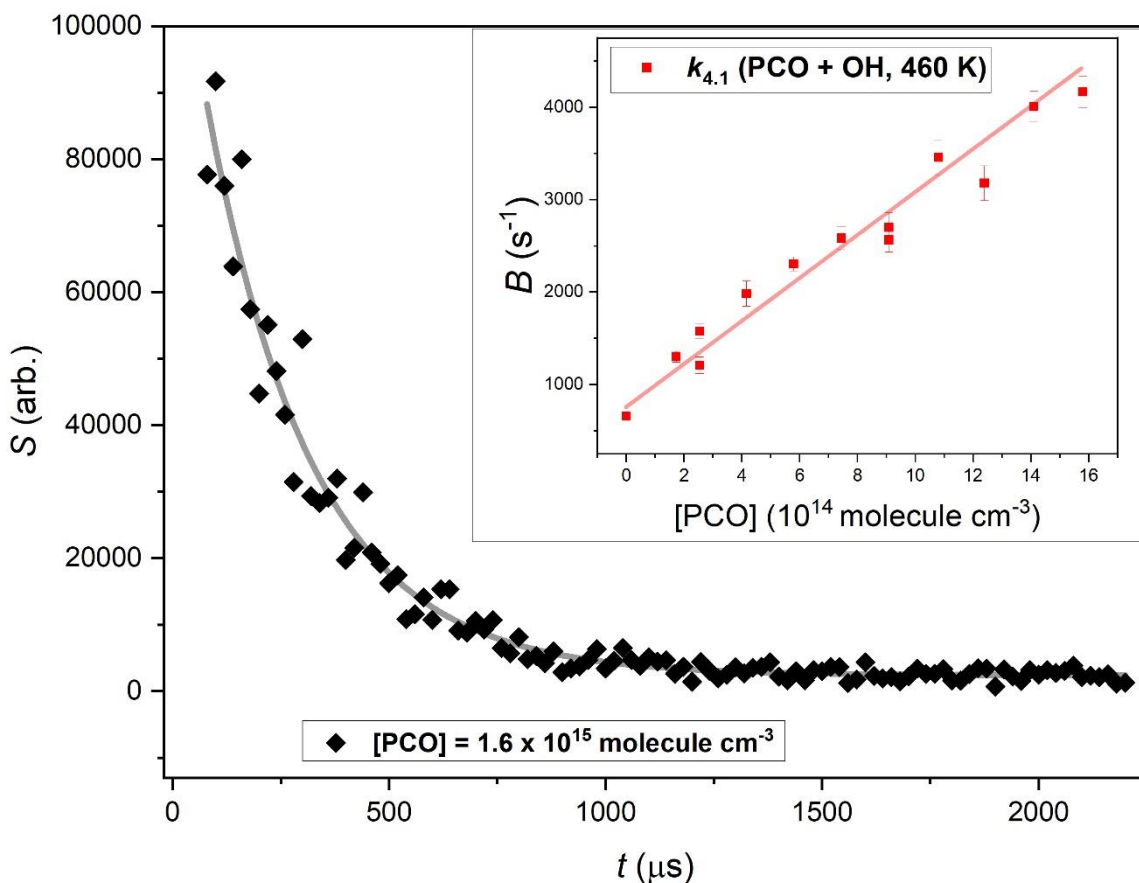
Figure 4. 2: Exemplary exponential decay of OH in the presence of excess $[(CH_3)_3CC(O)CH_3]$ = 1.6×10^{15} molecule cm^{-3}, fit with (Eq.2.25) to yield pseudo first-order rate coefficient B = (4090 ± 153) s^{-1}. Inset shows bimolecular plot used to determine $k_{4.1}$(460 K) = (2.3 ± 0.1) × 10^{-12} cm^3 molecule^{-1} s^{-1}.

After running the experiment at different pressures (30-70 Torr), in air and in N$_2$, making sure the reaction was not pressure dependant nor affected by the presence of oxygen, we measured the rate coefficient of the PCO breakdown reaction at room temperature and estimated a weighted average and standard error of

$k_{4.1}$ (296 K) = (1.23 ± 0.07) × 10^{-12} cm^3 molecule^{-1} s^{-1}

a value that is in excellent agreement with the solitary literature rate constant of $k_{4.1}$(296 K) = (1.21 ± 0.05) × 10^{-12} cm^3 molecule^{-1} s^{-1} (Wallington and Kurylo, 1987a). This uncertainty represents only the standard error, whereas a more conservative value, including potential systematic errors mainly coming from the estimation of the concentration, would include an uncertainty of 15% and a rate coefficient equal to $k_{4.1}$(296 K) = (1.2 ± 0.2) × 10^{-12} cm^3 molecule^{-1} s^{-1}. To further investigate the mechanism suggested by Wallington and Kurylo (1987a), the reaction was then studied within the temperature range of 292-485 K and the results were

summarised in Table 4.2, where second order rate constants with 1σ statistical errors were displayed.

Table 4.2 – absolute determinations of $k_{4.1}$ from this work

Reaction	*T* (K)	*P* (Torr) [a]	[OVOC] [c]	*n* [d]	*k* ± SE [e]
(R4.1)	297	46	11-112	10	1.06 ± 0.06
(R4.1)	297	46[b]	5.2-92	10	1.31 ± 0.06
(R4.1)	298	47	11.0-60	14	1.33 ± 0.06
(R4.1)	341	60	2.3-21	12	1.39 ± 0.11
(R4.1)	343	52	1.3-20	12	1.63 ± 0.15
(R4.1)	343	52	1.3-20	12	1.5 ± 0.10
(R4.1)	372	61	2.4-37.9	15	1.76 ± 0.09
(R4.1)	400	68	2.6- 28.4	12	1.82 ± 0.10
(R4.1)	424	63	2.4-22.5	12	1.59 ± 0.06
(R4.1)	424	63[b]	2.4-22.5	12	1.8 ± 0.05
(R4.1)	460	68	2.0-22.5	12	2.40 ± 0.11
(R4.1)	462	52	1.7-16	12	2.33 ± 0.13
(R4.1)	485	68	1.9-21	11	2.75 ± 0.14

Notes: [a] = pressure of N_2 bath gas except [b] = air bath gas; [c] = units for [OVOC] were 10^{14} molecule cm^{-3}; [d] = number of different [OVOC] in bimolecular plot; [e] = k values in units of 10^{-12} cm^3 molecule^{-1} s^{-1} ± standard error.

Also displayed in Figure 4.3 were results from this work on the well-characterised reaction between ethanol and OH (R4.6), which were obtained in back-to-back experiments alongside those for R4.1 and were listed in Table 4.3. The satisfactory agreement between the $k_{5.6}(T)$ determinations here and the extensive literature dataset (Dillon et al., 2005; Carr et al., 2008; Wallington and Kurylo, 1987b; Hess and Tully, 1988; Jiménez et al., 2003) lend more confidence to the results for $k_{4.1}(T)$ from this work.

$$CH_3CH_2OH + OH \quad \rightarrow products \hspace{5cm} (R4.6)$$

Table 4.3 – absolute determinations of $k_{4.6}$ from this work

Reaction	*T* (K)	*P* (Torr) [a]	[OVOC] [c]	*n* [d]	*k* ± SE [e]
(R4.6)	295	57	2.3-32.7	15	3.12 ± 0.11
(R4.6)	297	49	4.8-29.4	8	3.2 ± 0.2
(R4.6)	297	49	4.8-29.4	8	3.0 ± 0.2
(R4.6)	345	71	3.3-23.4	10	3.66 ± 0.11
(R4.6)	408	70	2.8-16.1	12	4.04 ± 0.14
(R4.6)	447	70	2.5-15	10	4.48 ± 0.11

Notes: [a] = pressure of N_2 bath gas except [b] = air bath gas; [c] = units for [OVOC] were 10^{14} molecule cm^{-3}; [d] = number of different [OVOC] in bimolecular plot; [e] = k values in units of 10^{-12} cm^3 molecule^{-1} s^{-1} ± standard error.

The Arrhenius plot (Figure 4.3) for the reaction of PCO with OH shows an approximatively linear behaviour within the range of temperature investigated in this work (292-845 K), best described by a 2-parameter Arrhenius equation. Interestingly, this was not what was expected from SAR, as the Arrhenius plot built from Jenkin et al. (2018) calculations (red solid line in Fig. 4.3) suggests the opposite trend, with a non-Arrhenius slope within the recommended temperature range (253-372 K). Most probably, the SAR method fails to predict the behaviour at T > 295 K, where there might a change of mechanism from the six-membered ring complex to the direct hydrogen abstraction. Further investigations at lower temperatures would clarify the molecule behaviour below 292 K and the possible change in the mechanism.
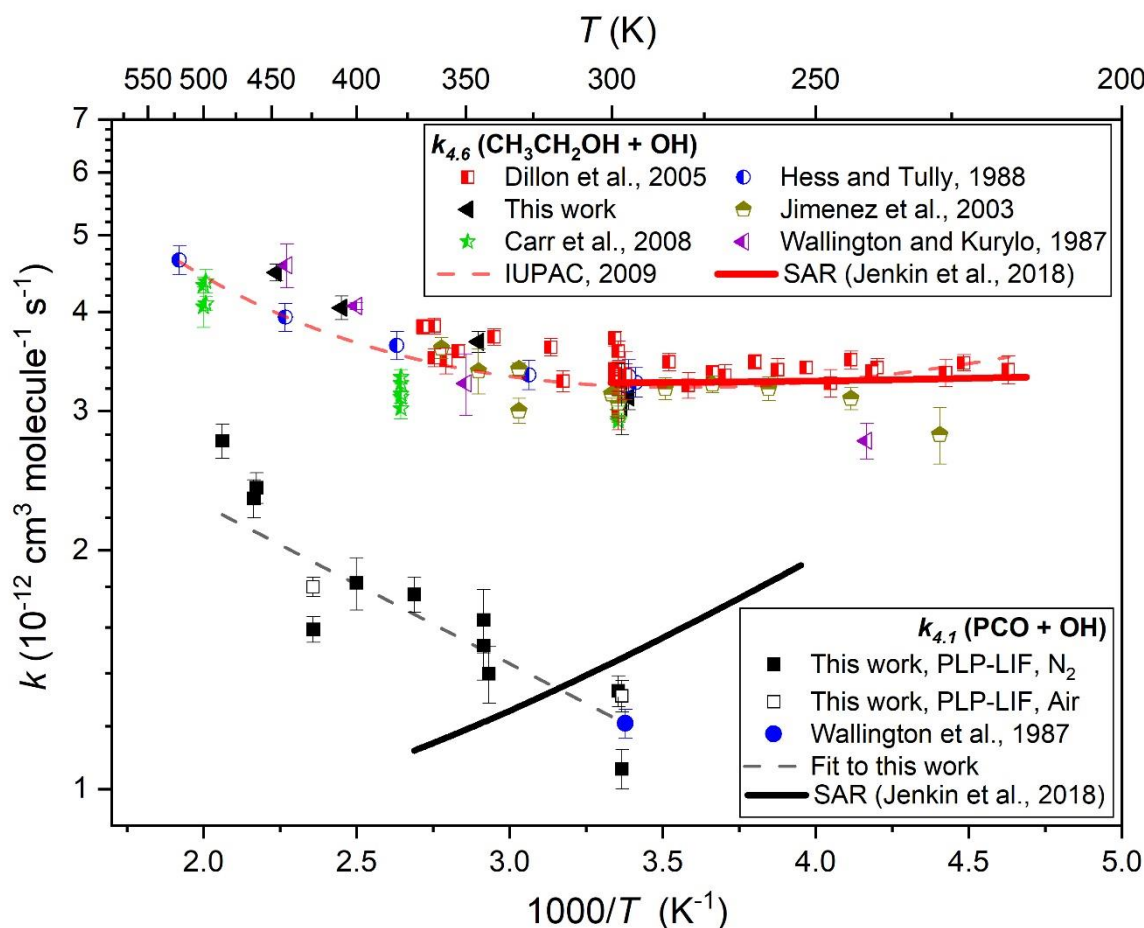
Figure 4. 3: Arrhenius plot for the reaction of PCO with OH: filled black square datapoints represent $k_{4.1}(T)$ determinations from this work using N_2 bath gas; open black squares using air; the filled blue circle indicates the solitary literature data point from Wallington and Kurylo (1987a); the solid black line represents $k_{4.1}(T)$ from the SAR proposed by Jenkin et al. (2018) and the red line is $k_{4.6}(T)$ again calculated from the same SAR method. Also displayed are $k_{4.6}(T)$ from this work (black triangles) and from literature (Dillon et al., 2005; Hess and Tully, 1989; Carr et al., 2008; Wallington and Kurylo, 1987b; Jiménez et al., 2003) and the IUPAC evaluation (Atkinson et al., 2006) leading to the three-parameter expression $k_{4.6}(T) = 6.70 \times 10^{-18}\ T^2 \exp(511/T)\ cm^3\ molecule^{-1}\ s^{-1}$, here represented with a red dashed line.

4.3. Rate Coefficient of OH and MPA (R4.2)

A set of experiments similar to the one carried out to determine $k_{4.1}$ was also used to $k_{4.2}$(296 - 485 K), results from which were presented in Table 4.3 and depicted in Arrhenius format on Figure 4.4. Again, many such experiments were conducted back-to-back with equivalent $k_{5.6}$ determinations (see section above). Control experiments were conducted at different pressures and in both N_2 and air bath gas to ensure the reactivity was not affected by these factors. A weighted mean of the three, room temperature determinations led to a value of

$k_{4.2}$(296 K) = (1.32 ± 0.01) × 10^{-12} cm^3 molecule^{-1} s^{-1}

Considering the estimated potential systematic uncertainties, notably in $[(CH_3)_3CC(O)OCH_3]$, which suggest a more conservative value of $k_{4.2}$(296 K) = (1.3 ± 0.3) × 10^{-12} cm^3 molecule^{-1} s^{-1}, this result essentially agrees with the literature rate coefficient of (1.20 ± 0.03) × 10^{-12} cm^3 molecule^{-1} s^{-1} (Wallington et al., 2001).

Table 4.3 – absolute determinations of $k_{4.2}$ from this work

Reaction	*T* (K)	*P* (Torr) [a]	[OVOC] [c]	*n* [d]	*k* ± SE [e]
(R4.2)	295	61.5	2.0-18	10	1.35 ± 0.13
(R4.2)	297	80	3.5-45	13	1.29 ± 0.04
(R4.2)	297	108	4.6-35	16	1.34 ± 0.06
(R4.2)	297	80 [b]	3.5-45	13	1.29 ± 0.03
(R4.2)	340	59	1.8-16	17	1.15 ± 0.08
(R4.2)	372	61	3.3-25	15	1.60 ± 0.06
(R4.2)	400	68	1.7-18.4	12	1.72 ± 0.10
(R4.2)	424	63 [b]	1.3-20	15	1.47 ± 0.05
(R4.2)	424	63	1.3-17	15	1.63 ± 0.06
(R4.2)	460	52	1.4-12	12	2.1 ± 0.2
(R4.2)	485	69	1.4-15.5	12	2.32 ± 0.14

Notes: [a] = pressure of N_2 bath gas except [b] = air bath gas; [c] = units for [OVOC] were 10^{14} molecule cm^{-3}; [d] = number of different [OVOC] in bimolecular plot; [e] = k values in units of 10^{-12} cm^3 molecule^{-1} s^{-1} ± standard error.
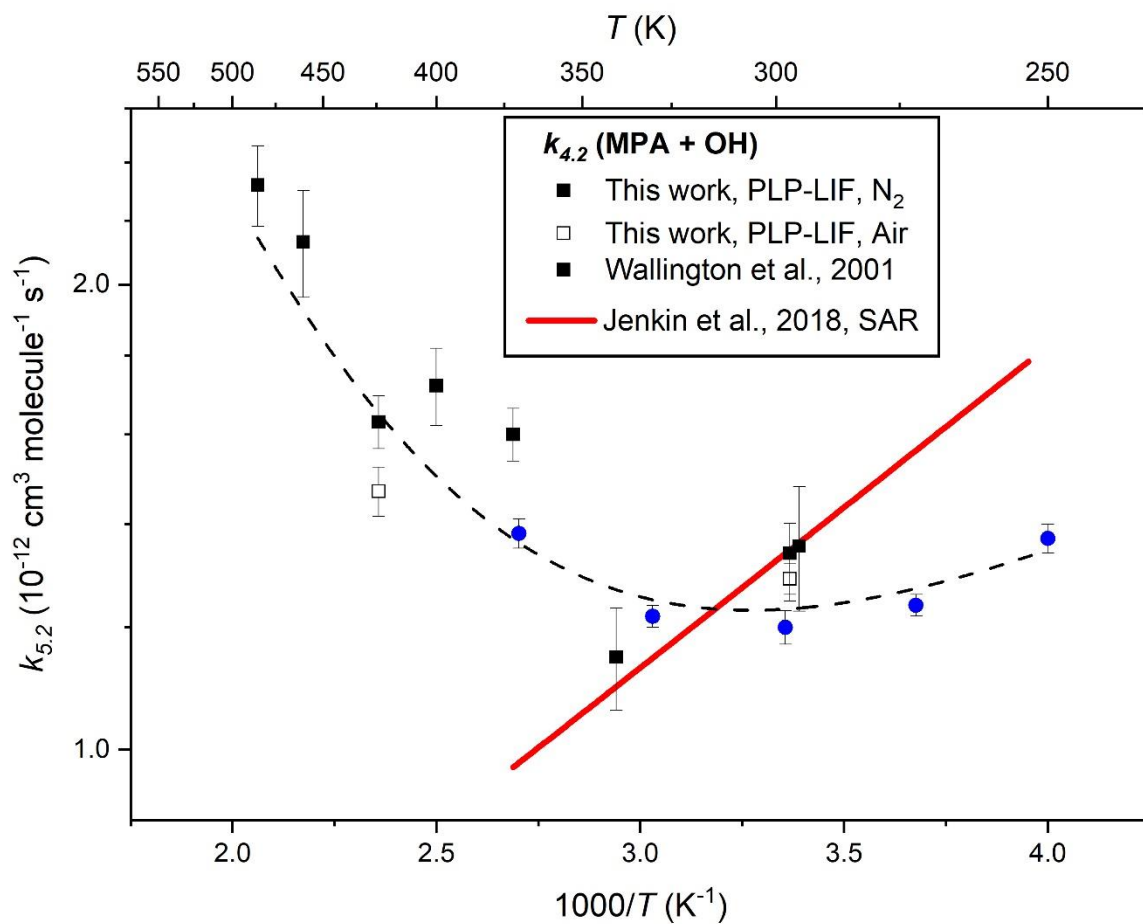
Figure 4. 4: Arrhenius plot for the reaction of MPA with OH (R4.2): filled black square datapoints represent $k_{4.2}(T)$ determinations from this work using N_2 bath gas; open black squares using air; the filled blue circles indicate literature data from Wallington et al. (1987); the black dashed line represents a fit to all experimental data to yield $k_{4.2}(T) = 5.0 \times 10^{-11}$ exp(-1743/T) + 4.3 $\times 10^{-13}$ exp(276/T). The solid red line represents $k_{4.2}(T)$ calculated from the SAR proposed by (Jenkin et al., 2018).

As is evident from Figure 4.4, results from this work confirmed the unusual non-Arrhenius behaviour found by Wallington et al. (2001), revealing a slight slope above 350 K. Such non-Arrhenius behaviour may be indicative of a change in the mechanism, with direct hydrogen abstraction dominating at high temperatures, whilst hydrogen bonded pre-reaction complexes play an important role at lower temperatures. A similar trend was observed for reactions of OH with other oxygenated compounds and seems to be typical of the carbonyl function (Wollenhaupt et al., 2000; Vasvári et al., 2001), which can interact with the OH radical through a H-bond complex. This complex acquires a 7-member ring structure in the case of H-abstraction from α C-H bonds, as shown in Fig. 4.5.

94
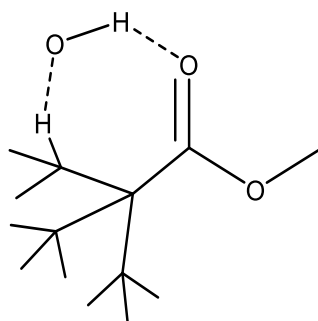
Figure 4. 5: 5-member ring complex forming during the interaction of OH with α C-H bonds.

4.4. Estimation of PCO Photolysis Rate Coefficient (*j*)

As anticipated in section 4.1, photolysis may play an important role in the decomposition of PCO and should be negligible for MPA. The forbidden $n \rightarrow \pi^*$ transition typical of ketones (see Section 1.3.3), is responsible for the UV-rays absorption in the troposphere by this class of molecules and can bring to photolysis and decomposition. To investigate the importance of this phenomenon, the absorption cross sections of PCO were studied in the spectral range of interest via UV-visible spectroscopy with the help of MChem student Abbie Robinson, and the results were compared with the available literature data (Section 4.4.1). Cross section measurements were then used for an approximate estimation of the photolysis rate coefficients (section 4.4.2).

4.4.1. UV-visible Study of PCO Absorption Cross Sections

Previous UV-visible spectra of PCO over the wavelength range of interest were not available, except for the absorption maximum recorded for PCO in water (Pocker et al., 1988) and in cyclohexane (Chimichi and Mealli, 1992) at 278 nm and 287 nm respectively. On the other hand, MEK has been intensively studied and numerous spectra were available in literature. Figure 4.6 displays some of the most relevant ones recorded in the gas-phase. The spectrum recorded by Martinez et al. (1992) is the one recommended by IUPAC (Atkinson et al., 2006) and was also confirmed by Brewer et al. (2019) in more recent studies.
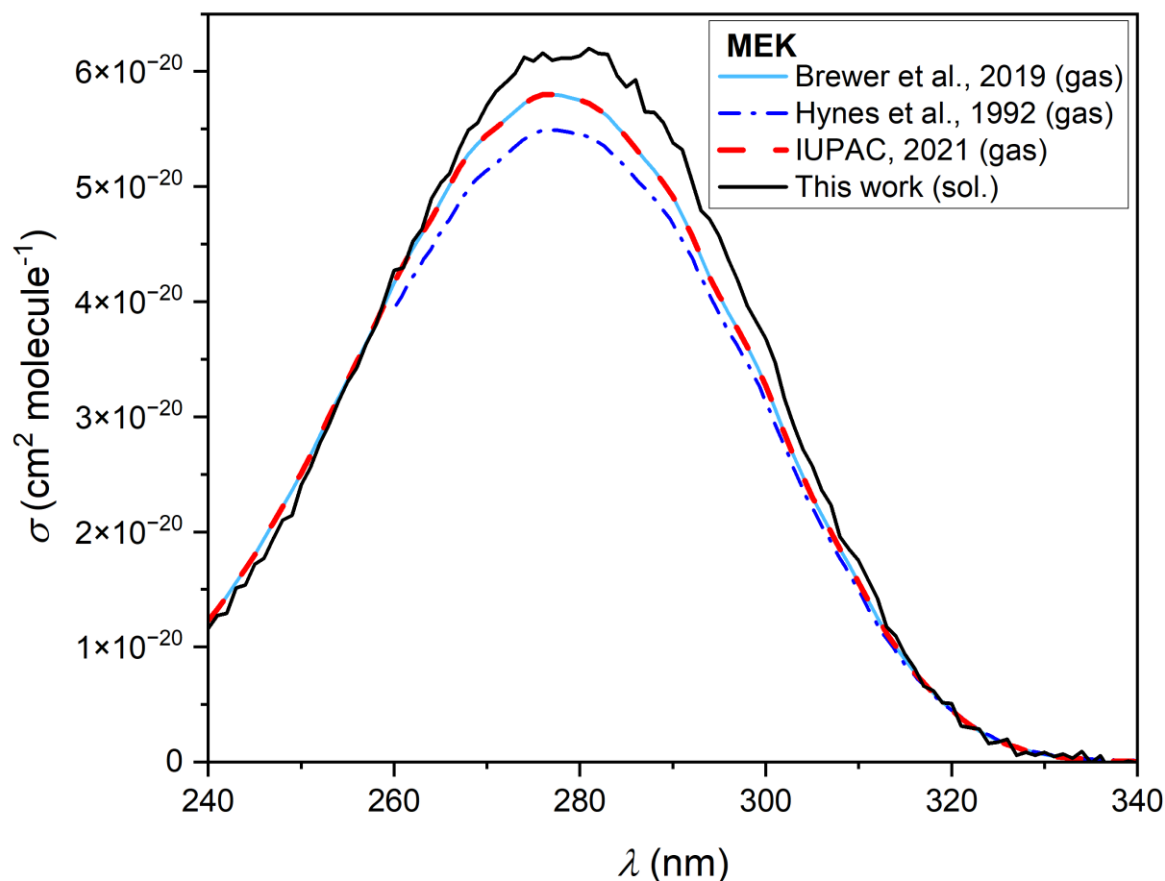
Figure 4. 6: Gas phase spectra of MEK recommended by IUPAC recorded by Martinez et al. (1992) (red dashed line), by Hynes et al. (1992) (dark blue dash-dotted line) and by Brewer et al. (2019) (light blue solid lines), together with the spectrum recorded in this work (black solid line) in cyclohexane solution.

Section 2.3 describes the method used in this study for the determination of the UV-visible spectra and the cross sections of PCO and MPA. In the lack of instrumentation for the gas-phase study, spectra were recorded in solution phase. That such dilute, solution phase spectra can yield useful results is demonstrated by equivalent spectra for MEK. Cross-section values similarly obtained in this work, dilute in cyclohexane were displayed on Fig. 4.7 alongside the gas-phase spectrum reported by Martinez et al. (1992) recommended by IUPAC (Atkinson et al., 2006).

The96oluteion phase determinations consistently overestimate reported gas phase values (e.g. at maximum value, $\sigma_{4.5(278\,nm)} = 6.2 \times 10^{-20}$ cm² molecule^{-1} from this work vs. $\sigma_{4.5(278\,nm)} = 5.8 \times 10^{-20}$ cm² molecule^{-1} in the gas phase). Whilst this was within the uncertainty estimated for this work (around 10%), observing the spectra over at least three repeats from different solutions the overestimation appears to be systematic and was also identified *in silico* by Basile Curchod and Daniel Hollas at the University of Bristol (Mapelli et al., 2023) ('theory' spectra in Fig. 4.7). A ratio of 0.93:1 between the integrated gas phase spectrum by Martinez et al. (1992) and the one recorded in solution in this work was estimated in the spectral range 300-330 nm. A similar ratio of 0.86:1 was estimated *in silico* (Mapelli et al., 2023).

The insert to Fig. 4.7 displays Beer-Lambert plots for data recorded in this work at 290 nm, yielding the molar absorption coefficients $\varepsilon_{4.3(290\,nm)} = (20.6 \pm 0.2)$ cm^{-1} M^{-1} for PCO and $\varepsilon_{4.5(290\,nm)} = (16.4 \pm 0.2)$ cm^{-1} M^{-1} for MEK. These coefficients can then be converted to the absorption cross sections, leading to $\sigma_{4.3(290nm)} = (8.0 \pm 0.8) \times 10^{-20}$ cm² molecule^{-1} for PCO and $\sigma_{4.5(290nm)}$

= $(6.0 \pm 0.6) \times 10^{-20}$ cm^2 molecule^{-1} for MEK. The UV spectra of PCO determined in this work were clearly characterised by larger cross sections in the actinic region (see Fig.4.7) and by a significantly red-shifted local maximum in absorption (286 nm vs. 278 nm) when compared to MEK. These observations will therefore have significant implications when revising estimates for photolysis rates of PCO, as more light is available at longer wavelengths (below). In accord with previous observations, UV-vis. spectra recorded for MPA showed no absorption over the wavelength range of interest, $290 < \lambda$ / nm < 370.
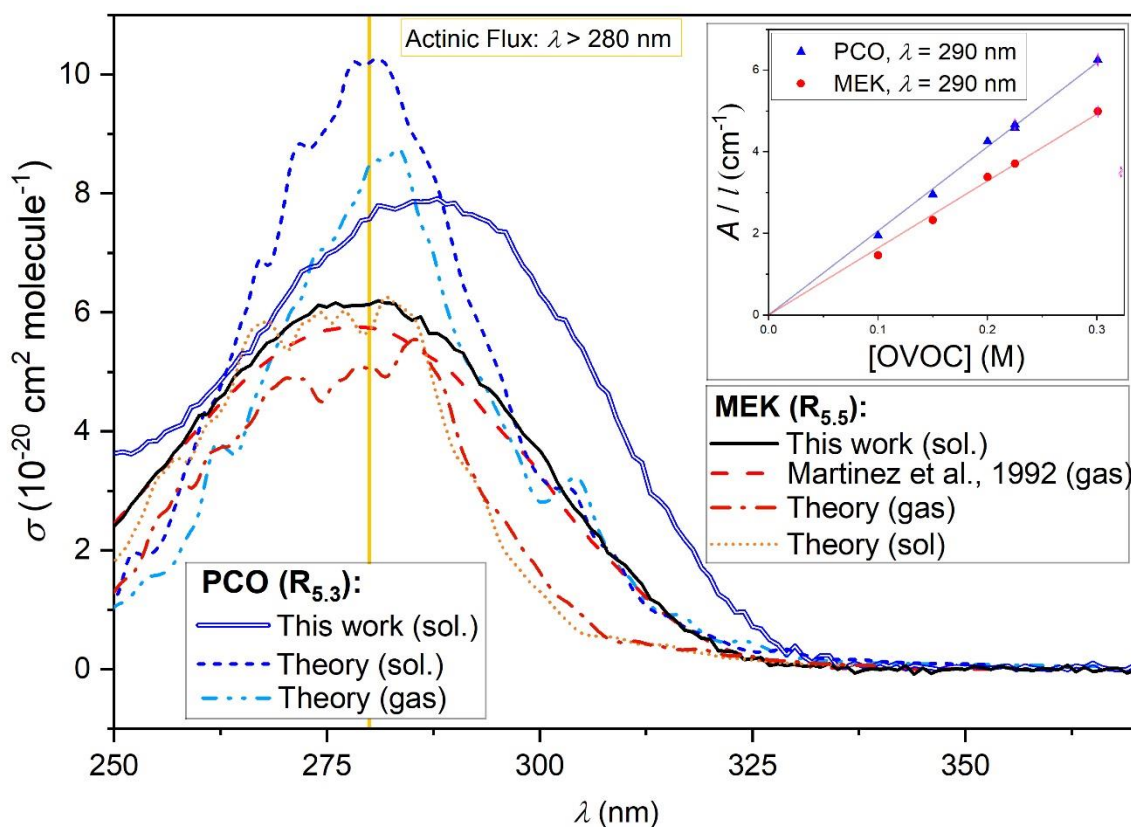
Figure 4. 7: Solution phase spectra of MEK (black line) and PCO (blue line) obtained dilute in cyclohexane in this work, alongside gas-phase spectrum of MEK (red dashed line) recorded by Martinez et al. (1992) and recommended by IUPAC. Calculated gas-phase spectrum of MEK (orange dot-dashed line), calculated spectra of PCO for the gas-phase (light blue dot-dashed line) and the solution-phase (dotted dark blue line)(Mapelli et al., 2023). The vertical line indicates the minimum wavelength for the actinic flux. The insert (top-right) displays Beer-Lambert plots obtained at 290 nm in this work, yielding a molar absorption coefficient $\varepsilon_{4.3(290 \, nm)} = (20.6 \pm 0.2)$ cm^{-1} M^{-1} for PCO and $\varepsilon_{4.5(290 \, nm)} = (16.4 \pm 0.2)$ cm^{-1} M^{-1} for MEK.

4.4.2. Estimation of photolysis rate coefficients (*j* values)

Having measured the absorption cross section of PCO, the photolysis rate can then be estimated according to Equation 1.5, which describes *j*, the first order photolysis rate coefficient, as a function of φ, the quantum yield, σ, the absorption cross section, and the actinic flux *F*. As for many other organic compounds, quantum yields for PCO are unknown, and the MCM uses MEK as a surrogate with reasonably established photochemistry. Accordingly, the photolysis rate was calculated using $\varphi = 0.16$, the quantum yield determined by Pinho et al. (2005) for the wavelength range 275 to 380 nm. This value is different than that recommended by IUPAC of $\varphi = 0.34$ (Atkinson et al., 2006; Raber and Moortgat, 1995),

with the value from Pinho et al. (2005) optimised with environmental chamber data. Also Romero et al. (2005) reported quantum yields lower than the one estimated by Raber and Moortgat (1995), and their work stress out the importance of investigating the temperature dependence and the spectral distribution of quantum yields to avoid overestimation. In this work photolysis rates were also calculated using the parameterized $\varphi\,(\lambda, [M], T)$ formulated by Romero et al. (2005), and the results showed an increment of a factor 1.2 when compared to the j-values determined using $\varphi = 0.16$.

The actinic flux used for the estimation of j values was obtained using the NCAR Tropospheric Ultraviolet and Visible (TUV) Radiation Model (Madronich and Flocke, 1997), with a solar zenith angle of 60° and an O_3 column of 350 DU (Dobson Units) (altitude 0 Km, albedo 0.1). The integrated photolysis rate coefficients were calculated via Eq.1.5 for MEK and PCO using the $\sigma(\lambda)$ values determined experimentally (UV-vis. experiments in cyclohexane solution) and the gas-phase $\sigma(\lambda)$ values available in literature in the case of MEK. An 'estimated gas' j-value was also calculated for PCO ($j_{4.3}$)

The results listed in Table 4.4 show how the photolysis rates calculated via different methods discussed above were quite similar and comparable to each other, and how the higher intensities of the absorption cross sections observed in the solution phase do not significantly affect the final j values when compared to the gas phase. In fact, looking at the MEK results, if the $\sigma(\lambda)$ suggests a lower j value for the gas phase, the results indicate the opposite, with $j_{4.5}$ (gas) = 0.9×10^{-6} s^{-1} in the gas phase and $j_{4.5}$ (sol.) = 0.8×10^{-6} s^{-1} for the solution phase. This unexpected difference depends on the fact that calculation of j is extremely sensitive to $\sigma(\lambda)$ in the wavelength range where the solar flux is more powerful ($\lambda > 320$ nm), and loose importance at shorter wavelengths. Accordingly, just a slight difference at the tail and baseline of the UV-vis. spectra at longer wavelengths, due to different methods used in recording the spectra, can affect the j value more than a substantial difference of absorption intensities at shorter wavelengths. However, such small differences in the photolysis rates reported in Table 4.4 indicate that j values determined from solution phase $\sigma(\lambda)$ were not far from the gas phase j estimated with the same method and can therefore be used as a good approximation. The values estimated for $j_{4.5}$ (gas) and $j_{4.5}$ (sol.) were also in reasonable agreement with the $j_{4.5} = 1.3 \times 10^{-6}$ s^{-1} calculated according to the MCM parameterisation at a similar zenith angle (Saunders et al., 2003).
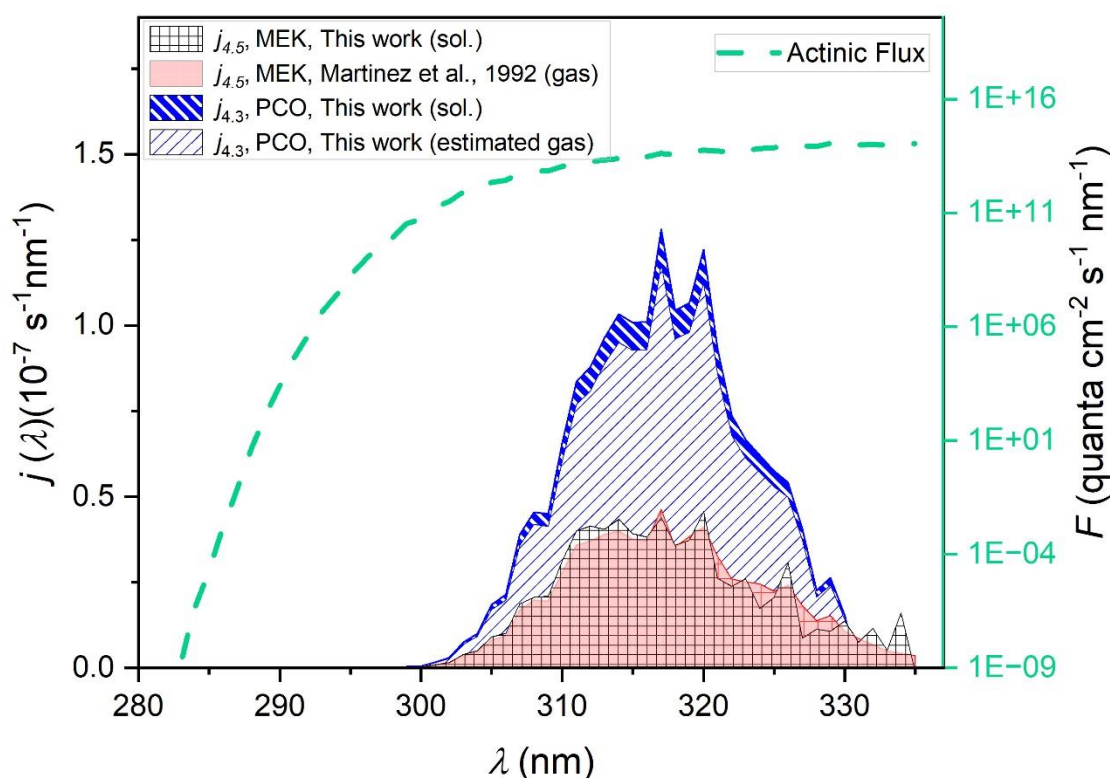
Figure 4. 8: *j*-values for the photodissociation of PCO (R$_{4.3}$) and MEK (R$_{4.5}$). calculated via Eq.1.5. An actinic flux (the green dashed line), for conditions of ϑ = 60° and 350 DU from the NCAR (TUV) Radiation Model, together with φ (275 − 380 nm) = 0.16 was used for all (Eq. 1.5) *j*-value calculations. The blue-fill striped area represents the $j_{4.3}(\lambda)$ estimated using $\sigma_{4.3}(\lambda)$ values determined in solution phase via UV-vis. experiments, the white, blue-striped area derives from use of the same $\sigma_{4.3}(\lambda)$ values recorded in solution, having applied the scaling factor of 0.93 to best reproduce gas-phase $\sigma_{4.3}(\lambda)$ values (section 5.4.1). Also displayed are $j_{4.5}(\lambda)$ for photolysis of MEK (R$_{4.5}$) calculated using $\sigma_{4.5}(\lambda)$ from the gas-phase spectrum of Martinez et al. (1992) (red squares area) and the $j_{4.5}(\lambda)$ estimated from the $\sigma_{4.5}(\lambda)$ values recorded via UV-vis. experiments in cyclohexane solution.

Table 4.4 − *j*-values estimated for R4.3 and R4.5

σ	Gas[a]		Sol.[b]		Sol. Scaled[c]	
ϕ	ϕ = 0.16[d]	ϕ = $\phi(T, \lambda)$[e]	ϕ = 0.16[d]	ϕ = $\phi(T, \lambda)$[e]	ϕ = 0.16[d]	ϕ = $\phi(T, \lambda)$[e]
$j_{4.5}$	0.85	1.02	0.82	1.05	0.76	0.98
$j_{4.3}$	-	-	2.3	2.95	2.4	2.7

Notes: *j*-values estimated for conditions of ϑ = 60° and 350 DU from the NCAR (TUV) Radiation Model, using [a] gas phase $\sigma(\lambda)$ by Martinez et al. (1992), [b] solution phase $\sigma(\lambda)$ determined in this work in cyclohexane and [c] scaled $\sigma(\lambda)$ estimated scaling the solution phase values by a factor 0.93 estimated from the ratio between the integrated gas and sol MEK spectra. *J*-values were estimated for two different quantum yield, [d] φ (275 − 380 nm) = 0.16 a constant average value estimated by Pinho et al. (2005), and [e] ϕ = $\phi(\lambda, T)$, the parametrised quantum yield formulated by Romero et al. (2005) calculated over the wavelength range 280-335 and at T= 296 K.

For clarity, Figure 4.9 reports only the photolysis rate for MEK, as estimated from the gas phase $\sigma_{4.5}(\lambda)$, leading to $j_{4.5}$ (gas) = 0.9 × 10^{-6} s^{-1}, and for PCO, as estimated from the scaled $\sigma_{4.3}(\lambda)$, leading to $j_{4.3}$ (scaled) = 2.3 × 10^{-6} s^{-1}. The comparison makes it evident how the use of $\sigma_{4.5}(\lambda)$ would lead to a substantial underestimation of $j_{4.5}$ by at least a factor 2.5.
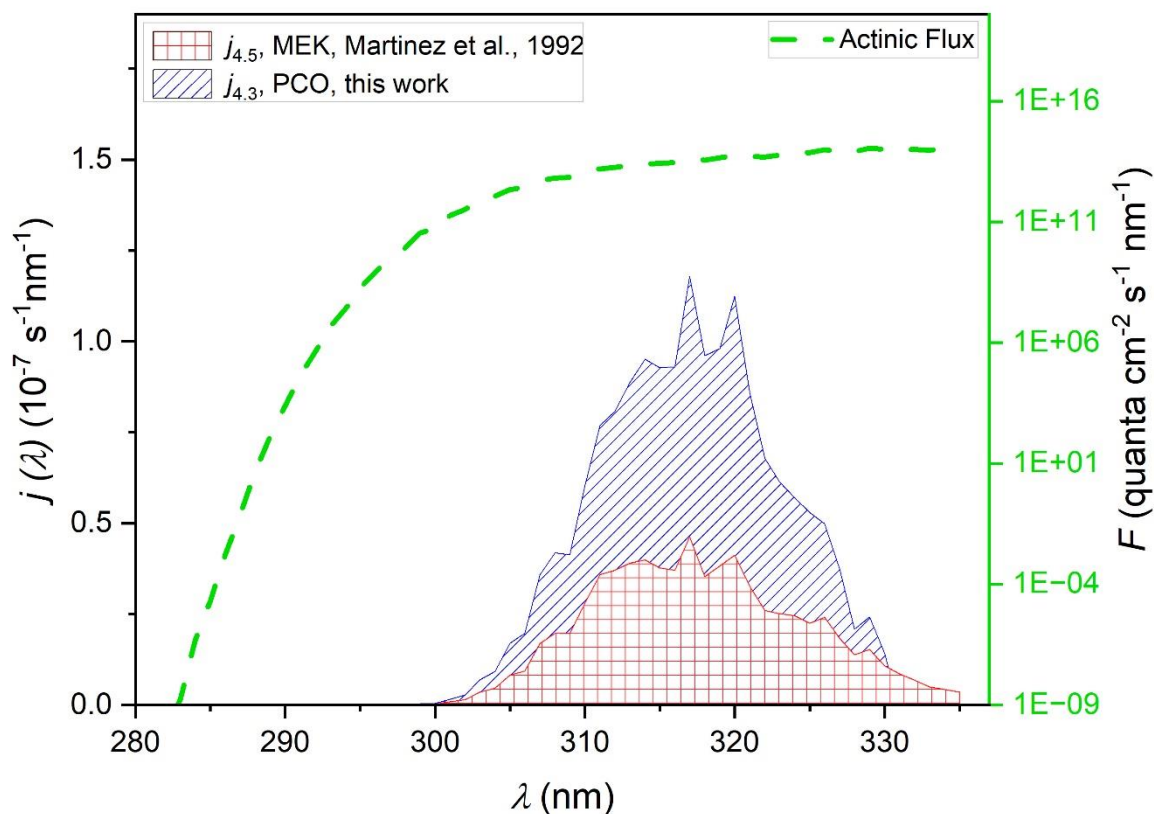
Figure 4. 9: *j*-values for the photodissociation of PCO (R$_{4.3}$) and MEK (R$_{4.5}$). calculated via Eq.1.5. An actinic flux (the green dashed line), for conditions of ϑ = 60° and 350 DU from the NCAR (TUV) Radiation Model, together with φ (275 − 380 nm) = 0.16 was used for all (Eq.1.5) *j*-value calculations. The blue striped area derives from use of $\sigma_{4.3}(\lambda)$ values recorded in experiments using cyclohexane solvent having applied the scaling factor of 0.93 to best reproduce gas-phase $\sigma_{4.3}(\lambda)$ values (see section 4.4.1), integrating to $j_{4.3}$ = 2.4 × 10^{-6} s^{-1}. Also displayed are *j*-values for photolysis of MEK (R$_{4.5}$) calculated using $\sigma_{4.5}(\lambda)$ from the gas-phase spectrum of Martinez et al. (1992) (red squares area, integrated to $j_{4.5}$ = 0.9 × 10^{-6} s^{-1}).

4.5. Atmospheric Implications and SAR Comparison

The atmospheric chemistry of PCO and MPA has been investigated and compared to the limited number of previous studies. Both MPA and PCO react slowly with OH when compared to toluene, which reacts with OH about five times faster than either of these oxygenates (Mellouki et al., 2021). In the following sections the experimental results for $k_{4.1}(T)$ and $k_{4.2}(T)$ were discussed and compared with SAR predictions (section 4.5.1), and the lifetimes and estimated POCP were reported (section 4.5.2 and 4.5.3).

4.5.1. *k*(*T*) Experimental Results and SAR Comparison

The study of R4.1 and R4.2 via PLP-LIF to determine the rate coefficients of these reactions led to the values reported above with their (statistical only) standard error. Considering the potential systemic errors, we quote more realistic values of $k_{4.1}$ (296 K) = (1.2 ± 0.2) × 10^{-12} cm^3 molecule^{-1} s^{-1} and $k_{4.2}$(296 K) = (1.3 ± 0.3) × 10^{-12} cm^3 molecule^{-1} s^{-1}, that take into account the error over the estimation of [VOC]. Both $k_{4.1}$ and $k_{4.2}$ were in good agreement with the

literature data by Wallington and Kurylo (1987a) and by Wallington et al. (2001). Whilst this agreement was pleasing, all three studies used similar PLP methods and thus have a similar reliance on [VOC] measurements; confirmation of these results by e.g. the relative rate technique would be worthwhile in future. These results were also in agreement with the rate coefficients estimated via the Structure Activity Relationship (SAR) method elaborated by Jenkin et al. (2018) (Table 4.1). In addition, SAR product distribution for R4.1 is in accordance with the one observed by (Wallington and Kurylo, 1987a) and recommended by the MCM (Master Chemical Mechanism)(Saunders et al., 2003), which indicate R4.1b as the dominant route (Fig. 4.1, Table 4.5).

Table 4.5 – Summary of $k_{4.1}$, $k_{4.2}$ and branching ratios.

K	This work	Wallington et al.	MCM[d]	SAR[e]
$k_{4.1}$[a]	1.2 ± 0.2	1.21 ± 0.05 [b]	1.2	1.46
%($k_{4.1a}$)	-	Minor	0	9%
%($k_{4.1b}$)	-	Major	100%	91%
$k_{4.2}$[a]	1.3 ± 0.3	1.20 ± 0.03 [c]	-	1.34
%($k_{4.2a}$)	-	16%	-	21%
%($k_{4.2b}$)	-	84%	-	79%

Notes: [a]k values in units of 10^{-12} cm^3 molecule^{-1} s^{-1}, $k_{4.1a}$, $k_{4.1b}$ and $k_{4.2a}$, $k_{4.2b}$ refers to Fig.4.1. All k values were recorded at ambient T [b] Wallington and Kurylo (1987a). [c] Wallington et al. (2001). [d] Master Chemical Mechanism (Saunders et al., 2003). [e] See Section 4.1 for SAR calculation.

However, as it is evident in Fig. 4.3 and Fig. 4.4, the temperature dependence of the SAR predictions is still unable to predict those observed experimentally for those two OVOC reactions. In the case of MPA, where results from this work together with literature data from Wallington et al. (2001) reveal a "U-shaped" non-Arrhenius $k(T)$ described by a 4-parameter expression, the SAR would appear to underestimate the relative importance of the conventional Arrhenius-like contribution to the overall $k(T)$, especially at $T > 300$ K. The SAR does appear to account for the complex non-Arrhenius behaviour at lower temperatures, where direct H-abstraction is slow and the reaction may proceed (by analogy with similar OH + OVOC reactions) via formation of 6-member ring complexes featuring a hydrogen bond between the carbonyl function and the OH radical. Jenkin et al. (1997) do note that additional rate coefficient data would be highly valuable for further evaluation and constraining of the SARs for OVOC and multifunctional species.

For OH + PCO (R4.1), the experimental results have not provided enough evidence for any complex non-Arrhenius temperature dependence; experiments at lower temperature may yet bring further clarification. The $k(T)$ values from SAR so predict a non-Arrhenius trend similar to the one calculated for MPA, somewhat different from the experimental results, although in reasonable agreement in ambient temperature. Some caution should therefore be exercised when using the SAR to estimate product yields for (R4.1 – R4.2), even at $T \approx 298$ K, where the SAR appears to predict accurate k-values but potentially for the wrong reasons.

4.5.2. Lifetime of MPA and PCO

From determinations of $k_{4.1}$(296 K) and $k_{4.2}$(296 K) in this work, we have estimated lifetimes (Eq. 4.1) for PCO and MPA with respect to reaction with OH in the troposphere:

$$\tau = \frac{1}{k_{4.x}[OH]} \qquad\qquad (Eq.4.1)$$

Where $k_{4.x}$ represents the rate constant for R4.1 or R4.2. Using a mean tropospheric [OH] = 1.13×10^6 molecule cm^{-3} (Lelieveld et al., 2016), the calculated lifetime with respect to OH is 9 days for PCO and 9 days for MPA. These lifetimes suggest a relatively low atmospheric reactivity, especially when compared to toluene (τ = 2 days) and may allow for some dispersal or the primary emission prior to formation of ozone and other secondary pollutants. As discussed above, the UV-visible spectrum of MPA suggests that photolysis in the troposphere (λ > 290 nm) is not significant, and the main chemical loss process is therefore reaction with OH. By contrast, PCO absorbs light at 290 nm and above (Fig. 4.7) and hence (by analogy to the known photochemistry of other ketones) will incur photolysis losses. The photolysis rate estimated in this work ($j_{4.3}$ = 2.3 × 10^{-6} s^{-1}) using the scaled solution-phase cross section data and the quantum yield recommended by the MCM, produces a lifetime of 5 days with respect to photolysis (τ_p) under the selected atmospheric conditions. Overall, the lifetime of PCO can be estimated using (Eq.4.2), shortening τ to 3 days (Table 4.6).

$$\frac{1}{\tau} = \frac{1}{\tau_p} + \frac{1}{\tau_{OH}} \qquad\qquad (Eq.4.2)$$

Although this result strongly depends on the atmospheric conditions considered, and despite the acknowledged uncertainty on the estimation of j because of lack of gas-phase absorption cross-section and quantum yield data, this shorter lifetime indicates how photolysis represents an important process for PCO and may outcompete reaction with OH as a removal pathway.

4.5.3. Photochemical Ozone Creation Potential of MPA and PCO

Photochemical parameters obtained in this work could be used in chemical models to investigate atmospheric impacts. Whilst such a modelling study is beyond the scope of this work, estimated impacts on O$_3$ production may be obtained using the procedure devised by Jenkin et al. (2017), that allows for calculated Photochemical Ozone Creation Potential (POCP$_E$) values for environmental assessments. The method was introduced by Jenkin et al. (2017) to take into account for size and structural features of the molecule, reactivity with OH and the presence of suitable chromophores. Here, POCP$_E$ values for North-Western European conditions were calculated for PCO and MPA (Table 4.6) using photochemical data determined in this work. The value of POCP$_E$ = 11 for MPA may be quoted with some confidence, given the good agreement in rate coefficients determined here and in previous work, and the absence of an active chromophore at relevant wavelengths. By contrast, three scenarios were considered for PCO, given the remaining uncertainties in the rate of R4.3. First, following the guidance in Jenkin et al. (2017), whereby one single value is recommended to account for photolysis of all aliphatic ketones, we calculated POCP$_E$ = 26 for PCO. However, this photolysis parameter appears to be based upon cross-section and quantum yield values from the MCM, determined for photolysis of MEK (R4.5). We cannot rule out that the (unmeasured) quantum yields for PCO photolysis are small; in our second scenario we estimate that a consequently small value of POCP$_E$ = 12 may be appropriate, (ϕ = 0 so no photolysis, OH loss only). A third scenario would account for the enhanced rate of photolysis of PCO due to the more intense and red-shifted $\sigma(\lambda)$ determined in this work,

and/or a higher quantum yield ($0.16 < \phi < 1$). A quantitative evaluation of this consequently enhanced $POCP_E > 26$ would require detailed modelling studies.

Table 4.6 – Lifetime and POCP$_E$ for PCO and MPA.

OVOC	Lifetime, τ (days)[a]			POCP$_E$[b]	
	τ_{OH}	τ_p	τ	POCP$_E$ (OH only)	POCP$_E$ (OH & photolysis)
MPA	9	-	9	11	11
PCO	9	5	3	12	26[c]

Notes: [a] atmospheric lifetime (τ) estimated using Eq. (4.1), based upon k(296 K) from this work and a value of [OH] = 1.13×10^6 molecule cm^{-3} (Lelieveld et al., 2016). [b] POCP$_E$ estimated according to Jenkin et al. (2017) method, see Appendix for more information. [c] does not take into account larger $j_{4.3}$ value and uses Jenkin et al. (2017) formula based on $\sigma_{4.5}(\lambda)$ and $\phi_{4.5}(\lambda)$.

Comparing these POCP$_E$ values to traditional hydrocarbon solvents that MPA and PCO are meant to replace (Byrne et al., 2018), these sustainable and non-toxic solvents show a much lower POCP$_E$. Toluene for instance has a POCP$_E$ of 45, which greatly exceed the POCP$_E$ scenarios estimated for PCO and MPA. Taken together, results from this work and elsewhere suggest that MPA has a moderate reactivity in the troposphere. PCO is likely more reactive due to photolysis (R4.5). Even if significant uncertainties remain regarding PCO photochemistry, the use of both PCO and MPA would appear to have several advantages and to not adversely impact on air quality when compared to traditional harmful and non-sustainable solvents.

5. Atmospheric Chemistry of CPME and CPO

Cyclopentyl methyl ether (formally methoxycyclopentane, $C_5H_9OCH_3$), henceforth CPME (Fig. 5.1), is a commercially available compound that was recently recommended as a sustainable alternative to traditional solvents in a wide range of industrial applications (Azzena et al., 2019; Abreu et al., 2016; De Gonzalo et al., 2019) (see Section 1.2.3). Widespread use of CPME would (considering CPME vapour pressure of 44 Torr at 20°C) lead to a substantial release of this oxygenated volatile organic compound (OVOC) into the atmosphere. Consequent impacts on air quality of OVOC release invariably include production of harmful secondary pollutants such as HCHO and O_3. There is a lack of photochemical data available for the breakdown of CPME in air. Given the absence of unsaturated C=C and of suitable chromophores, CPME is unlikely to react with O_3 or NO_3, or to absorb light available in the troposphere ($\lambda > 290$ nm). CPME degradation is therefore likely initiated by reaction with aggressive atmospheric radical oxidants such as the hydroxyl radical, OH, and atomic chlorine, Cl. This work details investigations into these most important gas-phase breakdown reactions for CPME (R5.1 and R5.2), to enable an assessment of its impact on air quality (Mellouki et al., 2015; Wang et al., 2022).

OH + CPME $\rightarrow$ (products) (R5.1)

Cl + CPME $\rightarrow$ (products) (R5.2)

Fig. 5.1 describes the alternative pathways for R5.1, which proceed via H abstraction from one of four C-H sites on CPME. A detailed mechanism for the subsequent oxidation chemistry, leading to formation of O_3 and carbonyl-containing products is provided in Figure 5.2. Interestingly, channels R5.1a and R5.1d are expected to lead to the formation of cyclopentanone (C_5H_8O, henceforth CPO), another solvent with potentially useful properties and for which important gas-phase photochemical information is limited.
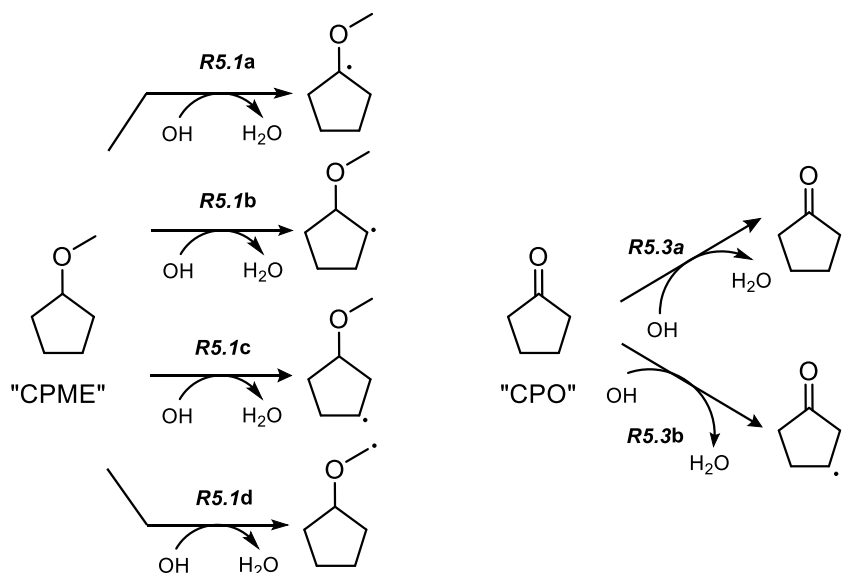
Figure 5. 1: Chemical structures and reaction pathways. Left represents the alternative pathways for CPME reaction with OH (R5.1), which proceed through H abstraction from one of four C-H sites. Right side of the figure represents the 2 alternative pathways for the reaction of CPO with OH (R5.3a and R5.3b) Equivalent reaction schemes leading to these radical products (and HCl) may be written for reactions of Cl-atoms with CPME (R5.2) and CPO (R5.4).
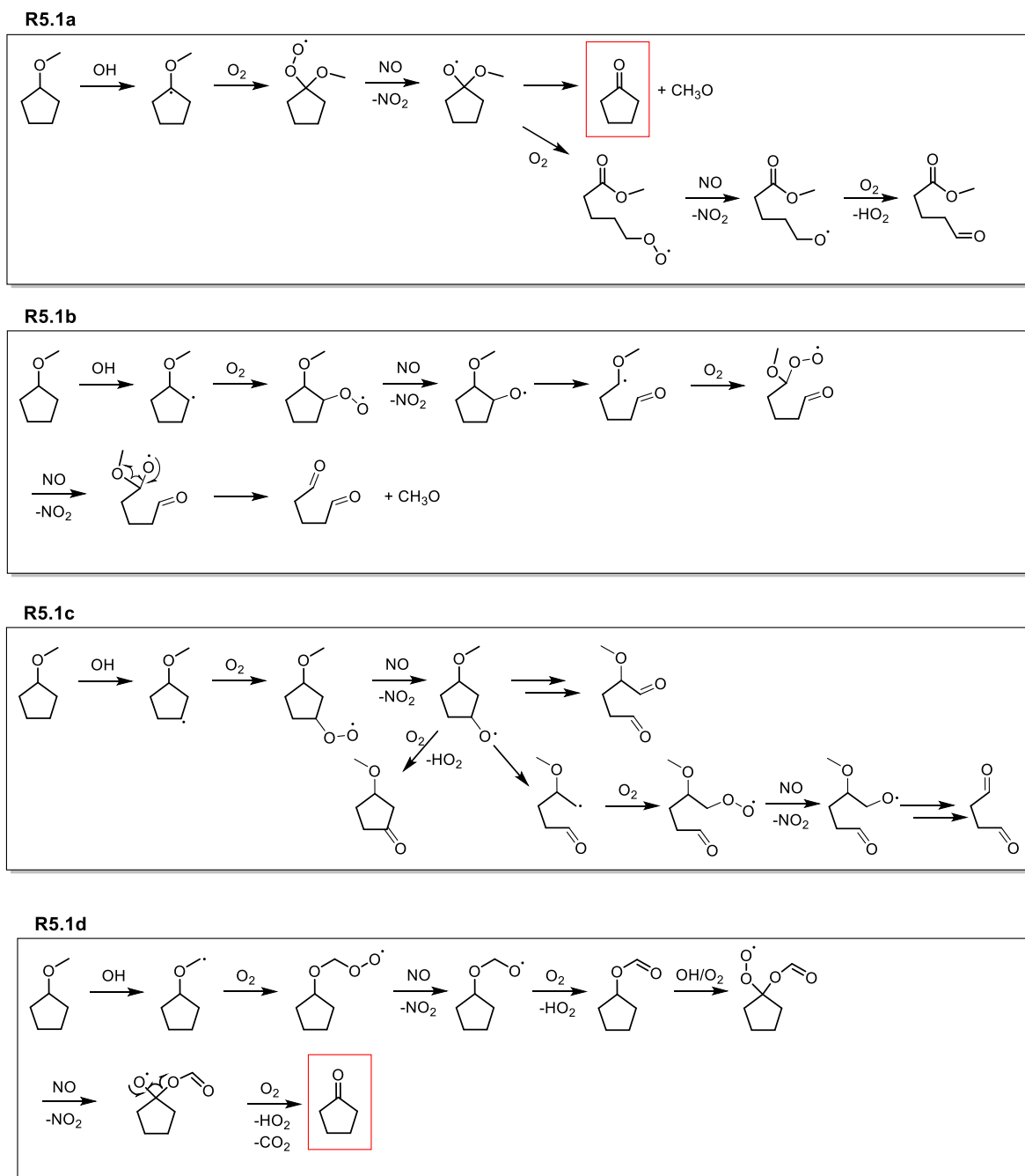
Figure 5. 2: Atmospheric oxidation mechanism initiated by R5.1, leading to the first stable oxygenated products. Route 5.1a and 5.1d are likely to lead to formation of CPO.

CPO is widely used as a platform molecule in a wide range of fields that include the pharmaceutical sector and the material industry. Its application as green solvent and bio-derived fuel has aroused great interest (Liu et al., 2019; Zhou et al., 2016; Bao, 2017; Duereh et al., 2018; Lawrenson et al., 2017) (see Section 1.2.4). As in the case of CPME, the lack of C=C double bonds suggests little reactivity towards O_3 and NO_3. The presence of carbonyl functionality indicates potential for photochemical degradation (R5.5) following absorption via the $\pi^* \leftarrow n$ electronic transition.

OH + CPO   →   (products)   (R5.3)

Cl + CPO   →   (products)   (R5.4)

$$h\nu + CPO \quad \rightarrow \quad (products) \qquad\qquad (R5.5)$$
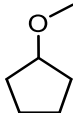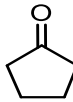
This work aims to improve knowledge of CPO degradation in the troposphere through the study of R5.3 and R5.5. Section 5.1 will introduce the literature studies available on the atmospheric chemistry of these compounds, and the calculated SAR rate coefficients for R5.1 and R5.3. The following sections provides a description of the experimental work and discussion of the results.

5.1.   Previous Studies and SAR Calculations

Despite the use of CPME and CPO as solvents and building blocks in industrial chemistry, their atmospheric chemistry remains rather unexplored. To the best of our knowledge, there are no gas phase studies of CPME reactions with OH (R5.1) and Cl (R5.2). CPO + OH (R5.3) has been studied by Dagaut et al. (1988), who used flash photolysis coupled to direct resonance fluorescence detection of OH to report $k_{5.3}$ (296 K) = (2.94 ± 0.18) × 10^{-12} cm^3 molecule^{-1} s^{-1}. In a recent work focused on the potential utility of CPO as a biofuel, Liu et al. (2019) reported $k_{5.3}(902 - 1297 \text{ K}) = 1.20 \times 10^{-10} \exp(\frac{2115}{T})$. CPO reaction with Cl (R5.4) was studied previously in two studies (Wallington et al., 1998; Takahashi et al., 2007). The results were in good agreement leading to $k_{5.4}$ (296 K) = 1.2 × 10^{-12} cm^3 molecule^{-1} s^{-1} and therefore the reaction was not further investigated in this work. The photolysis rate of CPO (R5.5) and identity of any products formed in the troposphere, is highly uncertain. Absorption cross sections in the spectral range of interest (λ > 290 nm) were reported by Nakashima et al. (1982b), though these were obtained in the liquid/solution phase. Further, quantum yields for R5.5 are unknown. Quantitative photolysis rate estimations and air quality assessments are therefore problematic.

SAR calculations for R5.1 and R5.3 were estimated using the Jenkin et al. (2018) method described in Section 1.5. The factors and coefficients used, together with the SAR rate coefficients were listed in Table 5.1.

Table 5.1: SAR calculations based on Jenkin et al. (2018) for R5.1 and R5.3.

Molecule	Group	k_x [a]	F_X [d]	F_Y [d]	F_Z [d]	F_{RING} [e]	k_{CH_x} [a]	n [b]	$\%k$ [c]	k [a]
CPME	α-CH$_2$	0.769	1.35	1.35	-	0.69	1.93	2	14	
	β-CH$_2$	0.769	3.5	1.35	-	0.69	5.01	2	36	
	O-CH$_3$	-	-	-	-	-	1.30	1	9	**13.85**
	O-CH	-	-	-	-	-	5.60	1	40	
CPO	α-CH$_2$	0.769	1.35	1	-	0.32	0.66	2	23	
	β -CH$_2$	0.769	1.35	3.4	-	0.32	2.26	2	77	**2.92**

Notes: **a)** Units are in 10^{-12} cm^3 molecule^{-1} s^{-1}. **b)** n = number of equivalent groups. **c)** Percentage distribution for the partial rate coefficients. **d)** F_x, F_y, and F_z are the substituent factor for the neighbour groups x, y and z respectively. **e)** F_{RING} is the ring factor that accounts for the ring strain.

SAR calculations predict a greater reactivity for CPME (13.85×10^{-12} cm^3 molecule^{-1} s^{-1}), which reflects not only a larger number of C-H bonds (12 C-H compared to 8 C-H of CPO) but also the activating effect of the ether group, notably higher than the ketone. However, it is interesting to note that CPME, with a number of C-H 1.5 times higher than CPO, is expected to react with OH 5 times faster than CPO (2.92×10^{-12} cm^3 molecule^{-1} s^{-1}). Looking at the partial rate coefficients calculated for CPME, this difference in reactivity relies mainly on the C-H bond next to the ether oxygen. Whilst all H-atoms in CPME were more reactive than their equivalents in CPO, the key is the highly reactive OCH, absent in CPO. This H-atom is strongly activated both by the inductive effect of the ethereal O-atom, and because abstraction here leads to a relatively stable tertiary radical centre Another important aspect concerns the ring strain of CPO, that is much stronger than in CPME. The linear ketone equivalent to CPO, 2-pentanone ($CH_3COC_3H_7$), is twice as reactive towards OH (k(298 K) = 4.5×10^{-12} cm^3 molecule^{-1} s^{-1} (Jiménez et al., 2005)), suggesting a significant effect of the ring structure on CPO reactivity

5.2. Rate Coefficient of OH with CPME (R5.1)

To the best of our knowledge this is the first study of the gas phase reactivity of CPME with OH (R5.1). The reaction was observed using two very different and complementary techniques, similarly to what was done for R3.1 (see Section 3.2). Rate coefficients were first determined with the PLP-LIF method at the University of York (Section 5.2.1), and then again with the RR approach at the University of Iaşi (Section 5.2.2). Results were compared and their implication for the atmospheric fate of CPME and CPO discussed in Section 5.7.

5.2.1. PLP-LIF results for CPME+OH (R5.1)

The PLP-LIF apparatus used for the study of R5.1 was described in Section 2.1, together with a detailed description of the method used for direct and absolute determination of the rate coefficients. Figure 5.3 reports three exemplary fluorescence decays of OH in the presence of different concentrations of CPME at T = 295 K. Values of B obtained from fits with (Eq. 3.5) were collected and plotted against corresponding values of [CPME] to obtain the linear relationship as depicted in the insert to Fig. 5.3. The slope from this plot is a measure of $k_{5.1}$(295 K), whilst the intercept (at around 640 s^{-1}) fitted against the concentrations to give a linear plot whose slope corresponds to the second order rate constant, which in the specific case of the figure was $k_{5.1}$ = (1.44 ± 0.05) × 10^{-11} cm^3 molecule^{-1} s^{-1}.
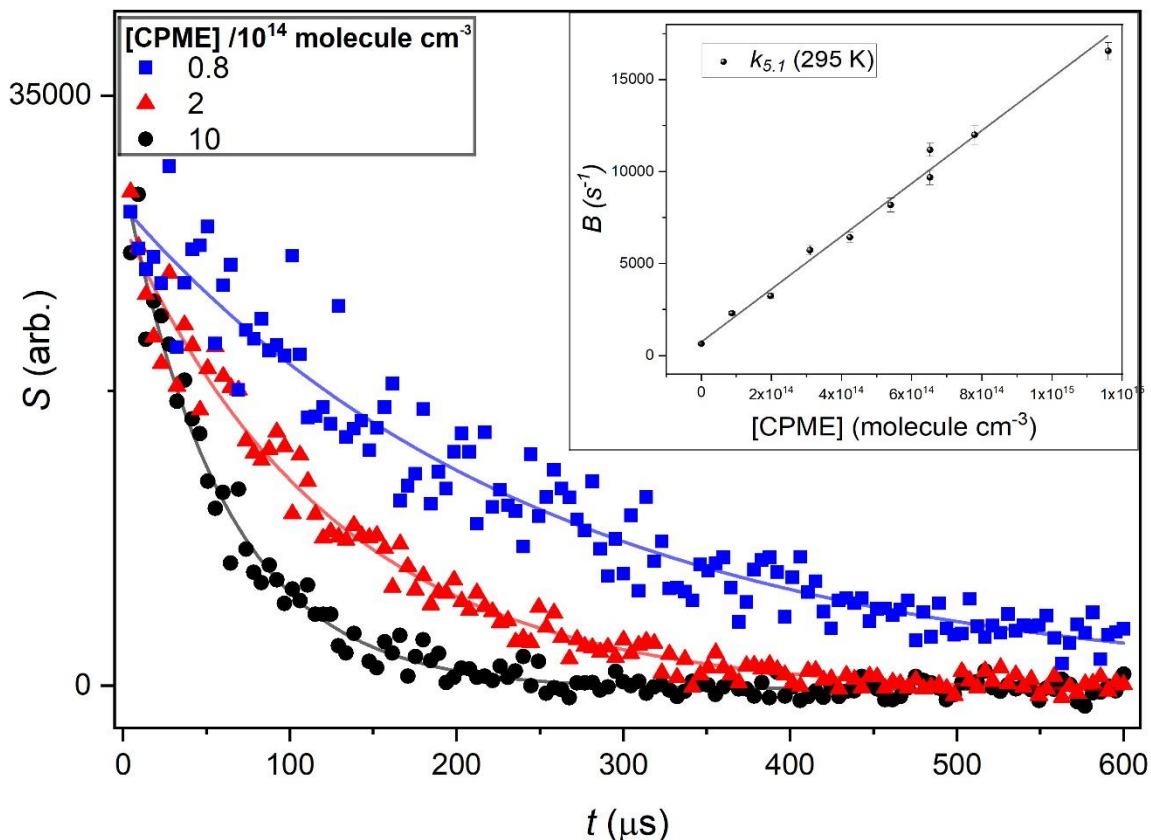
Figure 5. 3: Exemplary exponential decays of OH in the presence of excess [CPME] = 0.8×10¹⁴ molecule cm⁻³ (blue squares), [CPME] = 2×10¹⁴ molecule cm⁻³ (red triangles), [CPME] = 1×10¹⁵ molecule cm⁻³ (black circles), fit with (Eq. 2.25) to yield pseudo first-order rate coefficients respectively B =(3990 ± 334) s⁻¹, B =(7880 ± 250) s⁻¹ and B =(16720 ± 440) s⁻¹. The linear plot on the top right represents an example of bimolecular plot of B vs [CPME] yielding a rate coefficient $k_{5.1}$ = (1.44 ± 0.05) × 10⁻¹¹ cm³ molecule⁻¹ s⁻¹.

Experiments were repeated at different pressures and using a wide concentration range supplied from several preparations of CPME. No systematic changes in $k_{5.1}$ were observed; a weighted mean of the four values obtained close to room temperature (Table 5.2) and the relative standard error was

$k_{5.1(\text{PLP-LIF})}$(296 K) = (1.48 ± 0.08) × 10⁻¹¹ cm³ molecule⁻¹ s⁻¹

Experiments were then conducted at elevated temperatures, results from which were listed in Table 5.2 and depicted in Arrhenius format in Fig. 5.4. The complex, non-Arrhenius behaviour fit Eq. 5.1:

$$k(T) = A_1 \exp(b_1/T) + A_2 \exp(b_2/T) \qquad \text{(Eq. 5.1)}$$

Leading to $k_{5.1}$(295 − 464 K) = 3.4·10⁻¹⁰exp(-1900/T) + 1.2·10⁻¹²exp(720/T) cm³ molecules⁻¹ s⁻¹. A non-Arrhenius behaviour of such kind is not uncommon for OH + OVOC reactions (see section 1.3).

Table 5.2: Absolute PLP-LIF determinations of $k_{5.1}(T)$ for OH + CPME.

Reaction	T (K)	P (Torr)	n [a]	[CPME] [b]	$k \pm$ SE [c]
R5.1	295	62	10	0.7 - 9.8	1.44 ± 0.05
R5.1	296	34	21	3.0 - 24.8	1.38 ± 0.02
R5.1	296	97	23	6.3 - 20	1.51 ± 0.04
R5.1	298	37	15	0.5 - 10.9	1.58 ± 0.04
R5.1	321	62	12	0.7 - 9.8	1.47 ± 0.06
R5.1	321	70	12	0.7 - 9.4	1.36 ± 0.03
R5.1	322	70	12	1.4 - 8.2	1.26 ± 0.03
R5.1	345	71	12	1.3 - 7.6	1.12 ± 0.03
R5.1	345	71	12	1.3 - 7.0	1.12 ± 0.05
R5.1	370	70	16	1.3 - 7.2	1.13 ± 0.03
R5.1	370	67	12	1.3 - 7.5	1.09 ± 0.03
R5.1	408	70	12	1.1 - 6.4	1.12 ± 0.04
R5.1	408	64	12	1.2 - 6.9	1.12 ± 0.04
R5.1	447	70	12	1.0 - 6.0	1.05 ± 0.03
R5.1	449	64	11	1.1 - 6.4	1.05 ± 0.04
R5.1	464	61	17	1.7 - 10	1.30 ± 0.05

Notes: [a] **Number of datapoints in the bimolecular plot.** [b] **Concentration is expressed in 10^{14} molecule cm^{-3}.** [c] **Rate coefficients are in 10^{-11} cm^3 molecule^{-1} s^{-1} ± standard error.**
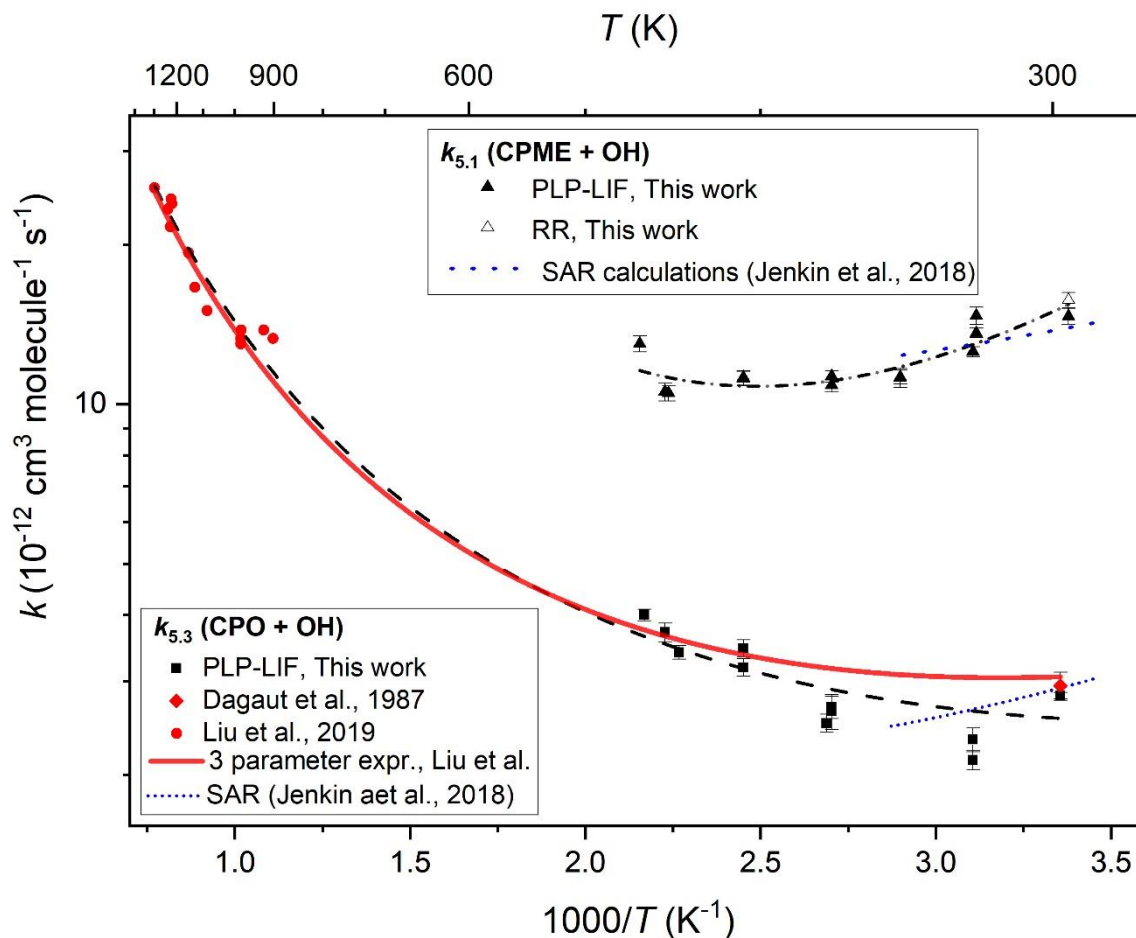
Figure 5. 4: Arrhenius plot displaying $k_{5.1}(T)$ and $k_{5.3}(T)$ results from this work and the available literature. OH + CPME (R5.1) data, all from this work (filled black triangles from PLP-LIF; open black triangle from RR) were fit with the four-parameter Eq. (5.1) to yield $k_{5.1}(295 - 464$ K) = $3.4 \cdot 10^{-10} \exp(-1900/T) + 1.2 \cdot 10^{-12} \exp(720/T)$ cm³ molecules⁻¹ s⁻¹ (the black dot-dashed line). For comparison, the blue dotted line represents calculated $k_{5.1}(298 - 370$ K) using the most recent SAR (Jenkin et al., 2018). OH + CPO (R5.2) data from this work are displayed as filled black squares, alongside results from Liu et al. (red circles) and Dagaut et al. (red diamond). The red line represents the three-parameter expression used by Liu et al. to fit the literature dataset; the black dashed line is an updated version of this three-parameter fit to include results from this work. Calculated $k_{5.3}(298 - 370$ K) using the SAR proposed by (Jenkin et al., 2018) is displayed as the blue short-dotted line.

5.2.2. RR Results for CPME+OH (R5.1) and CPME+Cl (R5.2)

Relative rate experiments were conducted in the 760 dm³ ESC-Q-UAIC environmental simulation chamber at the Alexandru Ioan Cuza University in Iasi, Romania. The apparatus has been described in Section 2.2 in detail (Roman et al., 2022; Mapelli et al., 2022). The quartz chamber was equipped with inlet ports, UV lamps for photolysis (generation of OH or Cl-atoms) and FTIR for observation of reference VOC, CPME, and CPME oxidation products. All experiments were conducted at P = 750 Torr (air) and T = (295 ±2) K. In preliminary experiments, wall deposition and photolysis rates (360 nm and 254 nm) were measured to ensure the validity of the experiment and to correct the reaction rate coefficients if needed.

Reference reactions (R2.12, R2.13, R2.15, R2.16, Table 2.4) were selected using the criteria presented in detail in Section 2.2.2. All spectral lines used in these determinations of $k_{5.1}$ and

$k_{5.2}$ were tested for proportionality to the concentration of CPME and the reference compounds.
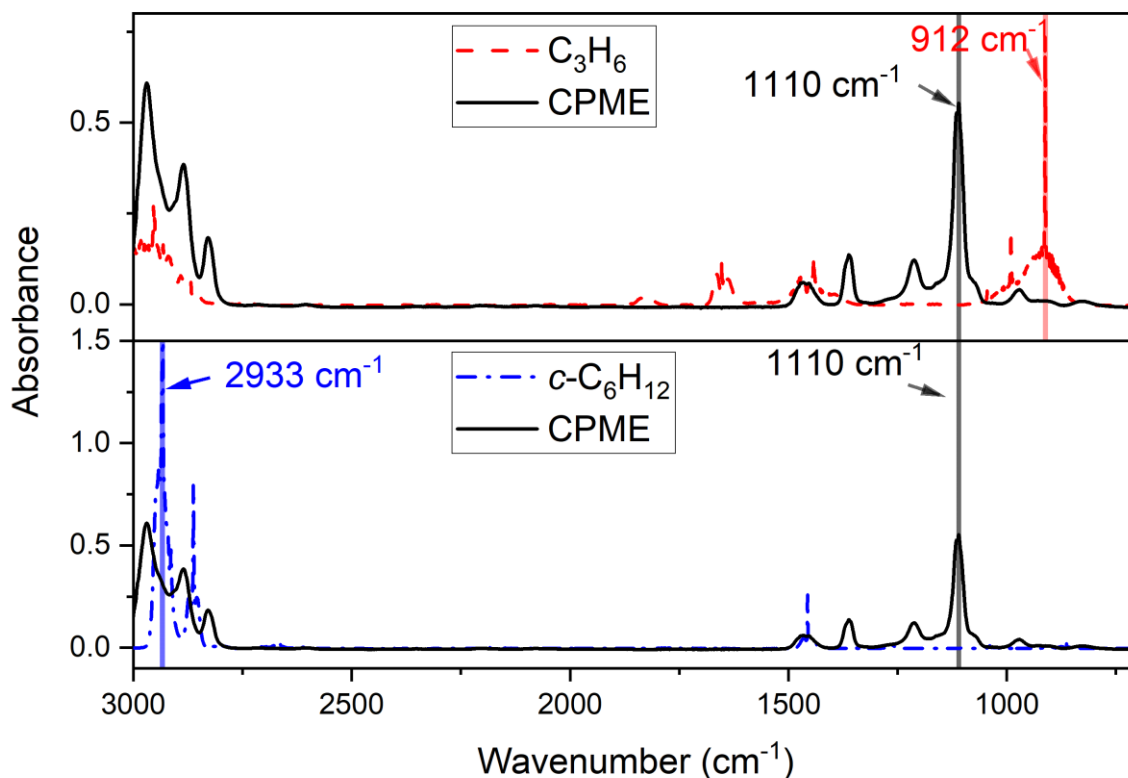
Figure 5. 5: FTIR gas spectra for CPME (black line) and C_3H_6 (red dotted line) and for CPME and c-C_6H_{12} (blue dash-dotted line) over the range 3000-700 cm⁻¹ used in relative rate determinations of $k_{5.1}$ and $k_{5.2}$. Spectra were recorded with 1 cm⁻¹ resolution.

As illustrated in Figure 5.5, the main peak selected for CPME was the one at 1110 cm⁻¹, whereas C_3H_6 absorption was measured at 912 cm⁻¹ and c-C_6H_{12} at 2933 cm⁻¹. In the case of c-C_6H_{12}, where the peak of interest was subjected to partial overlap with CPME spectrum, the subtraction was initially operated on CPME and only subsequently on the 2933 cm⁻¹ c-C_6H_{12} peak. For both reactions, subtraction of secondary peaks was also checked for confirmation. The OH radical was generated by two different methods: directly via photolysis of H_2O_2 (R2.1); alternatively, CH_3ONO was injected into the chamber for photolysis at 365 nm (R2.8). The presence of an excess of NO ensured rapid conversion to OH (R2.9-R2.10). Atomic chlorine was generated by the photolysis of Cl_2 at 365 nm (R1.13). As in the case of the RR study of R3.1 described in section 3.2 and 3.3, the chemical species of interest were monitored by FTIR spectroscopy, and their relative depletion rate was studied scanning an FTIR spectrum every 2 minutes. The absorbance at time zero, t_o, and at reaction time t of each recorded spectrum, were used to construct linear plots according to equation 2.35. Experiments conducted in the absence of radical precursors demonstrated that neither CPME nor the two reference VOCs (Table 2.4) were significantly impacted by wall-losses or photolytic removal indicating that corrections to subsequent kinetic data were unnecessary. Results from two of the studies conducted to determine $k_{5.1}$(296 K) and $k_{5.2}$(296 K) are displayed in Fig. 5.6 a and b. The depletions in CPME and in c-C_6H_{12} and C_3H_6 were analysed according to Eq. 2.35 which resulted in a linear relationship.
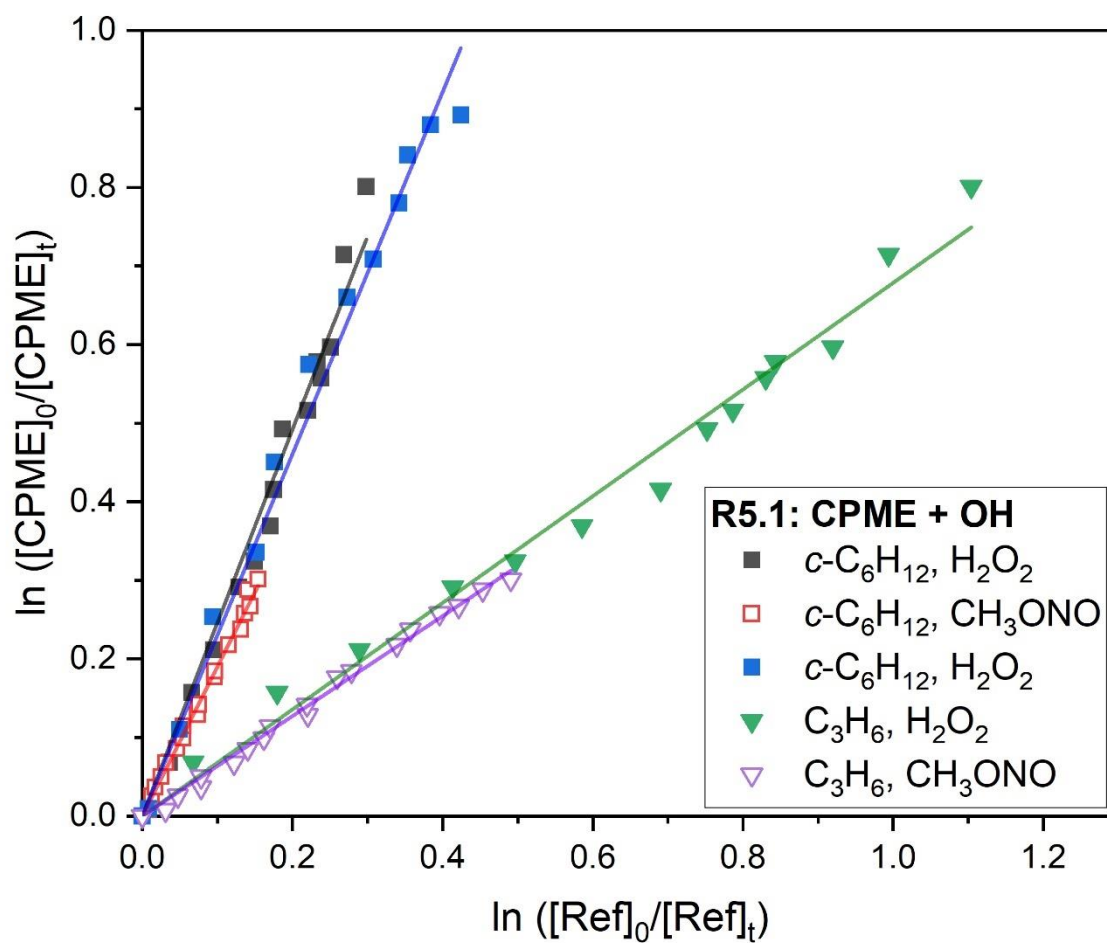
Figure 5. 6: Relative rate plot showing depletion in CPME via reaction with OH vs. that of the reference compounds. The triangle datapoints correspond to (R5.1) OH + CPME vs (R 2.13) OH + C_3H_6, whereas the square datapoints correspond to (R5.1) OH + CPME vs (R 2.12) OH + c-C_6H_{12}. Filled datapoints indicate experiments where the OH precursor was H_2O_2, whereas empty datapoints were used for CH_3ONO-precursor experiments.
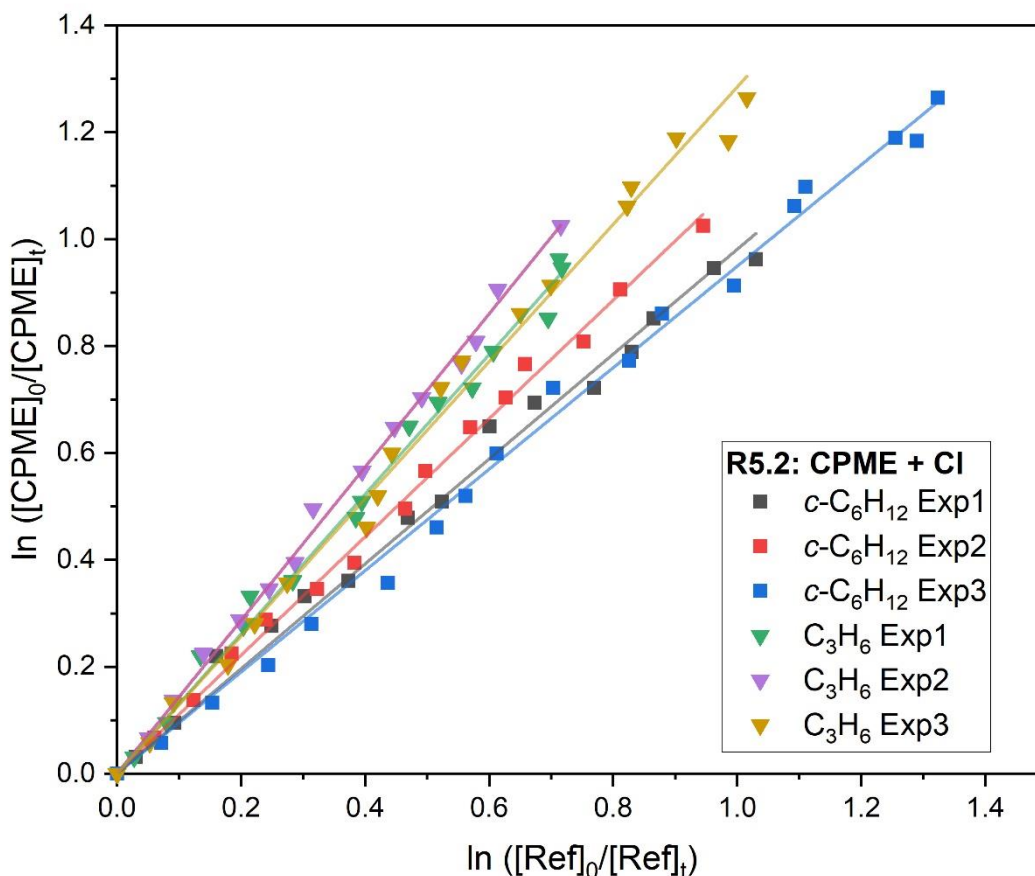
Figure 5. 7: Relative rate plot showing depletion in CPME via reaction with Cl vs. that of the reference compounds. The triangle datapoints correspond to (R5.2) Cl + CPME vs (R 2.16) Cl + C_3H_6, whereas the square datapoints correspond to (R5.2) Cl + CPME vs (R 2.15) Cl + c-C_6H_{12}.

Table 5.3: Relative rate experiments to determine $k_{5.1}$(296 K) for OH + CPME

OH precursor	Ref. VOC	λ / nm	[Ref]$_0$ [a]	[CPME]$_0$ [a]	$k_{5.1}$ / k_{refOH} [c]	$k_{5.1}$(296 K) $\pm$ SE [d]
H_2O_2	c-C_6H_{12}	254	5.14	4.75	2.30 ± 0.04	1.61 ± 0.03
H_2O_2	c-C_6H_{12}	254	5.14	4.67	2.46 ± 0.05	1.71 ± 0.03
H_2O_2	C_3H_6	254	3.30	4.67	0.68 ± 0.01	1.78 ± 0.02
CH_3ONO	C_3H_6	365	6.57	4.83	0.64 ± 0.01	1.67 ± 0.02

Notes: The experiments were conducted at p = 750 Torr (air) and T = 296 K; [a] = initial [Ref] and [CPME] values in 10^{13} molecule cm^{-3}; [b] = see Table 2.4 for values used here as k_{ref}; [c] = $k_{5.1}$(296 K) in units of 10^{-11} cm^3 molecules^{-1} s^{-1} ± standard error.

Relative rate plots obtained for R5.1 and illustrated in Fig. 5.6a showed a good proportionality. A weighted mean of the results listed in Table 5.3 yields a value of $k_{5.1,RR}$(296 K) = (1.69 ± 0.06) × 10^{-11} cm^3 molecule^{-1} s^{-1} from the relative rate studies of (R5.1) in this work, 0.06 representing the standard error. This value is 18% larger than the one obtained in absolute method, PLP-LIF experiments, of $k_{5.1(PLP-LIF)}$(296 K) = (1.48 ± 0.08) × 10^{-11} cm^3 molecule^{-1} s^{-1}. No previous measurements of this rate coefficient appear in the literature.

A similar series of RR experiments was conducted, using R1.13 generation of atomic chlorine for the study of CPME + Cl (R5.2) (Fig. 5.6b). Results are summarised in Table 5.4; a weighted

mean value of these six determinations yields $k_{5.2}$(296 K) = (3.2 ± 0.1) × 10^{-10} cm^3 molecule^{-1} s^{-1}. Also in this case, this is the first study of $k_{5.2}$ in the gas phase. An expected increase of reactivity for R5.2 with respect to R5.1 was observed.

Table 5.4. Relative rate determinations of $k_{5.2}$(296 K) for Cl + CPME

Ref. VOC	[Ref]$_0$ [a]	[CPME]$_0$ [a]	$k_{5.2}$ / k_{ref} [b]	$k_{5.2}$(296 K) ± SE[c]
c-C$_6$H$_{12}$	5.14	4.51	0.98 ± 0.01	3.24 ± 0.05
c-C$_6$H$_{12}$	5.14	4.35	1.11 ± 0.01	3.65 ± 0.03
c-C$_6$H$_{12}$	5.14	4.83	0.95 ± 0.01	3.13 ± 0.03
C$_3$H$_6$	6.57	4.51	1.31 ± 0.02	2.91 ± 0.04
C$_3$H$_6$	6.57	4.35	1.43 ± 0.01	3.20 ± 0.04
C$_3$H$_6$	6.57	4.83	1.28 ± 0.02	2.86 ± 0.03

Notes: All experiments were conducted at p = 750 Torr (air) and T = 296 K ; [a] = initial [Ref] and [CPME] values in 10^{13} molecule cm^{-3}; [b] = see Table 2.4 for k_{ref} values; [c] = $k_{5.2}$(296 K) in units of 10^{-10} cm^3 molecules^{-1} s^{-1} ± SE.

5.3.   Product Study for the Atmospheric Oxidation of CPME

The study of the oxidation products of reaction R5.1 and R5.2 was carried out to understand the reactivity of CPME and to investigate the reaction routes predicted via SAR calculations. The procedure used was very similar to the one described in Section 2.2, except that no reference compound was present, and a surplus of radical precursor was used such that CPME was almost completely depleted. The OH precursor used was H$_2$O$_2$ and the UV lamps were turned on at 254 nm. In addition to the FTIR monitoring of the chamber, an on-line Proton-Transfer-Reaction Mass Spectrometry (PTR- MS) analysis was also performed. Figure 5.7 represents a fraction of the FTIR spectra recorded in a typical experiment, showing the peak at 1110 nm, selected to measure the A^{VOC} (see section 2.2.2) of CPME in RR studies and in product studies.
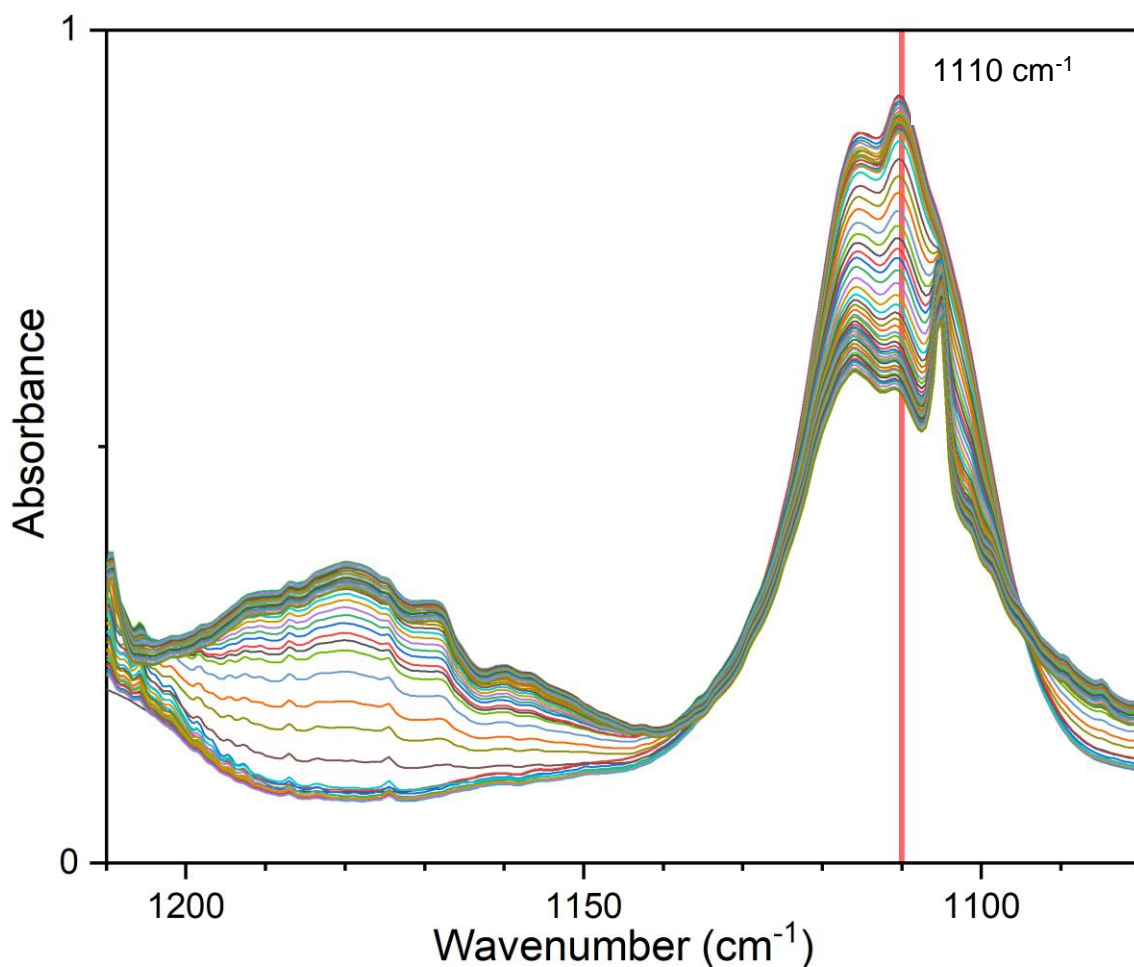
Figure 5. 8: FTIR spectra recorded during the chamber experiment for CPME. Spectra were collected every 2 minutes. The absorbance of CPME was recorded at 1110 cm⁻¹.

The mass-to-charge (m/z) values recorded during the experiment and potentially related to oxidation products were 84 and 98. Figure 5.9 summarizes the most stable oxidation products expected for the four alternative pathways of R5.1 with their atomic mass. Fragmentation of these compounds could also lead to the detection of m/z 84 and 95. The formation of these products was investigated studying the FTIR spectra recorded and comparing them to reference spectra.

CPME: PTR-MS results
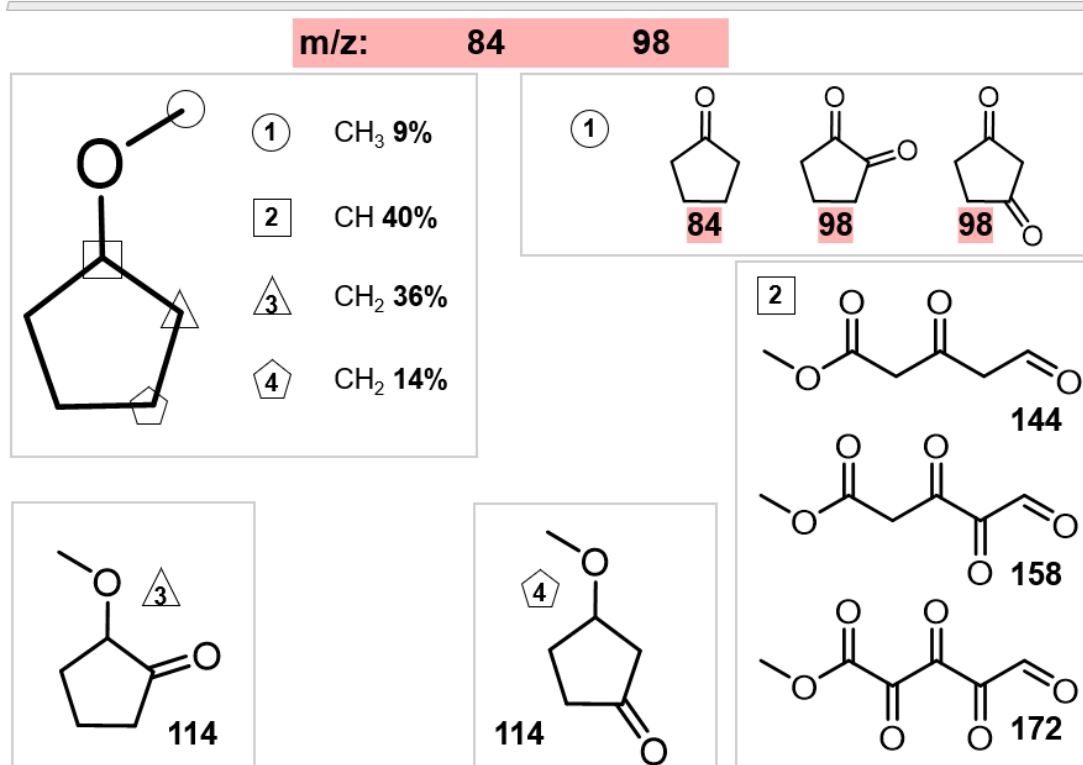
Figure 5. 9: Mass-to-charge (m/z) values encountered in the PTR-MS (84 and 98) together with the chemical structure of the potential oxidation products of CPME for the four alternatives reaction paths and their respective atomic mass. It is noted that the m/z could also derive from fragmentation of the oxidation products in the mass spectrometer.

The first potential product that was investigated was CPO. Being available in the lab, a CPO spectrum was recorded in the atmospheric chamber in the experimental conditions. Similar spectra were recorded for HCHO and H_2O_2. Fig 5.10 displays absorbance recorded during the product study, alongside CPO, CPME, HCHO and H_2O_2, reference spectra within the spectral range of interest for the characteristic FTIR peak of the carbonyl stretching vibration of CPO (around 1770 cm^{-1}). Despite the mechanism prediction (Figure 5.2) indicated two reaction routes leading to CPO, in the complex spectra recorded in the ESC-Q-UAIC chamber was not possible to clearly identify any developing peak assignable to CPO. It is unclear why this was the case, but the lack of the CPO peak does not necessarily exclude this molecule as a product of R5.1. The CPO peak may be hidden by other signals or may depend on the fact that CPO quickly reacts via R5.3 and R5.5, producing a signal that then disappear quickly. According to the results discussed in section 5.6.2, the second option is less likely to be plausible.
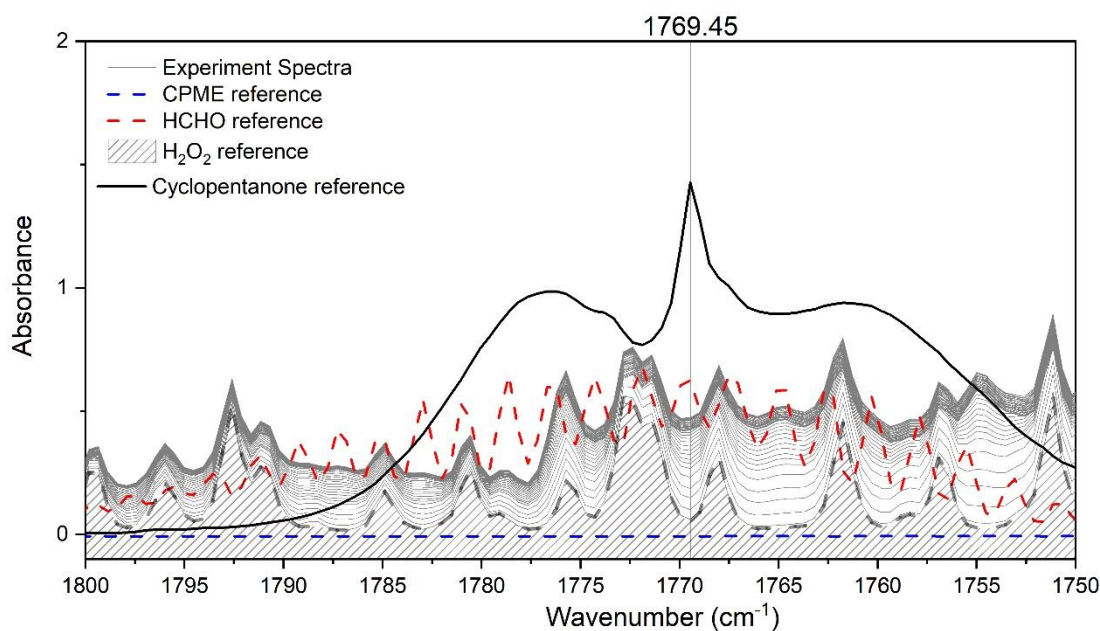
Figure 5. 10: Infrared spectra (1800-1750 cm⁻¹ enlargement) recorded during the product study experiment (in grey) together with the reference spectra of CPME (dashed blue line), HCHO (dashed red line), H₂O₂ (striped area), CPO (black line), recorded in similar conditions.

However, analysing other areas of the spectra it was possible to identify the outbreak of new peaks associated to formation of oxidation products. Figure 5.11 shows one of such peaks at around 1745 cm⁻¹, at least partially due to formation of H_2O_2. The shape of the peak suggests the contribution of another product to the spectra. Another peak at around 1755 cm⁻¹ was also identified as a potential oxidation product. The absorbance of the potential product signals was plotted as a function of time in Figure 5.12.
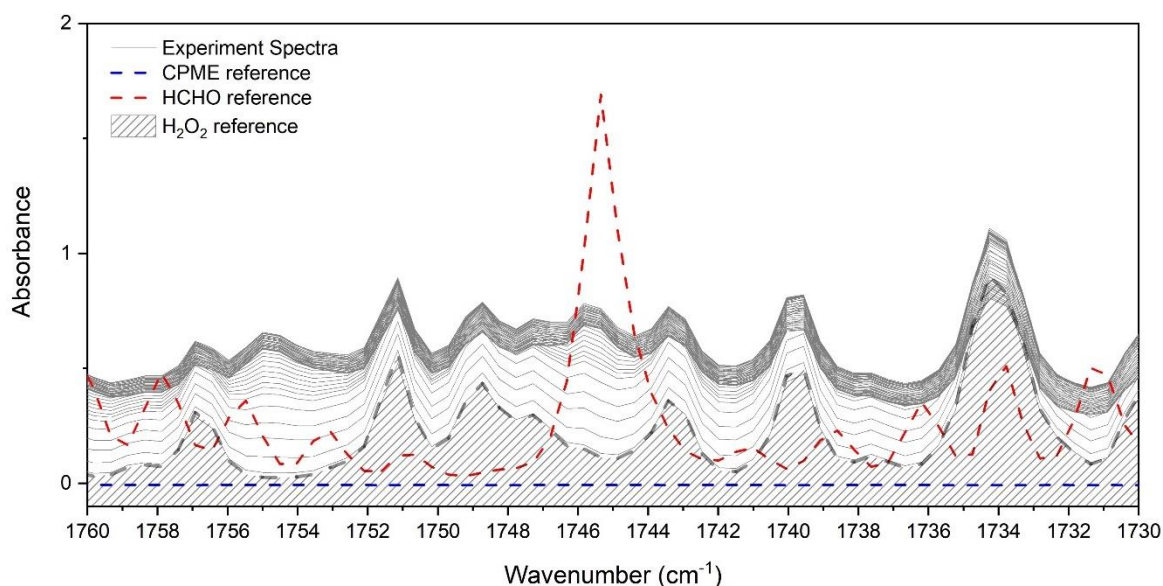
Figure 5. 11: Infrared spectra (1760-1730 cm⁻¹ enlargement) recorded during the product study experiment (in grey) together with the reference spectra of CPME (dashed blue line), HCHO (dashed red line), H₂O₂ (striped area), recorded in similar conditions.
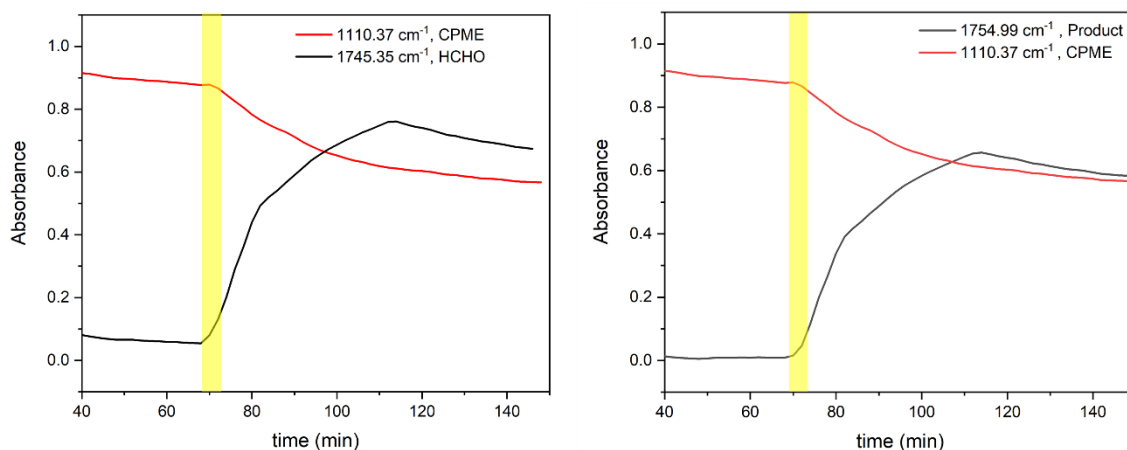
Figure 5. 12: Evolution of the 1745.35 cm⁻¹ peak (black line on the left) and 1754.99 cm⁻¹ peak (black line on the right), compared to the CPME characteristic peak at 1110.37 cm⁻¹ (red line). The yellow vertical stripe indicates the start of the 254 nm UV lamps at 70 min from the start of the experiment.

After a plateau of the absorbance intensity for the first 70 minutes of the experiment when the lamps were off, the CPME signal steadily dropped down, while the peaks associated to the products make their appearance in the spectra and reached a maximum at around 110 min of the experiment, when they slowly started to decrease in intensity together with CPME. After having thus confirmed the 1745 and 1754 cm⁻¹ peak assignment to H_2O_2 and other oxidation products, the search for the other molecules that could be related to the 84 and 98 m/z and to the FTIR carbonyl stretching was carried out via spectra comparison. Unfortunately, gas phase FTIR spectra for the molecules of interest was not available. As a surrogate of the experimental reference spectra, theory spectra elaborated by Conor Rankine via Quantum Chemical Calculations (QCC) with the CBS-QB3 method were used. First, the CPME theory spectrum was calculated and compared to the reference spectrum recorded in the chamber (Figure 5.13). The characteristic peak of CPME at 1110.37 cm⁻¹ resulted red-shifted to 1080.48 cm⁻¹, a difference that is significant to the goal of this work, meaning that the theory spectra were not precise enough to be used as surrogate to the experimental spectra. For instance, looking at the spectra calculated for 1,2-cyclopentadione, 1,3-cyclopentadione, 2-methoxycyclopentan-1-one and 3-methoxycyclopentan-1-one (Figure 5.14), it was observed that the signal of the carbonyl stretching were found respectively at 1755, 1737, 1763 and 1752 cm⁻¹. The difference between these characteristic peaks being lower than 30 cm⁻¹ and having no information whether the QCC red shift is systematic or not, it is not possible to assign the unknown peaks to any of the supposed products. Further experimental work and a more advanced level of QCC would be needed for a better understanding of the oxidation products developing from R5.1. However, the predicted spectra confirmed that some of the oxidation products are likely to absorb light at around 1100 cm⁻¹, possibly interfering with the CPME peak at high degree of conversion as discussed in section 5.2.2.
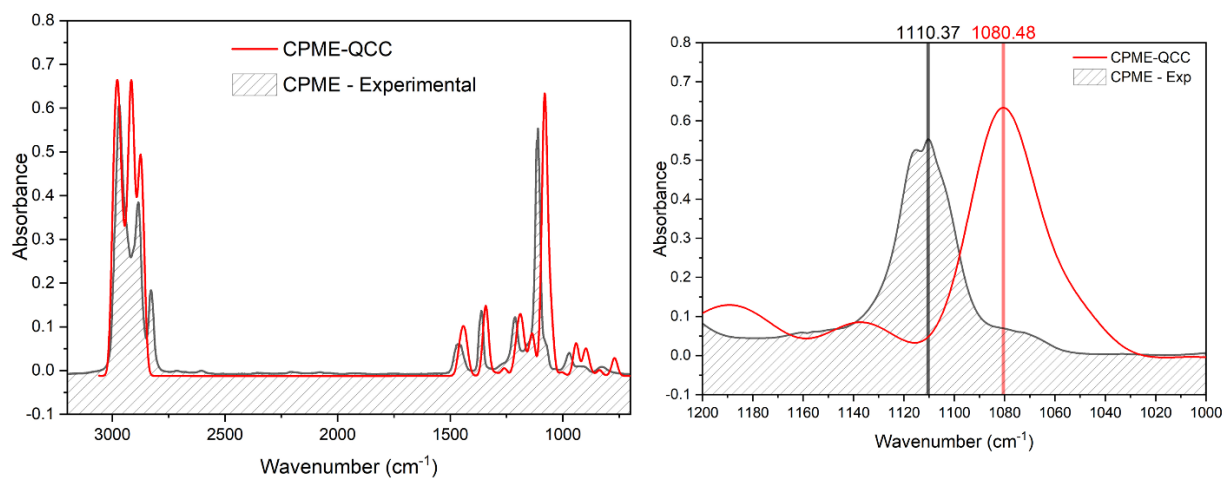
Figure 5. 13: Quantum Chemical Calculation (QCC) spectrum and experimental spectrum of CPME (3400-500 cm⁻¹) on the left, enlargement (1200-1000 cm⁻¹) of the characteristic peak on the right.
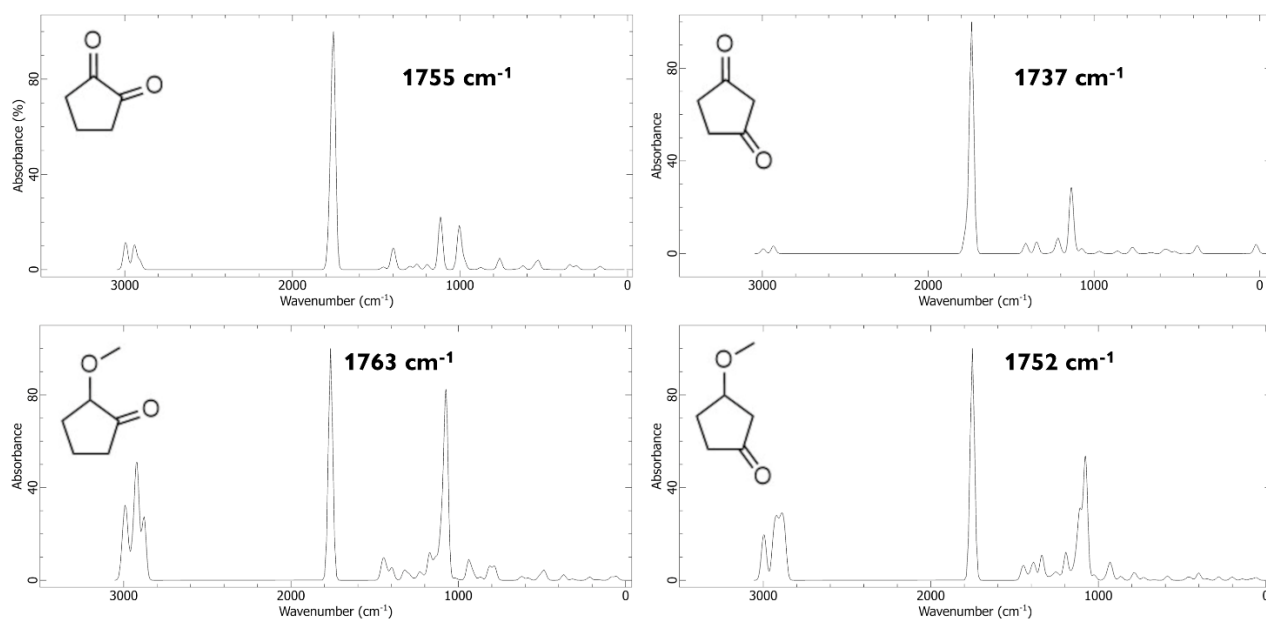
Figure 5. 14: QCC spectra of 1,2-cyclopentadione, 1,3-cyclopentadione, 2-methoxycyclopentan-1-one, 3-methoxycyclopentan-1-one.

5.4.   Rate Coefficient of OH and CPO (R5.3)

A series of PLP-LIF experiments was also conducted to study OH + CPO (R5.3). Rate coefficients were measured over the range of temperature 298 - 461 K with full results listed in Table 5.5. At room temperature, a value of $k_{5.3}(296\ \text{K}) = (2.82 \pm 0.04) \times 10^{-12}$ cm³ molecule⁻¹ s⁻¹ was determined, in good agreement with one previous study and with SAR calculations (Table 5.1). Similarly to what was done for PCO, the use of moderate laser fluences was important in this kind of experiments, as CPO absorbs UV light at 266 nm (see section 1.3.3). Using a cross-section determined in this work of $\sigma(266\ \text{nm}) = 2.96 \times 10^{-20}$ cm² molecule⁻¹, we

calculate again that < 0.1% of CPO could be converted to highly reactive species in the laser flash.

Fig. 5.4 uses Arrhenius format to display the full results for $k_{5.3}(296 - 461$ K) from this work, together with previous literature determinations. As observed previously for CPME and for other OVOC, $k_{5.3}(T)$ is complex and not conforming to regular Arrhenius form save perhaps at the highest temperatures.

Table 5.5: Absolute PLP-LIF determinations of $k_{5.3}(T)$ for OH + CPO.

Reaction	T (K)	P (Torr)	n [a]	[CPO] [b]	k ± SE [c]
R5.3	298	58	12	2.5 – 23.8	0.282 ± 0.004
R5.3	322	82	10	2.1 – 17.1	0.213 ± 0.009
R5.3	322	62	13	2.4 – 14.3	0.232 ± 0.012
R5.3	370	70	11	1.8 – 14.9	0.268 ± 0.013
R5.3	370	67	10	1.8 – 15.5	0.26 ± 0.02
R5.3	372	61	15	3.3 – 18.0	0.250 ± 0.010
R5.3	408	64	12	1.6 – 14.7	0.345 ± 0.013
R5.3	408	70	12	1.2 – 6.9	0.318 ± 0.012
R5.3	441	63	14	3.2 – 19.0	0.340 ± 0.011
R5.3	449	64	11	1.6 – 9.6	0.371 ± 0.015
R5.3	461	61	15	2.9 – 18.5	0.400 ± 0.010

Notes: [a] Number of datapoints in the bimolecular plot. [b] Concentration is expressed in 10^{14} molecule cm^{-3}. [c] Rate coefficients are in 10^{-11} cm^3 molecule^{-1} s^{-1} ± SE.

5.5. Estimation of CPO Photolysis Rate Coefficient

The importance of photolysis as a breakdown process for the removal of PCO was investigated via UV-visible spectroscopy and results were discussed in section 5.5.1 and 5.5.2. The forbidden $n \rightarrow \pi^*$ transition typical of ketones (see Section 1.3.3), is responsible for the UV-rays absorption in the troposphere by this class of molecules and can lead to photolysis and decomposition. The extent of photodecomposition depends on the overlap between the molecule absorption spectrum and the actinic flux, together with the BDE of the chemical bonds in the structure of the compound (see section 1.3.3). In this study, the absorption cross sections of CPO were recorded in the spectral range of interest via UV-visible spectroscopy with the help of MChem student Abbie Robinson, and results were compared with the available literature data (Section 5.5.1). Cross section measurements were then used for an approximate estimation of the photolysis rate coefficients (section 5.4.2). CPME showed no absorption across the range 280 – 360 nm and therefore his photolysis behaviour was not discussed.

5.5.1. UV-visible study of CPO Absorption Cross Sections and estimation of j values

The UV-vis spectrum of CPO was, in this work, recorded from dilute samples in cyclohexane solution. As displayed in Figure 5.14, this data agreed well with the spectral pattern previously reported by Nakashima et al. (1982b) in similar conditions. As expected from a ketone carbonyl function, the molecule absorbs over the spectral range of interest for the troposphere (λ > 290 nm). The spectrum was characterised by a series of vibrational structures with a maximum at about 300 nm. The absorption cross section at the maximum wavelength, calculated from the Beer-Lambert plot (Fig. 5.14) was equal to 7×10^{20} cm^2 molecule^{-1}, a value that is again in agreement with the literature data.

The *in silico* study carried out by Basile Curchod and Daniel Hollas for CPO corroborates the trends observed for PCO and MEK (Section 4.4.1) and confirmed that the (theoretical) gas-phase photoabsorption cross-sections appear to be weakly red-shifted (0.0275 eV in average) and its intensity weakened by a factor 0.855 with respect to the theoretical photoabsorption cross-section in cyclohexane (Curchod and Hollas, 2023). In the absence of any gas-phase data on CPO absorption in this wavelength range, we assumed that CPO would follow the same behaviour of MEK, and that the experimental gas-phase spectrum of CPO would show a ratio of around 0.9:1 between the integrated gas-phase and solution-phase UV-vis. spectra, as it was discussed for MEK in section 4.4.1.
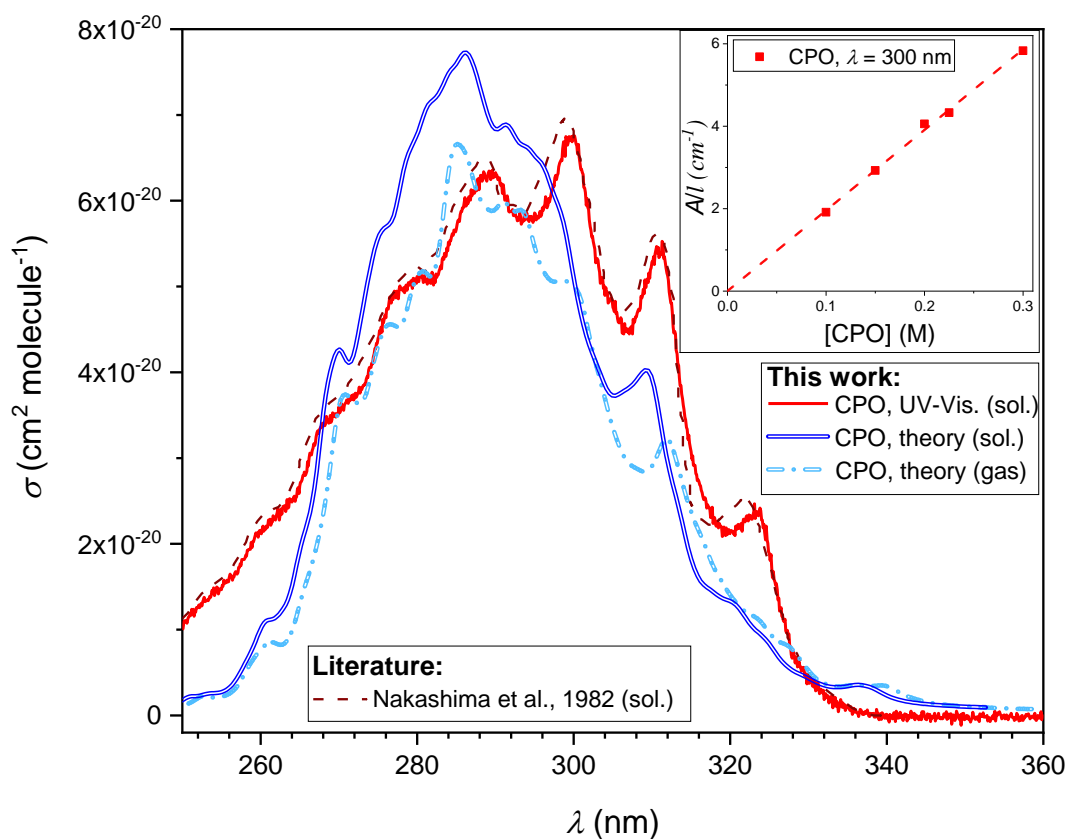
Figure 5. 15: UV-Vis spectrum of CPO recorded in cyclohexane from this work (red line) and from Nakashima et al. (1982b) in gas phase (dark red dashed line) over the spectral range 250-360 nm. The Beer-Lambert graph for CPO (red squares) determined at 300 nm is displayed in the insert (top right) of the Figure. Theoretical spectra (NEA[1000 geometries]/LR-TDDFT/TDA/wB97XD/def2-TZVP) of CPO in the gas phase (blue dashed line) and in cyclohexane (blue double line) are also displayed (Curchod and Hollas, 2023).

The estimation of the photolysis rate was then carried out according to Equation 1.5. As limited information was available on the quantum yield for the photodissociation (Calvert et al., 2011b), j was first calculated for the upper limits, assuming $\varphi = 1$. The photolysis rate was then calculated using $\varphi = 0.16$, that is the average of the optimised quantum yield of methyl ethyl ketone (MEK), as recommended by the MCM, which uses this parameter to define the photolysis rate of several ketones (Saunders et al., 2003; Jenkin et al., 1997). Lastly, as discussed in section 4.4.2, the parameterised quantum yield elaborated by Romero et al. (2005), $\varphi(\lambda, [M], T)$, was also used for the estimation of j. The solar irradiance was calculated with the NCAR (Madronich and Flocke, 1997) TUV model, for a zenith angles of 60° and 350 DU. As for the absorption cross sections, the solution-phase cross-sections determined via UV-Vis. spectrometry were used as well as the scaled cross-sections which are likely to be closer to the gas-phase. Results for all the estimated j were summarised in Table 5.6.
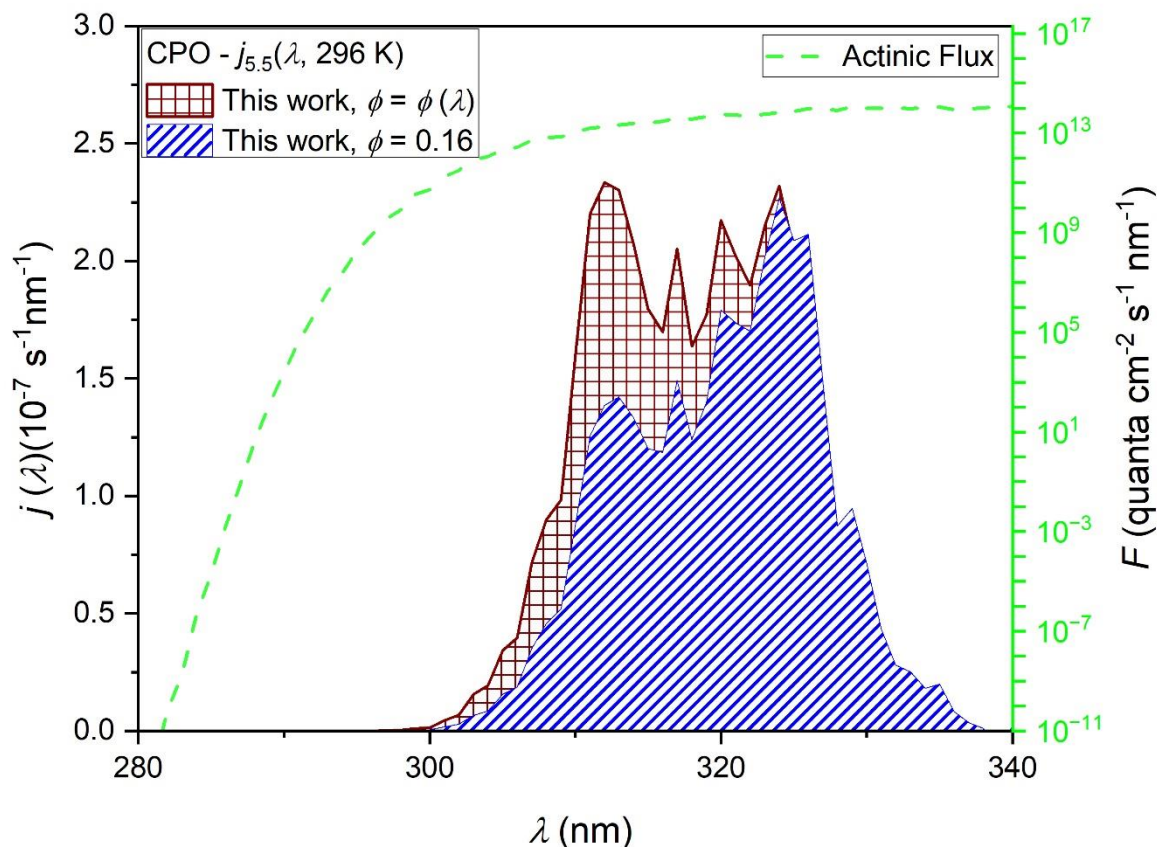
Figure 5. 16: Logarithm scale of the actinic flux F (green dashed line) at $\vartheta = 60°$ and 350 DU calculated with the NCAR (TUV) Radiation Model. CPO photolysis rate estimated using Eq. 1.5 using the scaled solution phase $\sigma(\lambda)$ and $\varphi = 0.16$, leading to $j_{5.5} = 3.4 \times 10^{-6}$ s^{-1} (blue striped area), and with $\varphi = \varphi(296\ K, \lambda)$ (Romero et al., 2005), leading to $j_{5.5} = 4.2 \times 10^{-6}$ s^{-1} (brown squared area).

Table 5.6: Estimated values for $j_{5.5}$.

	$\phi = 0.16^c$	$\phi = \phi(T, \lambda)^d$	$\phi = 1$
$j_{5.5}$ (sol.) [a]	3.6	4.5	22.7
$j_{5.5}$ (estimated gas) [b]	3.4	4.2	21.2

Notes: j-values in units of 10^{-6} s^{-1}, estimated for conditions of $\vartheta = 60°$ and 350 DU from the NCAR (TUV) Radiation Model, using [a] solution phase $\sigma(\lambda)$ determined in this work in cyclohexane and [b] scaled $\sigma(\lambda)$ estimated scaling the solution phase values by a factor 0.93 estimated from the ratio between the integrated gas and sol MEK spectra (see Section 4.4.1). J-values were estimated for three different quantum yields, $\varphi = 1$, [c] φ (275 - 380 nm) = 0.16 a constant average value estimated by Pinho et al. (2005), and [d] $\phi = \phi(\lambda, T)$, the parametrised quantum yield formulated by Romero et al. (2005) calculated over the wavelength range 280-335 and at T= 296 K.

In the atmospheric conditions considered, and $\varphi = 0.16$, the estimated photolysis rate coefficient was $j_{5.5} = 3.6 \times 10^{-6}$ s^{-1} for CPO using the cross sections measured in this work in cyclohexane. As discussed in section 4.4.1 (Mapelli et al., 2023), a scaling factor of 0.93, obtained from the comparison of experimental UV-vis. spectra in gas and solution phase, can be applied to the cross sections to estimate the photolysis rate. A slightly different value of $j_{5.5} = 3.4 \times 10^{-6}$ s^{-1} was obtained using this method. Similarly, a scaling factor of 0.855 (see above) determined *in silico* was applied to the cross sections to obtain a rate coefficient of $j_{5.5} = 3.1 \times 10^{-6}$ s^{-1}. The use of wavelength-dependent quantum yields formulated by Romero et al. (2005), lead to a slightly higher photolysis rate, with $j_{5.5} = 4.5 \times 10^{-6}$ s^{-1} for the rate coefficient

determined using the solution-phase cross sections recorded in cyclohexane, and $j_{5.5} = 4.2 \times 10^{-6}$ s^{-1} for the coefficient determined with the same cross sections scaled by a factor 0.93 (see above). As can be observed in Figure 5.15, the j-values estimated for $\varphi = 0.16$ increase with the increment of the solar flux. On the other hand, the use of a parameterised quantum yield leads to j-values that are less sensitive to the increment of solar flux and more equally distributed in the area where both the absorption cross sections and the solar flux are high. The third scenario of Table 5.6 represents the upper limit, with $\varphi = 1$ and consequently rate coefficients as high as 22.7×10^{-6} and 21.2×10^{-6}, a factor 5 larger than the j-values estimated with the expected quantum yields.

5.6. Atmospheric Implications and SAR comparison

The atmospheric degradation of CPME and CPO was investigated studying the reactions of these molecules with OH, Cl, and the light absorption in the troposphere. In the following sections, results were compared with literature data when available and with SAR predictions (section 5.6.1), and the rate coefficients determined in this work were used to calculate lifetimes in standard conditions (section 5.6.2) and POCP$_E$ values (section 5.6.3).

5.6.1. $k(T)$ Experimental Results and SAR Comparison

The rate coefficients for OH + CPME (R5.1) determined in this work by direct, absolute PLP-LIF, was $k_{5.1,\text{PLP-LIF}}(296 \text{ K}) = (1.48 \pm 0.08) \times 10^{-11}$ cm^3 molecule^{-1} s^{-1} whereas by indirect RR, it was $k_{5.1,\text{RR}}(296 \text{ K}) = (1.69 \pm 0.06) \times 10^{-11}$ cm^3 molecule^{-1} s^{-1}. These results were combined to give a mean averageand a standard error of $k_{5.1}(296 \text{ K}) = (1.59 \pm 0.05) \times 10^{-11}$ cm^3 molecule^{-1} s^{-1} (Fig. 5.16).
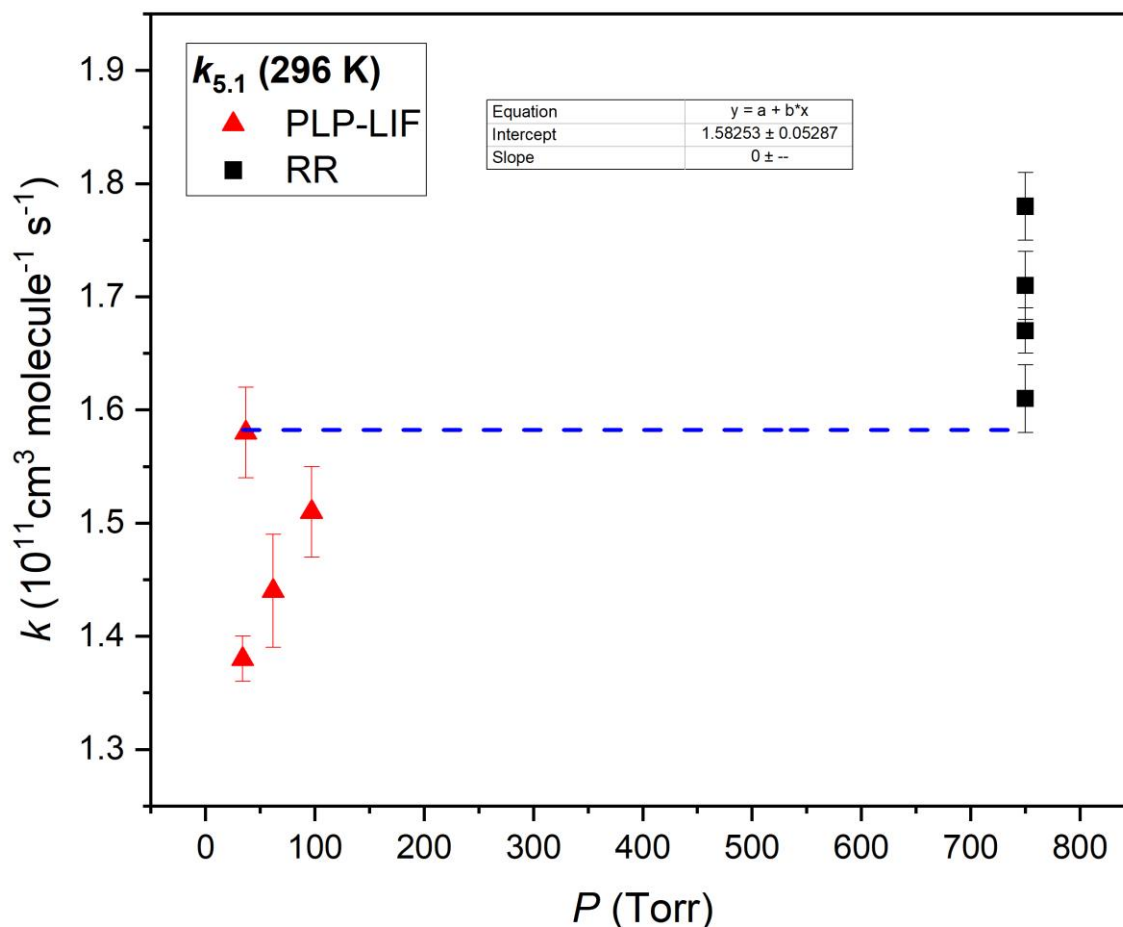
Figure 5. 17: Rate coefficients values for (R5.1) determined by PLP-LIF and RR experiments fitted with a liner plot of slope fixed at 0 to determine the average $k_{3.1}$ weighted on error bars.

These complementary methods, with different strengths and weaknesses, led to similar results, with an 18% difference between the absolute and the relative rate method. Although this difference is not far from the standard errors measured for the reaction, the higher values of RR results could be due to pressure dependence of the reaction. More experiments in the pressure range 100-700 Torr would be needed to confirm that.Critical assumptions underpin each kinetic technique, leading to not insubstantial sources of systematic uncertainty. PLP-LIF relies on an absolute determination of [CPME], which was known to an estimated uncertainty of ± 15%. The accuracy of RR determinations is limited by uncertainties in reference rate coefficients. For instance, IUPAC report an uncertainty $\Delta \log k$ = 0.1 or approximately 20% for OH + C_3H_6 + M and provide no such evaluation for OH + c-C_6H_{12}. Using the uncertainties available in literature (table 2.4) in Eq. 2.39, a systematic uncertainty of 25% was estimated for the RR results of R5.1. Consequently, we estimate that the total uncertainty, taking into account both random and systematic errors in these rate coefficient determinations, is approximately ± 20% and report a consolidated value of $k_{5.1}$(296 K) = (1.6 ± 0.3) × 10^{-11} cm³ molecule⁻¹ s⁻¹ from this work. Similarly, a more conservative value of $k_{5.2}$(296 K) = (3.2 ± 0.6) × 10^{-10} cm³ molecule⁻¹ s⁻¹ is recommended for Cl + CPME (R5.2). Whilst there appear to be no prior literature for this parameter, SAR calculations (see Section 5.1) may be used to predict a rate coefficient at $k_{5.1,SAR}$(295 K) = 1.4 × 10^{-11} cm³ molecule⁻¹ s⁻¹ (Jenkin et al., 2018), this value being in good agreement with our experimental results. This was confirmed

also from the temperature-dependence SAR prediction, which again is well aligned with our experimental results (Fig. 5.4). The SAR also suggests that the most reactive sites are adjacent to the ether functionality. However, product studies discussed in section 5.3 were not useful in confirming this prediction.

A similar condition was observed for OH + CPO (R5.3). In this case the reaction was studied exclusively via PLP-LIF technique, and the potential systematic error was estimated to lie around ±15%, leading to $k_{5.3}(296 \text{ K}) = (2.8 \pm 0.4) \times 10^{-12}$ cm^3 molecule^{-1} s^{-1}. Similarly to what was found for R5.1, the SAR provide in this case a very good prediction of the rate coefficient, with $k_{5.3, \text{SAR}}(296 \text{ K}) = 2.9 \times 10^{-12}$ cm^3 molecule^{-1} s^{-1}. This result was also in agreement with the previous experimental result found in literature (Dagaut et al., 1988).

5.6.2. Lifetimes and Photochemical Ozone Creation Potentials

The rate coefficients for chemical and photochemical routes leading to the breakdown of CPME and CPO were used for the estimation of their atmospheric lifetimes. As determined by direct PLP-LIF and RR measurements, CPME reacts much faster with OH than CPO, with an overall average rate constant equal to $k_{5.1}(296 \text{ K}) = (1.6 \pm 0.3) \times 10^{-11}$ cm^3 molecule^{-1} s^{-1}, one order of magnitude larger than the rate constant of CPO with OH, $k_{5.3}(296 \text{ K}) = (2.8 \pm 0.4) \times 10^{-12}$ cm^3 molecule^{-1} s^{-1}. A similar trend was observed for the reactivity with Cl, even though the difference is much more levelled, with a value of $k_{5.2} = (3.2 \pm 0.6) \times 10^{-10}$ cm^3 molecule^{-1} s^{-1}, that exceed $k_{5.4}$ only by a factor 3, as the reaction of CPO and Cl reported by Takahashi et al. (2007) indicate $k_{5.4} = (1.16 \pm 0.12) \times 10^{-10}$ cm^3 molecule^{-1} s^{-1}.

Whilst these results would suggest a lifetime that is by far smaller for CPME, inclusion of the photolysis rate in the overall lifetime estimation downsizes consistently this difference. Equation 5.2 brings together the rate constants from all the main degradation processes to estimate the overall lifetime of CPO and CPME in air:

$$\frac{1}{\tau} = \frac{1}{\tau_p} + \frac{1}{\tau_{OH}} + \frac{1}{\tau_{Cl}} \qquad \text{(Eq. 5.2)}$$

Where τ is the overall lifetime, τ_p is the lifetime relative to the photodissociation and τ_i is the lifetime relative to the reaction with the chemical species i, that are the other oxidant of interest, OH, Cl. Given the absence of double C-C bonds in CPO and CPME, the reactivity with O$_3$ and NO$_3$ were not included in the estimation of τ. The lifetimes calculated by Eq. 5.2 are summarised in Table 5.6.

Table 5.6: Atmospheric lifetime estimates for cyclopentanone (CPO) and cyclopentyl methyl ether (CPME).

Solvent	τ_p (hr)[a]	τ_{OH} (hr)[b]	τ_{Cl} (hr)[c]	τ_{TOT} (hr)[d]
CPME	-	15	90	13
CPO	77	87	230	35

Notes: [a] = The τ_p value is intended for a quantum yield of 0.16 as recommended by the MCM and cross section determined in cyclohexane in this work, scaled by a factor 0.93. [b] = lifetime for an OH average concentration of 1.13×10^6 molecule cm^{-3} (Lelieveld et al., 2016). [c] = lifetime for [Cl] = 1×10^4 molecule cm^{-3} (Li et al., 2018). The rate constant for the reaction with CPO used for the lifetime calculation is equal to 1.16×10^{-10} cm^3 molecule^{-1} s^{-1} as reported by Takahashi et al. (2007). [d] = overall lifetime derived from Equation 5.2.

The overall lifetime τ_{TOT} estimated for CPME in the selected conditions ([OH] = 1×10^6 molecule cm^{-3} (Lelieveld et al., 2016), [Cl] = 1×10^4 molecule cm^{-3} (Li et al., 2018)) is 13 hours. This value is a useful indicator of the compound reactivity, but it doesn't account for the

complexity of the atmosphere and the day-and-night cycle that will affect CPME's removal in the atmosphere.

The overall lifetime for CPO is 35 hours in the selected conditions (θ = 60°, 350 DU, [OH] = 1.13×10^6 molecule cm^{-3}, [Cl] = 1×10^4 molecule cm^{-3}) and a photolysis rate of j_{CPO} = 3.6×10^{-6} s^{-1} that was estimated using $\phi = \phi_{MEK}$ = 0.16. However, this value is highly uncertain because of the lack of quantum yield data; the CPO lifetime may be as small as 9 hours when φ = 1 and as large as 63 hours, if φ = 0. These results indicate that both molecules are very reactive in the troposphere, and that CPO's photo-reactivity is likely to be more variable and subject to the atmospheric conditions and altitude that may encourage degradation via photolysis. A deeper knowledge of the quantum yield for R5.5 would be crucial for a more reliable assessment of CPO's lifetime.

Having determined the rate coefficients for the main degradation processes in the troposphere, these can be used in the estimation of the Photochemical Ozone Creation Potential (POCP$_E$) formulated by Jenkin et al. (2017). We calculated a value of 45 for CPME and 26 for CPO (Table A3). This result reflects the higher reactivity of CPME towards OH and the supposedly low impact of CPO's photodecomposition on O$_3$ formation. In fact, the photolysis parameter P recommended by Jenkin et al. (2017) for cyclic ketones is equal to 0, and it is based on the low quantum yield of CHO for the production of radicals. However, the limited quantum yield data for CHO's photolysis (Calvert et al., 2011a), suggests that caution should be taken when using this approximation.

CPME has been recommended as a replacement for volatile non-polar solvents, such as toluene, dioxane and tetrahydrofuran (THF). The estimation of the lifetime and POCP$_E$ for these solvents are listed in Table 5.7 together with the results for CPME. The lifetime of CPME relative to OH oxidation is comparable with THF lifetime, which is around 12 h (Moriarty et al., 2003). A fairly similar situation can be observed for 1,4-dioxane, with an overall lifetime of 20 h (Giri et al., 2011; Porter et al., 1997). Toluene on the other hand, has a much longer lifetime of 45 h (Mellouki et al., 2021). If CPME's lifetime seems to be equal or lower than analogous solvents, on the other hand the POCP$_E$ values seem to level out to a value of 40-50 for CPME and all the other solvents considered, indicating that the impact of CPME on air quality will be on the same scale of other solvents it is likely to replace.

Table 5.7: Atmospheric lifetime POCP$_E$ of CPME and, THF, 1,4-Dioxane and Toluene.

Solvent	k_{OH} [a]	τ_{OH} (h)	References	POCP$_E$ [b]
CPME	$(1.59 \pm 0.13) \times 10^{-11}$	15	This work	45
THF	$(1.80 \pm 0.07) \times 10^{-11}$	12	(Moriarty et al., 2003)	56
1,4-Dioxane	$(1.26 \pm 0.02) \times 10^{-11}$	20	(Porter et al., 1997)	37
Toluene	$(5.60 \pm 0.06) \times 10^{-12}$	45	(Mellouki et al., 2021)	44

Notes: [a] rate coefficients in cm^3 molecule^{-1} s^{-1}. [b] POCP$_E$ values estimated according to Jenkin et al. (2017).

6. Conclusions

The urge to replace toxic and pollutant solvents in large scale chemical processes has brought to the scientific attention the selection of an alternative, often indicated as 'green' solvents. Despite solvent uses having been identified as one of the most important sources of air pollution, air quality considerations were seldom included in the 'green' solvent selection criteria. This work aimed to give prominence to this aspect, providing the chemical information needed for a better understanding of the atmospheric fate of some of these molecules. In particular, the atmospheric chemistry of five promising solvents (TMO, PCO, MPA, CPME, CPO) was investigated studying the reactivity of these OVOCs with OH and Cl, and, when relevant, their photolysis in the troposphere. TMO, PCO and MPA were designed or selected as 'green' solvents by the Green Chemistry Centre of Excellence (GCCE) of the University of York, whereas CPME has been marketed as 'green' solvent from chemical companies and its applications have been studied in several publications. Lastly CPO, a common building block compound, has found application as 'green' alternative to traditional solvents in a few scientific works. Kinetic studies of the reaction of OVOCs with OH were carried out through PLP-LIF experiments and, in the case of TMO and CPME, through RR experiments too. Results for TMO + OH and CPME + OH, which to the best of our knowledge were studied for the first time in this work, showed very good agreement between complementary PLP-LIF and RR studies, lending confidence to the results. Rate coefficients for MPA + OH, PCO + OH and CPO + OH were measured via PLP-LIF and showed good compliance with the scarce literature available. Summarising the kinetic results, PCO and MPA showed the mildest reactivity with OH, with $k_{4.1}(296 \text{ K}) = (1.2 \pm 0.2) \times 10^{-12}$ cm^3 molecule^{-1} s^{-1} and $k_{4.2}(296 \text{ K}) = (1.3 \pm 0.3) \times 10^{-12}$ cm^3 molecule^{-1} s^{-1}, followed by CPO, $k_{5.3}(296 \text{ K}) = (2.8 \pm 0.4) \times 10^{-12}$ cm^3 molecule^{-1} s^{-1} and by TMO, $k_{3.1}(296 \text{ K}) = (3.1 \pm 0.4) \times 10^{-12}$ cm^3 molecule^{-1} s^{-1}. Lastly, CPME recorded the fastest reactivity, with a rate coefficient of $k_{5.1}(296 \text{ K}) = (1.59 \pm 0.05) \times 10^{-11}$ cm^3 molecule^{-1} s^{-1}. Kinetics results were in agreement with SAR calculations (Jenkin et al., 2018) of OVOC + OH in all cases except for TMO, for which the SAR predicted a rate coefficient larger by a factor 3. In this case, SAR were not able to consider steric hindrance factors which make the H-bond interactions of TMO with OH at the CH$_2$ site of the molecule less favourable and formation of the pre-reaction complex more endothermic, slowing down the overall reactivity of the molecule. However, SAR were able to predict the extremely fast reactivity of CPME, giving the right emphasis to the activation of C-H bonds by the ether oxygen. The OVOCs studied in this work showed all an anti-Arrhenius temperature dependence, pointing out the complexity of the gas-phase reactivity of the oxygenated compounds, for which a change in the mechanism is likely to speed up the reaction at low and high temperature. Experiments at $T < 296$ K would be useful to confirm such trend and reduce remaining uncertainties in solvent lifetimes and hence air quality impacts. Of the five OVOCs studied, PCO and CPO present ketone functional group, known to undergo photolysis in the troposphere. This made necessary the investigation of light absorption from these molecules to obtain a broader picture of their chemical fate. UV-vis. studies of PCO and CPO indicated that photolysis could be an important removal process, competing with reaction with OH in conditions typical of the troposphere. Large uncertainties remain due to the lack of quantum yield data. More generally, data obtained here for MEK suggest that absorption experiments conducted dilute in inert solvents (e.g. cyclohexane) can be a useful proxy for gas-phase data. The reaction of OVOC with another important oxidiser of the atmosphere, Cl, was also investigated through RR experiments for TMO + Cl and CPME + Cl obtaining $k_{3.2}(296 \text{ K}) = (1.2 \pm 0.3) \times 10^{-10}$ cm^3 molecules^{-1} s^{-1} and $k_{5.2}(296 \text{ K}) = (3.2 \pm 0.6) \times 10^{-10}$ cm^3 molecule^{-1} s^{-1} respectively. Results showed a fast reactivity of Cl toward OVOC, which overcame the OH rate coefficients by at least one order of

magnitude, suggesting that in the presence of high Cl concentrations, this process could be competitive to the oxidation via OH. From the rate coefficients measured in this work, values of lifetimes for the average concentration of OH and Cl and for standard conditions of solar flux were estimated. MPA and PCO were the slowest reacting molecules with a lifetime of 9 days, followed by TMO with a lifetime of 3 days (80 hours), CPO with 63 hours, and CPME with 13 hours. Including the photolysis rate into the calculation, lifetime of PCO and CPO were estimated to drop down to 3 days and 35 hours respectively, in the selected conditions. However, these values are highly uncertain because of the lack of quantum yield information and could vary considerably. Lastly, $POCP_E$ values were also estimated according to Jenkin et al. (2017) procedure. MPA recorded the lowest $POCP_E$ with a value of 11, due to the slow reactivity with OH and no chance of photolysis in the troposphere. Similarly, a value of 18 was estimated for TMO. A value of 26 was calculated for both CPO and PCO. The two ketones showed a difference in reactivity with OH of a factor two, but while the photolysis parameter P was null for CPO because the first step of photodecomposition for this molecule does not lead to formation of radicals, a P of 14 was assigned to PCO, rising the $POCP_E$ consistently and reaching a value of 26 despite the milder reactivity with OH. Finally, the largest $POCP_E$ of 45 was estimated for CPME, which thanks to its fast reactivity with OH reached the high $POCP_E$ of toluene (44). Strong limitations to the use of $POCP_E$ for the assessment of OVOC were the lack of quantum yield information and thus the uncertainty on the photolysis parameter, together with the absence of a parameter for other oxidisers such as Cl. All in all, we conclude that this study provided useful kinetic data on the major removal pathways for five promising 'green' solvents. Experimental observations proved to be much needed for molecules with a certain degree of complexity, for which SAR are to this day still not reliable. Comparing the results with properties of the known problematic solvents that need replacement in the chemical industry, almost all the 'green' candidates observed, except for CPME, seem to have a milder reactivity in the troposphere that could be less problematic for air quality, according to the aspects considered in this work. However, it is important to stress out that lifetimes and $POCP_E$ of OVOCs, should be only treated as indicators of the general behaviour of the molecule. Before replacing toluene or any other traditional solvent used in large scale with one of these 'green' alternatives, a proper assessment of the impact on air quality, based on atmospheric modelling, would be required, and it would now be possible and more accurate using the rate coefficients determined in this work.

7. Abbreviations

2,2,5-TMO: 2,2,5-Trimethyloxolane
2,2-DMO: 2,2-Dimethyloxolane
2,5-DMO: 2,5-Dimethyloxolane
2-MO: 2-Methyloxolane
API: Active Pharmaceutical Ingredient
BDE: Bond Dissociation Energy
CPME: Cyclopentyl Methyl Ether
CPO: Cyclopentanone
ESP: Electrostatic Potential
FTIR: Fourier-Transform Infrared Spectroscopy
G4: Gaussian 4
GC: Gas Chromatography
GCCE: Green Chemistry Centre of Excellence
GC-MS: Gas Chromatography – Mass Spectrometry
IUPAC: International Union of Pure and Applied Chemistry
LIF: Laser Induced Fluorescence
MCM: Master Chemical Mechanism
MEK: Methyl Ethyl Ketone
MFC: Mass Flow Controller
MPA: Methyl Pivalate
MSDS: Material Safety Data Sheet
NCAR: National Centre for the Atmospheric Research
NEA: Nuclear Ensemble Approach
NIST: National Institute of Standards and Technology
OVOC: Oxygenated Volatile Organic Compound
PCO: Pinacolone
PLP: Pulsed Laser Photolysis
PM: Particulate Matter
PMT: Photomultiplier Tube
POCP: Photochemical Ozone Creation Potential
POCP$_E$: Estimated Photochemical Ozone Creation Potential
Pre-RC: Pre-Reaction Complex
Post-RC: Post-Reaction Complex
QMT: Quantum-Mechanical Tunnelling
RR: Relative Rate
SAR: Structure Activity Relationship
SOA: Secondary Organic Aerosol

TMO: 2,2,5,5-Tertramethyloxolane
TS: Transition State
TUV: Tropospheric Ultraviolet Visible
UV: Ultraviolet
UV-vis.: Ultraviolet-visible
VNP: Volatile Non-Polar
VOC: Volatile Organic Compound

8. Appendix A: Uncertainty of VOC concentration in PLP-LIF

Table A1: Uncertainty of Bulb Concentration determined via Eq.2.4-2.6 (Section 2.1.2)

ΔP (ΔP_{10Torr} or ΔP_{tot})[a]	CG[b]	ΔCG[c]	I[d]	ΔI[e]	Δc_{bulb}
0.23	0.98	0.02	1.30	0.09	**0.03**

Notes: values here reported were estimated for a typical VOC bulb with a concentration of 0.5 molecule cm³. [a] ΔP_{10Torr} is the mean difference between the minimum and maximum 1000 Torr gauge pressure readings for the corresponding value of the 10 Torr gauge read during different calibrations. [b] Mean Calibration Gradient. [c] Standard deviation of the CG. [d] Mean Intercept of the calibration plot. [e] Standard deviation of I.

Table A2: Uncertainty of gas flow rates in PLP-LIF apparatus (ΔF)

$$F = F_r \times CG + I$$
$$\Delta_F = \sqrt{(\Delta(F_r \times CG))^2 + (\Delta I)^2}$$

	ΔF_r	CG[b]	ΔCG[c]	I[d]	ΔI[e]	ΔF[f]
MFC1	0.63	0.98	0.02	1.30	0.09	**0.63**
MFC2	3.40	0.95	0.01	-8.58	4.16	**3.24**
MFC3	6.48	1.03	0.02	-1.09	1.43	**6.64**
MFC4	9.88	0.96	0.03	4.78	2.60	**9.48**
$\sum_i F_{MFC_i}$	20.0					
$\Delta\left(\sum_i F_{MFC_i}\right)$	3.3					

Notes: [a] ΔF_r is the mean difference between the minimum and maximum Flowmeter readings for the corresponding value of the MFC for different calibrations (sccm). [b] CG stand for mean Calibration Gradient. [c] ΔCG is the standard deviation of the CG. [d] Mean Intercept of the calibration plot. [e] Standard deviation of I.

Table A3: Exemplary estimates of the uncertainty of VOC concentration in the reactor cell.

F_{voc}[a]	c_{VOC}[b]	Δc_{VOC}[c]	%
10	0.71	0.08	10.9
20	1.60	0.15	9.2
30	2.50	0.22	8.6
40	3.43	0.29	8.4
50	4.37	0.36	8.2
60	5.33	0.43	8.1
70	6.31	0.50	8.0
80	7.31	0.58	7.9
90	8.33	0.66	7.9
100	9.37	0.74	7.9

Notes: c_{VOC} values here reported were estimated for a typical experiment at 298 K and 60 Torr, using a VOC bulb with a concentration of 0.5 molecule cm³. [a] F is the MFC3 flow rate (VOC flow) in sccm. [b] Concentration of VOC in the reactor cell expressed in 10^{14} molecule cm³. [c] Uncertainty in 10^{14} molecule cm³.

9. Appendix B: POCP$_E$ parameters from Jenkin et al. (2018) (EU)

$$\text{POCP}_E = (A \times \gamma_s \times R \times S \times F) + P + R_{O_3} - Q \qquad\qquad \text{(Eq.1.9)}$$

$$\gamma_s = \left(\frac{n_b}{6}\right) \times \left(\frac{28.05}{M}\right) \qquad \gamma_R = \left(\frac{k_{OH}}{k_{OH'}}\right) \times \left(\frac{6}{n_b}\right) \qquad S = (1-\alpha) \times exp\left(-C \times n_C^\beta\right) + \alpha \qquad R = 1 - (B \times \gamma_R + 1)^{-1}$$

Table A3: Parameters for the estimation of POCP$_E$ of the compounds of interest										
	TMO	**2-MO**	**2,5-DMO**	**2,2,5-TMO**	**2,2-DMO**	**THF**	**PCO**	**MPA**	**CPME**	**CPO**
A	100	100	100	100	100	100	100	100	100	100
n_B	24	13	17	20	17	11	15	15	16	13
M	128.21	86.13	100.16	114.19	100.16	72.11	100.16	116.16	100.16	84.12
γ_s	0.84	0.71	0.79	0.82	0.79	0.71	0.70	0.60	0.75	0.72
B	4	4	4	4	4	4	4	4	4	4
γ_r	0.10	1.12	2.05	0.55	0.62	1.26	0.06	0.07	0.72	0.17
R	0.28	0.82	0.89	0.69	0.71	0.83	0.20	0.21	0.74	0.40
k_{OH}[a]	3.1	19	45	14	14	18	1.2	1.3	15	2.8
$k_{OH'}(C_2H_4)$[a]	7.8	7.8	7.8	7.8	7.8	7.8	7.8	7.8	7.8	7.8
A	0.56	0.56	0.56	0.56	0.56	0.56	0.56	0.56	0.56	0.56
C	0	0	0	00	0	0	0	0	0	0
n_C	8	5	6	5	6	4	6	6	6	5
B	2.70	2.70	2.70	2.70	2.70	2.70	2.70	2.70	2.70	2.70
S	0.72	0.89	0.83	0.89	0.83	0.93	0.83	0.83	0.83	0.89
F	1	1	1	1	1	1	1	1	1	1
P	0	0	0	0	0	0	14	0	0	0
R_{O3}	0	0	0	0	0	0	0	0	0	0
Q	0	0	0	0	0	0	0	0	0	0
POCP$_E$	**17**	**51**	**59**	**50**	**47**	**56**	**26**	**11**	**45**	**26**
Notes:[a] Rate coefficients are in 10^{-12} cm^3 molecule^{-1} s^{-1}.										

10. Table of Figures

Chapter 1

Chapter 2

Chapter 3

Chapter 5

11.   References

Master Chemical Mechanism: http://mcm.leeds.ac.uk/MCM, last

Abreu, C. M. R., Maximiano, P., Guliashvili, T., Nicolas, J., Serra, A. C., and Coelho, J. F. J.: Cyclopentyl methyl ether as a green solvent for reversible-addition fragmentation chain transfer and nitroxide-mediated polymerizations, RSC Adv., 6, 7495-7503, 10.1039/C5RA21975B, 2016.

Alder, C. M., Hayler, J. D., Henderson, R. K., Redman, A. M., Shukla, L., Shuster, L. E., and Sneddon, H. F.: Updating and further expanding GSK's solvent sustainability guide, Green Chem., 18, 3879-3890, 10.1039/C6GC00611F, 2016.

Alwe, H. D., Walawalkar, M., Sharma, A., Pushpa, K. K., Dhanya, S., and Naik, P. D.: Rate Coefficients for the Gas-Phase Reactions of Chlorine Atoms with Cyclic Ethers at 298 K, Int. J. Chem. Kinet., 45, 295-305, 10.1002/kin.20765, 2013.

Anastas, P. and Eghbali, N.: Green Chemistry: Principles and Practice, Chem. Soc. Rev., 39, 301-312, 10.1039/B918763B, 2010.

Andersen, C., Nielsen, O. J., Østerstrøm, F. F., Ausmeel, S., Nilsson, E. J. K., and Sulbaek Andersen, M. P.: Atmospheric Chemistry of Tetrahydrofuran, 2-Methyltetrahydrofuran, and 2,5-Dimethyltetrahydrofuran: Kinetics of Reactions with Chlorine Atoms, OD Radicals, and Ozone, J. Phys. Chem. A, 120, 7320-7326, 10.1021/acs.jpca.6b06618, 2016.

Anderson, R. S., Huang, L., Iannone, R., and Rudolph, J.: Measurements of the 12C/13C kinetic isotope effects in the gas-phase reactions of light alkanes with chlorine atoms, J. Phys. Chem. A, 111, 495-504, 10.1021/jp064634p, 2007.

Atkinson, R.: Kinetics and mechanisms of the gas-phase reactions of the hydroxyl radical with organic compounds under atmospheric conditions, Chem. Rev., 86, 69-201, 10.1021/cr00071a004, 1986.

Atkinson, R., Baulch, D. L., Cox, R. A., Crowley, J. N., Hampson, R. F., Hynes, R. G., Jenkin, M. E., Rossi, M. J., and Troe, J.: Evaluated kinetic and photochemical data for atmospheric chemistry: Volume I - gas phase reactions of Ox, HOx, NOx and SOx species, Atmos. Chem. Phys., 4, 1461-1738, 10.5194/acp-4-1461-2004, 2004.

Atkinson, R., Baulch, D. L., Cox, R. A., Crowley, J. N., Hampson, R. F., Hynes, R. G., Jenkin, M. E., Rossi, M. J., and Troe, J.: Evaluated kinetic and photochemical data for atmospheric chemistry: Volume II - gas phase reactions of organic species, Atmos. Chem. Phys., 6, 3625-4055, 10.5194/acp-6-3625-2006, 2006.

Aycock, D. F.: Solvent Applications of 2-Methyltetrahydrofuran in Organometallic and Biphasic Reactions, Org. Process Res. Dev., 11, 156-159, 10.1021/op060155c, 2007.

Azzena, U., Carraro, M., Pisano, L., Monticelli, S., Bartolotta, R., and Pace, V.: Cyclopentyl Methyl Ether: An Elective Ecofriendly Ethereal Solvent in Classical and Modern Organic Chemistry, Chem. Sus. Chem., 12, 40-70, 10.1002/cssc.201801768, 2019.

Baasandorj, M., Papanastasiou, D. K., Talukdar, R. K., Hasson, A. S., and Burkholder, J. B.: (CH3)3COOH (tert-butyl hydroperoxide): OH reaction rate coefficients between 206 and 375 K and the OH photolysis quantum yield at 248 nm, Phys. Chem. Chem. Phys., 12, 12101-12111, 10.1039/c0cp00463d, 2010.

Bao, X. J., Y. ; Wang, C. ; Xu, H. ; Lattimore, T. ; Tang, L. : Laminar flame characteristics of cyclopentanone at elevated temperatures, Appl. Energy, 195, 671-680, 10.1016/j.apenergy.2017.03.031, 2017.

Beauregard, D.: Locating and estimating air emissions from sources of toluene, 1993.

Fluorescence Spectrum Viewer: https://www.aatbio.com/fluorescence-excitation-emission-spectrum-graph-viewer, last

Brewer, J. F., Papanastasiou, D. K., Burkholder, J. B., Fischer, E. V., Ren, Y., Mellouki, A., and Ravishankara, A. R.: Atmospheric Photolysis of Methyl Ethyl, Diethyl, and Propyl Ethyl Ketones: Temperature-Dependent UV Absorption Cross Sections, J. Geophys. Res., 124, 5906-5918, https://doi.org/10.1029/2019JD030391, 2019.

Byrne, F., Forier, B., Bossaert, G., Hoebers, C., Farmer, T. J., Clark, J. H., and Hunt, A. J.: 2,2,5,5-Tetramethyltetrahydrofuran (TMTHF): a non-polar, non-peroxide forming ether replacement for hazardous hydrocarbon solvents, Green Chem., 19, 3671-3678, 10.1039/C7GC01392B, 2017.

Byrne, F. P., Hodds, W. M., Shimizu, S., Farmer, T. J., and Hunt, A. J.: A comparison of the solvation power of the green solvent 2,2,5,5-tetramethyloxolane versus toluene via partition coefficients, J. Clean. Prod., 240, 118175, https://doi.org/10.1016/j.jclepro.2019.118175, 2019.

Byrne, F. P., Forier, B., Bossaert, G., Hoebers, C., Farmer, T. J., and Hunt, A. J.: A methodical selection process for the development of ketones and esters as bio-based replacements for traditional hydrocarbon solvents, Green Chem., 20, 4003-4011, 10.1039/c8gc01132j, 2018.

Byrne, F. P., Jin, S., Paggiola, G., Petchey, T. H. M., Clark, J. H., Farmer, T. J., Hunt, A. J., Robert McElroy, C., and Sherwood, J.: Tools and techniques for solvent selection: green solvent selection guides, Sustain. Chem. Process., 4, 7, 10.1186/s40508-016-0051-z, 2016.

Calvert, J., Mellouki, A., and Orlando, J.: Mechanisms of Atmospheric Oxidation of the Oxygenates, Oxford University Press, USA2011a.

Calvert, J. G., Orlando, J. J., Stockwell, W. R., and Wallington, T. J.: The Mechanisms of Reactions Influencing Atmospheric Ozone, Oxford University Press2015.

Calvert, J. G., Mellouki, A., Orlando, J. J., Pilling, M. J., and Wallington, T. J., Press, O. U. (Ed.): The mechanism of atmospheric oxidation of the oxygenates, 2011b.

Carr, S., Shallcross, D. E., Canosa-Mas, C. E., Wenger, J. C., Sidebottom, H. W., Treacy, J. J., and Wayne, R. P.: A kinetic and mechanistic study of the gas-phase reactions of OH

radicals and Cl atoms with some halogenated acetones and their atmospheric implications, Phys. Chem. Chem. Phys., 5, 3874-3883, 10.1039/B304298G, 2003.

Carr, S. A., Baeza-Romero, M. T., Blitz, M. A., Price, B. J. S., and Seakins, P. W.: Ketone photolysis in the presence of oxygen: A useful source of OH for flash photolysis kinetics experiments, Int. J. Chem. Kinet., 40, 504-514, 10.1002/kin.20330, 2008.

Ceacero-Vega, A. A., Ballesteros, B., Albaladejo, J., Bejan, I., and Barnes, I.: Temperature dependence of the gas-phase reactions of Cl atoms with propene and 1-butene between 285<T<313K, Chem. Phys. Lett., 484, 10-13, 10.1016/j.cplett.2009.10.080, 2009.

Chimichi, S. and Mealli, C.: A description of the effects of silyl vs. alkyl substituents in ketones in the light of oxygen-17 NMR data and with the help of qualitative MO theory, J. Molec. Struct., 271, 133-148, https://doi.org/10.1016/0022-2860(92)80216-5, 1992.

Christianson, M. G., Doner, A. C., Koritzke, A. L., Frandsen, K., and Rotavera, B.: Vacuum-ultraviolet absorption cross-sections of functionalized cyclic hydrocarbons: Five-membered rings, J. Quant. Spectros. Radiat. Transf., 258, 107274, 10.1016/j.jqsrt.2020.107274, 2021.

Clark, J., H., Hunt, A., Topi, C., Peggiola, G., and Sherwood, J.: CHAPTER 1 Introduction to Solvents and Sustainable Chemistry, in: Sustainable Solvents: Perspectives from Research, Business and International Policy, edited by: Chemistry, R. S. o., The Royal Society of Chemistry, 1-34, 10.1039/9781782624035-00001, 2017.

Curchod, B. F. E. and Hollas, D.: Personal Communication, 2023.

Curtiss, L. A., Redfern, P. C., and Raghavachari, K.: Gaussian-4 theory, J. Chem. Phys., 126, 124105, 10.1063/1.2436888, 2007.

Dagaut, P., Wallington, T. J., Liu, R., and Kurylo, M. J.: A kinetic investigation of the gas-phase reactions of hydroxyl radicals with cyclic ketones and diones: mechanistic insights, J. Phys. Chem., 92, 4375-4377, 10.1021/j100326a026, 1988.

de Gonzalo, G., Alcántara, A. R., and Domínguez de María, P.: Cyclopentyl Methyl Ether (CPME): A Versatile Eco-Friendly Solvent for Applications in Biotechnology and Biorefineries, ChemSusChem, 12, 2083-2097, 10.1002/cssc.201900079, 2019.

DeMore, W. B. and Bayes, K. D.: Rate Constants for the Reactions of Hydroxyl Radical with Several Alkanes, Cycloalkanes, and Dimethyl Ether, J. Phys. Chem. A, 103, 2649-2654, 10.1021/jp983273d, 1999.

Derwent, R. G., Jenkin, M. E., and Saunders, S. M.: Photochemical ozone creation potentials for a large number of reactive hydrocarbons under European conditions, Atmos. Environ., 30, 181-199, https://doi.org/10.1016/1352-2310(95)00303-G, 1996.

Dillon, T. J., Holscher, D., and Sivakumaran, V.: Kinetics of the reactions of HO with methanol (210−351 K) and with ethanol (216−368 K), Phys. Chem. Chem. Phys., 7, 349-355, 10.1039/b413961e, 2005.

Duereh, A., Guo, H. X., Honma, T., Hiraga, Y., Sato, Y., Smith, R. L., and Inomata, H.: Solvent Polarity of Cyclic Ketone (Cyclopentanone, Cyclohexanone): Alcohol (Methanol, Ethanol) Renewable Mixed-Solvent Systems for Applications in Pharmaceutical and Chemical Processing, Ind. Eng. Chem. Res., 57, 7331-7344, 10.1021/acs.iecr.8b00689, 2018.

U.S. Energy Information Administration: https://www.eia.gov/energyexplained/oil-and-petroleum-products/refining-crude-oil.php, last

EP: Directive 2010/75/EU of the european parliament and of the council, 2010.

Initial List of Hazardous Air Pollutants with Modifications - US Environmental Protection Agency: https://www.epa.gov/haps/initial-list-hazardous-air-pollutants-modifications, last

European Solvent Industry Group: https://www.esig.org/, last

Cernesim Simulation Chamber: https://www.eurochamp.org/simulation-chambers/CERNESIM, last

Fantechi, G., Jensen, N. R., Saastad, O., Hjorth, J., and Peeters, J.: Reactions of Cl Atoms with Selected VOCs: Kinetics, Products and Mechanisms, J. Atmos. Chem., 31, 247-267, 10.1023/A:1006033910014, 1998.

Farmer, T. J. and Mascal, M.: Platform Molecules, in: Introduction to Chemicals from Biomass, 89-155, https://doi.org/10.1002/9781118714478.ch4, 2015.

Faxon, C. B. and Allen, D. T.: Chlorine chemistry in urban atmospheres: a review, Environ. Chem., 10, 221-233, https://doi.org/10.1071/EN13026, 2013.

Finlayson-Pitts, B. J. and Pitts, J. N.: CHAPTER 5 - Kinetics and Atmospheric Chemistry, in: Chemistry of the Upper and Lower Atmosphere, edited by: Finlayson-Pitts, B. J., and Pitts, J. N., Academic Press, San Diego, 130-178, https://doi.org/10.1016/B978-012257060-5/50007-1, 2000.

Frisch, M. J., Trucks, G. W., Schlegel, H. B., Scuseria, G. E., Robb, M. A., Cheeseman, J. R., Scalmani, G., Barone, V., Petersson, G. A., Nakatsuji, H., Li, X., Caricato, M., Marenich, A. V., Bloino, J., Janesko, B. G., Gomperts, R., Mennucci, B., Hratchian, H. P., Ortiz, J. V., Izmaylov, A. F., Sonnenberg, J. L., Williams, Ding, F., Lipparini, F., Egidi, F., Goings, J., Peng, B., Petrone, A., Henderson, T., Ranasinghe, D., Zakrzewski, V. G., Gao, J., Rega, N., Zheng, G., Liang, W., Hada, M., Ehara, M., Toyota, K., Fukuda, R., Hasegawa, J., Ishida, M., Nakajima, T., Honda, Y., Kitao, O., Nakai, H., Vreven, T., Throssell, K., Montgomery Jr., J. A., Peralta, J. E., Ogliaro, F., Bearpark, M. J., Heyd, J. J., Brothers, E. N., Kudin, K. N., Staroverov, V. N., Keith, T. A., Kobayashi, R., Normand, J., Raghavachari, K., Rendell, A. P., Burant, J. C., Iyengar, S. S., Tomasi, J., Cossi, M., Millam, J. M., Klene, M., Adamo, C., Cammi, R., Ochterski, J. W., Martin, R. L., Morokuma, K., Farkas, O., Foresman, J. B., and Fox, D. J.: Gaussian 09 Rev. D.01 [code], 2016.

Gierczak, T., Gilles, M. K., Bauerle, S., and Ravishankara, A. R.: Reaction of Hydroxyl Radical with Acetone. 1. Kinetics of the Reactions of OH, OD, and 18OH with Acetone and Acetone-d6, J. Phys. Chem. A, 107, 5014-5020, 10.1021/jp027301a, 2003.

Giri, B. R. and Roscoe, J. M.: Kinetics of the reactions of Cl atoms with several ethers, J. Phys. Chem. A, 114, 8369-8375, 10.1021/jp1037409, 2010.

Giri, B. R., Roscoe, J. M., Gonzalez-Garcia, N., Olzmann, M., Lo, J. M. H., and Marriott, R. A.: Experimental and Theoretical Investigation of the Kinetics of the Reaction of Atomic Chlorine with 1,4-Dioxane, J. Phys. Chem. A, 115, 5105-5111, 10.1021/jp201803g, 2011.

Gołąbek, K., Shamzhy, M., Kubů, M., Soták, T., Magyarová, Z., Hronec, M., and Čejka, J.: Adsorption and catalytic study of cyclopentyl methyl ether formation: structure-activity interplay in medium-pore zeolites, Appl. Mater. Today, 28, 101505, https://doi.org/10.1016/j.apmt.2022.101505, 2022.

2010 to 2015 government policy: transport emissions: https://www.gov.uk/government/publications/2010-to-2015-government-policy-transport-emissions/2010-to-2015-government-policy-transport-emissions, last

Grochowski, M. R., Yang, W., and Sen, A.: Mechanistic study of a one-step catalytic conversion of fructose to 2,5-dimethyltetrahydrofuran, Chemistry, 18, 12363-12371, 10.1002/chem.201201522, 2012.

Hess, W. P. and Tully, F. P.: Catalytic conversion of alcohols to alkenes by OH, Chem. Phys. Lett., 152, 183-189, https://doi.org/10.1016/0009-2614(88)87352-4, 1988.

Hess, W. P. and Tully, F. P.: Hydrogen-Atom Abstraction from Methanol by OH, J. Am. Chem. Soc., 93, 1944-1947, 1989.

Höfer, R.: Chapter 1 History of the Sustainability Concept – Renaissance of Renewable Resources, in: Sustainable Solutions for Modern Economies, The Royal Society of Chemistry, 1-11, 10.1039/9781847552686-00001, 2009.

Hronec, M. and Fulajtarová, K.: Selective transformation of furfural to cyclopentanone, Catal. Commun., 24, 100-104, https://doi.org/10.1016/j.catcom.2012.03.020, 2012.

Hynes, A. J., Kenyon, E. A., Pounds, A. J., and Wine, P. H.: Temperature dependent absorption cross-sections for acetone and n-butanone—implications for atmospheric lifetimes, Spectrochim. Acta Part A Mol. Spectrosc., 48, 1235-1242, https://doi.org/10.1016/0584-8539(92)80260-4, 1992.

Illes, A., Farkas, M., Zugner, G. L., Novodarszki, G., Mihalyi, M., and Dobe, S.: Direct and relative rate coefficients for the gas-phase reaction of OH radicals with 2-methyltetrahydrofuran at room temperature, React. Kinet. Mech. Catal., 119, 5-18, 10.1007/s11144-016-1037-2, 2016.

Jacobson, M. Z.: Atmospheric Pollution: History, Science, and Regulation, Cambridge University Press, Cambridge, DOI: 10.1017/CBO9780511802287, 2002.

Jenkin, M. E., Derwent, R. G., and Wallington, T. J.: Photochemical ozone creation potentials for volatile organic compounds: Rationalization and estimation, Atmos. Environ., 163, 128-137, 10.1016/j.atmosenv.2017.05.024, 2017.

Jenkin, M. E., Saunders, S. M., and Pilling, M. J.: The tropospheric degradation of volatile organic compounds: A protocol for mechanism development, Atmos. Environ., 31, 81-104, 10.1016/s1352-2310(96)00105-7, 1997.

Jenkin, M. E., Saunders, S. M., Wagner, V., and Pilling, M. J.: Protocol for the development of the Master Chemical Mechanism, MCM v3 (Part B): tropospheric degradation of aromatic volatile organic compounds, Atmospheric Chemistry and Physics, 3, 181-193, 10.5194/acp-3-181-2003, 2003.

Jenkin, M. E., Valorso, R., Aumont, B., Rickard, A. R., and Wallington, T. J.: Estimation of rate coefficients and branching ratios for gas-phase reactions of OH with aliphatic organic compounds for use in automated mechanism construction, Atmos. Chem. Phys., 17, 9297–9328, 10.5194/acp-18-9297-2018, 2018.

Jimenez-Gonzalez, C., Ponder, C. S., Broxterman, Q. B., and Manley, J. B.: Using the Right Green Yardstick: Why Process Mass Intensity Is Used in the Pharmaceutical Industry To Drive More Sustainable Processes, Org. Process Res. Dev., 15, 912-917, 10.1021/op200097d, 2011.

Jiménez-González, C., Curzons, A. D., Constable, D. J. C., and Cunningham, V. L.: Cradle-to-gate life cycle inventory and assessment of pharmaceutical compounds, Int. J. Life Cycle Assess., 9, 114-121, 10.1007/BF02978570, 2004.

Jiménez, E., Gilles, M. K., and Ravishankara, A. R.: Kinetics of the reactions of the hydroxyl radical with CH_3OH and C_2H_5OH between 235 and 360 K, J. Photochem. Photobiol. A Chem., 157, 237-245, 10.1016/S1010-6030(03)00073-X, 2003.

Jiménez, E., Ballesteros, B., Martínez, E., and Albaladejo, J.: Tropospheric Reaction of OH with Selected Linear Ketones: Kinetic Studies between 228 and 405 K, Environ. Science Tech., 39, 814-820, 10.1021/es049333c, 2005.

Jones, L., Garland, L., Szanto, C., and King, K.: Air Pollutant Inventories for England, Scotland, Wales and Northern Ireland: 2005-2019 2021.

Joshi, D. R. and Adhikari, N.: An overview on common organic solvents and their toxicity, J. Pharm. Res. Int, 28, 1-18, 2019.

Kinsey, J. L.: Laser-Induced Fluorescence, Ann. Rev. Phys. Chem., 28, 349-372, 10.1146/annurev.pc.28.100177.002025, 1977.

Kwok, E. S. C. and Atkinson, R.: Estimation of hydroxyl radical reaction rate constants for gas-phase organic compounds using a structure-reactivity relationship: An update, Atmos. Environ., 29, 1685-1695, https://doi.org/10.1016/1352-2310(95)00069-B, 1995.

Lawrenson, S., North, M., Peigneguy, F., and Routledge, A.: Greener solvents for solid-phase synthesis, Green Chem., 19, 952-962, 10.1039/c6gc03147a, 2017.

Le Calvé, S., Hitier, D., Le Bras, G., and Mellouki, A.: Kinetic Studies of OH Reactions with a Series of Ketones, J. Phys. Chem. A, 102, 4579-4584, 10.1021/jp980848y, 1998.

Lelieveld, J., Gromov, S., Pozzer, A., and Taraborrelli, D.: Global tropospheric hydroxyl distribution, budget and reactivity, Atmos. Chem. Phys., 16, 12477-12493, 10.5194/acp-16-12477-2016, 2016.

Li, B., Ho, S. S. H., Li, X., Guo, L., Chen, A., Hu, L., Yang, Y., Chen, D., Lin, A., and Fang, X.: A comprehensive review on anthropogenic volatile organic compounds (VOCs) emission estimates in China: Comparison and outlook, Environment International, 156, 106710, https://doi.org/10.1016/j.envint.2021.106710, 2021.

Li, M. Z., Karu, E., Brenninkmeijer, C., Fischer, H., Lelieveld, J., and Williams, J.: Tropospheric OH and stratospheric OH and Cl concentrations determined from CH4, CH3Cl, and SF6 measurements, NPJ Clim. Atmos., 1, 10.1038/s41612-018-0041-9, 2018.

Liu, D., Giri, B. R., and Farooq, A.: Cyclic Ketones as Future Fuels: Reactivity with OH Radicals, J. Phys. Chem. A, 123, 4325-4332, 10.1021/acs.jpca.9b00691, 2019.

Lotze, H. K., Lenihan, H. S., Bourque, B. J., Bradbury, R. H., Cooke, R. G., Kay, M. C., Kidwell, S. M., Kirby, M. X., Peterson, C. H., and Jackson, J. B. C.: Depletion, degradation, and recovery potential of estuaries and coastal seas, Science, 312, 1806-1809, 10.1126/science.1128035, 2006.

Luque, J. and Crosley, D. R.: Transition probabilities and electronic transition moments of the A2Σ+−X2Π and D2Σ+−X2Π systems of nitric oxide, J. Chem. Phys., 111, 7405-7415, 10.1063/1.480064, 1999.

Madronich, S. and Flocke, S.: Theoretical estimation of biologically effective UV radiation at the Earth's surface., in: Solar ultraviolet radiation, Springer, Berlin, Heidelberg, 23-48, 1997.

NIST Chemical Kinetics Database: https://kinetics.nist.gov/, last access: November 2022.

Mapelli, C., Donnelly, J. K., Hogan, Ú. E., Rickard, A. R., Robinson, A. T., Byrne, F., McElroy, C. R., Curchod, B. F. E., Hollas, D., and Dillon, T. J.: Atmospheric oxidation of new "green" solvents – Part 2: methyl pivalate and pinacolone, Atmos. Chem. Phys., 23, 7767-7779, 10.5194/acp-23-7767-2023, 2023.

Mapelli, C., Schleicher, J. V., Hawtin, A., Rankine, C. D., Whiting, F. C., Byrne, F., McElroy, C. R., Roman, C., Arsene, C., Olariu, R. I., Bejan, I. G., and Dillon, T. J.: Atmospheric breakdown chemistry of the new "green" solvent 2,2,5,5-tetramethyloxolane via gas-phase reactions with OH and Cl radicals, Atmos. Chem. Phys., 22, 14589-14602, 10.5194/acp-22-14589-2022, 2022.

Martinez, R. D., Buitrago, A. A., Howell, N. W., Hearn, C. H., and Joens, J. A.: The near U.V. absorption spectra of several aliphatic aldehydes and ketones at 300 K, Atmos. Environ. Part A. Gen. Top., 26, 785-792, https://doi.org/10.1016/0960-1686(92)90238-G, 1992.

McNaught, A. D., appliquée, U. i. d. c. p. e., Wilkinson, A., Jenkins, A. D., Pure, I. U. o., and Chemistry, A.: IUPAC Compendium of Chemical Terminology: The Gold Book, International Union of Pure and Applied Chemistry2006.

Mellouki, A., Le Bras, G., and Sidebottom, H.: Kinetics and Mechanisms of the Oxidation of Oxygenated Organic Compounds in the Gas Phase, Chem. Rev., 103, 5077-5096, 10.1021/cr020526x, 2003.

Mellouki, A., Wallington, T. J., and Chen, J.: Atmospheric chemistry of oxygenated volatile organic compounds: impacts on air quality and climate, Chem. Rev., 115, 3984-4014, 10.1021/cr500549n, 2015.

Mellouki, A., Ammann, M., Cox, R. A., Crowley, J. N., Herrmann, H., Jenkin, M. E., McNeill, V. F., Troe, J., and Wallington, T. J.: Evaluated kinetic and photochemical data for atmospheric chemistry: volume VIII - gas-phase reactions of organic species with four, or more, carbon atoms (>= C-4), Atmos. Chem. Phys., 21, 4797-4808, 10.5194/acp-21-4797-2021, 2021.

Montero-Montoya, R., López-Vargas, R., and Arellano-Aguilar, O.: Volatile Organic Compounds in Air: Sources, Distribution, Exposure and Associated Illnesses in Children, Ann Glob Health, 84, 225-238, 10.29024/aogh.910, 2018.

Montgomery, J. A., Frisch, M. J., Ochterski, J. W., and Petersson, G. A.: A complete basis set model chemistry. VI. Use of density functional geometries and frequencies, J. Chem. Phys., 110, 2822-2827, 10.1063/1.477924, 1999.

Moriarty, J., Sidebottom, H., Wenger, J., Mellouki, A., and Le Bras, G.: Kinetic Studies on the Reactions of Hydroxyl Radicals with Cyclic Ethers and Aliphatic Diethers, J. Phys. Chem. A, 107, 1499-1505, 10.1021/jp021267i, 2003.

NAEI Emission Data https://naei.beis.gov.uk/data/data-selector?view=air-pollutants, last

Nakashima, K., Uchida-Kai, K., Koyanagi, M., and Kanda, Y.: Solvent Effect on the Intensities of Forbidden Bands of Molecules, Bull. Chem. Soc. Jpn., 55, 415-419, 1982a.

Nakashima, K., Uchida-Kai, K., Koyanagi, M., and Kanda, Y.: Solvent Effect on the Intensities of Forbidden Bands of Molecules, Bulletin of the Chemical Society of Japan, 55, 415-419, 1982b.

https://www.nobelprize.org/prizes/chemistry/1967/summary/, last access: November 2021.

Norrish, R. G. W. and Porter, G.: Chemical Reactions Produced by Very High Light Intensities, Nature, 164, 658-658, 10.1038/164658a0, 1949.

ONS, O. f. N. S.-. The spatial distribution of industries in Great Britain: 2015, https://www.ons.gov.uk/employmentandlabourmarket/peopleinwork/employmentandemployeetypes/articles/thespatialdistributionofindustriesingreatbritain/2015, 2015.

Parrique, T., Barth, J., Briens, F., Kerschner, C., Kraus-Polk, A., Kuokkanen, A., and Spangenberg, J., H.: Decoupling Debunked: Evidence and arguments against green growth as a sole strategy for sustainability, European Environmental bureau, 2019.

Phanopoulos, A., White, A. J. P., Long, N. J., and Miller, P. W.: Catalytic Transformation of Levulinic Acid to 2-Methyltetrahydrofuran Using Ruthenium–N-Triphos Complexes, ACS Catal., 5, 2500-2512, 10.1021/cs502025t, 2015.

Phillips, G. J., Tang, M. J., Thieser, J., Brickwedde, B., Schuster, G., Bohn, B., Lelieveld, J., and Crowley, J. N.: Significant concentrations of nitryl chloride observed in rural continental Europe associated with the influence of sea salt chloride and anthropogenic emissions, Geoph. Research Letters, 39, https://doi.org/10.1029/2012GL051912, 2012.

Pinho, P. G., Pio, C. A., and Jenkin, M. E.: Evaluation of isoprene degradation in the detailed tropospheric chemical mechanism, MCM v3, using environmental chamber data, Atmos. Environ., 39, 1303-1322, 10.1016/j.atmosenv.2004.11.014, 2005.

Pocker, Y., Ronald, B. P., and Anderson, K. W.: Epoxides in vicinal diol dehydration. 7. A mechanistic characterization of the spontaneous ring opening process of epoxides in aqueous solution: kinetic and product studies, J. Am. Chem. Soc., 110, 6492-6497, 10.1021/ja00227a033, 1988.

Porter, E., Wenger, J., Treacy, J., Sidebottom, H., Mellouki, A., Teton, S., and LeBras, G.: Kinetic studies on the reactions of hydroxyl radicals with diethers and hydroxyethers, J. Phys. Chem. A, 101, 5770-5775, 10.1021/jp971254i, 1997.

Prat, D., Wells, A., Hayler, J., Sneddon, H., McElroy, C. R., Abou-Shehadad, S., and Dunne, P. J.: CHEM21 selection guide of classical- and less classical-solvents, Green Chem., 18, 288, 10.1039/c5gc01008j, 2016.

Prat, D. P., O. ; Flemming, H. W.; Letestu, S.: Sanofi's Solvent Selection Guide: A Step Toward More Sustainable Processes, 2013.

Prinn, R. G.: The Cleansing Capacity of the Atmosphere, Annu. Rev. Environ. Resour., 28, 29-57, 10.1146/annurev.energy.28.011503.163425, 2003.

https://pubchem.ncbi.nlm.nih.gov/, last

Raber, W. H. and Moortgat, G. K.: Photooxidation of selected carbonyl compounds in air: methyl ethyl ketone, methyl vinyl ketone, methacrolein and methylglyoxal, in: Progress and Problems in Atmospheric Chemistry, 318-373, 10.1142/9789812831712_0009, 1995.

Raff, J. D., Stevens, P. S., and Hites, R. A.: Relative Rate and Product Studies of the OH–Acetone Reaction, J. Phys. Chem. A, 109, 4728-4735, 10.1021/jp0501547, 2005.

Ragothaman, A. and Anderson, W. A.: Air Quality Impacts of Petroleum Refining and Petrochemical Industries, Environments, 4, 66, 2017.

Ran, Y., Byrne, F., Ingram, I. D. V., and North, M.: Resin Swelling in Mixed Solvents Analysed using Hansen Solubility Parameter Space, Chemistry – A European Journal, 25, 4951-4964, https://doi.org/10.1002/chem.201900228, 2019.

Ravishankara, A. R. and Davis, D. D.: Kinetic rate constants for the reaction of hydroxyl with methanol, ethanol, and tetrahydrofuran at 298 K, J. Phys. Chem., 82, 2852-2853, 10.1021/j100515a022, 1978.

Roman, C., Arsene, C., Bejan, I. G., and Olariu, R. I.: Investigations into the gas-phase photolysis and OH radical kinetics of nitrocatechols: implications of intramolecular interactions on their atmospheric behaviour, Atmos. Chem. Phys., 22, 2203-2219, 10.5194/acp-22-2203-2022, 2022.

Romero, M. T., Blitz, M. A., Heard, D. E., Pilling, M. J., Price, B., Seakins, P. W., and Wang, L.: Photolysis of methylethyl, diethyl and methylvinyl ketones and their role in the atmospheric HOx budget, Faraday Discuss., 130, 73-88; discussion 125-151, 519-124, 10.1039/b419160a, 2005.

Saunders, S. M., Jenkin, M. E., Derwent, R. G., and Pilling, M. J.: Protocol for the development of the Master Chemical Mechanism, MCM v3 (Part A): tropospheric degradation of non-aromatic volatile organic compounds, Atmos. Chem. Phys., 3, 161-180, 10.5194/acp-3-161-2003, 2003.

Seinfeld, J. H. and Pandis, S. N.: Atmospheric Chemistry and Physics: From Air Pollution to Climate Change, Wiley2016.

Shannon, R. J., Blitz, M. A., Goddard, A., and Heard, D. E.: Accelerated chemistry in the reaction between the hydroxyl radical and methanol at interstellar temperatures facilitated by tunnelling, Nat Chem, 5, 745-749, 10.1038/nchem.1692, 2013.

Greener solvent alternatives: https://www.sigmaaldrich.com/deepweb/assets/sigmaaldrich/product/documents/115/677/greener_solvent_alternatives.pdf, last

Sims, I. R.: Low-temperature reactions: Tunnelling in space, Nature Chemistry, 5, 734-736, 10.1038/nchem.1736, 2013.

Singh, R., Singh, R., and Shukla, A.: Volatile Organic Compounds in India: Concentration and Sources, J. Civ. Environ. Eng., 6, 251, 10.4172/2165-784X.1000251, 2016.

Spicer, C. W., Chapman, E. G., Finlayson-Pitts, B. J., Plastridge, R. A., Hubbe, J. M., Fast, J. D., and Berkowitz, C. M.: Unexpectedly high concentrations of molecular chlorine in coastal air, Nature, 394, 353-356, 10.1038/28584, 1998.

Stepien, D. K., Diehl, P., Helm, J., Thoms, A., and Püttmann, W.: Fate of 1,4-dioxane in the aquatic environment: from sewage to drinking water, Water Res., 48, 406-419, 10.1016/j.watres.2013.09.057, 2014.

Takahashi, K., Iwasaki, E., Matsumi, Y., and Wallington, T. J.: Pulsed laser photolysis vacuum UV laser-induced fluorescence kinetic study of the gas-phase reactions of Cl(2P3/2) atoms with C3-C6 ketones, J. Phys. Chem. A, 111, 1271-1276, 10.1021/jp066410c, 2007.

Talukdar, R. K., Gierczak, T., McCabe, D. C., and Ravishankara, A. R.: Reaction of Hydroxyl Radical with Acetone. 2. Products and Reaction Mechanism, J. phys. Chem. A, 107, 5021-5032, 10.1021/jp0273023, 2003.

Tango, W. J., Link, J. K., and Zare, R. N.: Spectroscopy of K2 Using Laser-Induced Fluorescence, j. chem. phys., 49, 4264-4268, 10.1063/1.1669869, 1968.

Thion, S., Togbé, C., Dayma, G., Serinyel, Z., and Dagaut, P.: Experimental and Detailed Kinetic Modeling Study of Cyclopentanone Oxidation in a Jet-Stirred Reactor at 1 and 10 atm, Energy Fuels, 31, 2144-2155, 10.1021/acs.energyfuels.6b02061, 2017.

Thornton, J. A., Kercher, J. P., Riedel, T. P., Wagner, N. L., Cozic, J., Holloway, J. S., Dubé, W. P., Wolfe, G. M., Quinn, P. K., Middlebrook, A. M., Alexander, B., and Brown, S. S.: A large atomic chlorine source inferred from mid-continental reactive nitrogen chemistry, Nature, 464, 271-274, 10.1038/nature08905, 2010.

Trowse, B. R., Byrne, F. P., Sherwood, J., O'Brien, P., Murray, J., and Farmer, T. J.: 2,2,5,5-Tetramethyloxolane (TMO) as a Solvent for Buchwald–Hartwig Aminations, ACS Sustain. Chem. Eng., 9, 17330-17337, 10.1021/acssuschemeng.1c06292, 2021.

Tsai, W.-T.: Environmental hazards and health risk of common liquid perfluoro-n-alkanes, potent greenhouse gases, Environ. Int., 35, 418-424, https://doi.org/10.1016/j.envint.2008.08.009, 2009.

https://www.undp.org/sustainable-development-goals/no-poverty?gclid=Cj0KCQjwkqSlBhDaARIsAFJANkg7VXUXV6CcV5Dk8MlXk4Amb-O0dKW1LATaiYEvdvut5LtOtV05MIAaAnevEALw_wcB, last

United Nation Environment Programme - Montreal Protocol: https://www.unep.org/ozonaction/who-we-are/about-montreal-protocol, last

Vasvári, G., Szilágyi, I., Bencsura, Á., Dóbé, S., Bérces, T., Henon, E., Canneaux, S., and Bohr, F.: Reaction and complex formation between OH radical and acetone, Phys. Chem. Chem. Phys., 3, 551-555, 10.1039/B009601F, 2001.

Vereecken, L., Aumont, B., Barnes, I., Bozzelli, J. W., Goldman, M. J., Green, W. H., Madronich, S., Mcgillen, M. R., Mellouki, A., Orlando, J. J., Picquet-Varrault, B., Rickard, A. R., Stockwell, W. R., Wallington, T. J., and Carter, W. P. L.: Perspective on Mechanism Development and Structure-Activity Relationships for Gas-Phase Atmospheric Chemistry, International Journal of Chemical Kinetics, 50, 435-469, https://doi.org/10.1002/kin.21172, 2018.

Voráč, J., Dvořák, P., and Mrkvičková, M.: Laser-Induced Fluorescence of Hydroxyl (OH) Radical in Cold Atmospheric Discharges, in: Photon Counting, edited by: Britun, N., and Nikiforov, A., IntechOpen, Rijeka, 10.5772/intechopen.72274, 2018.

Wallington, T. J. and Kurylo, M. J.: Flash photolysis resonance fluorescence investigation of the gas-phase reactions of hydroxyl radicals with a series of aliphatic ketones over the temperature range 240-440 K, J. Phys. Chem., 91, 5050-5054, 10.1021/j100303a033, 1987a.

Wallington, T. J. and Kurylo, M. J.: The gas phase reactions of hydroxyl radicals with a series of aliphatic alcohols over the temperature range 240-440 K, Int. J. Chem. Kinet., 19, 1015-1023, 10.1002/kin.550191106, 1987b.

Wallington, T. J., Guschin, A., and Hurley, M. D.: Comment:A kinetic study of chlorine radical reactions with ketones by laser-photolysis technique by Olsson et al, Int. J. Chem. Kinet., 30, 309-310, 10.1002/(sici)1097-4601(1998)30:4<309::aid-kin10>3.0.co;2-c, 1998.

Wallington, T. J., Dagaut, P., Liu, R., and Kurylo, M. J.: Rate constants for the gas phase reactions of OH with C5 through C7 aliphatic alcohols and ethers: Predicted and experimental values, Int. J. Chem. Kinet., 20, 541-547, 10.1002/kin.550200704, 1988.

Wallington, T. J., Siegl, W. O., Liu, R., Zhang, Z., Huie, R. E., and Kurylo, M. J.: The atmospheric reactivity of alpha-methyltetrahydrofuran, Environ. Sci. Technol., 24, 1596-1599, 10.1021/es00080a022, 1990.

Wallington, T. J., Ninomiya, Y., Mashino, M., Kawasaki, M., Orkin, V. L., Huie, R. E., Kurylo, M. J., Carter, W. P. L., Luo, D., and Malkina, I. L.: Atmospheric Oxidation Mechanism of Methyl Pivalate, (CH3)3CC(O)OCH3, J. Phys. Chem. A, 105, 7225-7235, 10.1021/jp010308s, 2001.

Wang, W. J., Yuan, B., Peng, Y. W., Su, H., Cheng, Y. F., Yang, S. X., Wu, C. H., Qi, J. P., Bao, F. X., Huangfu, Y. B., Wang, C. M., Ye, C. S., Wang, Z. L., Wang, B. L., Wang, X. M., Song, W., Hu, W. W., Cheng, P., Zhu, M. N., Zheng, J. Y., and Shao, M.: Direct observations indicate photodearadable oxygenated volatile organic compounds (OVOCs) as larger contributors to radicals and ozone production in the atmosphere, Atm. Chem. Phys., 22, 4117-4128, 10.5194/acp-22-4117-2022, 2022.

Watanabe, K.: The toxicological assessment of cyclopentyl methyl ether (CPME) as a green solvent, Molecules, 18, 3183-3194, 10.3390/molecules18033183, 2013.

Watanabe, K., Yamagiwa, N., and Torisawa, Y.: Cyclopentyl Methyl Ether as a New and Alternative Process Solvent, Org. Process Res. Dev., 11, 251-258, 10.1021/op0680136, 2007.

World Health Organization - IARC monographs on the evaluation of carcinogenic risks to humans.: http://monographs.iarc.fr/ENG/Classification/index.php, last

Winterton, N.: The green solvent: a critical perspective, Clean Technol. Environ. Policy, 23, 2499-2522, 10.1007/s10098-021-02188-8, 2021.

Wollenhaupt, M., Carl, S. A., Horowitz, A., and Crowley, J. N.: Rate Coefficients for Reaction of OH with Acetone between 202 and 395 K, J. Phys. Chem. A, 104, 2695-2705, 10.1021/jp993738f, 2000.

Yamada, T., Taylor, P. H., Goumri, A., and Marshall, P.: The reaction of OH with acetone and acetone-d6 from 298 to 832 K: Rate coefficients and mechanism, J. Chem. Phys., 119, 10600-10606, 10.1063/1.1619950, 2003.

Zhang, R. M., Truhlar, D. G., and Xu, X.: Kinetics of the Toluene Reaction with OH Radical, Research, 2019, 5373785, 10.34133/2019/5373785, 2019.

Zhou, C.-W., Simmie, J. M., Pitz, W. J., and Curran, H. J.: Toward the Development of a Fundamentally Based Chemical Model for Cyclopentanone: High-Pressure-Limit Rate Constants for H Atom Abstraction and Fuel Radical Decomposition, J. Phys. Chem. A, 120, 7037-7044, 10.1021/acs.jpca.6b03994, 2016.

Zhou, H., Song, J., Meng, Q., He, Z., Jiang, Z., Zhou, B., Liu, H., and Han, B.: Cooperative catalysis of Pt/C and acid resin for the production of 2,5-dimethyltetrahydrofuran from biomass derived 2,5-hexanedione under mild conditions, Green Chem., 18, 220-225, 10.1039/C5GC01741F, 2015.